The use of surface generation in the design and analysis of linkages with different types of singularities in the configuration space

Lopez-Custodio, Pablo

Awarding institution:
King's College London

KING'S COLLEGE LONDON

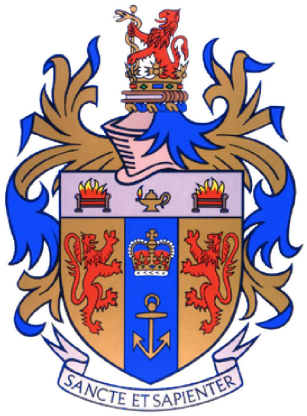

DOCTORAL THESIS

The use of surface generation in the design and analysis of linkages with different types of singularities in the configuration space

---

Author:
Pablo César LÓPEZ-CUSTODIO

Supervisor:
Prof. Jian S. DAI

A thesis submitted in fulfillment of the requirements for the degree of Doctor of Philosophy in Robotics

in the

Centre for Robotics Research
Department of Engineering

December 24, 2020

KING'S COLLEGE LONDON

Abstract

Faculty of Natural & Mathematical Sciences
Department of Engineering

Doctor of Philosophy in Robotics

The use of surface generation in the design and analysis of linkages with different types of singularities in the configuration space

by Pablo César LÓPEZ-CUSTODIO

In mechanisms theory it is often desired to come up with techniques that allow reducing a complex mechanical problem to a simpler mathematical task. The use of surfaces generated by kinematic chains in the analysis and design of linkages reduces the problem to the analysis of surfaces in three dimensional space. Hence, the rich knowledge on surfaces and their intersections becomes a powerful tool to solve the problem.

Surfaces generated by kinematic chains were used to aid the design of linkages since as early as the 70s. However, after a few publications, several of which remained rather obscure conference papers, the technique was abandoned. More recently, the analysis of the intersection of surfaces was applied in the design of reconfigurable mechanisms, a topic still not of the interest of researchers when generated surfaces were explored first. This recent application opened the doors to the question whether the use of surfaces could help the design and analysis of linkages for other purposes and unsolved problems in the research field.

Therefore, in this thesis, surfaces generated by kinematic chains are further explored to bring fresh results including kinematotropic linkages, paradoxical reconfigurable linkages, reconfigurable parallel manipulators that can change their number of degrees of freedom between three different values, and spatial linkages with a cusp in their configuration space. Furthermore, the use of generated surfaces will prove the existence of other types of singularities which had not being explored before, namely the intersection of cusp and curves, and the intersection of cusp and surfaces. Similarly, in this thesis, a method for designing linkages with a tangential intersection in the configuration space is presented for the first time.

In this thesis, the use of generated surfaces is combined with other techniques including group theory and screw theory, while local analysis is carried out by computation of the kinematic tangent cone at the analysed configuration. The results presented in this thesis prove the reduction to generated surfaces is an effective tool in research in mechanisms theory.

Acknowledgements

I would like to thank my mum Alicia Custodio-Malagón for her courage, support and patience. I thank my brothers Juan and Martín López-Custodio for being always a helping hand during these three and a half years. I also thank my father, Sigfrido López-Zamudio, who always supported me during the first year of this PhD and whose courage motivated me to obtain the results here presented.

I thank my supervisor, Professor Jian S. Dai, for his backing, help and advice, and for having given me the opportunity to work in one of his EPSRC projects. I thank Professor José María Rico for not only being a collaborator, an adviser, and a BSc and MSc supervisor, but also a friend and a mentor. Similarly, I would like to thank Professor Andreas Müller for teaming up with me in several of the topics presented in this thesis and for providing encouragement and theoretical advice to my research. I also thank Dr. Gerardo Pérez-Soto, who eagerly helped me in the processes needed to start the PhD.

I thank my friends for their unconditional support: Henry Torres, Rubén "el seco" Martínez, Iván "el rocker" Guzmán, Dr. Jorge "el jorjo" Salmón, George "el flaco" Abrahams, Anastasita Zaleska, Jack "Yako" Kingers, Iveta Ivanova, Dr. Marc "la rata" Mora, Mayela Romero, Amaresh Shukla, Pablo "el wano" Olvera, Elena Santojas, Dr. Tsvetan "Steve" Jivkov, Tamás "the crazy Hungarian" Körmendi, Oliver Denton-Turner and Dr. Nilushi Wijeyasinghe.

I thank the Mexican National Council for Science and Technology (CONACyT) and the Advanced Kinematics and Reconfigurable Robotics Lab at KCL for the economic support required during my doctoral studies. I also acknowledge the financial support from the Engineering and Physics Sciences Research Council (EPSRC), projects with identifiers EP/P026087/1 and EP/S019790/1.

Contents

Abstract iii

Acknowledgements v

1 Introduction 1

2 Fundamentals 5
2.1 Notation . . . 5
2.2 The special Euclidean group, SE(3) . . . 6
2.3 The Lie algebra of the special Euclidean group . . . 8
2.4 Higher order kinematic analyses . . . 11
2.5 The kinematic tangent cone . . . 13
2.6 Reconfigurable mechanisms . . . 15
2.7 Generated surfaces in mechanisms theory . . . 17
2.8 Computational tools used in this thesis . . . 21
2.9 Chapter conclusions . . . 21

3 Toroid-toroid intersections: Bricard line-symmetric mechanisms 23
3.1 Background . . . 23
3.2 Toroids generated by kinematic dyads . . . 25
3.3 The line-symmetric Bricard linkage generator of concentric toroids . . . 27
3.4 Concentric toroid-toroid intersection . . . 29
3.5 The bitangent planes and singularities . . . 30
3.6 Villarceau circles in the toroids intersection and reconfigurability to Bennett mechanisms . . . 32
3.7 A linkage with two Bricard and two Bennett motion branches . . . 33
3.8 The Altmann linkage as a member of this family of special Bricard linkages . . . 36
3.9 Chapter conclusions . . . 37

4 Toroid-toroid intersections: Bricard plane-symmetric mechanisms 39
4.1 Background . . . 39
4.2 Singular toroids generated by RR kinematic chains . . . 40
4.3 Concentric singular toroids generated by the plane-symmetric Bricard linkage 41
4.4 Concentric singular toroid-toroid intersection . . . 43
4.5 Tangent intersections of concentric singular toroids . . . 44
4.6 Isolated points of tangency and Bricard structures . . . 46
4.7 Motion branch reconfiguration through the coincident singularity . . . 49
4.8 Bricard branches as a link between crank-rocker spherical 4R branches . . . 50
4.9 An example with two spherical 4R branches connected through two Bricard plane-symmetric branches . . . 55

5 Design of kinematotropic mechanisms using coincident surfaces: the Bohemian dome **59**
5.1 Background . . . 59
5.2 A method for designing kinematotropic mechanisms based on coincidence of surfaces . . . 60
5.3 The symmetric Bohemian dome and its two generators . . . 62
5.3.1 The symmetric Bohemian dome . . . 62
5.3.2 Two different generators for the same Bohemian dome . . . 63
5.3.3 The two branches of motion of the Bohemian dome generator . . . 64
First parameterization of $\mathcal{S}_A$ . . . 64
Second parameterization of $\mathcal{S}_A$ . . . 66
Some remarks on the shape of $\mathcal{S}_A$ . . . 67
5.4 A kinematotropic linkage that generates coincident Bohemian domes . . . 68
5.5 Relationship between the intersection of generated surfaces and motion branches 69
5.6 Intersection curves . . . 70
5.6.1 Case 3: $\mathcal{S}_A \cap \mathcal{B}$ . . . 70
5.6.2 Case 4: $\mathcal{S}_A \cap \mathcal{S}_B$ . . . 72
5.7 Summary of motion branches . . . 74
5.8 Singularities in the configuration space . . . 76
5.8.1 Singularities occurring in case 1 . . . 76
5.8.2 Singularities occurring in cases 2 and 3 . . . 78
5.8.3 Singularities occurring in case 4 . . . 79
5.9 Chapter conclusions . . . 80

6 A Kinematotropic parallel manipulator with three motion branches, each of different mobility **83**
6.1 Background . . . 83
6.2 Geometry of the parallel mechanism . . . 84
6.3 Motion of point E when leg C is disconnected . . . 86
6.4 Description of the motion of the parallel mechanism when leg C is connected 89
6.5 Mobility analysis at both singular configurations . . . 90
6.5.1 3 DOF to 2 DOF: singularity $\mathbf{q}_{3,2}$ . . . 90
6.5.2 3 DOF to 1 DOF: singularity $\mathbf{q}_{3,1}$ . . . 91
6.6 Chapter conclusions . . . 93

7 A synthesis method for 1-DOF mechanisms with a cusp in the configuration space **95**
7.1 Background . . . 95
7.2 Planar Mechanisms with Cusp Singularities in the C-Space . . . 96
7.2.1 The Double-Watt Mechanism . . . 96
7.2.2 Generalization to Other Planar Mechanisms . . . 97
7.3 Generation of Spatial Curves Whose Projections on Certain Planes Exhibit Inflection Points . . . 99
7.3.1 The Basic Principle . . . 99
7.3.2 Generating Curves with Inflection Points by Projecting the Intersection of Surfaces . . . 101
7.4 Construction of cusp mechanisms . . . 103
7.4.1 Mechanical Generators for the Intersection of Surfaces . . . 103
7.4.2 Interconnection of the Curve Generator with its Mirrored Copy . . . 104
7.4.3 Summary of the Proposed Method . . . 104
7.5 Examples . . . 105

7.5.1 A Spatial Mechanism Generating Planar Curves . . . 106
7.5.2 A Double-Koenigs Mechanism . . . 108
7.5.3 A Kinematotropic Double-Bricard Mechanism . . . 112
7.6 Chapter conclusions . . . 115

8 Tangential intersection of branches of motion 117
8.1 Background . . . 117
8.2 Transversal and tangential intersections in the configuration space . . . 120
8.3 Identification of tangential intersections of branches of motion of the same dimension . . . 122
8.4 Design of 1-DOF linkages with a tangential intersection in the configuration space . . . 123
8.5 Examples . . . 124
8.5.1 Case 1: A line-symmetric-based 7R mechanism . . . 124
8.5.2 Case 2: A Schatz-based 7R mechanism . . . 126
8.6 Chapter conclusions . . . 130

9 Solutions for IKP and FKP of an Exechon parallel robot using a generated toroid 131
9.1 Background . . . 131
9.2 Geometry of the ideal Exechon robot . . . 133
9.3 The Exechon robot with offset errors in the base revolute joints . . . 134
9.3.1 Geometry of the inserted offsets . . . 134
9.3.2 Mobility of the parallel module of the Exechon robot with offsets . . . 136
9.4 Inverse kinematics of the Exechon robot with offsets in the base revolute joints 137
9.4.1 Analysis of the parallel module for the IKP . . . 137
9.4.2 Analysis of the serial module for the IKP . . . 142
9.5 Forward kinematics of the Exechon robot with offsets in the base R joints . . . 143
9.5.1 Analysis of the parallel module for the FKP . . . 143
9.5.2 Analysis of the serial module for the FKP . . . 145
9.6 Constraint system . . . 145
9.7 Effects of offsets in the position of the moving platform . . . 146
9.8 Chapter conclusions . . . 148

10 General Conclusions 151

A Solutions for the toroids parameters in the line-symmetric case 153

B Wrench of constraints of leg 2 of the Exechon PKM 155

C Multiple solutions for the IKP and the FKP of the Exechon robot 157
C.1 Solutions of the IKP of the parallel module . . . 157
C.2 Solutions of the FKP of the parallel module . . . 157

References 161

List of Figures

2.1 Composition of Euclidean displacements ψ_1 and ψ_2. Figure taken from [29] . 6
2.2 All subgroups of SE(3) and their relation of inclusion. The dimension is indicated by the numbers on the right. This figure is adapted from [46] 8
2.3 Serial kinematic chain with n joints. Figure taken from [50] 11
2.4 Bifurcation in the configuration space of a planar 4-bar mechanism. 14
2.5 The Nuremberg scissors, a kinematotropic linkage. 17
2.6 Two surface generators and a resulting closed-loop linkage. 19
2.7 A degree 8 algebraic surface generated by a hybrid kinematic chain. 20

3.1 The general line-symmetric case of Bricard linkage. 24
3.2 An RR dyad generating a general toroid. 26
3.3 The line-symmetric Bricard linkages that can be analyzed as the intersection of two concentric toroids. 27
3.4 Diagram of the line-symmetric case with $s_A = s_B = 0$. a) Assembly with $v_A = -v_B$ and b) assembly with with $v_A = v_B$. 28
3.5 Intersection of toroids A and B and their bi-tangent plane with the XZ plane. . 31
3.6 Cases with circles (in bold curves) in the intersection. a) Villarceau circles and b) secondary circles. In both cases points 1 through 4 are permanent points of tangency. In b) 5 and 6 are points of tangency in the XZ plane . . . 33
3.7 A toroid and a rotated copy of itself sharing secondary circles: a) $\theta = 2\gamma^*$, and b) $\theta = \pi - 2\gamma^*$ 34
3.8 An example of reconfigurable Bricard linkage which can evolve to two different types of Bennett linkage. The intersection of the two concentric toroids is composed of 4 circles $\mathscr{C}_i$, $i = 1,\ldots,4$. The bifurcation points are labeled as P_i, $i = 1,\ldots,6$. The linkage is shown in a singular configuration with $E = P_5$. 35
3.9 The four curves of u_A versus u_B obtained from the motion branches of the linkage. Bifurcation points are located in relation with fig. 3.8. a) toroidal representation, b) Cartesian plot. 35
3.10 Different positions for an example of line-symmetric mechanism where the generated toroids intersect in two circles. 36

4.1 The general plane-symmetric case of Bricard linkage. 40
4.2 An RR dyad generating a singular toroid ($r = l, s = 0$). 41
4.3 The concentric singular toroids intersection: a) surfaces, b) resultant Bricard plane-symmetric mechanism. 42
4.4 Common perpendicular diagram for the plane-symmetric linkage. 43
4.5 Two singular toroids that are tangent to each other in the $X_A Z_A$ plane. 45
4.6 A Bricard plane-symmetric linkage with finite mobility zero in its two different assembly modes. 47
4.7 A Bricard plane-symmetric linkage with finite mobility zero in the assembly mode with $E(\mathbf{q}_1) = P_1$. 48
4.8 A case with two singular curves in the intersection: a) $\mathscr{B}_A$ and $\mathscr{B}_B$ curves, b) surfaces and intersection. 49

4.9 A reconfigurable Bricard plane-symmetric linkage in its spherical 4R operation mode, with its two secondary circles tangent to each other and to curve $\mathscr{C}_1$ and the mechanism is about to escape to V_1. 51
4.10 A plane-symmetric configuration of a spherical 4R linkage with two opposite links of the same angle. 51
4.11 Tangent vectors to the intersection curves at the coincident singularities, for the three possible cases: $r_A > r_B$, $r_A = r_B$ and $r_A < r_B$ 54
4.12 Two cases of branch reconfiguration diagrams when the intersection of concentric singular toroids is composed of two singular curves: a) $r_A < r_B$ and $\gamma_A \neq \gamma_B$ (example presented in this subsection); b) $r_A = r_B$ and $|\gamma_A| = |\gamma_B|$. . . 55
4.13 A reconfigurable Bricard plane-symmetric linkage that allows the reconfiguration between two spherical 4R branches through two Bricard branches. The intersection of the concentric singular toroids is composed of two singular curves. 56
4.14 Several configurations of the plane-symmetric Bricard linkage when the intersection of concentric toroids contains two singular curves. 57

5.1 A kinematotropic mechanism obtained from coincident cylinders: a) singular configuration, b) 2-DOF regular configuration and c) 1-DOF regular configuration 62
5.2 The symmetric Bohemian dome, a) construction, b) two different sets of circles that generate the same surface 63
5.3 Two mechanical generators for the symmetric Bohemian dome: a) generator A with base circle C_{A1} on $xy-$plane, b) generator B with base circle C_{B1} on $yz-$plane 64
5.4 Bohemian dome hybrid generator in an antiparallel configuration. 65
5.5 Two solutions for the parallelogram 4-bar linkage. 66
5.6 The intersection of antiparallel bars drawing an ellipse. 67
5.7 Surface $\mathcal{S}_A$ generated by the Bohemian dome generator in antiparallel mode, for a case with $l_3 = l_2/2$. a) Surface showing several circles drawn on it, b) cut view showing self-intersections 68
5.8 A kinematotropic linkage that generates coincident Bohemian domes. 68
5.9 Case 3: $\mathcal{S}_A \cap \mathcal{B}$. 71
5.10 Intersection curves obtained in SolidWorks in case 3: a) whole set of curves, b) curves $SB1,\ldots,SB4$, c) curves $SB5$ and $SB6$, d) $SB7,\ldots,SB10$ 72
5.11 a) Case 4: $\mathcal{S}_A \cap \mathcal{S}_B$. b) Four curves meeting at Q_4 in case 4. 73
5.12 Intersection curves obtained in SolidWorks for case 4: a) whole set of curves, b) curves $SS1$ and $SS3$, c) curves $SS2$ and $SS4$, d) curves $SS5,\ldots,SS8$ 75
5.13 The linkage in different configurations belonging to three branches of the Case 1. 76
5.14 The linkage in different configurations belonging to four branches of the Case 2. 77
5.15 The linkage in a configurations belonging to V_{SB8} in Case 3. 77
5.16 The linkage in different configurations belonging to three branches of the Case 4. 78
5.17 Connections between motion branches through singular configurations of the linkage. 80

6.1 The kinematotropic parallel mechanism to be analyzed. 84
6.2 Leg 1 of the parallel mechanism. 85
6.3 Leg C of the parallel mechanism. 85
6.4 Leg 1 in singular configuration a) $\mathbf{q}^{\mathrm{G}}_{\mathrm{PT}}$ and b) $\mathbf{q}^{\mathrm{G}}_{\mathrm{PR}}$. 87

6.5 The two surfaces generated by the 3-RGR-1-CU parallel mechanism. 89
6.6 3-RGR-1-CU parallel mechanism in a) singular configuration $\mathbf{q}_{3,2} \in V_3 \cap V_2$, b) a regular configuration in V_2 and c) a regular configuration in V_3. 92
6.7 3-RGR-1-CU parallel mechanism in a) singular configuration $\mathbf{q}_{3,1} \in V_3 \cap V_1$, b) a regular configuration in V_1 and c) a regular configuration in V_3. 94

7.1 Double-Watt mechanism presented by Connelly and its generated coupler curves. 97
7.2 Curves generated by the coupler bars of both 4-bar Watt loops in the Connelly mechanism. 97
7.3 An example of Evans straight line mechanism. 98
7.4 The double-Evans cusp mechanism: a) Cusp singularity. b) and c) two configurations near the cusp. 98
7.5 a) A curve (and its reflection) in 3-space which can be projected onto a plane as a curve with an inflection point. b) A sphere of radius l and center moving through such curve. 100
7.6 The curve $\mathscr{C}_1$ as the intersection of two cylinders and its projection onto rectifying plane. a) The projection happens at a non-zero torsion point and the surfaces are reflected. b) The projection occurs at a zero-torsion point. . . 102
7.7 The Viviani curve as an intersection of surfaces and its projection onto a plane parallel to the tangent plane at the self-crossing. 102
7.8 The four different cases of one-loop mechanisms obtained from the intersection of surfaces. 104
7.9 The general form of a cusp mechanism in the case in which two revolute joints allow the motion about E_1 and E_2 at $\mathscr{C}_1$ and $\mathscr{C}_2$, respectively. 105
7.10 The intersection of two surfaces that leads to a planar curve with inflection points. a) Surfaces setup. b) Overconstrained mechanism that generates such curve. c) Reflection of the intersection curve 106
7.11 a) A mechanism that generates two planar curves of the cosine form in a cusp configuration. b) Topological graph 107
7.12 The intersection of two cylinders that has a projection with an inflection point. a) Surfaces setup. b) The Koenigs joint that generates such intersection. c) reflection of the intersection curve 109
7.13 A double-Koenigs mechanism in a cusp configuration. 110
7.14 Different branches of the configuration space intersecting at $\mathbf{q}_0$. 111
7.15 The intersection of two toroids that has a projection with an inflection point. a) Surfaces setup. b) The Bricard plane-symmetric 6R mechanism that generates such intersection. c) reflection of the intersection curve. 113
7.16 A double-Bricard mechanism in a cusp configuration. 114
7.17 Different branches of the configuration space intersecting at $\mathbf{q}_0$. 116

8.1 A 4-bar mechanism and a singularity in its configuration space. 118
8.2 A configuration space with a tangential and a transversal intersection at $\mathbf{q}_0$. . 120
8.3 Intersection of 1-dimensional subvarieties: a) transversal case and b) tangential case. 121
8.4 Joint axes of a 1-DOF mechanism with tangential intersections in the configuration space. 123
8.5 A line-symmetric-based 7R mechanism with a tangential intersection in the configuration space. 125
8.6 Branches of motion of the line-symmetric-based 7R mechanism. 127

8.7 A Schatz-based 7R mechanism with a tangential intersection in the configuration space. . . . 128
8.8 Branches of motion of the Schatz-based 7R mechanism. . . . 130

9.1 Diagram of a more general Exechon robot, taken from [168]. . . . 132
9.2 The ideal Exechon hybrid robot 133
9.3 Structural dimensions of the ideal Exechon hybrid robot and planes Π and Λ . 134
9.4 Exechon robot with offset errors in the base R joints 135
9.5 Equivalent mechanisms obtained by reducing the parallel module of the Exechon robot with offsets inserted. . . . 136
9.6 Definition of coordinate system C and variables a) α and b) θ. . . . 138
9.7 Point A_{2b} lying on a toroid. . . . 139
9.8 Four possible configurations of legs 1 and 3 for the same pose of the end-effector and leg 2. . . . 141
9.9 Initial configuration of the serial module. . . . 142
9.10 Constraint system of leg 1. . . . 145
9.11 Contour plot of the workspace of the ideal Exechon robot approximated using the tested configurations. Level 1, $z_0 = 794.1$; level 2, $z_0 = 749.2$; level 3, $z_0 = 704.3$; level 4, $z_0 = 659.4$; level 5, $z_0 = 614.5$; level 6, $z_0 = 569.6$; level 7, $z_0 = 524.7$; level 8, $z_0 = 479.8$; and level 9, $z_0 = 434.9$ 147
9.12 Workspace of Exechon robot with projections on the $y_O z_O$ and $x_O y_O$ planes (top right and bottom right, respectively). The clearer the dots, the larger the deviation of the moving platform if all offsets are introduced except that of leg 3. . . . 148

C.1 16 solutions for the inverse kinematics problem of the parallel module with ${}^O\mathbf{r}_S = (300, 500, 900)$ mm. With every solution, the obtained vector $[q_{13}, q_{24}, q_{33}]$ is presented. (continues in figure C.2) 158
C.2 (continuation of figure C.1) 16 solutions for the inverse kinematics problem of the parallel module with ${}^O\mathbf{r}_S = (300, 500, 900)$ mm. With every solution, the obtained vector $[q_{13}, q_{24}, q_{33}]$ is presented. . . . 159
C.3 16 solutions for the FKP of the parallel module with $q_{13} = 670$mm, $q_{24} = 570$mm and $q_{33} = 800$mm. With every solution, the obtained vector ${}^O\mathbf{r}_S$ is presented. (continues in Fig. C.4) 160
C.4 (Continuation of Fig. C.3) 16 solutions for the FKP of the parallel module with $q_{13} = 670$mm, $q_{24} = 570$mm and $q_{33} = 800$mm. With every solution, the obtained vector ${}^O\mathbf{r}_S$ is presented. . . . 160

List of Tables

8.1 Different types of intersections between motion branches. (*Examples of mechanisms exhibiting singularities of the cases 1 and 2 are very common. The references cited here are just a sample of publications focusing exclusively in this kind of mechanisms.) 119

9.1 Dimensions and joint limits of the example. 146
9.2 Comparison of the position, ${}^{O}\mathbf{r}_{S}$, and orientation, ${}^{O}_{S}\mathbf{R}$, of the end effector and constraint of leg 2, ${}^{O}\mathbf{W}_{c21}$, between the ideal case and the case with 1mm offset inserted in all base joints except that of leg 3. 148

List of Abbreviations

R	**R**evolute joint
P	**P**rismatic joint
H	**H**elical joint
C	**C**ylindrical joint
U	**U**niversal joint
S	**S**pherical joint
DH	**D**enavit-**H**artenberg
FKP	**F**orward **K**inematics **P**roblem
IKP	**I**nverse **K**inematics **P**roblem
PKM	**P**arallel **K**inematic **M**achine
C-Space	**C**onfiguration space
w.r.t.	**W**ith **r**espect **t**o
w.l.o.g.	**W**ithout **l**oss **o**f **g**enerality
e.g.	**E**xempli **g**ratia
i.e.	**I**d **e**st

List of Symbols

$\mathbb{S}$	Circle.
$\mathbb{R}$	Real numbers.
$\mathbb{Z}$	Integer numbers.
$\mathbb{Z}_+$	Natural numbers.
$\mathbb{T}^n$	n-dimensional torus.
$\mathbb{V}^n$	Cartesian product of any n fields.
$\mathbb{K}[x_1,\ldots,x_n]$	The set of all polynomials in $x_1,\ldots,x_n$ with coefficients in the field $\mathbb{K}$
$\emptyset$	The empty set.
im	Image of a map.
dim	Dimension.
sing	Singular part of a variety.
span	Linear span.
rank	Rank of a matrix.
ker	Kernel of a linear transformation.
$\text{aug}(\mathbf{v}_1,\ldots,\mathbf{v}_n)$	Augmented matrix with columns $\mathbf{v}_1,\ldots,\mathbf{v}_n$.
$\text{skew}(\mathbf{v})$	Skew matrix of $\mathbf{v}\in\mathbb{R}^3$.
$()^{\text{t}}$	Transpose of a matrix.
$\mathcal{N}_P$	Neighborhood around point P.
id_G	Identity element of group G.
∇	Gradient of a multivariable scalar function.
$\mathcal{L}(U_1,\ldots,U_n;W)$	The vector space of multilinear transformations from $U_1\times\ldots\times U_n$ to W.
$\mathscr{L}(\hat{\mathbf{u}},P)$	The line that is parallel to $\hat{\mathbf{u}}\in\mathbb{S}^2$ and contains point P.
$\pi_{\hat{\mathbf{u}}}(\mathbf{v})$	Projection of vector $\mathbf{v}\in\mathbb{R}^3$ onto a plane that is perpendicular to $\hat{\mathbf{u}}\in\mathbb{S}^2$ and contains the origin.
$d(P,Q)$	Euclidean distance between points P and Q.
$\varnothing$	Diameter
$T_P\mathcal{A}$	Tangent space to the analytic variety $\mathcal{A}$ at the point $P\in\mathcal{A}$.
$[,]$	Lie bracket in se(3).
$\text{Rot}(\theta,\hat{\mathbf{u}})$	Rotation matrix in SO(3) that generates a rotation of θ radians about an axis parallel to $\hat{\mathbf{u}}\in\mathbb{S}^2$ and passing through the origin of the specified coordinate system.
$\text{Ref}(\hat{\mathbf{u}})$	Reflexion matrix in O(3)\SO(3) that generates a reflexion about a plane that contains the origin and has normal $\hat{\mathbf{u}}\in\mathbb{S}^2$.
$\text{HT}(\mathbf{R},\mathbf{t})$	Homogeneous transformation matrix in $\mathbb{R}^{4\times4}$ and SE(3), obtained from $\mathbf{R}\in\text{SO}(3)$ and $\mathbf{t}\in\mathbb{R}^3$.
$\mathbf{S}$	An infinitesimal screw. Sometimes, specially when a coordinate system is specified, $\mathbf{S}$ represents the screw coordinates in $\mathbb{R}^6$ of such element of se(3).
$\text{Adj}(\psi)$	Adjoint representation of displacement $\psi\in\text{SE}(3)$.
$\exp(a\mathbf{S})$	Exponential mapping that generates a finite displacement in SE(3) of magnitude a, about/along axis $\mathbf{S}\in$se(3).

V	(Feasible) configuration space of a kinematic chain.
$C_P^{\mathrm{K}}V$	Kinematic tangent cone at $P \in V$.
$\alpha_{i,j}$	DH parameter of twist angle between axes i and j in the proximal convention
$a_{i,j}$	DH parameter of link length between axes i and j in the proximal convention
d_i	DH parameter of axial displacement through axis i in the proximal convention
$Y_R(\hat{\mathbf{u}}, Q)$	Cylinder of radius R and axis $\mathscr{L}(\hat{\mathbf{u}}, Q)$.
$K_\gamma(\hat{\mathbf{u}}, Q)$	Cone with vertex at Q, axis parallel to $\hat{\mathbf{u}}$ and inclination angle γ.
$T_{l,r,\gamma,s}(\hat{\mathbf{u}}, Q)$	Toroid with base circle of radius l, secondary circle of radius r, angle between the normals of these circles γ and secondary offset s. $\hat{\mathbf{u}}$ is parallel to the toroid's axis and Q is the origin.
$W_{h,\gamma,d}(\hat{\mathbf{u}}_1, \hat{\mathbf{u}}_2, Q)$	Ruled helicoid where h is the pitch; γ, the angle between rules and axis; $\hat{\mathbf{u}}_1$, the vector parallel to the axis and in positive direction of the helix; $\hat{\mathbf{u}}_2$, perpendicular vector to the axis and the initial rule pointing outside the helicoid; and Q the origin.

In loving memory of Sigfrido López-Zamudio (1956-2017)

Chapter 1

Introduction

The design and analysis of mechanisms for specific tasks or purposes is a complex problem. Sometimes it becomes convenient to visualize in 3-dimensional space what a kinematic chain is able to do, and therefore, it is easier to manipulate its parameters to obtain the desired behaviour of the linkage. This idea leads to the method of generated surfaces.

This is a rather old technique, since as early as the 60s, Jenkins et al. [1] not only established the technique but also presented must of the useful properties of these surfaces and their intersection. Relatively few publications on the topic can be found in the literature, most of them were actually published immediately after Jenkins' paper. In this period, Torfason [2], [3] presented a table with beautiful hand-made illustrations of the possible shapes of surfaces generated by kinematic dyads, he would solve the intersection of these surfaces using numerical methods with the computational power of the time. Hunt, who also coauthored Jenkins' paper [1], seemed to be very interested in the technique and would refer to it several times to explain different phenomena, including dwell motion [4], constant-velocity coupling [5] and the existence of paradoxical linkages [6].

Surfaces as the key in the design and analysis of mechanisms became fairly uncommon after the 70s. It is likely that the work presented by Hunt, Crossley, Torfason and Jenkins covered most of the topics that were of interest at the time. On top of this, the complexity of computing the intersection between two surfaces may have undermined the appeal of the method. And it is in the 90s when Liu and Zsombor-Murray [7] publish a paper tackling such a problem of computing the intersection of two generated surfaces, although their discussion is limited to quartics, the most common shapes generated by 2-DOF kinematic dyads are actually quartics, e.g. a general RR chain generates a toroid, and an RP chain, a hyperboloid. Yet geometry remains the most powerful tool in mechanisms theory, and therefore, the use of surfaces was never completely abandoned. For example, in more recent publications, Lee and Hervé [8] draw on the intersection of two cylinders to describe the motion of RCCR constant-velocity shafts, commonly called Koenigs joints. Lee and Hervé also seemed to have the same fascination for generated toroids that Hunt had and went more in depth in explaining the four different types of paradoxical Bennett linkages using toroids [9]. Su and McCarthy [10] presented a fresh application of the method by letting the mobile platform of PKMs move on three surfaces, each generated by a leg, a method for the synthesis of PKMs was then obtained.

The search for reconfigurable mechanisms, which increased during the first two decades of this century saw a new application for the method of generated surfaces. López-Custodio et al. [11] explained how to manipulate surfaces to design reconfigurable linkages with constant and variable mobility.

Although Jenkins et al. [1] had warned that a crossing of two curves in the intersection set of two surfaces would lead to a singularity between two "branches", the possibility was never explored, maybe because reconfigurable mechanisms was still not a topic of interest at the time. However, nowadays, reconfigurable mechanisms is big topic in mechanisms theory, the fascination for drastic transformations in the way a linkage works has become the term

"reconfigurable mechanisms" into an umbrella that encompasses a wide variety of devices. This term includes *kinematotropic linkages* which can vary their number of degrees of freedom [12]–[17], *deployable linkages*, which can drastically change in size and shape (see for example [18]–[21]), and *metamorphic linkages* [22], [23], which involve link annexation and topology change or joint property change to achieve reconfiguration which can also result in a mobility change [24]–[28].

After the method of generated surfaces was used to aid the design of reconfigurable mechanisms and [11] and [29] were published, several questions arose:

1. In [29], López-Custodio stated that apparently the intersection of two helicoids would lead to a linkage with an infinity of branches of motion, something that had never been reported before, however it was not possible to prove this because the intersection set is too complex to be computed with the tools in hand. A first question was whether this suspicion was correct.

2. One of the examples presented in [11] was an Altmann linkage obtained by the intersection of two (right) tori and by applying the method for reducing a S pair into two R joints, which was presented in the same contribution. The Altmann linkage is a very special case of line-symmetric Bricard linkage, a paradoxical linkage. An immediate question was then, can general toroids be manipulated to design other Bricard paradoxical linkages that are reconfigurable?

3. Jenkins et al. [1], as the vast majority of the publications related to generated surfaces, used dyads (2-joint serial chains) as mechanical generators of the surfaces. However, they explained that any 2-DOF kinematic chain can be used as generator. This possibility was never explored. What kind of surfaces can be generated by closed-loop and hybrid 2-DOF kinematic chains? Will they be useful in the design of mechanisms?

4. Apparently, Su and McCarthy [10] were the only researchers who used surfaces in to design parallel manipulators. But they did not use the idea of intersecting surfaces and let a point in the linkage follow the intersection set. Can interesting parallel manipulators be designed by intersecting surfaces?

5. This research opened the doors to apply this method to other unsolved questions in mechanisms theory. What other applications to modern problems can be given to the technique of generated surfaces?

The first question would have been answered by the author of this thesis in [30], where families of mechanisms with an infinity of branches of motion were presented for the first time. This thesis work aims to answer the other four questions. As such, the following original contributions are presented:

- Reconfigurable Bricard 6R linkages are designed systematically by manipulating the intersection of two toroids. Families of reconfigurable line-symmetric and plane-symmetric Bricard 6R linkages are obtained.

- From the previous point, a purely geometrical explanation for the Bennett and spherical 4R behaviors of Bricard linkages that are sometimes reported in the literature, is presented.

- A plane-symmetric Bricard linkage with no movable configurations is obtained. Examples of rigid Bricard linkages are rare. The author of this thesis is only aware of the line-symmetric example discussed in [31]–[33]. However, such an example is always movable when the assembly preserves the line symmetry, while its rigid assembly,

known as 'chair form', is not line-symmetric. The Bricard 6R linkage presented in this thesis maintains its plane symmetry in its pair of rigid assemblies.

- A method for the design of kinematotropic linkages using generated surfaces is presented for the first time. Although in [11] it was shown that mobility change is possible by taking advantage of conic singularities, the obtained results were rather simple, relying on partitioned mobility.
- A new explanation for the mobility of Wohlhart's queer square mechanism [12] is presented. The explanation is part of the design of a more complex linkage.
- The self-intersections of surfaces are proved to lead to branches of motion that had not been explained before in the method of generated surfaces.
- The generation of surfaces is used for the first time in the design of a reconfigurable parallel manipulator.
- A parallel manipulator that can change its mobility between three different values is obtained from the previous point. Kinematotropic mechanisms with more than two different values of finite mobility are rather rare. The only non-degenerate example known by the author of this thesis is Wohlhart's 'star cube' [17], [34].
- 1-DOF spatial mechanisms with a cusp in the configuration space are presented for the first time.
- Two new types of c-space singularities are identified in examples of cusp mechanisms: a cusp intersecting a regular curve, and a cusp touching a surface.
- A method for the design of mechanisms with tangential intersections of branches of motion is presented for the first time.
- A method for the identification of tangential intersections using local information is presented for the first time.
- The kinematics of a generalized Exechon robot is obtained. Such a generalization accounts offsets at the base joints of the robot.

This is a thesis written in the mode of incorporation of publications. Each chapter is a publication which was adapted to work as a chapter of a single document, rather than a stand-alone manuscript. Notation and terminology was also homogenised. The thesis is organised as follows:

- Chapter 2 presents a brief review of the fundamental mathematical tools used in the thesis as well as the concepts of mechanism theory required in the thesis.
- Chapter 3 considers the line-symmetric case of Bricard linkages as the intersection of two toroids in order to design reconfigurable paradoxical linkages. This chapter is based on:

  [35] P.C. López-Custodio, J.S. Dai, and J.M. Rico, "Branch reconfiguration of Bricard linkages based on toroids intersections: Line-symmetric case," *ASME Journal of Mechanisms and Robotics*, vol. 10, no. 3, pp. 031003-1–031003–11, 2018.

- Chapter 4 considers the plane-symmetric case of Bricard linkages as the intersection of two toroids in order to design reconfigurable paradoxical linkages. This chapter is based on:

  [36] P.C. López-Custodio, J.S. Dai, and J.M. Rico, "Branch reconfiguration of Bricard linkages based on toroids intersections: Plane-symmetric case," *ASME Journal of Mechanisms and Robotics*, vol. 10, no. 3, pp. 031002-1–031002–12, 2018.

- Chapter 5 presents a method for the design of kinematotropic linkages, as an example, a hybrid kinematic chain is used to generate a Bohemian dome. This chapter is based on:

  [37] P.C. López-Custodio and J.S. Dai, "Design of a variable-mobility linkage using the Bohemian dome," *ASME Journal of Mechanical Design*, vol. 141, no. 9, pp. 092303-1–092303-12, 2018.

- Chapter 6 presents a kinematotropic parallel manipulator which was designed considering the intersection of surfaces generated by the mobile platform. This chapter is based on:

  [38] P.C. López-Custodio, A. Müller and J.S. Dai, "A Kinematotropic Parallel Mechanism Reconfiguring Between Three Motion Branches of Different Mobility," In: Uhl T. (eds) *Advances in Mechanism and Machine Science. IFToMM WC 2019. Mechanisms and Machine Science*, vol 73. Springer, Cham. 2611-2620, (2019)

- Chapter 7 presents the design of mechanisms with a cusp in the configuration space. The method is the first of its kind and is based on the manipulation of intersection curves between surfaces. This chapter is based on:

  [39] P.C. López-Custodio, A. Müller, J.M. Rico and J.S. Dai, "A synthesis method for 1-DOF mechanisms with a cusp in the configuration space," *Mechanisms and Machine Theory*, vol 132, 154-175, (2019).

- Chapter 8 presents the first design method for mechanisms with tangential intersection of branches of motion. Although this method is not based on generated surfaces, it is intrinsically connected to the problem of cusp singularities in chapter 7. This chapter is based on:

  [40] P.C. López-Custodio, A. Müller and J.S. Dai, "Tangential intersection of branches of motion," *Mechanisms and Machine Theory*, vol 147, 103730, (2020).

- Chapter 9 presents a rather simple and straightforward application of a toroid in the solution of the IKP and the FKP of a parallel manipulator. This chapter is based on:

  [41] P.C. López-Custodio, J.S. Dai, R. Fu, and Y. Jin, "Kinematics and constraints of the Exechon robot accounting offsets due to errors in the base joint axes," *ASME. J. Mechanisms Robotics*, vol 12, no 2, 021109, (2020).

- Finally, in chapter 10 some general conclusions are drawn.

Chapter 2

Fundamentals

In this chapter, a background of the theory and methods used in this thesis is presented. The chapter then starts with mathematical concepts and then it moves towards applications in mechanisms theory. Firstly, in Section 2.1 some remarks on notation are given. A brief introduction to the special Euclidean group, SE(3), and its Lie algebra, se(3), is given in sections 2.2 and 2.3, respectively. These two sections aim to present a basic description of SE(3) and se(3) in a language that is more familiar for mechanisms theory researchers than the one generally used in differential geometry books. Once se(3) is introduced in Section 2.3, screw theory can be used, so the problem of kinematic higher order analyses is discussed in Section 2.4. The properties of the configuration space of a linkage and how to locally analyse it using the expressions from Section 2.4, is discussed in 2.5. With machinery developed in these sections, Sections 2.6 and 2.7 introduce, in a natural way, the concept of reconfigurable mechanisms and how this and other types of linkages can be designed using generated surfaces. Finally, in Section 2.8, the different computational tools used in this thesis are briefly discussed.

Several concepts discussed in this chapter have been adapted from [29], [42].

2.1 Notation

The symbols used in this thesis are explained at the beginning of the document. However, extra information about notation and how this is applied is explained in this section.

The notation used for coordinate systems transformations in [43] is adopted in this thesis. Coordinate systems will normally be named with italic capital letters starting at A, i.e. A, B, C,... Due to the large amount of symbols, in chapter 9 *only*, coordinate systems are denoted by capital non-italic letters. ${}^{A}_{B}\mathbf{R} \in \mathrm{SO}(3)$ is the rotation matrix that represents the orientation of coordinate system B w.r.t. A. ${}^{A}_{B}\mathbf{T} \in \mathrm{SE}(3) \subset \mathbb{R}^{4\times 4}$ is the homogeneous transformation matrix that represents the position and orientation of frame B, w.r.t. frame A, then ${}^{B}_{A}\mathbf{T} = {}^{A}_{B}\mathbf{T}^{-1}$.

Points are denoted by capital italic letters starting at O, i.e. O, P, Q,... $\mathbf{r}_{Q/P} \in \mathbb{R}^3$ is the vector with tail at P and tip at Q. If the coordinates of this vector are written in frame A, we write ${}^{A}\mathbf{r}_{Q/P} \in \mathbb{R}^3$. Let frames A and B have origins at O_A and O_B, respectively. Then ${}^{A}\mathbf{r}_{P} := {}^{A}\mathbf{r}_{P/O_A}$ represents the coordinates of point P in frame A. Clearly, ${}^{A}\mathbf{r}_{Q/P} = {}^{A}\mathbf{r}_{Q} - {}^{A}\mathbf{r}_{P}$.

In order to avoid an abuse in notation or the introduction of more symbols, homogeneous transformation matrices are only for conceptual use in this thesis. Therefore, we prefer to write the position of point P in frame B using rotation matrices as follows: ${}^{B}\mathbf{r}_{P} = {}^{B}\mathbf{r}_{O_A} + {}^{B}_{A}\mathbf{R}\,{}^{A}\mathbf{r}_{P}$.

Unit vectors are are written with a hat, e.g. $\hat{\mathbf{u}} \in \mathbb{S}^2$. The ordered triad $\{\hat{\mathbf{i}}_A, \hat{\mathbf{j}}_A, \hat{\mathbf{k}}_A\}$ represent the unit vectors along the $X-$, $Y-$ and $Z-$axes of frame A. Clearly, ${}^{A}\hat{\mathbf{i}}_A := (1,0,0)$, ${}^{A}\hat{\mathbf{j}}_A := (0,1,0)$ and ${}^{A}\hat{\mathbf{k}}_A := (0,0,1)$

2.2 The special Euclidean group, SE(3)

A *group* $(G, \circ)$ is a set G endowed with a binary operation $\circ$, such that the following axioms are satisfied $\forall g, g_1, g_2, g_3 \in G$:

1. Closure w.r.t. $\circ$: $g_1 \circ g_2 \in G$
2. $\circ$ is associative: $g_1 \circ (g_2 \circ g_3) = (g_1 \circ g_2) \circ g_3$
3. $\exists \mathrm{id}_G \in G$ such that: $\mathrm{id}_G \circ g = g \circ \mathrm{id}_G$
4. $\exists g^{-1}$ such that: $g \circ g^{-1} = g^{-1} \circ g = \mathrm{id}_G$

If, in addition, $\circ$ is commutative, i.e. $g_1 \circ g_2 = g_2 \circ g_1$, G is said to be an *abelian group*. A *subgroup* is any subset of G which, when endowed with the same operation, is also a group by itself.

The set of transformations that preserve the Euclidean distance between points form a group along with the composition operation represented in fig. 2.1. This group is called the Euclidean group, E(n), in an $n-$dimensional space. In this thesis n is always 3.

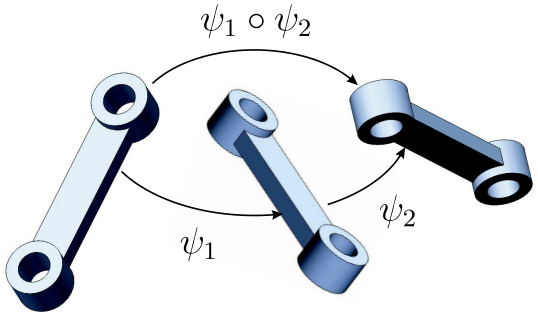

FIGURE 2.1: Composition of Euclidean displacements ψ_1 and ψ_2. Figure taken from [29]

The Euclidean group encompasses translations, rotations and reflexions. Therefore O(3), the *orthogonal group* corresponding to all rotations and reflexions, is a subgroup of E(3). Translations and rotations are commonly known as *rigid body transformations*. These transformations, along with the composition operation, form a subset called the *special Euclidean group*, SE(3). Note that since O(3) is a subgroup of E(3), then SO(3), the special orthogonal group consisting of all rotations, is a subgroup of SE(3). Note that SE(3) is not an abelian group as, in general, the composition of transformations is not commutative.

There exist several representations of SE(3) using different algebraic structures. In this thesis only two of them are applied. The first one is the set of all homogeneous transformation matrices in $\mathbb{R}^{4\times4}$:

$$\mathrm{SE}(3) := \left\{ \begin{pmatrix} \mathbf{R} & \mathbf{t} \\ \mathbf{0} & 1 \end{pmatrix} \middle| \mathbf{R} \in \mathrm{SO}(3) \subset \mathbb{R}^{3\times3}, \mathbf{t} \in \mathbb{R}^3 \right\}$$

where SE(3) is endowed with the typical operation of matrix multiplication to form the group. Remember that $\mathbf{R} \in \mathrm{SO}(3)$ implies both $\mathbf{R}^{\mathrm{t}}\mathbf{R} = \mathbf{I}_3 = \mathbf{R}\mathbf{R}^{\mathrm{t}}$ and $\det(\mathbf{R}) = 1$. In this thesis, a homogeneous transformation matrix can be assembled by its rotation and translation components through the map $\mathrm{HT}(\mathbf{R}, \mathbf{t})$, where $\mathbf{R} \in$SO(3) and $\mathbf{t} \in \mathbb{R}^3$.

The transformation matrices in this representation map points in the physical space, i.e. given the coordinates of a point attached to a rigid body, one can find the coordinates of the same point after the transformation has been applied. The second representation of SE(3) used in this thesis works on lines rather than points, this is particularly useful in screw theory

when working with Plücker coordinates of lines. Such a representation will be introduced in the next section. The representation by *dual quaternions* is another widely used representation of SE(3) which is not applied in this thesis.

The subgroups of SE(3) have been widely studied and have important applications in mechanisms theory and robotics, being Hervé [44] the first in noticing the importance of these subgroups and giving an organised list of them. However, it has been argued [45] that these subgroups had been reported earlier by different mathematicians. The following is an exhaustive list of the subgroups of SE(3):

- **Special Euclidean Group**, SE(3): Improper subgroup.
- **Shoenflies displacements**, X: Rotations about an axis of fixed direction and all translations.
- **Spherical displacements**, SO(3): The special orthogonal group represents all rotations around the origin.
- **General planar displacements**, G: All translations parallel to a fixed plane and rotation about an axis parallel to such plane. Note that G is equal to SE(2).
- **Pure translation**, T(3): All translations.
- **Planar translation of screw motions**, Y: All translations parallel to a fixed plane and screw motion about an axis parallel to such plane.
- **Planar translation**, T(2): All translations parallel to a fixed plane.
- **Cylindrical motions**, C: Rotation about a fixed axis and translation along the same axis.
- **Rotation**, R: Rotation about a fixed axis. Note that R is equal to SO(2).
- **Linear translation**, T(1): Translation along a fixed direction.
- **Screw motion**, H: Screw motion along a fixed axis.
- **Identity**, $\mathrm{id}_{\mathrm{SE(3)}}$: Trivial subgroup.

These subgroups have different dimensions according to the restrictions imposed to the displacements. Fig. 2.2 shows the relation of inclusion of all the subgroups of SE(3) and their dimension.

SE(3) and all of its subgroups can be parametrized in continuous variables. For example, the group of cylindrical displacements about the $Z-$ axis can be parametrized as:

$$\mathrm{C}_Z = \left\{ \begin{pmatrix} \cos a & -\sin a & 0 & 0 \\ \sin a & \cos a & 0 & 0 \\ 0 & 0 & 1 & b \\ 0 & 0 & 0 & 1 \end{pmatrix} \middle| \, a \in \mathbb{T}, b \in \mathbb{R} \right\}$$

Similarly, SO(3) can be parametrized in three angles $\theta_1, \theta_2, \theta_3 \in \mathbb{T}$ representing the roll, pitch and yaw rotations. Since the variables in these parameterizations are always continuous, SE(3) has the structure of a manifold, this property also allows us to talk about their dimension. In addition, the multiplication of two matrices representing the parameterization of elements of SE(3) results in a matrix whose entries are smooth functions of the same variables. Then, it is said that the composition operation in SE(3) is a smooth map. A similar conclusion can be done for the inversion of an element in SE(3). These three properties of

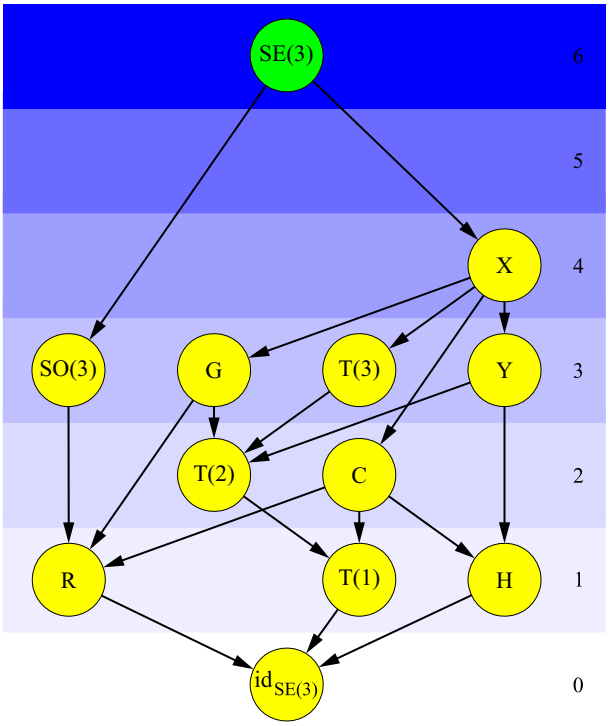

FIGURE 2.2: All subgroups of SE(3) and their relation of inclusion. The dimension is indicated by the numbers on the right. This figure is adapted from [46]

SE(3), manifold structure, smoothness of its binary operation and smoothness of the inversion, make SE(3) a *Lie group* and, as such, it is possible to apply differential calculus to it, therefore it is also said that SE(3) is a *differentiable manifold*.

2.3 The Lie algebra of the special Euclidean group

The non-linear nature of the special Euclidean group makes it difficult to work with. Fortunately, its qualification as a Lie group allows us to obtain a linearization of it, which locally reveals the structure of the group. This linearization is its tangent space at its identity and is given by:

$$T_{\mathrm{id}_{\mathrm{SE}(3)}}\mathrm{SE}(3) := \left\{ \left. \frac{\mathrm{d}\gamma(t)}{\mathrm{d}t}\right|_{t=0} \middle| \, \gamma : \mathbb{R} \to \mathrm{SE}(3) \ni \gamma(0) = \mathrm{id}_{\mathrm{SE}(3)} \right\}$$

In this definition, γ is a one-parameter curve on SE(3) such that it crosses $\mathrm{id}_{\mathrm{SE}(3)}$. Therefore, $T_{\mathrm{id}_{\mathrm{SE}(3)}}\mathrm{SE}(3)$ is a vector space spanned by the tangent vectors to 1-dimensional curves at the origin. Since SE(3) consists of all rigid body displacements, $T_{\mathrm{id}_{\mathrm{SE}(3)}}\mathrm{SE}(3)$ represents the set of all possible velocities at the beginning of motion. Formally, $T_{\mathrm{id}_{\mathrm{SE}(3)}}\mathrm{SE}(3)$ should be denoted by $\mathfrak{se}(3)$, however, in this thesis simple lowercase font is used:

$$\mathrm{se}(3) := T_{\mathrm{id}_{\mathrm{SE}(3)}}\mathrm{SE}(3)$$

se(3) has an algebra[1] structure under the Lie bracket $[,] : \mathrm{se}(3) \times \mathrm{se}(3) \to \mathrm{se}(3)$. The Lie bracket is anti-symmetric and satisfies the *Jacobi identity*, respectively:

- $[\mathbf{X},\mathbf{Y}] = -[\mathbf{Y},\mathbf{X}], \forall \mathbf{X},\mathbf{Y} \in \mathrm{se}(3)$

[1] An *algebra* is a vector space which also presents closure under an additional operation.

- $[\mathbf{X},[\mathbf{Y},\mathbf{Z}]]+[\mathbf{Z},[\mathbf{X},\mathbf{Y}]]+[\mathbf{Y},[\mathbf{Z},\mathbf{X}]]=0, \forall \mathbf{X},\mathbf{Y},\mathbf{Z}\in \mathrm{se}(3)$

Hence, it is said that se(3) is the *Lie algebra* of SE(3). The Lie bracket can be defined as the time derivative at $t=0$ of the conjugation of an element of se(3) by an element of SE(3). Let $\mathbf{X},\mathbf{Y}\in\mathrm{se}(3)$ such that $\mathbf{Y}$ is the tangent to the curve $\gamma:\mathbb{R}\to$SE(3), then the Lie bracket is defined as [47]:

$$[\mathbf{X},\mathbf{Y}] := \left.\frac{\mathrm{d}\left(\gamma(t)\mathbf{Y}\gamma^{-1}(t)\right)}{\mathrm{d}t}\right|_{t=0} \tag{2.1}$$

Since this Lie algebra gives us a linear local approximation of SE(3), it would be very useful to move from this linearization to SE(3) again, namely, given a tangent vector $\mathbf{X}\in$ se(3) identify the corresponding curve $\gamma\subset$ SE(3) to which $\mathbf{X}$ is tangent at $\mathrm{id}_{\mathrm{SE}(3)}$. This is possible using the exponential map $\exp:\mathrm{se}(3)\to\mathrm{SE}(3)$, defined by:

$$\exp(t\mathbf{X})=\gamma(t)$$

where $\gamma:\mathbb{R}\to\mathrm{SE}(3)$ is the corresponding curve to which $\mathbf{X}\in\mathrm{se}(3)$ is tangent at the identity.

To give an expression of the structure of se(3), consider a representation of SE(3) by homogeneous transformation matrices. Let $\mathbf{T}:=\mathrm{HT}(\mathrm{Rot}(a,\hat{\mathbf{s}}),\mathbf{t})\in\mathrm{SE}(3)$ be a homogeneous transformation matrix. Direct time derivation of $\mathbf{T}$ at $t=0$ leads to a first representation of se(3):

$$\mathrm{se}(3) := \left\{ \left.\frac{\mathrm{d}\mathbf{T}}{\mathrm{d}t}\right|_{t=0} = \begin{pmatrix} \omega(0)\mathrm{skew}(\hat{\mathbf{s}}) & \mathbf{v}(0) \\ \mathbf{0} & 0 \end{pmatrix} \middle| \, \omega(0)\in\mathbb{R}, \hat{\mathbf{s}}\in\mathbb{S}^2, \mathbf{v}(0)\in\mathbb{R}^3 \right\} \tag{2.2}$$

where $\omega(0)$ is the magnitude of the angular velocity at $t=0$, $\mathbf{v}(0)$ is the velocity of the origin at $t=0$, and if $\hat{\mathbf{s}}:=(s_1,s_2,s_3)$, then:

$$\mathrm{skew}(\hat{\mathbf{s}}) = \begin{pmatrix} 0 & -s_3 & s_2 \\ s_3 & 0 & -s_1 \\ -s_2 & s_1 & 0 \end{pmatrix}$$

From this representation, it is clear that dim(se(3))=6. This must be no surprise since the manifold structure of SE(3) implies that $\dim(T_\psi\mathrm{SE}(3))=\dim(\mathrm{SE}(3)), \forall\psi\in\mathrm{SE}(3)$.

It can be seen that se(3) is isomorphic to $\mathbb{R}^6$, therefore, a very convenient representation of se(3) is given by:

$$\mathrm{se}(3) := \left\{ (\omega\hat{\mathbf{s}};\mathbf{v}) \,|\, \omega\hat{\mathbf{s}},\mathbf{v}\in\mathbb{R}^3 \right\} \cong \mathbb{R}^6 \tag{2.3}$$

In the literature [48], $\mathbf{V}=(\omega\hat{\mathbf{s}};\mathbf{v})$ is commonly known as a *twist* or a *velocity state*. A remarkable fact is that these vectors $\mathbf{V}$ can further be decomposed as follows:

$$(\omega\hat{\mathbf{s}};\mathbf{v}) = \omega(\hat{\mathbf{s}};h\hat{\mathbf{s}}+\hat{\mathbf{s}}\times\mathbf{r}_O) \tag{2.4}$$

These are the Plücker coordinates of a line parallel to $\hat{\mathbf{s}}$ that contains a point with position vector $\mathbf{r}_O\in\mathbb{R}^3$. In addition, $h\in\mathbb{R}$ represents the magnitude of the linear velocity along the direction of the angular velocity. It can be seen that Eq. (2.4) represents the coordinates of a *screw* with pitch h, we denote these screws by $\mathbf{S}\in\mathrm{se}(3)$.

With the representation of se(3) through screw coordinates, we can now give an equation for the Lie bracket of two screws. It can be proved [49] that considering $\mathbf{X}:=(\mathbf{a}_1;\mathbf{b}_1)$ and $\mathbf{Y}:=(\mathbf{a}_2;\mathbf{b}_2)$ and replacing them in Eq. (2.1), the following expression for the Lie bracket is obtained:

$$[(\mathbf{a}_1;\mathbf{b}_1),(\mathbf{a}_2;\mathbf{b}_2)] = (\mathbf{a}_1 \times \mathbf{a}_2; \mathbf{a}_1 \times \mathbf{b}_2 - \mathbf{a}_2 \times \mathbf{b}_1)$$

This definition matches with the commutator of matrices.

Now let us introduce a new concept that will be useful to give an equivalent interpretation of the Lie product. For each $\psi \in \mathrm{SE}(3)$, define the automorphism $\mathrm{Ad} : \mathrm{SE}(3) \to \mathrm{Aut}(\mathrm{SE}(3))$ such that it can act on a second element of SE(3), $\varphi \in \mathrm{SE}(3)$, as $\mathrm{Ad}(\psi)(\varphi) := \psi \circ \varphi \circ \psi^{-1}$. We call this the *adjoint action* of SE(3).

Now let $\mathbf{T} \in \mathbb{R}^{4\times4}$ be the homogeneous transformation matrix representing the displacement $\psi \in \mathrm{SE}(3)$, and let $\mathbf{S} \in \mathbb{R}^6$ be the screw coordinates of an element of se(3) such that $\mathbf{S}_{4\times4} \in \mathbb{R}^{4\times4}$ is the same element written in 4×4 matrix form, as in Eq. (2.2). Then $\mathrm{Ad}(\psi)$ can act on such an element of se(3) as follows:

$$\mathrm{Ad}(\psi)(\mathbf{S}_{4\times4}) = \mathbf{T}\mathbf{S}_{4\times4}\mathbf{T}^{-1} = \mathbf{S}'_{4\times4} \in \mathrm{se}(3)$$

Then the result of the adjoint action on an element of se(3) is another element of se(3). Let $\mathbf{S}' \in \mathbb{R}^6$ be the screw coordinates of $\mathbf{S}'_{4\times4} \in \mathbb{R}^{4\times4}$, then the adjoint action can be written as a 6×6 matrix that transforms $\mathbf{S}$ by premultiplication as follows:

$$\mathrm{Adj}(\psi)\mathbf{S} = \mathbf{S}', \;\; \mathrm{Adj}(\psi) \in \mathbb{R}^{6\times6}$$

where $\mathrm{Adj} \in \mathbb{R}^{6\times6}$ should not be mistaken with $\mathrm{Ad} \in \mathrm{Aut}(\mathrm{SE}(3))$. This leads to an alternative representation of SE(3) given by 6×6 matrices. This is called the *adjoint representation* of SE(3) and is defined as follows:

$$\mathrm{SE}(3) := \left\{ \begin{pmatrix} \mathbf{R} & \mathbf{0}_{3\times3} \\ \mathrm{skew}(\mathbf{t})\mathbf{R} & \mathbf{R} \end{pmatrix} \middle| \, \mathbf{R} \in \mathrm{SO}(3), \mathbf{t} \in \mathbb{R}^3 \right\} \tag{2.5}$$

Since the screw coordinates represent lines with a pitch, the adjoint representation of SE(3) in Eq. (2.5) is used to apply an Euclidean displacement to a screw. Then, the definition of the Lie bracket in Eq. (2.1) has an equivalent interpretation using screw coordinates. It can be proved [50], [51] that the Lie bracket of two screws represents the time derivative at $t = 0$ of the action of the adjoint representation of a displacement along one of the screws on the other, namely:

$$[\mathbf{S}_1, \mathbf{S}_2] = \frac{\mathrm{d}}{\mathrm{d}t}\left(\mathrm{Adj}(\exp(a\mathbf{S}_1))\mathbf{S}_2\right)\Big|_{t=0}, \;\; \mathbf{S}_1, \mathbf{S}_2 \in \mathrm{se}(3), a \in \mathbb{R}$$

Geometrically speaking, $[\mathbf{S}_1, \mathbf{S}_2]$ is a screw that is coincident with the common perpendicular of $\mathbf{S}_1$ and $\mathbf{S}_2$. If these screws are parallel, the product vanishes as expected from its nilpotency property.

A *subalgebra* of se(3) is any subset of se(3) which is an algebra by itself. For every subgroup of any Lie group, there is a corresponding subalgebra. In this thesis, subalgebras are denoted with the same symbol as its corresponding subgroup but using lowercase letters. For example, so(3) is the subalgebra of spherical displacements. These subalgebras can also be parametrized, for example the subalgebra of cylindrical displacements about the Z axis, c_Z, is given by:

$$\mathrm{c}_Z := \{\, (0,0,a;0,0,b) \,|\, a,b \in \mathbb{R}\}$$

From this parameterization, it is clear that c_Z is a vector space of dimension 2, which is, as expected, equal to the dimension of C_Z.

2.4 Higher order kinematic analyses

In this section, equations for the time derivatives of the pose of the end-effector of a serial kinematic chain are presented in terms of screw coordinates. These equations are presented here in the form that they were determined by López-Custodio et al. [50] by direct derivation of the Jacobian matrix by means of the Lie bracket. Equivalent expressions were determined previously by Rico et al. [48], Müller [52] and Lerbet [53]. In [50] all these different expressions were proved to be equivalent.

Equations for the first-, second-, third- and fourth-order analyses are enlisted in this section. Although explicit equations for orders higher than four are not presented, a method for the recursive determination of the kinematics of any order can be found in [54].

In order to represent the motion of the end-effector of a serial kinematic chain, consider the $n-$joint chain shown in fig. 2.3. Let $\mathbb{V}^n := \mathbb{T}^{n_r} \times \mathbb{R}^{n_p+n_h}$, where n_r, n_p and n_h are the number of R, P and H joints in the kinematic chain. We define $\mathbf{q}(t) := (q_1(t), \ldots, q_n(t)) \in \mathbb{V}^n$ as the vector of joint variables of the kinematic chain at time t. Hence, $\mathbf{q}$ wholly describes the configuration of the chain at time t. For the sake of lightening the notation, we drop t.

Let $0 < m \leq n$, the twist of link m w.r.t. link $m-1$ is given by the screw $\mathbf{S}_m(\mathbf{q})$. Note that if the joint is a helical joint (H), $h \in \mathbb{R} \setminus \{0\}$ in Eq. (2.4); if it is a revolute joint (R), the screw has pitch $h = 0$; and if the joint is a prismatic joint (P), then $h = \infty$ and the screw has coordinates $(\mathbf{0}; \mathbf{v})$. Only 1-DOF lower kinematic pairs are considered in this thesis, i.e. H, R and P joints. Spherical (S), universal (U) and cylindrical (C) joints are considered as serial connections of R and H joints.

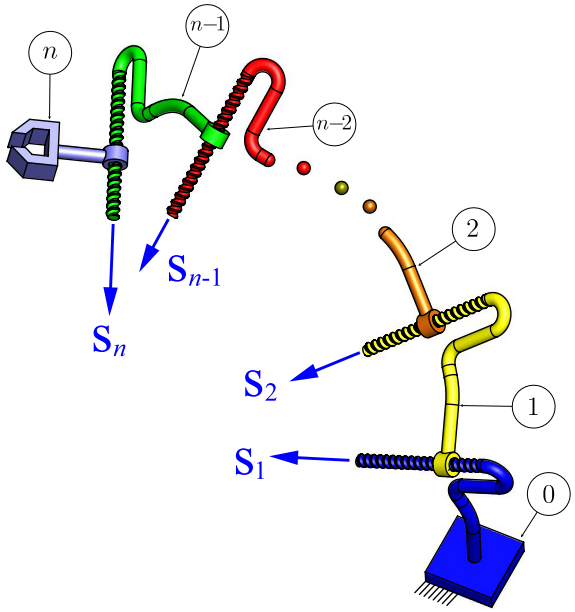

FIGURE 2.3: Serial kinematic chain with n joints. Figure taken from [50]

The equations for higher-order kinematic analyses in terms of screw coordinates, are considerably long expressions. For the sake of compactness, we define the following multilinear maps, where **only for these expressions** an abuse in notation has been done by considering $\underbrace{\mathbb{R}^n \times, \ldots, \times \mathbb{R}^n}_{k \text{ times}} = \mathbb{R}^{n \times k}$. Note that these maps are different for each configuration $\mathbf{q}$, however, for the sake of lightening the notation $\mathbf{q}$ has been dropped from the screws $\mathbf{S}_i$:

$$
\begin{aligned}
J_1(\mathbf{q}) : \mathbb{R}^n \to \mathrm{se}(3) \qquad & \mathbf{w} := (w_1 \ldots, w_n) \mapsto \sum_{k=1}^{n} w_k \mathbf{S}_k = \mathbf{J}(\mathbf{q})\mathbf{w}, \\
J_2(\mathbf{q}) : \mathbb{R}^{n\times 2} \to \mathrm{se}(3) \qquad & (\mathbf{w},\mathbf{x}) \mapsto \sum_{j<k} w_j x_k \left[\mathbf{S}_j, \mathbf{S}_k\right], \\
J_{3,1}(\mathbf{q}) : \mathbb{R}^{n\times 3} \to \mathrm{se}(3) \qquad & (\mathbf{w},\mathbf{x},\mathbf{y}) \mapsto \sum_{j<k} w_j x_j y_k \left[\mathbf{S}_j, [\mathbf{S}_j, \mathbf{S}_k]\right], \\
J_{3,2}(\mathbf{q}) : \mathbb{R}^{n\times 3} \to \mathrm{se}(3) \qquad & (\mathbf{w},\mathbf{x},\mathbf{y}) \mapsto \sum_{i<j<k} w_i x_j y_k \left[\mathbf{S}_i, [\mathbf{S}_j, \mathbf{S}_k]\right], \\
J_{4,1}(\mathbf{q}) : \mathbb{R}^{n\times 4} \to \mathrm{se}(3) \qquad & (\mathbf{w},\mathbf{x},\mathbf{y},\mathbf{z}) \mapsto \sum_{j<k} w_j x_j y_j z_k \left[\mathbf{S}_j, [\mathbf{S}_j, [\mathbf{S}_j, \mathbf{S}_k]]\right], \\
J_{4,2}(\mathbf{q}) : \mathbb{R}^{n\times 4} \to \mathrm{se}(3) \qquad & (\mathbf{w},\mathbf{x},\mathbf{y},\mathbf{z}) \mapsto \sum_{i<j<k} w_i x_i y_j z_k \left[\mathbf{S}_i, [\mathbf{S}_i, [\mathbf{S}_j, \mathbf{S}_k]]\right], \\
J_{4,3}(\mathbf{q}) : \mathbb{R}^{n\times 4} \to \mathrm{se}(3) \qquad & (\mathbf{w},\mathbf{x},\mathbf{y},\mathbf{z}) \mapsto \sum_{i<j<k} w_i x_j y_j z_k \left[\mathbf{S}_i, [\mathbf{S}_j, [\mathbf{S}_j, \mathbf{S}_k]]\right]. \\
J_{4,4}(\mathbf{q}) : \mathbb{R}^{n\times 4} \to \mathrm{se}(3) \qquad & (\mathbf{w},\mathbf{x},\mathbf{y},\mathbf{z}) \mapsto \sum_{h<i<j<k} w_h x_i y_j z_k \left[\mathbf{S}_h, [\mathbf{S}_i, [\mathbf{S}_j, \mathbf{S}_k]]\right] \qquad (2.6)
\end{aligned}
$$

where $\mathbf{J}(\mathbf{q}) := \mathrm{aug}(\mathbf{S}_1(\mathbf{q}), \ldots, \mathbf{S}_n(\mathbf{q}))$ is the *Jacobian* matrix of the kinematic chain at the configuration of analysis $\mathbf{q}$. In every case $J_{k,j}(\mathbf{q}) \in \mathcal{L}(\underbrace{\mathbb{R}^n, \ldots, \mathbb{R}^n}_{k\,\text{times}}; \mathrm{se}(3))\ \forall k = 1, \ldots, 4$.

Using these multilinear maps, the following expressions for the velocity, $\mathbf{H}^{(1)}$ (1st order); acceleration, $\mathbf{H}^{(2)}$ (2nd order); jerk, $\mathbf{H}^{(3)}$ (3rd order); and jounce, $\mathbf{H}^{(4)}$ (4th order), of link n w.r.t. link 0 are obtained at $\mathbf{q}$.

$$
\begin{aligned}
\mathbf{H}^{(1)}(\mathbf{q},\mathbf{x}_1) &= J_1(\mathbf{q})(\mathbf{x}_1) = \mathbf{J}(\mathbf{q})\mathbf{x}_1, && (2.7)\\
\mathbf{H}^{(2)}(\mathbf{q},\mathbf{x}_1,\mathbf{x}_2) &= J_1(\mathbf{q})(\mathbf{x}_2) + J_2(\mathbf{q})(\mathbf{x}_1,\mathbf{x}_1), && (2.8)\\
\mathbf{H}^{(3)}(\mathbf{q},\mathbf{x}_1,\mathbf{x}_2,\mathbf{x}_3) &= J_1(\mathbf{q})(\mathbf{x}_3) + 2J_2(\mathbf{q})(\mathbf{x}_1,\mathbf{x}_2) + J_2(\mathbf{q})(\mathbf{x}_2,\mathbf{x}_1) + J_{3,1}(\mathbf{q})(\mathbf{x}_1,\mathbf{x}_1,\mathbf{x}_1) + \\
&\quad 2J_{3,2}(\mathbf{q})(\mathbf{x}_1,\mathbf{x}_1,\mathbf{x}_1), && (2.9)\\
\mathbf{H}^{(4)}(\mathbf{q},\mathbf{x}_1,\mathbf{x}_2,\mathbf{x}_3\mathbf{x}_4) &= J_1(\mathbf{q})(\mathbf{x}_4) + 3J_2(\mathbf{q})(\mathbf{x}_1,\mathbf{x}_3) + J_2(\mathbf{q})(\mathbf{x}_3,\mathbf{x}_1) + 3J_2(\mathbf{q})(\mathbf{x}_2,\mathbf{x}_2) + \\
&\quad 3J_{3,1}(\mathbf{q})(\mathbf{x}_1,\mathbf{x}_1,\mathbf{x}_2) + 3J_{3,1}(\mathbf{q})(\mathbf{x}_1,\mathbf{x}_2,\mathbf{x}_1) + 6J_{3,2}(\mathbf{q})(\mathbf{x}_1,\mathbf{x}_1,\mathbf{x}_2) + \\
&\quad 3J_{3,2}(\mathbf{q})(\mathbf{x}_1,\mathbf{x}_2,\mathbf{x}_1) + 3J_{3,2}(\mathbf{q})(\mathbf{x}_2,\mathbf{x}_1,\mathbf{x}_1) + J_{4,1}(\mathbf{q})(\mathbf{x}_1,\mathbf{x}_1,\mathbf{x}_1,\mathbf{x}_1) + \\
&\quad 3J_{4,2}(\mathbf{q})(\mathbf{x}_1,\mathbf{x}_1,\mathbf{x}_1,\mathbf{x}_1) + 3J_{4,3}(\mathbf{q})(\mathbf{x}_1,\mathbf{x}_1,\mathbf{x}_1,\mathbf{x}_1) + \\
&\quad 6J_{4,4}(\mathbf{q})(\mathbf{x}_1,\mathbf{x}_1,\mathbf{x}_1,\mathbf{x}_1) && (2.10)
\end{aligned}
$$

where, $\mathbf{x}_i := \mathrm{d}^i\mathbf{q}/\mathrm{d}t^i \in \mathbb{R}^n$ are the vectors of joint velocities, accelerations, jerks and jounces.

If link n in fig. 2.3 is rigidly attached to fixed link 0, a closed-loop kinematic chain is obtained. The result is a single-loop *linkage* or *mechanism*. Note that in such a device, $\mathbf{V}^n$ and all of its derivatives are equal to 0. Therefore, for closed loops, Eqs. (2.7) to (2.10) can be written in general as:

$$\mathbf{J}(\mathbf{q})\mathbf{x}_i = \Lambda(\mathbf{q},\mathbf{x}_1,\ldots,\mathbf{x}_{i-1}) \qquad (2.11)$$

where $\Lambda \in \mathrm{se}(3)$ is a screw which includes all the terms of the higher order equation apart from the first one which is simply the linear map J_1. In fact, Eq. (2.11) holds for any order $i \in \mathbb{Z}_+ \setminus \{0\}$.

Note that if $i = 1$, Eq. (2.11) is the homogeneous linear equation $\mathbf{J}(\mathbf{q})\mathbf{x}_1 = \mathbf{0}$ which always has a solution $\mathbf{x}_1 \in \ker(\mathbf{J}(\mathbf{q}))$. These results, including Eq. (2.11), are the key for local analysis of linkages, which is explained in the following section.

2.5 The kinematic tangent cone

In the previous section, $\mathbf{q}(t) \in \mathbb{V}^n$ was introduced as the vector of joint variables which fully defines the configuration of an $n-$joint kinematic chain at time t. Since such a vector varies with time, we now define $V \subseteq \mathbb{V}^n$ as the set of all possible vectors $\mathbf{q}$ at any time. V is called the *configuration space* of the kinematic chain. For an open-loop chain it is clear that $V = \mathbb{V}^n$. However, for a closed-loop chain, vectors $\mathbf{q}$ must satisfy certain geometric restrictions that allow the chain to remain assembled during motion. These restrictions are included in a *constraint loop equation*, $f(\mathbf{q}(t)) = \mathbf{0}, \forall t$. Now consider a γ-loop linkage, then for every loop a constraint loop equation $f_i(\mathbf{q}(t)) = \mathbf{0}$, $i = 1, \ldots, \gamma$ must be fulfilled. It is clear now that, for a linkage with γ loops, $V \neq \mathbb{V}^n$ since V can be defined as:

$$V := \{\mathbf{q} \in \mathbb{V}^n \,|\, f_i(\mathbf{q}) = \mathbf{0}, i = 1, \ldots, \gamma\} \subset \mathbb{V}^n$$

Since f_i are *analytic functions*, i.e. they can be expressed as a Taylor expansion, V represents the set of solutions to an analytic function, this mathematical object is called *real analytic variety* [55][2], in contrast to a differentiable manifold, we allow V to have singularities of multiple types. In fact, we can somehow see V as the union of several manifolds which may or may not intersect.

The fact that V can be seen as the union of several manifolds makes it very tempting to obtain its tangent space to get a local picture of it as it was done in Section 2.3. Let us assume for a moment that V is a differentiable manifold. Then the tangent space, $T_{\mathbf{q}}V$, at a point $\mathbf{q} \in V$ is spanned by the set of vectors $\dot{\mathbf{q}} = \mathbf{x}_1 \in \mathbb{R}^n$ which can be seen as the possible joint velocities at $\mathbf{q}$:

$$T_{\mathbf{q}}V = \{\mathbf{x}_1 \,|\, \mathbf{J}(\mathbf{q})\mathbf{x}_1 = \mathbf{0}\} = \ker(\mathbf{J}(\mathbf{q})) \tag{2.12}$$

Since we are considering V to be smooth at $\mathbf{q}$, we get $\dim(T_{\mathbf{q}}V) = \dim(\mathcal{N}_{\mathbf{q}} \cap V)$. The dimension of V at $\mathbf{q}$ represents the number of degrees of freedom or the *mobility* of the kinematic chain at $\mathbf{q}$, the manifolds in V can have different dimensions, this is why the mobility of a linkage is said to be a local property. Observe that $\dim(T_{\mathbf{q}}V) = \dim(\ker(\mathbf{J}(\mathbf{q}))) = n - \operatorname{rank}(\mathbf{J}(\mathbf{q}))$. This is the main reason why many researchers rely on the Jocobian matrix of a linkage to obtain information including mobility. For example, it is a widely used technique to compute mobility by means of the dimension of the system of constraints of parallel robots. Unfortunately, these results fail wherever V ceases to be a manifold, which happens if $\mathbf{q} \in \operatorname{sing}(V)$.

To illustrate a simple situation in which $T_{\mathbf{q}}V$ fails in locally describing V, consider a planar 4R mechanism in which the opposite links have the same length. Since this is a 4R linkage we have joint variables vectors $\mathbf{q} \in \mathbb{T}^4$ and $V \subset \mathbb{T}^4$. This mechanism can reach a flat configuration $\mathbf{q}_0$ in which the axes of all its joints lie on the same plane. Hunt [58] notes that, from $\mathbf{q}_0$, the mechanism can be unfolded "in two essentially different ways": in the first way opposite links remain parallel to each other forming a parallelogram, in the second way of unfolding the linkage this parallelism does not exist, these configurations are commonly known as *antiparallelogram* configurations. Fig. 2.4 shows the mechanism in the flat configuration $\mathbf{q}_0$, in a parallelogram configuration $\mathbf{q}_1$ and in an antiparallelogram configuration $\mathbf{q}_2$.

[2] In this thesis, the concept of analytic variety is used only to describe the configuration space of a linkage, but an algebraic geometry approach is not used. For a direct application of algebraic geometry in mechanisms analysis see [56], [57]

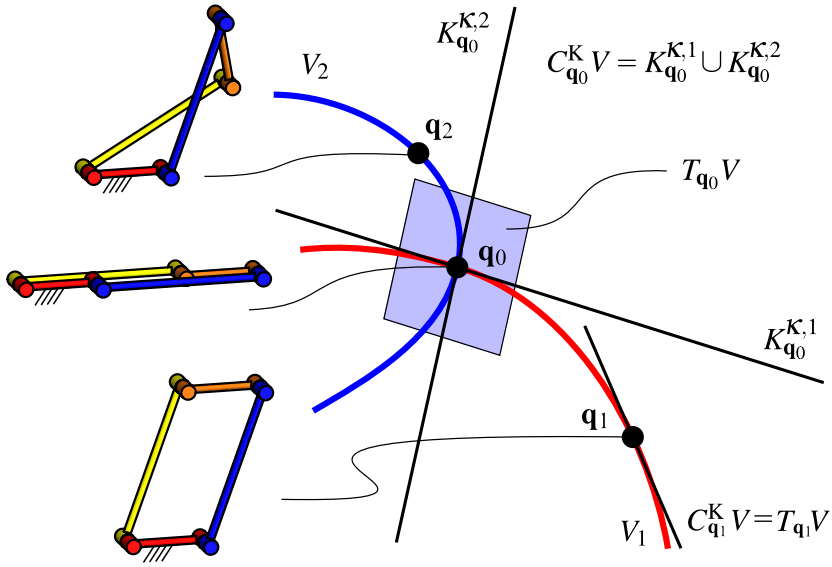

FIGURE 2.4: Bifurcation in the configuration space of a planar 4-bar mechanism.

Since it is well-known that this is a 1-DOF mechanism, it can be seen that V includes two 1-dimensional manifolds V_1 and V_2 in an ambient space $\mathbb{T}^4$. These two manifolds are said to be *subvarieties* of V. As depicted in fig. 2.4, both subvarieties intersect at $\mathbf{q}_0$, therefore, $\mathbf{q}_0$ is said to be a *bifurcation* point of V. From fig. 2.4 it is clear that the set of tangents to V at $\mathbf{q}_0$ is the union of two 1-dimensional vector spaces, each one being tangent to each curve intersecting at $\mathbf{q}_0$. However, since $T_{\mathbf{q}_0}V = \ker(\mathbf{J}(\mathbf{q}_0))$, the tangent space to V at $\mathbf{q}_0$ must be a vector space and, therefore, it cannot represent the union of two lines. The vector space nature of $T_{\mathbf{q}_0}V$ suggests that it is generated by the linear span of all the vectors that are tangent to V at $\mathbf{q}_0$. Hence, $T_{\mathbf{q}_0}V$ is the plane containing the two lines, i.e. the tangent plane to V_1 and V_2 at $\mathbf{q}_0$, a 2-dimensional vector space.

It is disappointing that $\dim(T_{\mathbf{q}_0}V) = 2$, as we know that this is a 1-DOF linkage. It is also confusing that the local picture we get from $T_{\mathbf{q}_0}V$ suggests that V is a 2-DOF manifold.

V, like any other analytic variety, presents this important problem. To fix this, Whitney [59] studied the tangents to this abstract objects. One can suspect from fig. 2.4 that the tangents to analytic varieties generate a *cone*, rather than a vector space. A cone is a different object which is only closed under scalar multiplication, but not under vector addition. The union of two vector spaces is, therefore, a cone. Indeed, Whitney introduced the concept of *tangent cone* to an analytic variety. Not only does the concept work at singularities like the bifurcation of our 4-bar linkage, the cone also degenerates into a vector space when no bifurcation is present, being equal to the tangent space, as shown in fig. 2.4 at regular point $\mathbf{q}_1$. Lerbet [53] was the first in noting the effectiveness of this concept in mechanisms theory. Müller would follow him with a number of papers on this topic [52], [54], [60]–[62].

In order to obtain the tangent cone to V we note that since the vectors that lie on $T_{\mathbf{q}}V$ but are not tangent to either V_1 or V_2 are not actual tangent vector to V, they do not represent feasible velocities of the joint variables. In order to unmask these vectors that are not actually joint velocities, note that if a vector represents feasible joint velocities, then it not only fulfills the equation for velocity analysis, Eq. (2.7), but it also must satisfy the kinematic equations of any order. We can then construct the *kinematic tangent cone* to V at any point $\mathbf{q}$, $C^{\mathrm{K}}_{\mathbf{q}}$, using the kinematic higher order expressions in Section 2.4. Let

$$K^1_{\mathbf{q}} := \ker(\mathbf{J}(\mathbf{q})) = T_{\mathbf{q}}V$$

then $C_{\mathbf{q}}^{\mathrm{K}}$ is approximated by successive approximations $K_{\mathbf{q}}^{i}$ as follows:

$$K_{\mathbf{q}}^{i} := \left\{ \mathbf{x}_1 \in K_{\mathbf{q}}^{i-1} \;\middle|\; \mathbf{H}^{(i)}(\mathbf{q}, \mathbf{x}_1, \ldots, \mathbf{x}_i) = \mathbf{0} \right\}, \forall i \in \mathbb{Z}_+ \setminus \{0,1\} \tag{2.13}$$

The kinematic tangent cone is then obtained as:

$$C_{\mathbf{q}}^{\mathrm{K}} V = \lim_{m \to \infty} \bigcap_{i=1}^{m} K_{\mathbf{q}}^{i} = K_{\mathbf{q}}^{\kappa} \tag{2.14}$$

where κ is the order at which $\dim(K_{\mathbf{q}}^{i}) = \dim(K_{\mathbf{q}}^{\kappa}), \forall i > \kappa$. Unfortunately, proving that κ has been determined using higher order analysis is still an open problem.

Returning to our 4-bar mechanism, it is clear now that in fig. 2.4 the tangent space to V_1 is the 1-dimensional vector space $K_{\mathbf{q}_0}^{\kappa,1}$, while the tangent space to V_2 is $K_{\mathbf{q}_0}^{\kappa,2}$, then the tangent cone at $\mathbf{q}_0$ is given by $C_{\mathbf{q}_0}^{\mathrm{K}} V = K_{\mathbf{q}_0}^{\kappa,1} \cup K_{\mathbf{q}_0}^{\kappa,2}$. If we were to obtain the tangent cone in the non-singular point $\mathbf{q}_1$ (see fig. 2.4) we would find that $\kappa = 1$ and $C_{\mathbf{q}_0}^{\mathrm{K}} V = K_{\mathbf{q}_0}^{1} = T_{\mathbf{q}_0} V$, which is simply a 1-dimensional vector space. There is no limit for the number of subvarieties intersecting at a point in V, an example with as many as eight 3-dimensional manifolds intersecting at a point is presented in [63]

With this example, Hunt [58] called this flat configuration an *uncertainty configuration*. $\mathbf{q}_0$ is a singularity of V. Singularities in the configuration space have been widely studied [64]–[66]. Note that, in our 4-bar mechanism at $\mathbf{q}_0$ $\dim(T_{\mathbf{q}_0} V) = \dim(\ker(\mathbf{J}(\mathbf{q}_0))) = n - \mathrm{rank}(\mathbf{J}(\mathbf{q}_0)) = 2$, while at $\mathbf{q}_1$, $\dim(T_{\mathbf{q}_1} V) = n - \mathrm{rank}(\mathbf{J}(\mathbf{q}_1)) = 1$. This is consistent with the common interpretation of singularities as the points where the rank of the Jacobian matrix decreases. There are other types of singularities in the configuration space which are much less common and which are discussed in chapters 8 and 7.

Now we can also give more precise definitions of mobility. In all cases it is important to remember that mobility is a *local* property which is defined for every point in V. For any point $\mathbf{q} \in V$, we define the following concepts:

- The *instantaneous mobility* is simply the dimension of the tangent space $F_1(\mathbf{q}) := \dim(T_{\mathbf{q}} V) = n - \mathrm{rank}(\mathbf{J}(\mathbf{q}))$
- The $i-$th *order mobility* is the dimension of the $i-$th approximation to the tangent cone, $F_i(\mathbf{q}) := \dim(K_{\mathbf{q}}^{i})$. Hence, the instantaneous mobility is the first order mobility.
- The *finite mobility*, $F(\mathbf{q})$, is the dimension of the manifold which $\mathbf{q}$ belongs to. If $\mathbf{q} \notin \mathrm{sing}(V)$, then $F(\mathbf{q}) = F_1(\mathbf{q})$, in fact, $F(\mathbf{q}) = F_i(\mathbf{q}), \forall i \in \mathbb{Z}_+ \setminus 0$. If $\mathbf{q} \in \mathrm{sing}(V)$ such that m subvarieties intersect at $\mathbf{q}$, then $F(\mathbf{q})$ is not defined, however, $C_{\mathbf{q}}^{\mathrm{K}} V = \cup_j^m K_{\mathbf{q}}^{\kappa,j}$ allows us to find the finite mobility at points in its neighborhood by means of $\dim(K_{\mathbf{q}}^{\kappa,j}) = \dim(V_j)$. The importance of the finite mobility at $\mathbf{q}$ relies on the fact that $F(\mathbf{q}) = F(\mathbf{p})$, where $\mathbf{p} \in \mathcal{N}_{\mathbf{q}}$, therefore $F(\mathbf{q})$ expresses the number of degrees of freedom of finite displacements around $\mathbf{q}$. This is why, in the past, $F(\mathbf{q})$ was commonly known as *full-cycle mobility* [58]. However, regardless being related to finite motion, $F(\mathbf{q})$ is still a local property and thus the adjective "full-cycle" may result misleading.

2.6 Reconfigurable mechanisms

The fact that the planar 4R mechanism analyzed in the previous section has a configuration space that contains two subvarieties turns out to be an interesting and useful property as one can get different outputs for the same input, e.g., in our 4-bar linkage moving through V_1 will lead to an output angle that is the same as the input one, while when moving through

V_2 gives an output angle that is different to the input one. A remarkable property of our 4-bar mechanism is that we can get both input-output relations without disassembling the mechanism by crossing the singularity $\mathbf{q}_0$ where one can choose between the two different ways to unfold the linkage. The question now arises whether mechanisms can be designed to exploit this "multifunctionality" property. The answer is yes, and researchers have been working on this topic for a while in what has been named *reconfigurable mechanisms*, (see for example [24], [25], [67], [68] for some general insights on the topic).

Nevertheless, the term "reconfigurable mechanisms" is an umbrella that encompasses a wide variety of devices which not necessary have the same property we just mentioned. For example, some linkages also achieve reconfiguration by means of variable or lockable joints [67], [69]–[71]. In this thesis, only reconfigurable mechanisms whose configuration space contains at least two intersecting subvarieties and have simple (non-variable) R, P and H joints are investigated. Examples of this type of reconfigurable mechanisms include [8], [11], [27], [30], [63], [72]–[79].

In this thesis, the different subvarieties in the configuration space of a linkage are called *branches of motion* [27], [72]. Due to the application given to the different subvarieties, sometimes they are also referred to as *motion mode* [64], [80], [81] or *motion phase* [67], [69], [70], although this term has also been applied to the different topologies obtained after physical limit or variable joints produce reconfiguration. In addition, in [64], the different subvarieties are called *regions* of the configuration space. There is no limit for the number of branches of motion in the configuration space of mechanism, in [30] mechanisms with an infinity of branches of motions were designed and presented.

Another very interesting type of reconfigurable mechanism arises from the fact that in the theory built in Section 2.5 the different subvarieties are not required to be of the same dimension. The intersection of two of them with different dimension would imply that the linkage is able to change its number of degrees of freedom.

Fig. 2.5 shows a very familiar planar 2-loop linkage called the *Neuremberg scissors*. Similarly to the 4-bar mechanism studied in Section 2.5, this linkage can reach a flat configuration $\mathbf{q}_0 \in V$, in which all the axes are coplanar. From this configuration, the linkage can be unfolded in two different ways: the first way to do it is the typical way of operating the linkage, in which, with 1-DOF each loop looks like a planar 4-bar mechanism (see configuration $\mathbf{q}_1$ in fig. 2.5); the second way to unfold the mechanism happens when the axes of opposite joints in each loop remain collinear. In the latter case, the linkage can be used as an open 2R kinematic chain as shown in configuration $\mathbf{q}_2$ in fig. 2.5, hence, the linkage has now 2-DOF.

It can be concluded that the Nuremberg scissors can change their finite mobility from 1 to 2 when crossing $\mathbf{q}_0$. V contains (at least) two branches of motion (subvarieties), V_1 and V_2, such that $\dim(V_1) = 1$ and $\dim(V_1) = 2$. The tangent space to V_1, $K^{\kappa,1}_{\mathbf{q}_0}$ at the singularity is a line, while the tangent space to V_2 at the same point, $K^{\kappa,2}_{\mathbf{q}_0}$ is a plane. Clearly, $T_{\mathbf{q}_0}V = \text{span}(K^{\kappa,1}_{\mathbf{q}_0}, K^{\kappa,2}_{\mathbf{q}_0})$ and, therefore, $\dim(T_{\mathbf{q}_0}V) = 3$. On the other hand, $C^{\mathrm{K}}_{\mathbf{q}_0}V = K^{\kappa,1}_{\mathbf{q}_0} \cup K^{\kappa,2}_{\mathbf{q}_0}$. It is concluded that $F_1(\mathbf{q}_0) = 3$, however, $F(\mathbf{q}'_1) = 1$ and $F(\mathbf{q}'_2) = 2$, where $\mathbf{q}'_1 \in \mathcal{N}_{\mathbf{q}_0} \cap V_1$ and $\mathbf{q}'_2 \in \mathcal{N}_{\mathbf{q}_0} \cap V_2$.

Mechanisms with the same property of mobility change present in the Neuremberg scissors were elegantly coined by Wohlhart as *kinematotropic mechanisms* [12]. Although it has to be warned that more recently the term has been applied to other reconfigurable mechanisms that do not change their mobility, see for example [82]. The complexity of kinematotropic linkages make them less common that the constant-mobility reconfigurable mechanisms. Examples and design methods of kinematotropic mechanisms can be found in [12]–[17], [34], [63], [83], [84].

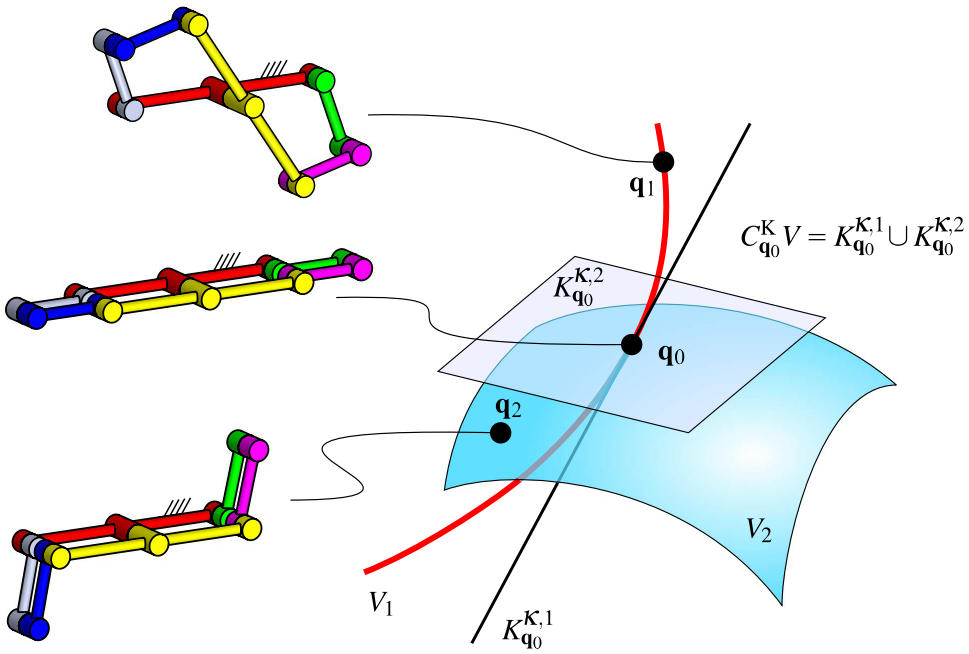

FIGURE 2.5: The Nuremberg scissors, a kinematotropic linkage.

2.7 Generated surfaces in mechanisms theory

In the design and analysis of mechanisms it becomes convenient to be able to visualize in 3-dimensional space what a kinematic chain is able to do, and therefore, it is easier to manipulate its parameters to obtain the desired behaviour of the linkage. This is possible applying the method of generated surfaces [1]–[3]. The idea is to disassemble a linkage in 2-DOF kinematic chains and look at the surface that a point in the chain generates in the 3-dimensional space. The technique is now explained in terms of the machinery previously developed in this chapter.

We start with a dyad A, i.e. a serial kinematic chain with 2 joints, so that $\mathbf{q}^A \in V^A = \mathbb{V}^2$ is the vector of joint variables. Since this is a 2-DOF kinematic chain, a point $E_A(\mathbf{q}^A)$ attached to the end-effector will draw a surface $\mathcal{S}_A := \{E_A(\mathbf{q}^A) \,|\, \mathbf{q}^A \in V^A\} \subset \mathbb{R}^3$. Note that the shape of $\mathcal{S}_A$, not only depends on the type of joints and the link between them, but also on the choice of E_A at the end-effector. Cases in which $\dim(\mathcal{S}_A) = 0, 1$ are degenerated cases that are not of interest.

Different parameterizations can be obtained for $\mathcal{S}_A$. However, the map E_A provides a very useful parameterization in terms of the joint variables $(q_{A1}, q_{A2}) := \mathbf{q}^A$. Another important tool for this technique is expressing $\mathcal{S}_A$ by means of its *implicit form* $\phi_A(x,y,z) = 0$, where $\phi : \mathbb{R}^3 \to \mathbb{R}$ is a function such that:

$$\mathcal{S}_A := \{\mathbf{r}_{E_A} = (x,y,z) \,|\, \phi(x,y,z) = 0\}$$

Let $\sigma_A : U_A \to \mathbb{R}^3$ be a parameterization of $\mathcal{S}_A$, so that $\mathcal{S}_A = \mathrm{im}(\sigma(U_A))$ and $U_A \subseteq \mathbb{R}^2$ is given in variables (u_A, v_A). A point (u_A^p, v_A^p) is said to be *regular* under σ_A if $\mathcal{S}_A$ does not present self-intersection at $\sigma_A(u_A^p, v_A^p)$ and:

$$\left.\frac{\partial \sigma_A}{\partial u_A}\right|_{(u_A^p, v_A^p)} \times \left.\frac{\partial \sigma_A}{\partial v_A}\right|_{(u_A^p, v_A^p)} \neq \mathbf{0}$$

Otherwise, the point is said to be *singular*. If either $\partial\sigma_A/\partial u_A|_{(u_A^p, v_A^p)} = \mathbf{0}$ or $\partial\sigma_A/\partial v_A|_{(u_A^p, v_A^p)} =$

$\mathbf{0}$, then the singularity is said to be a *conic singularity*. These singularities will play a key role in chapter 4. The vertex of a cone is an immediate example of conic singularity.

Note that the above defined singularity depends on the parameterization. A singular point under a certain parameterization might be regular on the surface itself. However, if it is not possible to define a tangent plane on to a surface at a given point, then the parameterization must be singular at the point in U that maps to such a point on the surface.

As an example of this, first consider a unit sphere $\mathcal{S}_S$ parameterized by $\sigma_S(u,v) := (\cos v\cos u, \cos v\sin u, \sin v)$ and with implicit form $\phi_S := x^2+y^2+z^2-1$. Since the normal $\nabla\phi_S = (2x,2y,2z)$ always exists, there is a plane that is tangent to $\mathcal{S}_S$ at each of its points, and $\mathcal{S}_S$ is always regular. However, at the poles defined by the parameterization σ_S, i.e. $\sigma_S(u,\pm\pi/2) := (0,0,\pm 1)$, $\partial\sigma_S/\partial u$ vanishes. Therefore, these are singular points of σ_S, but regular on $\mathcal{S}_S$. Now consider a torus, $\mathcal{S}_T$, whose base circle has the same radius as its secondary circle. Let this torus be parameterized by $\sigma_T(u,v) := ((1+\cos v)\cos u, (1+\cos v)\sin u, \sin v)$ and have implicit form $\phi_T := (\sqrt{x^2+y^2}-1)^2+z^2-1$. It can be seen that the normal is not defined at the origin as $\nabla\phi_T|_{(0,0,0)}$ is not defined. Therefore, the surface is not regular at the origin, and the points $(u,\pm\pi) \in U$ that map to the origin must be singular in σ_T.

We now introduce a second dyad B, which has all the properties previously described for dyad A. Hence, a surface $\mathcal{S}_B$ is generated by point $E_B(\mathbf{q}^B)$, where $\mathbf{q}^B \in V^B$ is the vector of joint variables. Fig. 2.6 shows both dyads and their generated surfaces. Fig. 2.6 $\mathcal{S}_A$ is a torus obtained using an RR chain, while $\mathcal{S}_B$ is a right cylinder obtained using a PR chain.

Position both kinematic chains in such a way that $\mathcal{S}_A$ and $\mathcal{S}_B$ intersect, then make $E_A = E_B$ by joining the end-effector of both chains with a spherical joint with centre at $E := E_A = E_B$. The result is a closed-loop non-overconstrained linkage with mobility one, if the S joint is represented by three R joints, then the number of joints and links is 7. This new mechanism has has a configuration space $V \subset \mathbb{V}^7$ and vectors of joint variables $\mathbf{q} := (q_{A1}, q_{A2}, q_{S1}, q_{S2}, q_{S3}, q_{B2}, q_{B1})$, where q_{S1}, q_{S2} and q_{S2} are the joint variables of the three R joints representing the S joint.

In [11], [29], the possibility of reducing the S joint to one or two R joints was also explored. For example, the S joint in our example in fig. 2.6 can be replaced by an R joint with axis parallel to $\mathbf{S}_{A1}||\mathbf{S}_{B1}$, placed adjacent to joint $B2$ and second R joint parallel to $\mathbf{S}_{A2}$, placed adjacent to joint $A2$. The result is the overconstrained linkage shown at the bottom of figure 2.6.

It can be seen that since $E_A(\mathbf{q}^A) \in \mathcal{S}_A$ and $E_B(\mathbf{q}^B) \in \mathcal{S}_B$, then $E(\mathbf{q}) \in \mathcal{S}_A \cap \mathcal{S}_B$. So point E is confined to move in the intersection of both surfaces. In our case in fig. 2.6, the intersection is a single curve $\mathscr{C}$. However, in general, $\mathcal{S}_A \cap \mathcal{S}_B$ may include several curves and isolated points or, if $\mathcal{S}_A = \mathcal{S}_B$, then the intersection is a surface. This last case is not as trivial as it sounds since different mechanical generators can be obtained for the same surface, this will be important in chapter 5.

Note that, if $\mathcal{S}_A$ is free of singularities, $\sigma_A(q_{A1}, q_{A2}) = E_A(q_{A1}, q_{A2})$, is a bijection from V^A to $\mathcal{S}_A$. A similar statement can be made for dyad B. This is not true though when the surface has self-intersections as if $\sigma_A(\mathbf{q}_1^A)$ is a self intersection, then there is another point $\mathbf{q}_2^A \in V^A$ such that $\sigma_A(\mathbf{q}_1^A) = \sigma_A(\mathbf{q}_2^A)$. However, in general, $\mathcal{S}_A \cap \mathcal{S}_B$ describes V almost perfectly. Hence, the mobility of the linkage at a point $\mathbf{q} \in V$ should be nothing more than the dimension of the component of $\mathcal{S}_A \cap \mathcal{S}_B$, where $E(\mathbf{q})$ is. Considering other specific situations, the finite mobility of the closed-loop linkage at $\mathbf{q} \in V$ is:

- 0-DOF if $E(\mathbf{q})$ is an isolated point,
- 1-DOF if $E(\mathbf{q})$ lies on a curve $\mathscr{C}$,

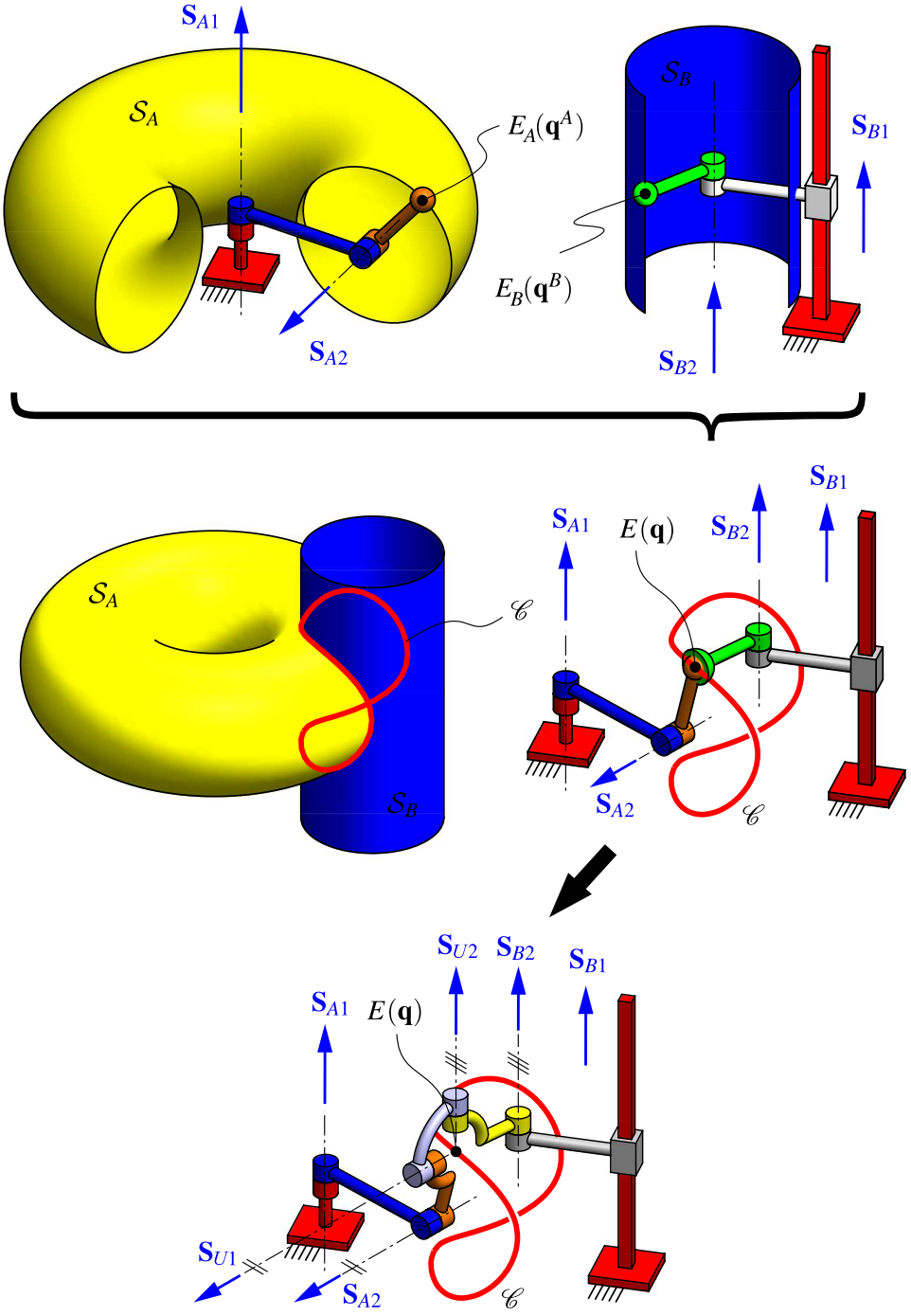

FIGURE 2.6: Two surface generators and a resulting closed-loop linkage.

- 1-DOF if w.l.o.g. $E(\mathbf{q})$ is regular at $\mathcal{S}_B$ but it is a conic singularity in $\mathcal{S}_A$ such that $\partial\sigma_A/\partial q_{A1} \times \partial\sigma_A/\partial q_{A2} = 0$, not only for (q_{A1}, q_{A2}) but for a neighborhood around it.
- 2-DOF if $E(\mathbf{q})$ is a conic singularity in both surfaces such that, for $i = A, B$, $\partial\sigma_i/\partial q_{i1} \times \partial\sigma_i/\partial q_{i2} = 0$, not only for (q_{i1}, q_{i2}), but for a neighborhood around it.
- 2-DOF if $\mathcal{S}_A = \mathcal{S}_B$,

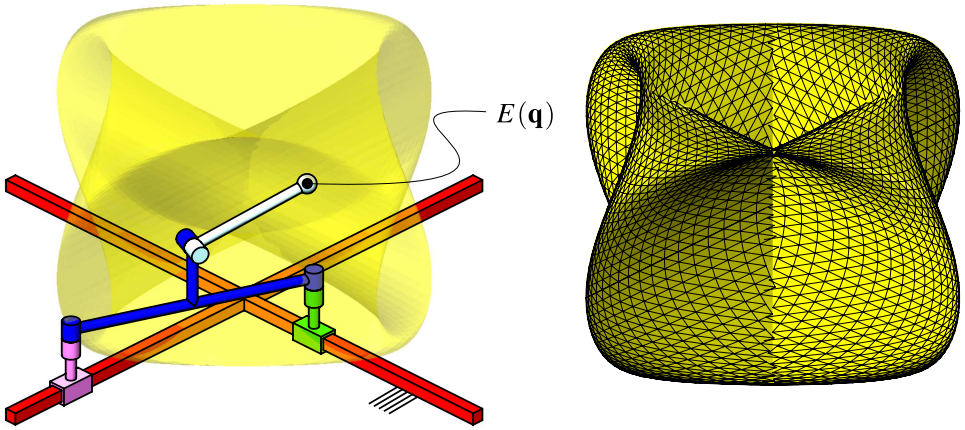

FIGURE 2.7: A degree 8 algebraic surface generated by a hybrid kinematic chain.

From the list above, the cases involving points which keep on being conic singularities in their neighborhood can be exemplified by the poles of a unit sphere of parametrized as $\sigma(u,v) = (\cos v \cos u, \cos v \sin u, \sin v)$. It is easy to prove that $\partial\sigma/\partial u = 0$ for all $(u, \pm\pi/2)$, $u \in \mathbb{T}$. Therefore, $\sigma(u, \pm\pi/2) = (0, 0, \pm 1)$ is always a pole and a conic singularity.

López-Custodio et al. [11], [29], exploited the properties of the intersection of surfaces to design reconfigurable mechanisms. From the discussion above, it is natural to conclude that a reconfigurable mechanism can be designed by intersecting two surfaces and forcing the intersection to have two curves that intersect at (at least) one point. Such a situation can be obtained by making the surfaces tangent to each other. Other interesting examples can be obtained from the previous discussion on mobility by taking advantage of the conic singularities. Namely, a reconfigurable mechanism can be designed if the intersection contains a curve which crosses a point that is a conic singularity in one of the surfaces. Even more interestingly, a kinematotropic linkage can be obtained if the intersection is designed to contain a curve that crosses a point that is a conic singularity in both surfaces.

Although in most of the research done so far using generated surfaces only dyads are considered as mechanical generators of the surfaces, actually any 2-DOF kinematic chain can generate a surface. Fig. 2.7 shows a *hybrid* mechanism, i.e. a linkage that combines serial and parallel topologies. To build the linkage a planar PPRR mechanism is first assembled, this particular 1-DOF mechanism is called the trammel of Archimedes. Then, an extra link is connected to the coupler of the trammel of Archimedes by means of an R joint. A point E attached to this extra link will sweep a circle along the curves drawn by the trammel of Archimedes. The result, also shown in fig. 2.7, in algebraic surface of degree 8 which has multiple self-intersections all contained in two orthogonal planes. In chapter 5 a similar surface, the Bohemian dome, is used to design a kinematotropic linkage, taking advantage of its self-intersections.

2.8 Computational tools used in this thesis

Throughout this thesis, the solution to systems of non-linear equations is required. Typical examples are the systems of equations obtained from the intersection of two toroids in Section 3.4, and that obtained from the intersection of a Bohemian dome and another quartic surface in Section 5.6.1. In this thesis, whenever a system of equations obtained from the intersection of surfaces is solved, closed-form solutions are obtained. This is achieved by means of the direct call of the command `solve` from Maple©.

However, in the case of the system of equations in section 9.5.1, whose solution is needed to obtain the forward kinematics of a generalized Exechon PKM, no closed-form solution is available. In such case, the command `fsolve` from the Maple© is applied. This command will return a single solution within the specified bounds of the search space. Similarly, the command `fsolve` is used to solve the single-variable expression obtained from Eq. (9.9).

SolidWorks© is used to model all the mechanisms presented in the figures of this thesis. The 'intersection curve' tool from SolidWorks© was used to draw the intersection between surfaces shown in the figures. These curves were visually compared to the plots of the parameterizations obtained in Maple©. Since neither Maple© nor Matlab© offer a direct tool for vector plotting, Geogebra© allowed the visual comparison between the vectors and screws drawn in SolidWorks© and the ones obtained in Maple©.

Due to its preferable function plotting tool, Matlab© was required for generating figures 9.11 and 9.12.

2.9 Chapter conclusions

In this chapter, we briefly revisited a few concepts that are applied throughout the thesis. The importance of the kinematic tangent cone in the analysis of reconfigurable mechanisms was explained in a natural way from the concept of configuration space. Notation and terminology was also introduced. Notation will vary a bit in chapter 7 where a total of four surfaces are involved in the design of the mechanism, and in chapter 9, where existing points A and B should not be mistaken as frames, hence the latter are referred to with non-italic letters, e.g. A and B.

Chapter 3

Toroid-toroid intersections: Bricard line-symmetric mechanisms

In this chapter a family of line-symmetric Bricard mechanisms are investigated by means of two generated toroids. The intersection of these toroids will reveal that the members of this family are always reconfigurable linkages. These toroids are considered to be concentric and present certain symmetries that lead to the line-symmetric case. By manipulating the construction parameters of the toroids all possible bifurcation points are explored.

The study will reveal the presence of Villarceau and secondary circles in the toroids intersection. Therefore, a way to reconfigure the Bricard linkage to a pair of different types of Bennett mechanism is uncovered. As an example, a linkage with two Bricard and two Bennett motion branches will be explored. It will be seen that the Altmann linkage is a member of this family of special line-symmetric Bricard linkages. The method is applied to the plane-symmetric case in Chapter 4.

This chapter is based on the journal publication:

[35] P.C. López-Custodio, J.S. Dai, and J.M. Rico, "Branch reconfiguration of Bricard linkages based on toroids intersections: Line-symmetric case," *ASME Journal of Mechanisms and Robotics*, vol. 10, no. 3, pp. 031003-1-–031003–11, 2018. DOI:10.1115/1.4038981.

3.1 Background

The fascination for the six types of overconstrained 6R linkages discovered by Bricard [85], [86] has left almost a century of research on their geometry and mobility that even led to the discovery of more general forms of these loops [87]. Hunt [88], Phillips [89], Baker [90] and Bricard himself [86], among others, thoroughly analyzed these closed loops obtaining striking findings on their geometry. Even though nowadays the mysteries related to the mobility of the Bricard mechanisms have been clarified, there is still room for research related to the application, optimization and particularly reconfigurability of these closed loops. This chapter focuses on the latter.

Overconstrained mechanisms [91]–[93] present a mobility which cannot be revealed by the Kutzbach-Grübler criterion but can be obtained by using the modified mobility criterion [93]. The geometry of an overconstrained mechanism presents symmetries that make it movable. Bricard reported six movable 6R closed kinematic chains, each presenting specific symmetries that allowed the mobility of the overconstrained mechanism. Bricard proved that these symmetries allowed all the axes in the kinematic chains to belong to the same linear complex [58], [88], [94], [95]. The six cases reported by Bricard are the line-symmetric case,

the plane-symmetric case, the trihedral case, the line-symmetric octahedral case, the plane-symmetric octahedral case and the doubly collapsible octahedral case. The DH parameters for the first case are the following [90]:

$$a_{1,2} = a_{4,5}, a_{2,3} = a_{5,6}, a_{3,4} = a_{6,1},$$
$$\alpha_{1,2} = \alpha_{4,5}, \alpha_{2,3} = \alpha_{5,6}, \alpha_{3,4} = \alpha_{6,1},$$
$$d_1 = d_4, d_2 = d_5, d_3 = d_6.$$

The general line-symmetric case is depicted in fig. 3.1. In this case each member of the mechanism is symmetric to another member through a line $\mathscr{L}$ (fig. 3.1), which, therein, perpendicularly bisects a line segment that joins the corresponding points of these members. It is possible to find a line reciprocal to every axis of the mechanism, however, in general this will not intersect each axis, therefore the linear complex has a non-zero pitch. Refer to the Appendix to [96] to find the central axis of this linear complex, this axis turns out to intersect perpendicularly the line of symmetry.

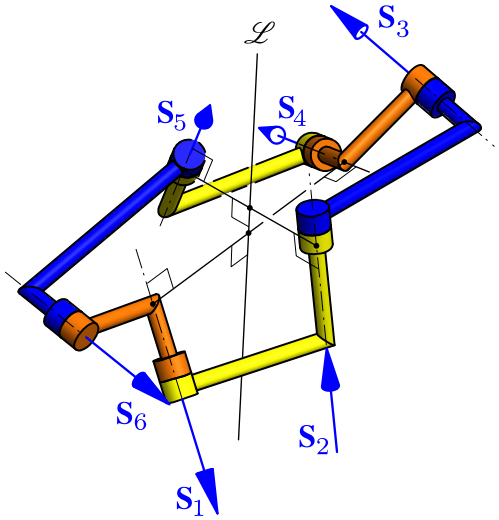

FIGURE 3.1: The general line-symmetric case of Bricard linkage.

Some examples of reconfigurable Bricard linkages have been reported [27], [73], [97], [98] and applications of the Bricard loops in large deployable structures have been presented [18]–[20]. However, the reconfigurability, particularly its intrinsic properties that cast light to design, have not been presented. In this chapter, the reconfigurability of the line-symmetric type of Bricard linkages is obtained by means of the intersection of generated toroids. The design is made by manipulating the construction parameters of two concentric toroids. Any possibility of tangency between the two surfaces is considered to obtain various cases of reconfigurability. It will be proven that certain members of this family of line-symmetric Bricard linkages can work as two different types of Bennett linkage.

Toroids play an important role in the theory of mechanisms as they are generated by a kinematic dyad conformed by two revolute joints with skew axes. It is known that the only subgroup of motion of the special Euclidean group, SE(3), that includes the motion generated by such a dyad is the whole Euclidean group. Thus, the analysis of linkages that include such dyad may lead to complications. Using the toroid as a generated surface the existence of several overconstrained linkages can be explained: The Bennett 4R linkage [9], [99]–[101], the Myard 5R mechanism [6] and the family of overconstrained 5R loops with two consecutive parallel axes presented by Baker [11], [102]. Toroids have also been used

in the analysis of 5R spatial mechanisms obtained from the combination of 4R mechanisms designed from the geometry of toroids [103], the derivation of equivalent lower pairs linkage for mechanisms involving a higher pair based on tori surface contact [104] and the analysis of RSSR linkages [105]

The original contributions of this chapter include: the design of linkages obtained from the intersection of surfaces by exploring all the possibilities of tangency between surfaces, the analysis of the line-symmetric case of Bricard linkage by means of the intersection of two concentric toroids, the design of the intersection set forcing it to include circles in order to obtain idle joints in the mechanism and the explanation of the relationship between the Bennett linkage and the Bricard line-symmetric mechanisms by means of the toroids geometry. In addition, very few contributions, including this chapter and probably only [73], not only present the analysis of examples of reconfigurable Bricard mechanisms, but also develop a method for the design of these mechanisms.

This chapter is organized as follows: Firstly the relationship between the configuration space and the toroid is reviewed, then the Bricard linkage is separated in its two toroid generators. The conditions for the mechanism to be able to move along the intersection are established. The intersection between the two toroids is obtained and then the points of tangency between the two surfaces are explored. With this aim, the mutual bi-tangent planes are analyzed, leading to the discovery of motion branches of the Bennett type for reconfiguration. An example of a mechanism with two Bricard and two Bennett motion branches is presented. Finally, some remarks about the Altmann linkage, which is well-known to be a special case of line-symmetric Bricard linkage, are made considering it as a member of the family of reconfigurable Bricard linkages studied in this chapter. A second part of this research dealing with the plane-symmetric case is presented in a Chapter 4.

3.2 Toroids generated by kinematic dyads

As seen in Chapter 2, for a kinematic chain with $n = 2$ kinematic pairs, the non-smooth map $E : V \to \mathbb{R}^3$, describes the position of a point $E(\mathbf{q})$ attached to the end effector of the dyad in the configuration $\mathbf{q}$. The image of E under the whole configuration space is a surface $\mathcal{S} := \mathrm{im}(E(V)) \subset \mathbb{R}^3$ whose shape depends not only on the DH parameters of the dyad, but also on the choice of the point that defines E, relative to the end effector link. Degenerated cases in which $\mathcal{S}$ is not a surface or it is a doubly covered plane are not of interest.

Consider an RR kinematic chain, if the axes of the revolute joints are skew, $\mathcal{S}$ is a toroid as shown in fig. 3.2. The toroid $T_{l,r,\gamma,s}(\hat{\mathbf{u}}, Q)$ has a base circle C_1 of radius l and center Q and lies on a plane perpendicular to $\hat{\mathbf{u}}$, a secondary circle $C_2(u)$ of radius r is swept through C_1 to generate the surface of revolution. The constant angle between the normals of the planes containing C_1 and C_2 is γ and the secondary offset, i.e. the distance from C_1 to the center of C_2 measured along the axis of C_2, is s. $\mathscr{B}$ is the closed curve obtained by intersecting the toroid with any plane containing the Z axis. In fig. 3.2, $\hat{\mathbf{u}} = \hat{\mathbf{k}}$ and $Q = O$, for the sake of shortening the notation we define this toroid as $T_{l,r,\gamma,s} := T_{l,r,\gamma,s}(\hat{\mathbf{k}}, O)$. The generator open kinematic chain is defined by $\alpha_{1,2} = \gamma$, $a_{1,2} = l$ and $d_2 = s$.

It has to be noted that the same surface is generated with the angles γ, $\gamma+\pi$, $-\gamma$, $-\gamma-\pi$ and $\pi-\gamma$. Thus, we define $\gamma^* \in (0, \frac{1}{2}\pi]$, which, along with l, r and s defines uniquely a toroid.

γ^* can be obtained from any value of γ according to:

$$\begin{aligned}
\gamma < \tfrac{1}{2}\pi &\Rightarrow \gamma^* = \gamma, \\
\tfrac{1}{2}\pi < \gamma < \pi &\Rightarrow \gamma^* = \pi - \gamma, \\
\pi < \gamma < \tfrac{3}{2}\pi &\Rightarrow \gamma^* = \gamma - \pi, \\
\tfrac{3}{2}\pi < \gamma < 2\pi &\Rightarrow \gamma^* = 2\pi - \gamma.
\end{aligned}$$

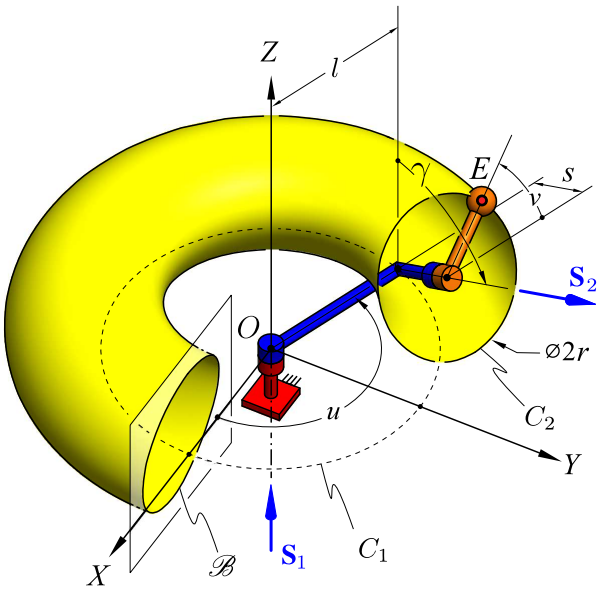

FIGURE 3.2: An RR dyad generating a general toroid.

Depending on the construction parameters of the toroid (l, r, s and γ), different shapes of surfaces are obtained. We use the classification presented in [6]. The *general form* with $s \neq 0$ and $\gamma \neq \pi/2$ is the most general case that can be generated by this dyad; for the *symmetrical form*, $s \neq 0$ but $\gamma = \pi/2$, which results in a symmetry with respect to the plane containing C_1; for the *flattened form* $s = 0$ but $\gamma \neq \pi/2$, and the toroid is also symmetric with respect to the plane containing C_1 but it appears flattened due to the inclination of C_2; finally, for the *common form* $s = 0$ and $\gamma = \pi/2$, which results in $\mathscr{B} = C_2$ and the toroid becomes a typical torus or right toroid. It is important to mention that, a common form with $r > l$ leads to two conic singularities symmetrically disposed in the axis $\mathscr{L}(\hat{\mathbf{u}}, Q)$ of the toroid.

Using the parameters shown in fig. 3.2 $(u, v) \in U = \mathbb{T}^2$ the following parameterization for the general form $T_{l,r,\gamma,s}$ can be obtained:

$$\begin{aligned}
\sigma(u,v) &= \mathrm{Rot}(u,\hat{\mathbf{k}})\left[\mathrm{Rot}(\gamma,\hat{\mathbf{i}})(r\mathrm{Rot}(v,\hat{\mathbf{k}})\hat{\mathbf{i}} + s\hat{\mathbf{k}}) + l\hat{\mathbf{i}}\right] \\
&= ((s\sin\gamma - r\cos\gamma\sin v)\sin u + (r\cos v + l)\cos u, \\
&\quad (-s\sin\gamma + r\cos\gamma\sin v)\cos u + (r\cos v + l)\sin u, \\
&\quad r\sin\gamma\sin v + s\cos\gamma)
\end{aligned} \tag{3.1}$$

and $T_{l,r,\gamma,s} = \mathrm{im}(\sigma(U))$. The implicit form $\phi \in \mathbb{R}[x,y,z]$ is a quartic on x, y, z such that $T_{l,r,\gamma,s} = \left\{\mathbf{r}_E \in \mathbb{R}^3 \,|\, \phi(\mathbf{r}_E) = 0\right\}$. This implicit form is given by [6]:

$$\phi(x,y,z) = \left(x^2 + y^2 + z^2 - l^2 - r^2 - s^2\right)^2 - 4l^2\left[r^2 - \left(\frac{z - s\cos\gamma}{\sin^2\gamma}\right)^2\right] \tag{3.2}$$

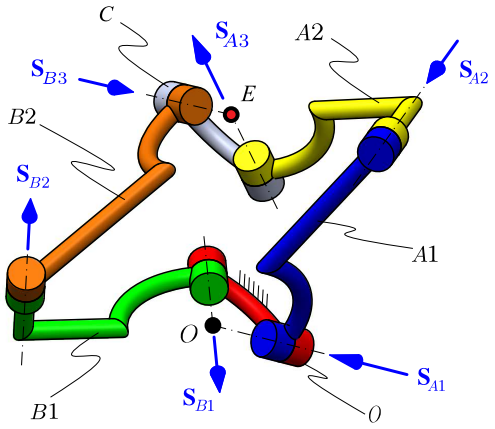

FIGURE 3.3: The line-symmetric Bricard linkages that can be analyzed as the intersection of two concentric toroids.

3.3 The line-symmetric Bricard linkage generator of concentric toroids

In the line-symmetric case of Bricard linkages any adjacent pair of revolute joints generate a toroid if the two axes are skew lines, i.e. the length-link parameter between the two axes is different to zero. Let $\alpha = \{1,\ldots,6\}$ be a cyclic sequence of numbers, if in the 6R Bricard linkage a link connecting the axes $\mathbf{S}_i$ and $\mathbf{S}_{i+1}$, $i \in \alpha$, has zero length, i.e. $a_{i,i+1} = 0$, and zero axial displacements, i.e. $d_i = d_{i+1} = 0$, then the point E common to $\mathbf{S}_i$ and $\mathbf{S}_{i+1}$ describes the intersection of two toroids with respect to the opposite link connecting axes $\mathbf{S}_{i-3}$ and $\mathbf{S}_{i+4}$. Thus the mechanism can be analyzed using the method of intersection of surfaces. In the octahedral cases both toroids degenerate into points. These degenerate cases are not addressed in this contribution, neither are the cases in which one of the toroids is any other degenerate form.

Due to symmetry, if $a_{i,i+1} = 0$ and $d_i = d_{i+1} = 0$, then $a_{i-3,i+4} = 0$ and $d_{i-3} = d_{i+4} = 0$. Therefore, the two generated toroids are concentric. Fig. 3.3 shows a general example of line-symmetric Bricard mechanism derived from the intersection of two concentric toroids. Torfason and Sharma [3] solved numerically the polynomial equations of the intersection of two toroids generated by a general RRSRR non-overconstrained mechanism. The intersection of two right torus is also of interest in computer graphics [106]. In this chapter, closed-form solutions for the concentric toroid-toroid intersection are obtained since the aim of the chapter is the analysis of bifurcations and the design for reconfigurability.

For the Bricard line-symmetric case, let the toroid $T_{l_A,r_A,\gamma_A,s_A}(\hat{\mathbf{k}}_A, O) = \{E_A(\mathbf{q}_A) \,|\, \mathbf{q}_A \in \mathbb{T}^2\}$ be generated by kinematic pairs $A1$ and $A2$, while $T_{l_B,r_B,\gamma_B,s_B}(\hat{\mathbf{k}}_B, O) = \{E_A(\mathbf{q}_B) \,|\, \mathbf{q}_B \in \mathbb{T}^2\}$ is generated by kinematic pairs $B1$ and $B2$, where $\mathbf{q}_i = (u_i, v_i)$, $i = A, B$ and the toroids are related to coordinate systems A and B, whose origins are coincident with O and Z_i axis is coincident with the $\mathbf{S}_{i1}$, $i = A, B$. To simplify the notation, let $T^A_{l_A,r_A,\gamma_A,s_A} := T_{l_A,r_A,\gamma_A,s_A}(\hat{\mathbf{k}}_A, O)$ and $T^B_{l_B,r_B,\gamma_B,s_B} := T_{l_B,r_B,\gamma_B,s_B}(\hat{\mathbf{k}}_B, O)$.

Since both open kinematic chains are connected by link C between coincident revolute joints $A3$ and $B3$, $E_A(\mathbf{q}_A) = E_B(\mathbf{q}_B) = E(\mathbf{q})$, where $\mathbf{q} := (q_{A1}, q_{A2}, q_{A3}, q_{B3}, q_{B2}, q_{B1}) \in V \subset \mathbb{T}^6$. The joint parameters can be measured as shown in fig. 3.2 and then $q_{A1} = u_A$, $q_{A2} = v_A$, $q_{B1} = u_B$ and $q_{B2} = v_B$. q_{A3} and q_{B3} are in symmetric concordance with u_B and u_A, respectively. Since $E(\mathbf{q}) \in T^A_{l_A,r_A,\gamma_A,s_A}$ and $E(\mathbf{q}) \in T^B_{l_B,r_B,\gamma_B,s_B}$ it follows that $E(\mathbf{q}) \in T^A_{l_A,r_A,\gamma_A,s_A} \cap T^B_{l_B,r_B,\gamma_B,s_B}$. Let $\mathcal{C} := T^A_{l_A,r_A,\gamma_A,s_A} \cap T^B_{l_B,r_B,\gamma_B,s_B}$, then $\mathcal{C}$ may feature $n \in \mathbb{Z}_+$ components such that $\mathcal{C} = \cup_{i=1}^n \mathcal{C}_i$. These components can be points, curves or, in the trivial case that both toroids are the same, a surface.

Both toroids are represented by their parameterizations ${}^{A}\sigma_A$ and ${}^{B}\sigma_B$ respectively referred to coordinate systems A and B. The relationship between the coordinate systems is given by the transformation matrix ${}^{A}_{B}\mathbf{T} \in \mathrm{SE}(3)$. Given $\mathbf{f} := {}^{i}\sigma_A - {}^{i}\sigma_B$, $i \in \{A,B\}$, the intersection $\mathcal{C}$ is computed by ${}^{i}\mathcal{C} = \{{}^{i}\sigma_A(u_A,v_A) \,|\, \mathbf{f}(u_A,v_A,u_B,v_B) = \mathbf{0}\} = \{{}^{i}\sigma_B(u_B,v_B) \,|\, \mathbf{f}(u_A,v_A,u_B,v_B) = \mathbf{0}\}$, $i \in \{A,B\}$. $\mathcal{C}$ may include isolated points and curves in $\mathbb{R}^3$ or it can be a surface, in the case that both toroids are the same surface.

Each component of $\mathcal{C}$ is related to a component of the configuration space V of the linkage, and thus, to a motion branch or assembly mode. However, in the case of these 6R mechanisms it has to be proved that the symmetries allow E to move throughout the intersection. It will be concluded that for the line-symmetric case an extra restriction is required. When a curve $\mathscr{C} \subset \mathcal{C}$ appears in the intersection, the equivalent component in V is 1-dimensional and the mechanism has 1 DOF, this leads to the typical motion of the overconstrained mechanism. On the other hand, if $\mathcal{C}$ features an isolated point, this point is equivalent to a 0-dimensional component in V and the mechanism can be assembled as a structure. However, if, for the same linkage, $\mathcal{C}$ also features a curve or a double-coincident conic singularity, the same mechanism can be assembled to have 1 finite degree of freedom.

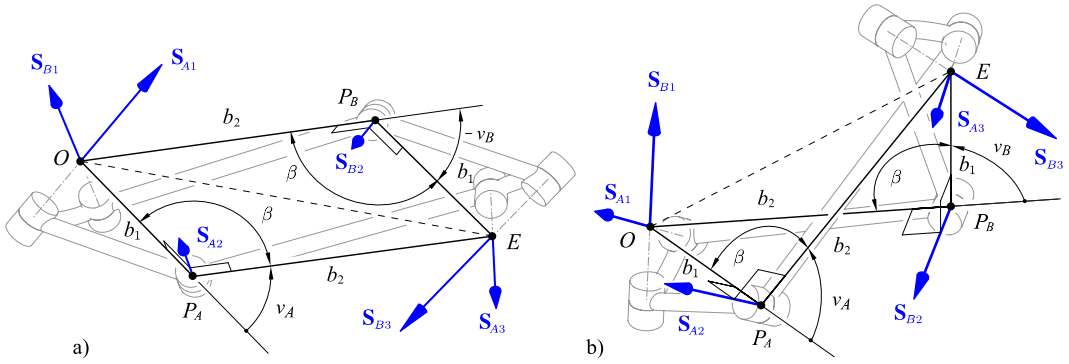

FIGURE 3.4: Diagram of the line-symmetric case with $s_A = s_B = 0$. a) Assembly with $v_A = -v_B$ and b) assembly with with $v_A = v_B$.

Refer to fig. 3.4 which depicts the common perpendiculars diagram for the line-symmetric case with $s_A = s_B = 0$. The axis of symmetry is given by $\mathscr{L}(\mathbf{r}_E \times (\mathbf{r}_{PA} - \mathbf{r}_{PB}), \frac{1}{2}\mathbf{r}_E)$. Observe that the common perpendiculars between the joint axes *always* assembly two equal triangles, OP_AE and OP_BE, drawn on planes perpendicular to $\mathbf{S}_{A2}$ and $\mathbf{S}_{B2}$ respectively. Therefore, the inner angles β (fig. 3.4) are always the same in both triangles. The condition $\beta + |v_i| = \pi$, $i = A,B \Rightarrow |v_A| = |v_B|$ allows the different possibilities shown in figures 3.4a and 3.4b. The change in the sign of v_i, $i = A,B$ does not affect the symmetry since the angles β are always the same for both triangles. The screw axes can be reversed from one assembly to another to obtain the proper signs of symmetry. Therefore it can be concluded that the symmetry is not lost while E moves through any component of $\mathcal{C}$. However, if $s_A = s_B \neq 0$ such a change in sign would break the symmetry. A change in the direction of the screw axes attempting to fix the symmetry would affect the topology of the mechanism due to the change of sign in the DH parameter d. In fact, it has been proven [107] that the change in sign in the articular variables, i.e. a negative relationship between them, is not a solution of the closure equations of the general line-symmetric case. The intersection of two concentric toroids with non-zero secondary offset would require a third revolute joint intersecting E and non-coplanar with $\mathbf{S}_{A3}$ and $\mathbf{S}_{B3}$ to ensure that E can move through any component of $\mathcal{C}$. Without this third revolute joint the mechanism would be movable only in certain components of $\mathcal{C}$ that do not break the symmetry. Due to this situation, only cases with $s_A = s_B = 0$, i.e. flattened forms, are studied here.

From the previous paragraph and the required conditions for the method of generated surfaces explained in Section 3.2, the special line-symmetric Bricard loops to be designed in this chapter present the following restrictions:

- $d_i = 0,\ i = 1,\ldots,6$, and
- $a_{i,i+1} = 0 \Leftrightarrow a_{i+1,i+2} \neq 0,\ i \in \{1,\ldots,6\}$

where $\{1,\ldots,6\}$ is a cyclic sequence. Hence, all the special Bricard linkages have two, and only two, opposite zero-length links and all the axial displacements are zero for all the joints.

3.4 Concentric toroid-toroid intersection

The line-symmetry condition applied to the intersection of toroids A and B forces the radius of the base circle of one toroid to be the same as the radius of the secondary circle of the other toroid. Therefore, let $b_1 := l_A = r_B$ and $b_2 := l_B = r_A$. Let the relationship between coordinate systems A and B be given by ${}^A_B\mathbf{T} = \mathrm{HT}(\mathrm{Rot}(\theta,\hat{\mathbf{j}}),\mathbf{0})$, such that the toroids are concentric and the axis of B is obtained by rotating the axis of A θ radians about the $Y := Y_A = Y_B$ axis.

The parameterizations of both surfaces referred to coordinate system A are:

$$
\begin{aligned}
{}^A\sigma_A(u_A,v_A) &= \Big((b_2+b_1\cos v_A)\cos u_A - b_1\cos\gamma_A\sin v_A\sin u_A,\ (b_2+b_1\cos v_A)\sin u_A \\
&\quad + b_1\cos\gamma_A\sin v_A\cos u_A,\ b_1\sin\gamma_A\sin v_A\Big) \\
{}^A\sigma_B(u_B,v_B) &= \Big(\cos\theta((b_1+b_2\cos v_B)\cos u_B - b_2\cos\gamma_B\sin v_B\sin u_B) + b_2\sin\theta\sin\gamma_B\sin v_B, \\
&\quad (b_1+b_2\cos v_B)\sin u_B + b_2\cos\gamma_B\sin v_B\cos u_B,\ \sin\theta(b_2\cos\gamma_B\sin v_B\sin u_B \\
&\quad -(b_2\cos v_B+b_1)\cos u_B) + b_2\cos\theta\sin\gamma_B\sin v_B\Big)
\end{aligned}
\tag{3.3}
$$

and the implicit forms are given by:

$$
\begin{aligned}
\phi_A(x,y) &= \left(x^2+y^2+z^2-{b_1}^2-{b_2}^2\right)^2 - 4{b_2}^2\left({b_1}^2 - \frac{z^2}{\sin^2\gamma_A}\right) \\
\phi_B(x,y) &= \frac{1}{\sin^2\gamma_A}\Big(-\left(x^2+y^2+z^2-{b_1}^2+2b_1b_2-{b_2}^2\right)\left(x^2+y^2+z^2-{b_1}^2-2b_1b_2\right. \\
&\quad \left.-{b_2}^2\right)\cos^2\gamma_A + +\left(-4x^2+4z^2\right){b_2}^2\cos^2\theta + 8\cos\theta\sin\theta xz{b_2}^2 + +{b_2}^4 + \left(2x^2-2y^2\right. \\
&\quad \left.-2z^2-2{b_1}^2\right){d_2}^2 + \left(x^2+y^2+z^2-{b_1}^2\right)^2\Big)
\end{aligned}
\tag{3.4}
$$

After solving $\mathbf{f}(u_A,v_A,u_B,v_B) = {}^A\sigma_B - {}^A\sigma_A = \mathbf{0}$, the values of u_A,v_A,u_B in terms of v_B are obtained. This expressions are listed in Appendix A. Four sets of solutions are found. As expected, v_A and v_B bear the condition of symmetry as shown in fig. 3.4. Taking

${}^A\sigma_B(u_B(v_B),v_B)$, the parameterizations for four 1-dimensional curves are found:

$$
\begin{aligned}
{}^A\varsigma_1(v_B) &= \left(\frac{(b_2\sin\gamma_B - b_1\cos\theta\sin\gamma_A)\sin v_B}{\sin\theta}, -\frac{\sqrt{K_1}}{\sin\theta\cos\gamma_B}, b_1\sin\gamma_A\sin v_B\right)\\
{}^A\varsigma_2(v_B) &= \left(\frac{(b_2\sin\gamma_B - b_1\cos\theta\sin\gamma_A)\sin v_B}{\sin\theta}, \frac{\sqrt{K_1}}{\sin\theta\cos\gamma_B}, b_1\sin\gamma_A\sin v_B\right)\\
{}^A\varsigma_3(v_B) &= \left(\frac{(b_2\sin\gamma_B + b_1\cos\theta\sin\gamma_A)\sin v_B}{\sin\theta}, -\frac{\sqrt{K_2}}{\sin\theta\cos\gamma_B}, -b_1\sin\gamma_A\sin v_B\right)\\
{}^A\varsigma_4(v_B) &= \left(\frac{(b_2\sin\gamma_B + b_1\cos\theta\sin\gamma_A)\sin v_B}{\sin\theta}, \frac{\sqrt{K_2}}{\sin\theta\cos\gamma_B}, -b_1\sin\gamma_A\sin v_B\right) \quad (3.5)
\end{aligned}
$$

where K_1 and K_2 are defined in Appendix A. Thus, $\mathcal{C} = \cup_{i=1}^{4}\mathcal{C}_i$, where $\mathcal{C}_i = \mathrm{im}(\varsigma_i(W))$, where $W \subseteq \mathbb{T}$. However, the expressions in Eq. (3.5) for the general intersection may take discontinuous forms containing parts of different components depending on each specific numerical case. By eliminating the discontinuities and rearranging the components, the correct parameterizations for each curve can be obtained.

3.5 The bitangent planes and singularities

If in the concentric toroid-toroid intersection there exist $i,j \ni i \neq j$ such that $\mathcal{C}_i \cap \mathcal{C}_j \neq \emptyset$ the mechanism is reconfigurable with at least 2 motion branches, which are connected through at least one configuration $\mathbf{q}_{ij} \in V_i \cap V_j$. It can be proved [11] that for the 1-dimensional components of V, the toroids are tangent to each other in $E(\mathbf{q}_{ij})$. The intersection is non-transverse in $E(\mathbf{q}_{ij})$ and it follows that if $\mathbf{q}_{ij} := (u_A^P, v_A^P, q_{A3}^P, q_{B3}^P, v_B^P, u_B^P)$, then $\mathbf{n}_A(E_A(u_A^P, v_A^P)) \times \mathbf{n}_B(E_B(v_B^P, u_B^P)) = \mathbf{0}$, where $\mathbf{n}_i : \mathcal{S}_i \to \mathbb{R}^3$ is the normal vector to the surface in the given point. This vector can be found by means of either the partial derivatives of the parameterization of the surface or the gradient of the implicit form. Here the latter is used, then the intersection is non-transverse if $\nabla\phi_A(x^P,y^P,z^P) \times \nabla\phi_B(x^P,y^P,z^P) = \mathbf{0}$, where $(x^P,y^P,z^P) = E(\mathbf{q}_{ij})$. The points in V that map to points of tangency *may* be bifurcation configurations of the mechanism. These points in V may represent the intersection of two components of V, or may be the self-crossing of the same component. The surfaces are also tangent to each other when they touch in one point, which would lead to an isolated point in V. In addition, if a continuum of points of tangency is found, the surfaces are touching in a curve in $\mathcal{C}$.

To find the points where the intersection becomes non-transverse, the real points $(x,y,z) \in \mathbb{R}^3$ that make $\nabla\phi_A(x,y,z) \times \nabla\phi_B(x,y,z) = \mathbf{0}$ and also satisfy $\phi_A(x,y,z) = \phi_B(x,y,z) = 0$. are explored. Four immediate results are found: $(0, b_1+b_2, 0)$, $(0, b_1-b_2, 0)$, $(0, -b_1-b_2, 0)$ and $(0, -b_1+b_2, 0)$. These four points are independent of any construction parameter of the toroids. The toroids are tangent to each other through these four points in the Y axis. This is a consequence of the symmetry condition $l_A = r_B, l_B = r_A$. The flattened toroids are symmetric with respect to the plane that contains its base circle, the intersection of these planes with toroids A and B lead to the same pair of concentric circles of radii b_1+b_2 and $|b_1-b_2|$. As the axis of B is rotated θ radians about the Y axis these two circles intersect in the four found points and the surfaces are always tangent there. Replacing $v_B \in \{0,\pi\}$ in parameterizations ς_i, $i = 1\ldots4$ it is found that these four points are the intersections between pairs of curves in $\mathcal{C}$. From these results it can be concluded that any line-symmetric mechanism of this family (featuring two opposite link-lengths equal to zero and all axial offsets equal to zero) is reconfigurable with at least 4 bifurcation configurations $\mathbf{q}_i^b \in V$, $i = 1\ldots4$, such that $E(\mathbf{q}_i^b) \in \{(0, b_1+b_2, 0), (0, b_1-b_2, 0), (0, -b_1-b_2, 0), (0, -b_1+b_2, 0)\}$. We call these four points the

permanent points of tangency, since they are always present in any member of this family of line-symmetric Bricard mechanisms.

When $E(\mathbf{q})$ reaches any of these points, the mechanism is in a flattened configuration and v_A and v_B are either 0 or π (which is equal to $-\pi$ in $\mathbb{T}$). Therefore, the change in the sign of v_B explained in fig. 3.4 will occur in these configurations. A degenerate case occurs when $\theta \in \{0,\pi\}$. In this case the 4 curves become the two circles in the X_AY_A plane with radii b_1+b_2 and $|b_1-b_2|$. Throughout these circles the intersection is transverse since the surfaces are touching each other in the circles. $A1$ and $B1$ become coaxial as well as $A3$ and $B3$, but $A2$ and $B2$ are idle. Thus, the mechanism has partitioned mobility with 2 DOF.

From $\nabla\phi_A(x,y,z)\times\nabla\phi_B(x,y,z)=\mathbf{0}$ other solutions, all implying $y=0$, are found. Therefore, any point of tangency lies on either the Y axis or the $XZ := X_AZ_A = X_BZ_B$ plane. The solutions in the XZ plane are large expressions that involve not only the construction parameters of the toroids, but also the angle between axes, θ. Consider the intersections of both toroids with the XZ plane, which are the $\mathscr{B}_A$ and $\mathscr{B}_B$ curves. If $\mathscr{B}_A$ and $\mathscr{B}_B$ are not tangent to each other, the only bifurcation points of the mechanism are the ones discussed in the previous paragraph. Now imagine that θ starts increasing from zero until $\mathscr{B}_A$ and $\mathscr{B}_B$ are tangent to each other. The following proposition reveals the values of θ for which this result holds:

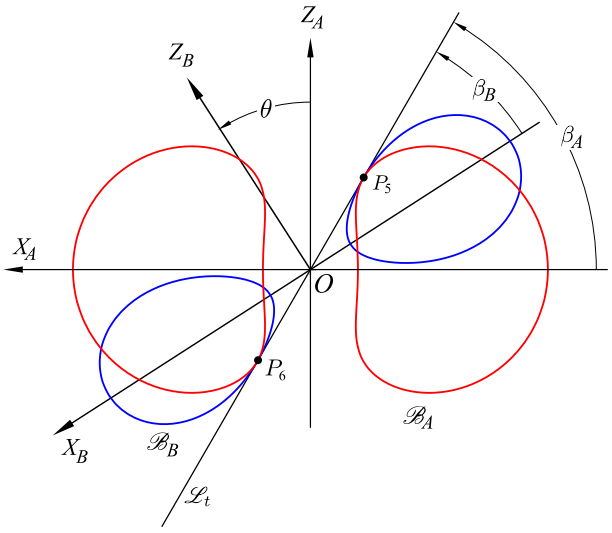

FIGURE 3.5: Intersection of toroids A and B and their bi-tangent plane with the XZ plane.

Proposition 3.5.1 *If two concentric toroids bearing line-symmetry properties have the same bi-tangent plane crossing their centers, then the points of tangency are the same for both toroids.*

Proof: Let the angle between the axes of the two concentric toroids be θ measured about the Y axis. Fig. 3.5 shows the intersection of the two toroids with the XZ plane with the Y axis pointing outside the sheet of paper. The intersection curves of toroids A and B with the plane are $\mathscr{B}_A$ and $\mathscr{B}_B$, respectively. The intersection of the coincident bi-tangent plane with the XZ plane is the line $\mathscr{L}_t$, this line makes angles β_A and β_B with the X_A and X_B axes, respectively. Implicit forms for curves $\mathscr{B}_A$ and $\mathscr{B}_B$ can be found from Eq. (3.4), such that $\mathscr{B}_i = \{(x,z)\in\mathbb{R}^2 \,|\, \phi_i(x,0,z)=0\}$, $i=A,B$. Taking the implicit form of $\mathscr{B}$, from any toroid $T_{l,r,\gamma,s}$ and computing its crossing points with any line intersecting the origin, it can be proved that, for any toroid, if $l>r$, $\beta = \pm\arcsin\big((r/l)\sin\gamma\big)$; and if $l<r$, $\beta\in\{\pm\gamma^*, \pi\pm\gamma^*\}$. In the case $l=r$, the toroid is singular and it is tangent to a cone in the singularity, $\mathscr{B}$ becomes one only 8-shaped singular curve and there is no bi-tangent plane intersecting O. If $l\neq r$,

there are four values of β that make the plane bi-tangent to the toroid, but since β and $\beta+\pi$ lead to the same plane due to symmetry, there are only two bi-tangent planes. Without loss of generality, let $r_A = l_B = b_1$ be larger than $r_B = l_A = b_2$, and take the solution in the third quadrant as in fig. 3.5, then $\beta_A = \gamma_A^*$ and $\beta_B = \arcsin((b_2/b_1)\sin\gamma_B)$. From fig. 3.5 it is clear that $\theta = \beta_A - \beta_A = \gamma_A^* - \arcsin((b_2/b_1)\sin\gamma_B)$. The other cases are symmetric to this.

Considering ${}^A\mathscr{L}_t = \{(x,y) \in \mathbb{R}^2 \,|\, z + \tan\beta_A x = 0\} = \{(x,y) \in \mathbb{R}^2 \,|\, z + \tan(\beta_B + \theta)x = 0\}$, it is easy to find the points $\{P_{5A}, P_{6A}\} = \mathscr{B}_A \cap \mathscr{L}_t$ and $\{P_{5B}, P_{6B}\} = \mathscr{B}_B \cap \mathscr{L}_t$. It will turn out that ${}^AP_{5A} = {}^AP_{5B} = \pm\sqrt{b_1^2 - b_2^2}\,(-\cos\gamma_A^*, 0, \sin\gamma_A^*)$ and ${}^AP_{6A} = {}^AP_{6B} = \pm\sqrt{b_1^2 - b_2^2}(\cos\gamma_A^*, 0, -\sin\gamma_A^*)$ and the plane is bi-tangent to both toroids in the same two points. ■

Without the symmetry condition, the toroids sharing the same bi-tangent plane may intersect the plane in different points.

3.6 Villarceau circles in the toroids intersection and reconfigurability to Bennett mechanisms

Using proposition 3.5.1 it can be concluded that whenever the bi-tangent planes of the toroids coincide the surfaces will be tangent to each other and two potential bifurcation points will appear in the XZ plane. Since, in fig. 3.5, $\mathscr{B}_A$ and $\mathscr{B}_B$ can appear in different sides of $\mathscr{L}_t$, this can happen for eight different values of θ:

$$\begin{gathered}
\beta_A + \beta_B, \\
\beta_A - \beta_B, \\
\pi - (\beta_A + \beta_B), \\
\pi - (\beta_A - \beta_B), \\
-(\beta_A + \beta_B), \\
-(\beta_A - \beta_B), \\
-(\pi - (\beta_A + \beta_B)), \\
-(\pi - (\beta_A - \beta_B))
\end{gathered}$$

It is known that the bi-tangent planes to any toroid intersect the latter in two circles [6] symmetrically disposed with the XZ plane (in our case). Since the bi-tangent plane is shared by both toroids these two circles are components of $\mathcal{C}$. If (w.l.o.g.) $r < l$ for toroid B, these circles are the famous Villarceau circles [108], of radii $l_B = b_1$, centers $(0, \pm(l_B - r_B), 0)$ and intersecting in P_5 and P_6, while for toroid A $l < r$ and the two circles are the secondary circles. One of these circles is generated by E rotating around $\mathbf{S}_{A2}$ while $u_A = \frac{1}{2}\pi$, then revolute joint $A1$ is idle for this branch of motion. Due to the line-symmetry condition revolute joint $B3$ must be idle too, then the mechanism evolves to a Bennett linkage in this branch of motion, since it is the only spatial skew 4R linkage that is movable.

It is well known [9], [99], [100] that a Bennett mechanism can be explained as a generator of a toroid where E is confined to move in a Villarceau circle by means of link between E and a revolute joint that generates the circle. Thus the Bennett conditions [109] must be present in this Bricard linkage: since $A1$ is idle, the DH parameter for the twist angle of now adjacent axes $\mathbf{S}_{B1}$ and $\mathbf{S}_{A2}$ is $\alpha_{B1,A2} = \gamma_A^* - \theta = \pm\arcsin((b_2/b_1)\sin\gamma_B)$ or, depending on the choice of θ, $\alpha_{B1,A2} = \gamma_A^* - \theta = \pi \pm \arcsin((b_2/b_1)\sin\gamma_B)$, as expected from the Bennett conditions. In the opposite circle $A1$ is active since it cannot be generated by E rotating around $\mathbf{S}_{A2}$. These two circles intersect the other two curves of $\mathcal{C}$ in the permanent points of tangency in the y_A axis, through which reconfigurability is possible. Fig. 3.6a shows this case in which the intersection includes the two Villarceau circles intersecting in points 6 and 5, which are points of tangency, the intersection also includes two other closed curves that are not circles.

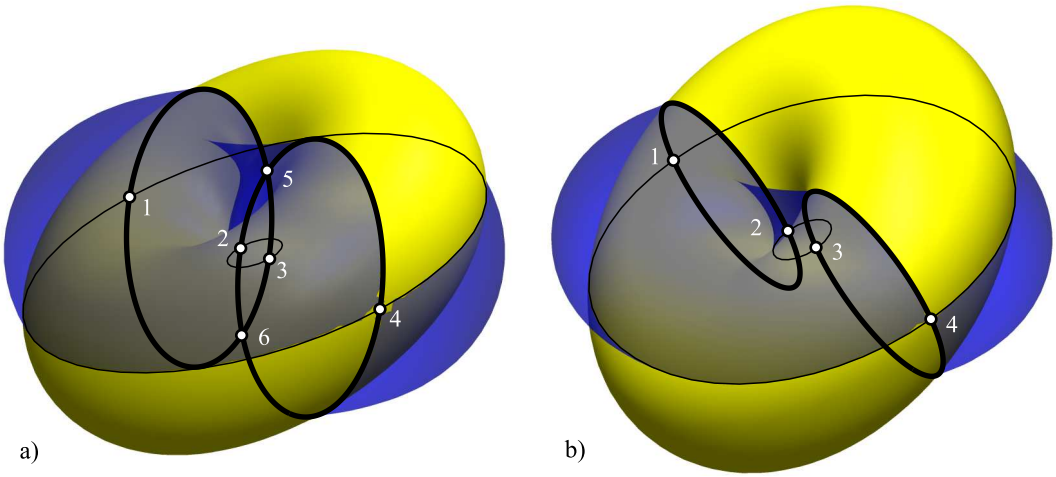

FIGURE 3.6: Cases with circles (in bold curves) in the intersection. a) Villarceau circles and b) secondary circles. In both cases points 1 through 4 are permanent points of tangency. In b) 5 and 6 are points of tangency in the XZ plane

Using Eq. (3.1) or (3.2) it can be proved that $T_{l,r,\gamma,0} = T_{r,l,\beta,0}$, if $\sin\beta = \pm(r/l)\sin\gamma$. Therefore, whenever $r\sin\gamma < l$, the Villarceau circles in the toroid can be used as secondary circles for the same toroid [6]. This property was used in [101] in the design of the different types of Bennett linkages. This different way of generating the same toroid can be used in the line-symmetric Bricard linkage, since, if $l = b_1$ and $r = b_2$, for the other generator $l = b_2$ and $r = b_1$, fulfilling the line-symmetry condition. Such a Bricard linkage would be obtained from the intersection of a toroid with $r\sin\gamma < l$ and a copy of itself rotated θ radians about the Y axis.

This result is interesting because in such case it is possible to force the two toroids to share a secondary circle. For this aim refer to fig. 3.7, where a toroid is intersecting a copy of itself which has been rotated θ degrees about the Y_A axis. On any non-right toroid two families of secondary circles can be drawn. Let the two secondary circles crossing the $Y_A = Y_B$ axis of toroid $i \in \{1,2\}$ be C_{2i} and C'_{2i} (each belonging to each family). By manipulating the rotation angle θ it is possible to make coincident a pair of these circles. As illustrated in fig. 3.7, from simple geometry it can be concluded that if $\theta = 2\gamma^*$, then $C_{2A} = C'_{2B}$ and if $\theta = \pi - 2\gamma^*$, then $C'_{2A} = C_{2B}$, where $\gamma^* = \gamma^*_A = \gamma^*_B$.

If θ is any of the two values obtained in the previous paragraph, then $\mathcal{C}$ includes two circles of radii $r = b_2$ and center at $\pm(0, b_1, 0)$, again two revolute joints are idle and the Bricard linkage evolves to a different 4R Bennett linkage. The Bennett condition is present in the evolved mechanism: if toroid A is the one generated with $l > r, \gamma_A = \gamma$ and toroid B is generated by a Villarceau circle ($r > l, \gamma_B = \beta_A = \pm\arcsin\big((r/l)\sin\gamma\big)$), then revolute joint $A1$ is idle in the branch of motion for which E generates the circle about $\mathbf{S}_{A2}$. Then, the DH parameter for the twist angle between now adjacent axes $\mathbf{S}_{B1}$ and $\mathbf{S}_{A2}$ is $\alpha_{B1,A2} = \theta - \gamma_A = \gamma$. On the other hand, $\alpha_{B1,B2} = \gamma_B = \beta_A = \pm\arcsin((r/l)\sin\gamma)$, which is the Bennett condition. Fig. 3.6b shows this case in which the intersection includes two disjoint secondary circles, the intersection also includes two other closed curves that are not circles.

3.7 A linkage with two Bricard and two Bennett motion branches

As an example consider the mechanism shown in fig. 3.8 which generates two concentric toroids for which $\gamma_A = -\frac{1}{6}\pi$, $r_A = b$, $l_A = b/\sqrt{3}$, $\gamma_B = \frac{1}{3}\pi$, $r_B = b/\sqrt{3}$, $l_B = b$ and $\theta = \frac{2}{3}\pi$.

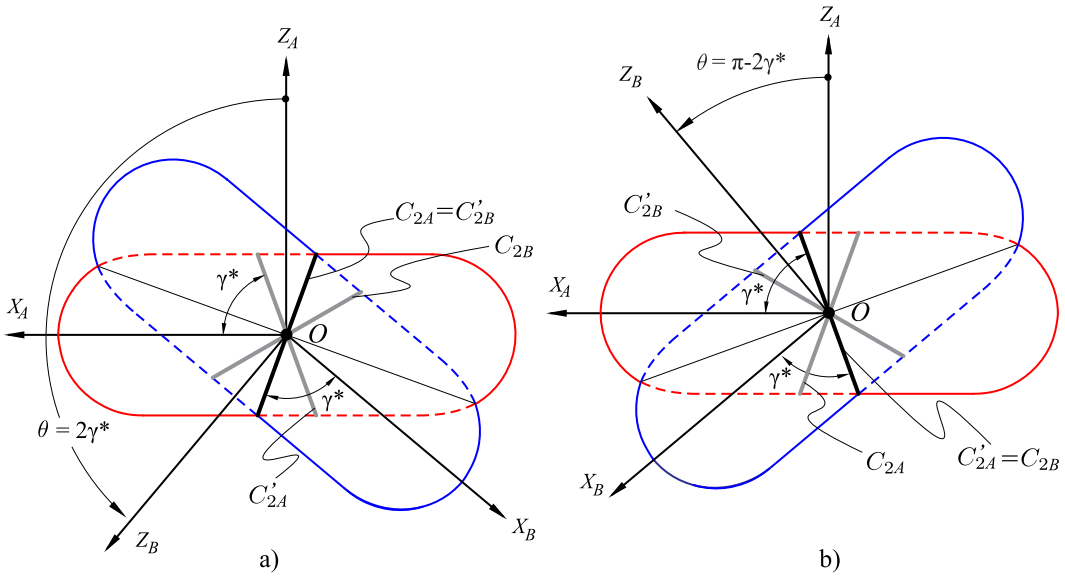

FIGURE 3.7: A toroid and a rotated copy of itself sharing secondary circles: a) $\theta = 2\gamma^*$, and b) $\theta = \pi - 2\gamma^*$

Both toroids are the same surface since $\gamma_A^* = \beta_B = \arcsin\left((r_B/l_B)\sin\gamma_B\right) = \frac{1}{6}\pi$, with toroid A obtained from its generator with $r > l$ and B from its generator with $r > l$. Also, note that $\theta = 2\gamma_B = \frac{2}{3}\pi$, therefore the intersection features two secondary circles, $\mathscr{C}_3$ and $\mathscr{C}_4$, like the ones in fig. 3.6b. In addition, $\theta = \pi - (\gamma_A + \beta_B) = \frac{2}{3}\pi$, therefore the intersection features two Villarceau circles, $\mathscr{C}_1$ and $\mathscr{C}_2$, like the ones in fig. 3.6a. Thus $\mathcal{C} = \mathscr{C}_1 \cup \mathscr{C}_2 \cup \mathscr{C}_3 \cup \mathscr{C}_4$ and the mechanism evolves in two different types of Bennett linkage, one related to a secondary circle and another related to a Villarceau circle. In the other two circles all joints are active.

The bifurcation points between secondary and Villarceau circles are the four permanent points of tangency, present in every mechanism of this family. The two Villarceau circles intersect in two bifurcation points in the XY plane. Figure 10 shows the two concentric toroids and different configurations of the linkage. It can be observed that if V_i is the component of V related to the circle $\mathscr{C}_i$, $i = 1\ldots4$, then in V_2 and V_3 the linkage behaves as a Bennett mechanism, as joints $A1$ and $B3$ are idle in V_2 , while joints $B1$ and $A3$ are idle in V_3 . In V_1 and V_4 all joints are active. Since the same link-lengths appear in the two Bennett motion branches, but the angles between active adjacent joints change, the mechanism is able to work in two different types of Bennett mechanism, from the four well-known cases [9]. The change between the two Bennett motion branches happens in the flattened configuration for which $E = P_2 = \mathscr{C}_2 \cap \mathscr{C}_3$.

The fig. 3.9a shows a representation of $\mathbb{T}^2$ with the curves of u_A versus u_B for each motion branch. A flat plot of a cycle of the curves is shown in fig. 3.9b. Each bifurcation point in fig. 3.8 is indicated in the plot as a corresponding intersection of curves. However, it has to be noted that even though the curves for V_1 and V_4 intersect in three points, only P_3 located as $(\frac{1}{2}\pi, \frac{1}{2}\pi)$, is a bifurcation point. In the other two crossing points the other parameters, v_A and v_B, should not coincide.

A similar mechanism which is a special case of this family of reconfigurable linkages was presented in a previous paper [11] without any further explanation on how to obtain such linkage. Reconfigurable mechanisms that are able to switch between two types of Bennett linkage were obtained in [110], by adding two revolute joints, the necessary change of orientation of the four axes was obtained, however there is no Bricard branches in such linkages since there is no branch of motion with the 6 joints active. The reconfigurable mechanism presented in [73] features two Bricard and one Bennett branch, such mechanism was obtained

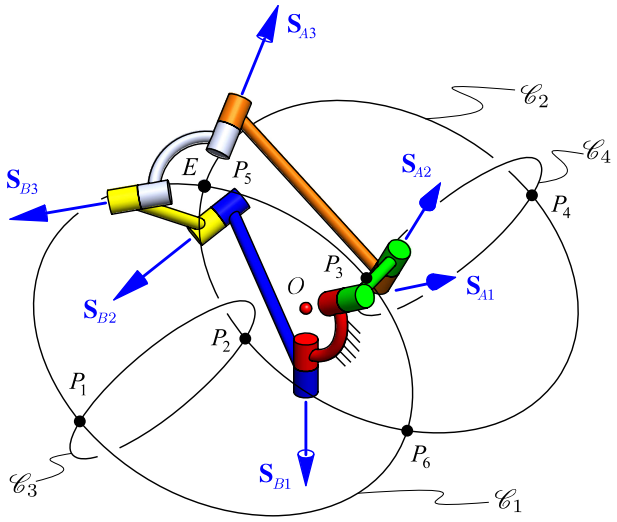

FIGURE 3.8: An example of reconfigurable Bricard linkage which can evolve to two different types of Bennett linkage. The intersection of the two concentric toroids is composed of 4 circles $\mathscr{C}_i$, $i = 1,\ldots,4$. The bifurcation points are labeled as P_i, $i = 1,\ldots,6$. The linkage is shown in a singular configuration with $E = P_5$.

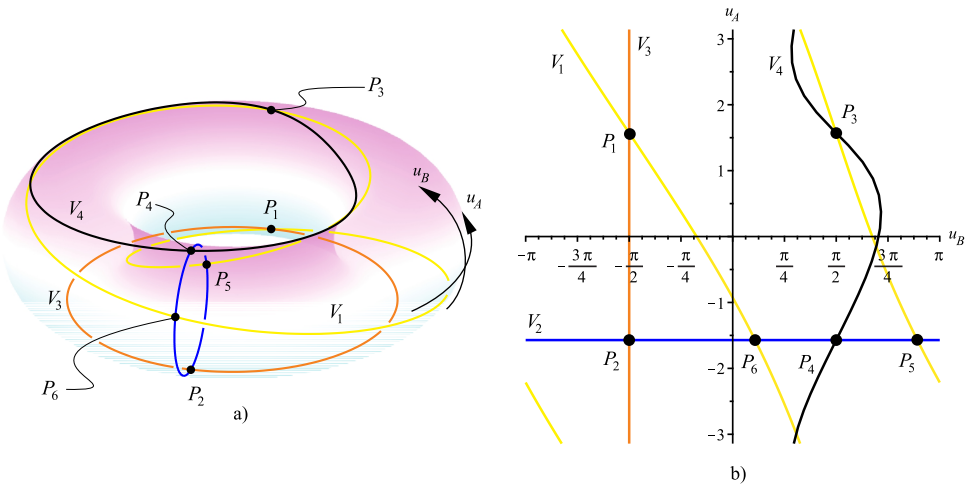

FIGURE 3.9: The four curves of u_A versus u_B obtained from the motion branches of the linkage. Bifurcation points are located in relation with fig. 3.8. a) toroidal representation, b) Cartesian plot.

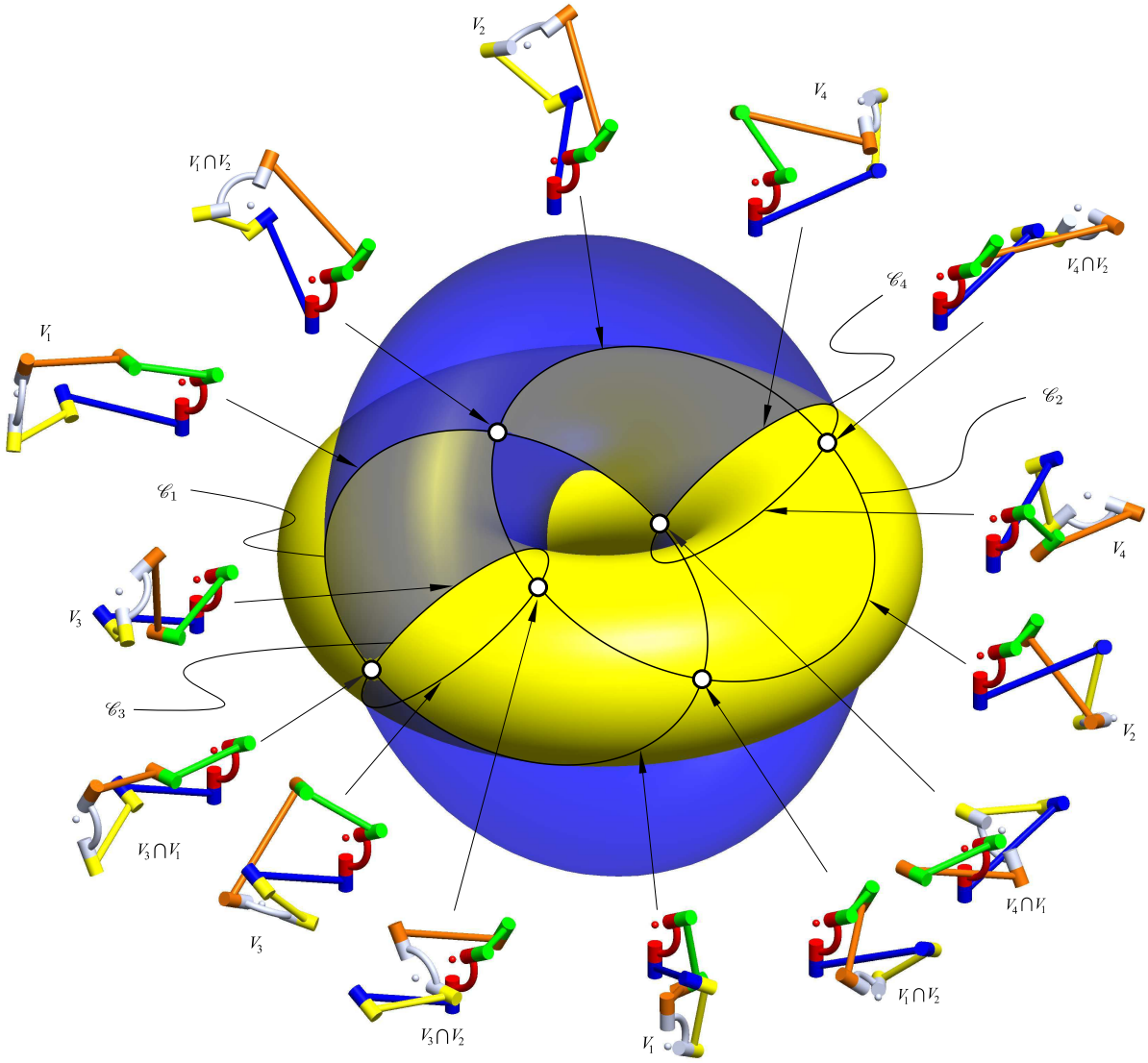

FIGURE 3.10: Different positions for an example of line-symmetric mechanism where the generated toroids intersect in two circles.

applying the concept of spatial triangle.

3.8 The Altmann linkage as a member of this family of special Bricard linkages

The Altmann linkage [89], [111], [112] is an example belonging to this family of reconfigurable Bricard linkages. For this very special case $\gamma_A^* = \gamma_B^* = \theta = \frac{1}{2}\pi$. Both toroids are right torus of the common form. The torus for which $r > l$ is singular with the two conic singularities lying on the axis of the torus. However, it is easy to prove that these singularities are never part of the intersection of the tori in the Altmann linkage case. The intersection features four curves crossing the four permanent points of tangency as in the general cases explained in this chapter.

Throughout the motion of the Altmann linkage all joint axes intersect in two points, thus all of them belong to the same special lineal complex for it is always possible to locate the central axis intersecting these two points. It is easy to present a configuration of a mechanism

belonging to the family presented in this chapter, in which a line intersects all the joints axes. The intersection of these two planes containing axes $\{\mathbf{S}_{A1}, \mathbf{S}_{B1}\}$ and $\{\mathbf{S}_{A3}, \mathbf{S}_{B3}\}$ is always perpendicular to the line of symmetry, hence, through this line it is possible to draw two skew symmetric axes for $\mathbf{S}_{A2}$ and $\mathbf{S}_{B2}$ and the axis of the special linear complex would be the intersection of such planes. However, this setup would change in the next instant and the found line will no longer intersect all axes. In the Altmann linkage the two points where the axes intersect lie on the intersection of the two planes, this intersection is the central axis of the linear complex, which, as expected, intersects perpendicularly the axis of symmetry. In general, the joint axes of the family of mechanisms presented in this section belong to the same non-special linear complex whose axis can be found geometrically following the Appendix to [96]. Baker [113] was able to generalize the Altmann linkage keeping its peculiarity of axes permanently intersecting in two points. Cui and Dai [114] explore the 6R linkages with axes intersecting in two points but in adjacent groups of three joint axes.

Another member of this family of Bricard variations is the reconfigurable linkage with both line and plane symmetries reported in [97], if $R = 0$ in such paper, i.e. the axial displacement parameter for the joints with intersecting axes, the mechanism becomes a special case of the family of Bricard variations presented in this chapter with both toroids singular.

3.9 Chapter conclusions

A family of reconfigurable line-symmetric Bricard variations was obtained applying the method of generated surfaces. It was concluded that the generated toroids are always concentric and have symmetrical flattened forms. The general intersection of these toroids lead to a maximum of four curves. Any possibility of tangency between the surfaces was explored. The four permanent points of tangency in the line-symmetric case proved that this family of Bricard variations is always reconfigurable. The Bennett condition was found in the case of line-symmetric toroids that are also tangent to each other in the $X_A Z_A$ plane, allowing the linkage to evolve into a 4R mechanism. Looking for other circles in the general intersection of these toroids, another type of Bennett branch of motion was found when the intersection includes the secondary circles.

An example in which the four curves in the intersection are circles was presented. Applying the theory developed, the computation of the intersection for this specific case is not required and the curves are recognized as two Villarceau circles and two secondary circles which alternate two Bricard and two Bennett branches of motion.

Chapter 4

Toroid-toroid intersections: Bricard plane-symmetric mechanisms

Continuing with the representation of Bricard linkages as the intersection of toroids, in this chapter a family of reconfigurable plane-symmetric Bricard mechanisms is designed. An analysis of the intersection of these two toroids reveals the presence of coincident conical singularities which leads to the design of plane-symmetric linkages that can be reconfigured to spherical 4R mechanisms. By examining the tangents to the curves of intersection at the conical singularities it is found that the mechanisms can be reconfigured between the two possible branches of spherical 4R motion without disassembling them and without requiring the usual special configuration connecting the branches.

The study of tangent intersections between concentric singular toroids also reveals the presence of isolated points in the intersection which suggests that some linkages satisfying the Bricard plane-symmetry conditions are actually structures with zero finite degrees of freedom but with higher instantaneous mobility.

This chapter is based on the journal publication:

[36] P.C. López-Custodio, J.S. Dai, and J.M. Rico, "Branch reconfiguration of Bricard linkages based on toroids intersections: Plane-symmetric case," *ASME Journal of Mechanisms and Robotics*, vol. 10, no. 3, pp. 031002-1–031002–12, 2018. DOI:10.1115/1.4039002.

4.1 Background

After applying the method of generated surfaces to the line-symmetric case of Bricard overconstrained 6R linkage, the method is now applied to the design of reconfigurable Bricard plane-symmetric loops. The plane-symmetric case is characterized by the following DH parameters [90]:

$$\begin{aligned} &a_{6,1} = a_{1,2}, a_{2,3} = a_{5,6}, a_{3,4} = a_{4,5}, \\ &\alpha_{1,2} + \alpha_{6,1} = 2\pi, \alpha_{2,3} + \alpha_{5,6} = 2\pi, \alpha_{3,4} + \alpha_{4,5} = 2\pi, \\ &d_1 = d_4 = 0, d_2 = -d_6, d_3 = -d_5. \end{aligned} \tag{4.1}$$

where the positive direction of the z_i axes[1] is given by the screw direction shown in Fig. 4.1. In this case each member of the mechanism is symmetric to another member through a plane π (Fig. 4.1). Therefore, axes $\mathbf{S}_2$ and $\mathbf{S}_6$ ($\mathbf{S}_3$ and $\mathbf{S}_5$) intersect in a point lying on π

[1] In [90] Baker sets the positive direction in such a way that the parameters d_i are always positive, obtaining DH parameters slightly different but equivalent to the ones used in this chapter, where the directions are simply reflected by plane π in fig. 4.1.

and axes $\mathbf{S}_1$ and $\mathbf{S}_4$ also lie on π. Hence, a line containing the points of intersection of pairs of axes $\{\mathbf{S}_2,\mathbf{S}_6\}$ and $\{\mathbf{S}_5,\mathbf{S}_3\}$ lies on π and, therefore also intersects $\mathbf{S}_1$ and $\mathbf{S}_4$. Such line is the central axis of the linear complex [58], [88], [94], [95] which the six axes belong to. The pitch of such linear complex is zero since the central axis always intersects the six axes.

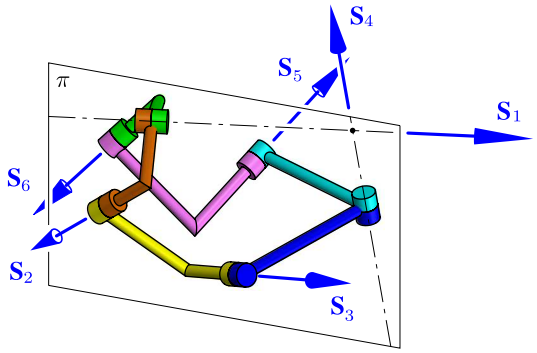

FIGURE 4.1: The general plane-symmetric case of Bricard linkage.

The plane-symmetric Bricard linkage is analyzed in this chapter by means of the intersection of two generated toroids, building a complete theory of the reconfigurability of these linkages. The design is made by manipulating the construction parameters of two concentric singular toroids. An interesting result is the discovery of spherical 4R mechanisms evolved from the plane-symmetric linkages that are always able to reconfigure between their two branches without being disassembled and without passing through the special configuration that connects the branches in common 4R linkages. To the knowledge of the author of this thesis, this is the first time that a mechanism with such reconfiguration between disjoint spherical 4R branches is presented and studied. However, Bricard 6R mechanisms that also work as spherical 4R linkages were first presented in [115].

This chapter is organized as follows: The toroids, its generators and its singular forms are revisited in Section 4.2. Then, in Section 4.3, it is found out that some examples of Bricard plane-symmetric linkages can be explained and designed as the intersection of concentric singular toroids. This intersection is analyzed in Section 4.4. In Section 4.5 any possibility of tangent intersection is explored. In section 4.7 reconfiguration through coincident singularities of the toroids is explained. In Section 4.8 the two branches of spherical 4R motion are studied in order to figure out how to reconfigure the linkage from Bricard branches to spherical 4R branches. Finally, two examples are presented in Section 4.9.

4.2 Singular toroids generated by RR kinematic chains

In section 3.2, a discussion on general toroids generated by RR dyads was presented. Now, the particular case in which the radius of the secondary and base circles are the same, $l = r$, and there is no secondary offset, $s = 0$, is discussed. Such a toroid, $T_{r,r,\gamma,0}$, can be generated by the following parameterization:

$$\sigma(u,v) = r\Big((\cos v+1)\cos u-\cos\gamma\sin v\sin u, \cos\gamma\sin v\cos u+(\cos v+1)\sin u, \sin\gamma\sin v\Big) \in \mathbb{R}^3 \tag{4.2}$$

and $T_{l,r,\gamma,s} = \mathrm{im}(\sigma(\mathbb{T}^2))$. In a similar way, the implicit form $\phi \in \mathbb{R}[x,y,z]$ is reduced to:

$$\phi(x,y,z) = \left(x^2+y^2+z^2-2r^2\right)^2 - 4r^2\left(r^2-\frac{z^2}{\sin^4\gamma}\right) \tag{4.3}$$

and $T_{r,r,\gamma,s} = \left\{ \mathbf{r}_E \in \mathbb{R}^3 \,|\, \phi(\mathbf{r}_E) = 0 \right\}$. For this case, it is easy to prove that:

$$\left.\frac{\partial \sigma}{\partial u}\right|_{(u,v)=(u,\pi)} = \mathbf{0} \Rightarrow \left.\left(\frac{\partial \sigma}{\partial u} \times \frac{\partial \sigma}{\partial v}\right)\right|_{(u,v)=(u,\pi)} = \mathbf{0}, \forall u \in \mathbb{T},$$

Therefore it can be concluded that $(u,\pi) \in \mathbb{T}^2$ is a conical singularity of $T_{r,r,\gamma,0}$. Hence, we call $T_{r,r,\gamma,0}$ a *singular toroid*[2]. In this case the singularity maps to the point $\sigma(u,\pi) = \mathbf{0} = O$. Fig. 4.2 shows $T_{r,r,\gamma,0}$ with the singularity coincident with the origin. $\mathscr{B}$, the intersection of the toroid and any plane containing the Z axis, becomes an 8-shaped curve that is symmetric with respect to the intersection of the XY plane and the plane containing $\mathscr{B}$. The self-crossing of $\mathscr{B}$ occurs at O.

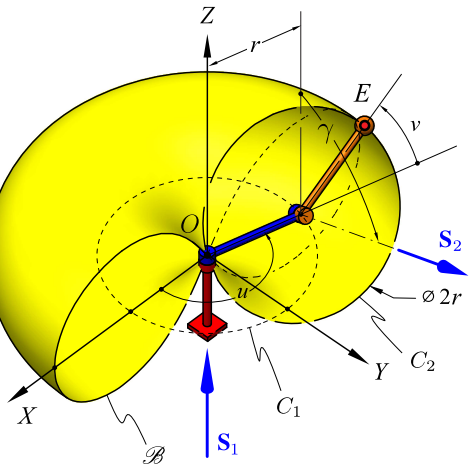

FIGURE 4.2: An RR dyad generating a singular toroid ($r = l, s = 0$).

4.3 Concentric singular toroids generated by the plane-symmetric Bricard linkage

In the plane-symmetric case of Bricard linkage any adjacent pair of revolute joints with skew axes generates a toroid. For a general plane-symmetric linkage, like the one shown in Fig. 4.1, let $a_{2,3} = 0$. Then the point of intersection of $\mathbf{S}_2$ and $\mathbf{S}_3$ describes a toroid with respect to the fixed link between axes $\mathbf{S}_6$ and $\mathbf{S}_5$, this is generated by joints with axes $\mathbf{S}_6$ and $\mathbf{S}_1$. Furthermore, the same point describes another toroid with respect to the fixed link, this time generated by joints with axes $\mathbf{S}_4$ and $\mathbf{S}_5$. Since the same point describes two toroids, such point is confined to move in the intersection of these toroids.

From the restrictions for plane symmetry in Eq. (4.1) , observe that if $a_{2,3} = 0$ then $a_{5,6} = 0$. This implies that both toroids are concentric, as shown in Fig. 4.3a. Furthermore, since $a_{6,1} = a_{1,2}$ and $a_{3,4} = a_{4,5}$, then $r = l$ for both toroids. Finally, since $d_1 = d_4 = 0$ both toroids have secondary offset $s = 0$. From these observations it can be concluded that both generated toroids are singular, with the singularity coinciding with the intersection of fixed axes $\mathbf{S}_6$ and $\mathbf{S}_5$. Summarizing, in addition to the restrictions on the DH parameters of the plane-symmetric linkage in Eq. (4.1), the following conditions are required to analyze and

[2]Conical singularities also appear when $\gamma = \pi/2$ and $r > l$. This is a singular right torus, two conical singularities appear symmetrically disposed in the Z axis. This class of torus never appear in plane-symmetric mechanisms and thus they are not considered here.

design these mechanisms using the intersection of two toroids:

$$\begin{aligned} &\bullet \quad d_i = 0, i = 1,\ldots,6 \\ &\bullet \quad a_{2,3} = a_{5,6} = 0 \end{aligned} \tag{4.4}$$

Fig. 4.3b shows an example of plane-symmetric Bricard linkage that generates two singular toroids. For the sake of identifying the construction parameters of each toroid, the joints have been renamed with respect to Fig. 4.1: $\mathbf{S}_{A1} = \mathbf{S}_6$, $\mathbf{S}_{A2} = \mathbf{S}_1$, $\mathbf{S}_{A3} = \mathbf{S}_2$, $\mathbf{S}_{B3} = \mathbf{S}_3$, $\mathbf{S}_{B2} = \mathbf{S}_4$ and $\mathbf{S}_{B1} = \mathbf{S}_5$. In such case, a singular toroid $T^i_{r_i,r_i,\gamma_i,0} := T_{r_i,r_i,\gamma_i,0}(\hat{\mathbf{k}}_i, O)$ is generated by the joints with axes $\mathbf{S}_{i1}$ and $\mathbf{S}_{i2}$ and is referred to coordinate systems i, $i = A,B$. The point that describes the intersection $\mathcal{C} := T^A_{r_A,r_A,\gamma_A,0} \cap T^B_{r_B,r_B,\gamma_B,0}$ is the intersection of axes $\mathbf{S}_{A3}$ and $\mathbf{S}_{B3}$ and is called E. The point where $\mathbf{S}_{A1}$ and $\mathbf{S}_{B1}$ intersect is called O.

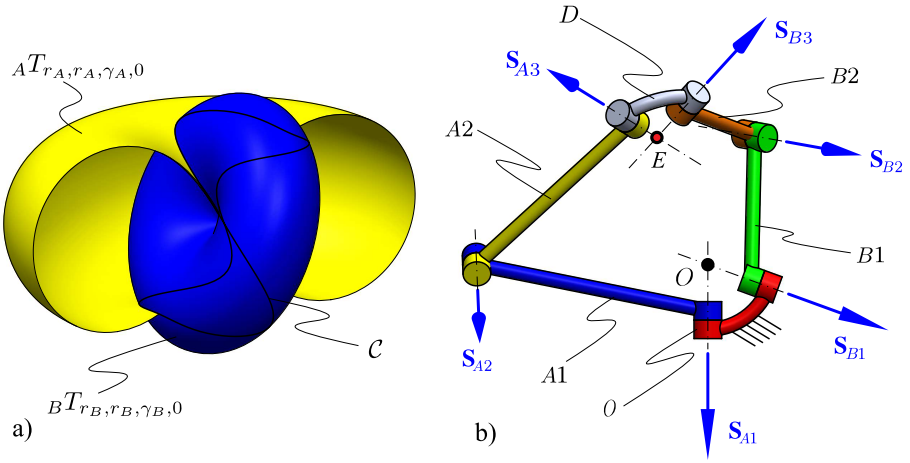

FIGURE 4.3: The concentric singular toroids intersection: a) surfaces, b) resultant Bricard plane-symmetric mechanism.

For each toroid $T^i_{r_i,r_i,\gamma_i,0} := \{E_i(\mathbf{q}_i) \,|\, \mathbf{q}_i \in \mathbb{T}^2\}$, $i = A,B$, the joint variables vector is given by the variables of the parameterization in Eq. (4.2), so that $\mathbf{q}_i = (u_i, v_i) \in \mathbb{T}^2$. Once the link D joins axes $\mathbf{S}_{A3}$ and $\mathbf{S}_{B3}$, $E_A(\mathbf{q}_A) = E_B(\mathbf{q}_B) = E(\mathbf{q})$, where $\mathbf{q} := (u_A, v_A, q_{A3}, q_{B3}, v_B, u_B) \in V \subset \mathbb{T}^6$, where V is the configuration space of the linkage whose elements have to fulfill the closure equation of the loop. Observe that, due to symmetry, q_{A3} and q_{B3} are in linear correspondence with u_A and u_B, respectively. Hence, finding the intersection $\mathcal{C}$ completely describes the behavior of the mechanism. In fact, finding a parameterization of $\mathcal{C}$ in terms of any of the four variables of the toroids would be equivalent to solve the position analysis of the mechanism.

$\mathcal{C}$ may be composed of several components such that $\mathcal{C} = \cup_{i=1}^n \mathcal{C}_i$, where $\dim(\mathcal{C}_i) \leq 2$ and $n \in \mathbb{Z}^*$. Each component of $\mathcal{C}$ is related to a component of the configuration space V. When $\mathcal{C}_i$ is a curve $\mathscr{C} \subset \mathcal{C}$, $\dim(V_i) = 1$, where V_i is the corresponding component of V, and the mechanism has 1 D.O.F. when assembled in this mode, this leads to the typical overconstrained behavior of the linkage. On the other hand, if $\mathcal{C}_i$ is an isolated point and $\dim(V_i) = 0$. In such component of V, the mechanism can be assembled as a structure.

An important phenomenon occurs when two conical singularities coincide. We call this coincidence the *coincident singularities*. The arrangement of singular toroids for plane-symmetric linkages includes coincident singularities since both toroids are concentric. In the general method of generated surfaces the two generators are connected by a spherical pair, it was proved [11] that for such linkages when E is in the coincident singularities the mechanism has 2 D.O.F. since variables u_A and u_B can take any value without restriction while v_A and v_B remain constant. However, for the problem of plane-symmetric Bricard linkages

the spherical pair has been reduced to a pair of coincident revolute joints. When E reaches the coincident singularities it coincides with O, therefore the axes $\mathbf{S}_{A1}$, $\mathbf{S}_{B1}$, $\mathbf{S}_{A3}$ and $\mathbf{S}_{B3}$ are intersecting in the coincident singularities while the joints with axes $\mathbf{S}_{A2}$ and $\mathbf{S}_{B2}$ remain idle. u_A and u_B are now dependent one from another since the linkage becomes a spherical 4R mechanism. This property will be thoroughly studied in section 4.8.

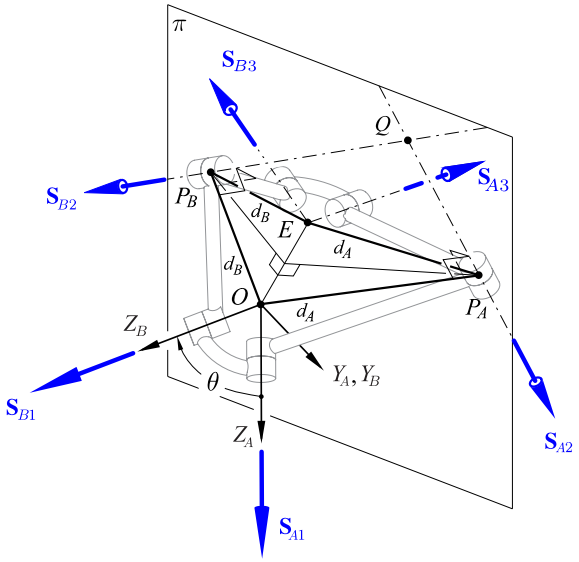

FIGURE 4.4: Common perpendicular diagram for the plane-symmetric linkage.

Refer to fig. 4.4 which shows the common perpendiculars diagram of the plane-symmetric mechanism obtained from the intersection of two toroids. In any configuration the common perpendiculars between the adjacent joint axes conform two isosceles triangles, OP_AE and OP_BE, these triangles share the same base OE, the lines from the mid-point of EO to P_A and P_B are perpendicular to OE and therefore, a plane π containing these two lines is perpendicular to the planes that contain the two triangles. The axes $\mathbf{S}_{A2}$ and $\mathbf{S}_{B2}$ contain P_B and P_A, respectively, and are perpendicular to the planes including the triangles OP_AE and OP_BE, respectively. Hence, both axes belong to π and therefore they either intersect or are parallel. This ensures that the symmetry condition is always present while E moves through all the components of $\mathcal{C}$.

4.4 Concentric singular toroid-toroid intersection

To analyze the intersection of toroids in the plane-symmetric case, $\mathcal{C} = T^A_{r_A,r_A,\gamma_A,0} \cap T^B_{r_B,r_B,\gamma_B,0}$, let the relationship between coordinate systems A and B be given by ${}^A_B\mathbf{T} = \mathrm{HT}(\mathrm{Rot}(\theta,\hat{\mathbf{j}}),\mathbf{0})$, so that the toroids are concentric and the axis of B is obtained by rotating the axis of A θ radians about the $Y := Y_A = Y_B$ axis.

The parameterizations of both surfaces referred to coordinate system A are:

$$ {}^A\sigma_A(u_A,v_A) = r_A \begin{pmatrix} (\cos v_A + 1)\cos u_A - \cos\gamma_A \sin v_A \sin u_A \\ \cos\gamma_A \sin v_A \cos u_A + \sin u_A \cos v_A + \sin u_A \\ \sin\gamma_A \sin v_A \end{pmatrix}^{\mathrm{t}} $$

$$
{}^{A}\sigma_B(u_B,v_B) = r_B \begin{pmatrix} ((\cos v_B+1)\cos u_B - \cos\gamma_B \sin v_B \sin u_B)\cos\theta + \sin\theta\sin\gamma_B\sin v_B \\ \cos\gamma_B \sin v_B \cos u_B + \sin u_B \cos v_B + \sin u_B \\ ((-\cos v_B-1)\cos u_B + \cos\gamma_B \sin v_B \sin u_B)\sin\theta + \cos\theta\sin\gamma_B\sin v_B \end{pmatrix}^{\mathrm{t}} \tag{4.5}
$$

and the implicit forms are given by:

$$
\begin{aligned}
{}^{A}\phi_A(x,y,z) &= \left(x^2+y^2+z^2-{r_A}^2-{r_B}^2\right)^2 - 4{r_B}^2\left({r_A}^2 - \frac{z^2}{\sin^2\gamma_A}\right) \\
{}^{A}\phi_B(x,y,z) &= \frac{1}{\sin^2\gamma_B}\Big[-(x^2+y^2+z^2)(x^2+y^2+z^2-4{r_B}^2)\cos^2\gamma_B + (-4x^2{r_B}^2 \\
&\quad +4z^2{r_B}^2)\cos^2\theta + 8\cos\theta\sin\theta xz{r_B}^2 + z^4 + (2x^2+2y^2-4{r_B}^2)z^2 + x^4 \\
&\quad +2x^2y^2+y^4-4y^2{r_B}^2\Big]
\end{aligned} \tag{4.6}
$$

A direct way to find $\mathcal{C}$ is to solve ${}^{A}\sigma_A - {}^{A}\sigma_B = \mathbf{f}(u_A,v_A,u_B,v_B) = \mathbf{0}$. However, in this case it turns out to be more complicated. An alternative technique, taken from [106], is applied instead: Since, for any of both implicit forms referred to coordinate system A, $(x,y,z) = {}^{A}\sigma_A(u_A,v_A) = {}^{A}\sigma_B(u_B,v_B)$, then ${}^{A}\phi_B({}^{A}\sigma_A(u_A,v_A)) = 0$ is a scalar equation with two variables from which the restrictions $u_A(v_A)$ or $v_A(u_A)$ can be obtained. This restriction fully defines $\mathcal{C}$ since it can be replaced in ${}^{A}\sigma_A$ to obtain the whole parameterization of the intersection, for example using the restriction $u_A(v_A)$: ${}^{A}\mathcal{C} = \{{}^{A}\sigma_A(u_A(v_A),v_A)\,|\,v_A \in W \subset \mathbb{T}\}$. Consider the parameterization of A being substituted in the implicit form of B:

$$
\begin{aligned}
&{}^{A}\phi_B({}^{A}\sigma_A(u_A,v_A)) = -\frac{4r_A^2}{\sin^2\gamma_B}(\cos v_A+1)\Big[r_B^2\cos^2\gamma_A(\cos v_A-1)(\sin^2 u_A + (\cos^2 u_A \\
&-2)\cos^2\theta) - r_B^2(\cos v_A+1)\cos^2 u_A - 2r_B^2\sin u_A\cos\gamma_A(\sin\gamma_A\sin\theta\cos\theta(\cos v_A-1) \\
&-\cos u_A \sin v_A \sin^2\theta) + r_B^2\cos^2\theta((\cos v_A+1)\cos^2 u_A + \cos v_A - 1) \\
&-2r_B^2\sin\gamma_A\cos\theta\sin\theta\sin v_A\cos u_A - \sin^2\gamma_B(\cos v_A+1)(r_A^2(1+\cos v_A) - 2r_B^2)\Big] = 0
\end{aligned} \tag{4.7}
$$

An immediate first possibility is observed: $v_A = \pi$. This solution leads to the coincident singularities in which $E(\mathbf{q}) = O$, $\forall \mathbf{q} \in V_1$, where V_1 is the spherical $4R$ component of V related to the coincident singularities. Since making 0 the first factor in Eq. (4.7) would compromise the construction parameters of the toroids, the only remaining possibility is solving the third factor. This factor is solved to obtain the restriction $u_A(v_A)$, two solutions are found which are not presented here due to reasons of space since these are quite long expressions. In a similar manner, two solutions for the restriction $v_A(u_A)$ are obtained. Therefore, $\mathcal{C}$ may feature a maximum of two curves. Expressions for a parameterization of these components can be computed as explained in the previous paragraph, however, due to the length of the terms involved in the restriction $u_A(v_A)$, these are not presented here.

4.5 Tangent intersections of concentric singular toroids

If in the concentric toroid-toroid intersection $\exists i,j \ni \mathcal{C}_i \cap \mathcal{C}_j \neq \emptyset$ the mechanism is reconfigurable with at least 2 motion branches, which are connected through at least one configuration $\mathbf{q}_{ij} \in V_i \cap V_j$. It can be proved [11] that for the 1-dimensional components of V, the toroids are tangent to each other at $E(\mathbf{q}_{ij})$. The intersection is non-transverse in $E(\mathbf{q}_{ij})$. Therefore,

$\nabla\phi_A(x^P,y^P,z^P)\times\nabla\phi_B(x^P,y^P,z^P)=\mathbf{0}$, where $(x^P,y^P,z^P)=E(\mathbf{q}_{ij})$. The points in V that map to points of tangency *may* be bifurcation configurations of the mechanism. These points in V may represent the intersection of two components of V, or may be the self-crossing of the same component. The surfaces are also tangent to each other when they touch in one point, which would lead to an isolated point in V. In addition, if a continuum of points of tangency is found, the surfaces are touching in a curve that is a component of $\mathcal{C}$.

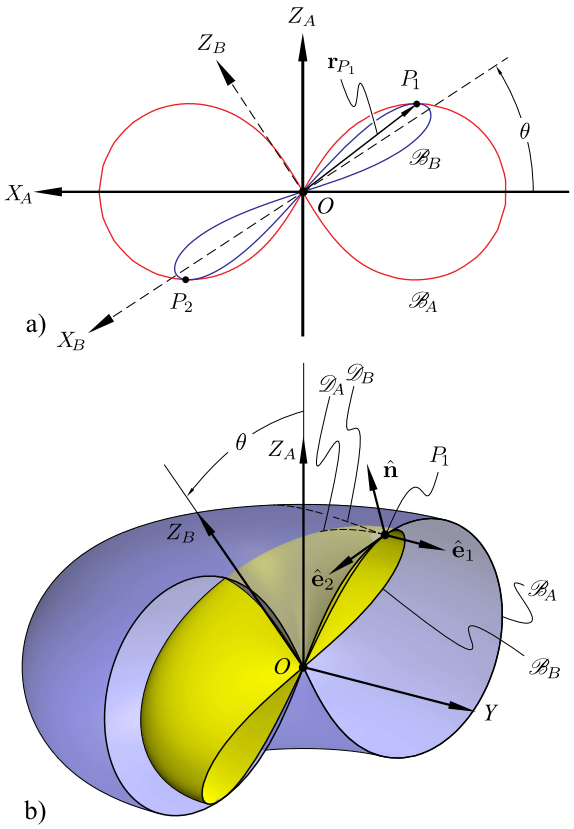

FIGURE 4.5: Two singular toroids that are tangent to each other in the X_AZ_A plane.

To find the points where the intersection may become non-transverse, the real points $(x,y,z)\in\mathbb{R}^3$ that make $\nabla\phi_A(x,y,z)\times\nabla\phi_B(x,y,z)=\mathbf{0}$ and also satisfy $\phi_A(x,y,z)=\phi_B(x,y,z)=0$ are explored. Two points in the Y axis are found, however, they imply $r_A=r_B$, so that the points are $(0,r_A,0)=(0,r_B,0)$ and $(0,-r_A,0)=(0,-r_B,0)$. This case leads to a mechanism that is both line- and plane-symmetric. This example was analyzed before in [97] and the line-symmetric case was investigated in chapter 3. The other solutions that do not degenerate the toroids imply $y=0$. Therefore, any point of tangency must lie in the X_AZ_A plane if the linkage is not the plane- and line-symmetric case. The solutions in the X_AZ_A plane are large expressions that involve not only the construction parameters of the toroids, but also the angle θ. Considering the singular curves $\mathscr{B}_A$ and $\mathscr{B}_B$ obtained by $\mathscr{B}_i=\{(x,y)\in\mathbb{R}^2\,|\,\phi_1(x,0,y)=0\}$ (fig. 4.5a), it is found that the curves become tangent to each other if:

$$\cos\theta=\pm\frac{\sqrt{(r_B^2\cos^2\gamma_B+r_A^2\sin^2\gamma_B)(r_A^2\cos^2\gamma_A+r_B^2\sin^2\gamma_A)}}{r_Ar_B} \tag{4.8}$$

Each possibility leads to two solutions, therefore there are in total 4 values of θ that make the surfaces tangent to each other in the X_AY_A plane. Note that the argument of the square root is always positive, however, to obtain real values of θ, it is necessary that

$(r_B^2\cos^2\gamma_B + r_A^2\sin^2\gamma_B)(r_A^2\cos^2\gamma_A + r_B^2\sin^2\gamma_A) \leq r_A^2 r_B^2$, since $\cos\theta \in [-1,1]$. After some algebra it is concluded that if $r_A > r_B$ then[3] $|\sin\gamma_B| > |\sin\gamma_A| \Rightarrow \sin\gamma_B^* > \sin\gamma_A^*$ and if $r_A < r_B$ then $|\sin\gamma_A| > |\sin\gamma_B| \Rightarrow \sin\gamma_A^* > \sin\gamma_B^*$. W.l.o.g. Fig. 4.5, shows the case in which $r_A > r_B \Rightarrow \sin\gamma_A^* > \sin\gamma_B^*$. This makes toroid B looking more flattened than toroid A.

4.6 Isolated points of tangency and Bricard structures

The nature of the intersection when the two concentric singular toroids are tangent to each other in the $X_A Z_A$ plane is now investigated. For this aim, consider the following proposition:

Proposition 4.6.1 *The intersection of two concentric singular toroids with different radius contains only two isolated points if the toroids are tangent to each other at some point.*

Proof: Let the two singular toroids to be intersected be $T^A_{r_A,r_A,\gamma_A,0}$ and $T^B_{r_B,r_B,\gamma_B,0}$, where $r_A \neq r_B$, thus the only possibility for tangent intersection is that the surfaces are tangent to each other in the $X_A Z_A$ plane. Replacing the values of θ from Eq. (4.8) in the parameterizations of the surfaces and trying to find $\mathcal{C}$ would lead to quite complicated expressions. A simpler way to proceed is to analyze the normal curvatures of the toroids in one of the points where the surfaces are tangent. The normal curvatures of both surfaces must be the same in the direction that is tangent to the intersection curve. If there is no intersection curve and the surfaces are only touching in such point, the curvatures are always different for both surfaces in any direction. Since normal curvature is invariant to frame transformations both toroids can be analyzed in their own coordinate systems. According to Euler's formula, the normal curvature is given by: $\kappa(\psi) = \kappa_1\cos^2\psi + \kappa_2\sin^2\psi$, where κ_1 and κ_2 are the curvatures in the principal directions $\hat{\mathbf{e}}_1$ and $\hat{\mathbf{e}}_2$ and ψ is the angle that defines the direction of the normal curvature with respect to one of the principal directions.

The singular toroids are surfaces of revolution with $\mathscr{B}$ being rotated about the Z axis. It is known (see for example [116]) that in surfaces of revolution the principal curvatures are the tangents to the meridian and parallel crossing the point in analysis. Hence, for the arrangement shown in Fig. 4.5b $\hat{\mathbf{e}}_1 = \hat{\mathbf{j}}$ and $\hat{\mathbf{e}}_2 = \hat{\mathbf{t}}$, where $\hat{\mathbf{t}}$ is the mutual tangent vector to $\mathscr{B}_A$ and $\mathscr{B}_B$ at P_1. If the intersection includes a curve crossing P_1, it should be possible to find an angle $\psi \in \mathbb{T}$, such that:

$$\begin{aligned} \kappa_{1A}\cos^2\psi + \kappa_{2A}\sin^2\psi &= \kappa_{1B}\cos^2\psi + \kappa_{2B}\sin^2\psi \\ \Leftrightarrow \frac{\kappa_{1A}-\kappa_{1B}}{\kappa_{2B}-\kappa_{2A}} &= \tan^2\psi \geq 0 \end{aligned} \tag{4.9}$$

where κ_{iA} and κ_{iB}, $i = 1,2$, are the principal curvatures at P_1 of toroids A and B, respectively. From Fig. 4.5b Note that κ_{2j}, $j = A,B$ are the curvatures of plane curves $\mathscr{B}_j$, while κ_{1j} are the curvatures of plane curves $\mathscr{D}_j$ obtained by intersecting the toroids with the plane that contains P_1 and is spanned by $\hat{\mathbf{e}}_1 = \hat{\mathbf{j}}$ and $\hat{\mathbf{n}}$. If, w.l.o.g. $r_A > r_B$ as shown in Fig. 4.5, it is clear that $\kappa_{2B} > \kappa_{2A}$ and $\kappa_{2B} - \kappa_{2A} > 0$. Hence, in order to have a real solution of Eq. (4.9), it is necessary that $\kappa_{1A} - \kappa_{1B} > 0$. These curvatures can be computed using the following expression [117]:

$$\kappa_{1j} := \kappa(\phi_j, \hat{\mathbf{j}})(P_1) = \left.\frac{\hat{\mathbf{j}}^T \mathrm{Hess}(\phi_j(x,y,z))\hat{\mathbf{j}}}{|\nabla\phi_j(x,y,z)|}\right|_{(x,y,z)=P_1}, \; j = A,B$$

[3] As explained in Section 3.2, the same toroid can be generated using different angles γ. From these, we take γ^* in $(0,\pi/2]$, which is unique for any toroid.

where, Hess : $\mathbb{R}[x,y,z] \to M^{3\times3}(\mathbb{R})$ is the Hessian matrix of the given implicit form. Upon calculations it is concluded that:

$$\kappa_{1j} = \frac{|\sin\gamma_j|(|\mathbf{r}_{P_1}|^2 - 2r_j^2)}{2|\mathbf{r}_{P_1}|r_j\sqrt{|\mathbf{r}_{P_1}|^2 - 2(|\mathbf{r}_{P_1}|^2 - 2r_j^2)\cos^2\gamma_j}}, \; j = A,B \tag{4.10}$$

where $|\mathbf{r}_{P_1}|$,is the magnitude of the position vector of P_1, which is the same value for both toroids and is invariant to frame transformations. $|\mathbf{r}_{P_1}|$ is calculated using the value of θ in Eq. (4.8), leading to:

$$|\mathbf{r}_{P_1}| = 2\sqrt{\frac{r_B^4\sin^2\gamma_A\cos^2\gamma_B - r_A^4\sin^2\gamma_B\cos^2\gamma_A}{r_B^2\sin^2\gamma_A\cos^2\gamma_B - r_A^2\sin^2\gamma_B\cos^2\gamma_A + (r_A^2 - r_B^2)\sin^2\gamma_A\sin^2\gamma_B}}$$

Replacing this value in Eq. (4.10) and carrying out simplifications it can be concluded that, $\kappa_{1A} - \kappa_{1B}$ has the same sign as $r_B - r_A$. Therefore, if $r_A > r_B$ (as first supposed for this proof), $\kappa_{1A} - \kappa_{1B} < 0$, $\tan^2\psi < 0 \Rightarrow \psi \notin \mathbb{T}$ and there is no real solution for Eq. (4.9). Hence, both toroids are touching each other in P_1 and P_2 but these are isolated points in $\mathcal{C} = \{P_1, P_2, O\}$. ■

Two important conclusions can be drawn from proposition 4.6.1: First, a Bricard linkage fulfilling the plane symmetry conditions can be a 0-DOF structure which can be assembled in two different configurations. However, if the linkage is assembled in $E(\mathbf{q}) = O$ the same linkage has 1 DOF and works as a spherical 4R mechanism. In such case, V is composed of 3 regions: 2 isolated points and a 1-dimensional curve in $\mathbb{T}^6$. And second, there is no way to reconfigure these mechanisms directly from one curve to another unless the mechanism is also line-symmetric.

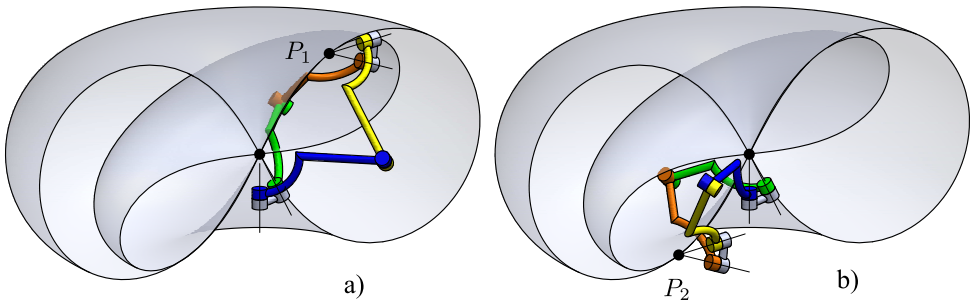

FIGURE 4.6: A Bricard plane-symmetric linkage with finite mobility zero in its two different assembly modes.

As an example of this situation, consider the plane-symmetric linkage with the following DH parameters:

$$\begin{array}{lll} \alpha_{A1,A2} = \frac{4}{3}\pi, & \alpha_{B2,B1} = \frac{5}{6}\pi, & \alpha_{B1,A1} = \arccos\left(\frac{247}{280}\right), \\ a_{A1,A2} = 10, & a_{B2,B1} = 7, & a_{B1,A1} = 0 \\ \alpha_{A2,A3} = \frac{2}{3}\pi, & \alpha_{B3,B2} = \frac{7}{6}\pi, & \alpha_{A3,B3} = -\arccos\left(\frac{247}{280}\right), \\ a_{A2,A3} = 10, & a_{B3,B2} = 7, & a_{A3,B3} = 0 \end{array} \tag{4.11}$$

and $d_i = 0$ for all joints. These parameters satisfy the conditions in Eqs. (4.1) and (4.4) and, therefore, the mechanism is plane-symmetric and it generates the intersection of two concentric singular toroids. From these parameters it can be seen that $\gamma_A^* = \frac{1}{3}\pi$, $r_A = 10$, $\gamma_B^* = \frac{1}{6}\pi$, $r_B = 7$ and $\theta = \arccos\left(\frac{247}{280}\right)$, which turns out to be one of the 8 values that can

be obtained from Eq. 4.8. Thus, the Bricard mechanism must be a structure with 0 DOF if assembled in any of the two isolated points. If assembled with $E = O$ the linkage should behave as a spherical 4-bar mechanism, however, observe that such spherical mechanism would have twist angles $2\gamma_A = \frac{2}{3}\pi$, $2\gamma_B = \frac{1}{3}\pi$ and two links with angles $\arccos\left(\frac{247}{280}\right)$, the largest angle is $\frac{2}{3}\pi$ but $\frac{2}{3}\pi > \frac{1}{3}\pi + 2\arccos\left(\frac{247}{280}\right)$, therefore the spherical mechanism cannot be assembled. The only two possible assembly modes are those for which the linkage is a structure, namely $E(\mathbf{q}_1) = P_1$ and $E(\mathbf{q}_2) = P_2$, these are presented in fig. 4.6.

Consider the linkage assembled in an isolated point $E(\mathbf{q}_1) = P_1$ in fig. 4.8, some interesting results regarding the reciprocal system of the screw system of the linkage are now obtained: First, the plane of symmetry is perpendicular to and bisects the segment OE, which lies on the X_AZ_A plane, thus the plane of symmetry is perpendicular to the X_AZ_A plane. As a consequence of this, $\mathbf{S}_{A3}$ and $\mathbf{S}_{B3}$ lie on the plane X_AZ_A, since their symmetric members, $\mathbf{S}_{A1}$ and $\mathbf{S}_{B1}$ lie on X_AZ_A which is perpendicular to the plane of symmetry. Then, the axis of the special linear complex is the intersection of the plane of symmetry and the X_AZ_A plane as expected from Section 2.

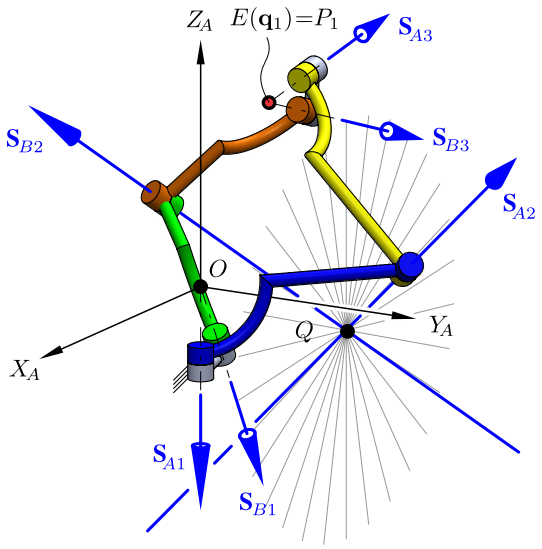

FIGURE 4.7: A Bricard plane-symmetric linkage with finite mobility zero in the assembly mode with $E(\mathbf{q}_1) = P_1$.

Knowing the value of θ, it is possible to calculate both u_A and u_B for any of the two configurations in which the linkage can be assembled without using the coincident singularities and making it a spherical 4R linkage. With u_A and u_B, the following Plücker coordinates are obtained for the screws $A2$ and $B2$, respectively:

$$
\begin{aligned}
{}^{A}\mathbf{S}_{A2}(\mathbf{q}_1) &= \left(\frac{3\sqrt{17391}}{682}, \frac{\sqrt{48081}}{341}, \frac{1}{2}; \frac{15\sqrt{5797}}{341}, \frac{10\sqrt{16027}}{341}, -5\sqrt{3}\right), \\
{}^{A}\mathbf{S}_{B2}(\mathbf{q}_1) &= \left(\frac{63\sqrt{5797}}{6820}, \frac{\sqrt{16027}}{341}, \frac{7\sqrt{3}}{20}; \frac{5\sqrt{17391}}{341}, \frac{7\sqrt{48081}}{341}, -5\right).
\end{aligned}
$$

Previously, it was proved that $\mathbf{S}_{A2}$ and $\mathbf{S}_{B2}$ always intersect. If the screws are defined by $\mathbf{S}_i = (\hat{\mathbf{s}}_i; \mathbf{m}_i)$, $i = A2, B2$, such intersection point is given by $P = (\hat{\mathbf{s}}_{A2} \cdot \mathbf{m}_{B2})^{-1}\mathbf{m}_{A2} \times \mathbf{m}_{B2}$. However, it turns out that for this example $({}^{A}\mathbf{m}_{A2} \times {}^{A}\mathbf{m}_{B2}) \cdot {}^{A}\mathbf{j} = 0$, which means that P lies on the X_AZ_A plane. This implies that a pencil of lines in the X_AZ_A plane can be drawn with center in P and each line in the pencil will be reciprocal to all the axes of the linkage. Hence,

the reciprocal system is a 2-system and the first order mobility of the linkage is 2. A velocity analysis applied to this structure would reveal that the linkage has 2 degrees of freedom since the tangent space of V in such configuration is a 2-dimensional space. A tangent cone [50], [53], [59]–[61], [118] analysis was made for this configuration. While the first order approximation is a 2-dimensional vector space, as expected, the second order approximation is 0-dimensional, proving that the mechanism is actually a structure. It is then said that the structure has second order rigidity [119].

4.7 Motion branch reconfiguration through the coincident singularity

Reconfiguration of motion branches can be achieved using the coincident singularities of the concentric toroids if there are curves crossing it. Due to the symmetry of the intersection, and since there are no points of tangency (excluding the known exceptions), it can be concluded that the intersection will have any of the following forms:

1. Two regular disjoint curves and the coincident singularities point
2. One singular 8-shaped curve with its self-crossing coincident with the coincident singularities,
3. Two singular 8-shaped curves that share the same self-crossing point which is coincident with the coincident singularities.

The first case is generated by non-reconfigurable mechanisms since there is no way to migrate from one curve to another or to visit the coincident singularities. The second case is reconfigurable with two motion branches: a Bricard 6R operation mode and a spherical 4R mechanism mode. The third case is the most interesting since the configuration space includes two Bricard branches which can be visited by the mechanism without disassembling it and, in addition, the linkage can undergo spherical 4R motion branches.

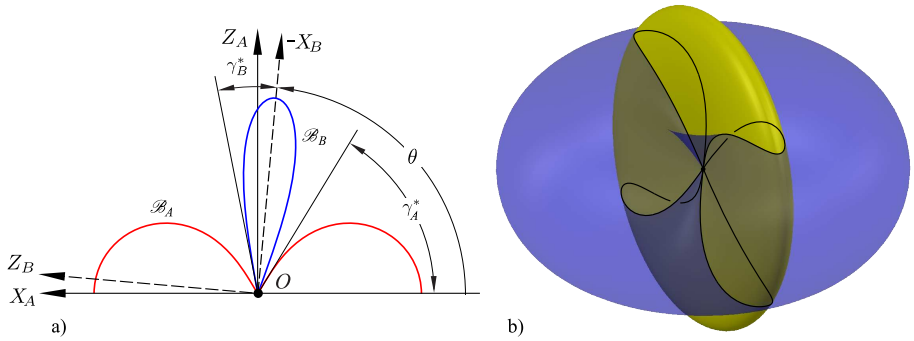

FIGURE 4.8: A case with two singular curves in the intersection: a) $\mathscr{B}_A$ and $\mathscr{B}_B$ curves, b) surfaces and intersection.

In figure 4.8, note that if in the X_AZ_A plane $\mathscr{B}_A \cap \mathscr{B}_B = \{O\}$ the intersection of the toroids includes two singular curves as in the third case of intersection. Since the toroids are symmetric with the X_AZ_A plane, if $\mathscr{B}_B$ crosses $\mathscr{B}_A$ in four points, the intersection curve never includes O, as in the first case of intersection. If $\mathscr{B}_B$ crosses $\mathscr{B}_A$ in two points, the intersection curve crosses O and then intersects the X_AZ_A plane in the two points where $\mathscr{B}_B$ crosses $\mathscr{B}_A$, the intersection of toroids is then a sole singular curve, as in the second case of intersection. Now imagine that the two points where the intersection crosses the X_AZ_A move through $\mathscr{B}_A$ approaching O, since the intersection is symmetric with the X_AZ_A plane, the curve starts to

sharpen in such points until they reach O and the intersection becomes two singular curves. Refer to figure 4.8a, it is easy to prove that the tangent to $\mathscr{B}_i$, $i = A,B$ makes an angle γ_i^* with the x_i axis. Then the conditions that make $\mathscr{B}_B$ intersect $\mathscr{B}_A$ only in O are the following:

$$\begin{aligned} &\gamma_A^* + \gamma_B^* < \frac{\pi}{2} \\ &\gamma_A^* + \gamma_B^* < \theta < \pi - \gamma_A^* - \gamma_B^* \end{aligned} \tag{4.12}$$

In the remaining part of the chapter we focus exclusively in mechanisms whose generated toroids fulfill conditions 4.12, since these are the most complicated cases.

4.8 Bricard branches as a link between crank-rocker spherical 4R branches

Let $\mathcal{C} = \mathscr{C}_1 \cup \mathscr{C}_2$, like in the third case of intersection, then $\mathscr{C}_1 \cap \mathscr{C}_2 = \{O\}$. it has to be considered that, even though the two curves intersect in one point, if V_i is the component of V related to $\mathscr{C}_i$, then $V_1 \cap V_2 = \emptyset$, which means that the mechanism cannot reconfigure from V_1 to V_2 directly. This is a consequence of the double-singularity O. In any regular point in a surface all curves intersecting the point do it with the same values of $(u,v) \in U$, as σ is a bijection from U to $\mathcal{S} \setminus \text{sing}(\mathcal{S})$. But since in the conic singularity of the singular toroids $\partial\sigma/\partial u = \mathbf{0}$ there are an infinity of pairs (u,v) that map to O and the only way to escape from the singularity is moving in the direction of the isoparametric curve of v, since $\partial\sigma/\partial v \neq \mathbf{0}$ is such point. These isoparametric curves are the secondary circles, their tangent vectors in the singularity generate a cone that is tangent to the toroid in the singularity. Any two curves on the toroid crossing the singularity with non-parallel tangent vectors at O will have different values $(u(t), v(t))$ at O, since they reached the point in different secondary circles.

The previous paragraph implies that in general the mechanism cannot move from V_1 to V_2 since E reaches O in different configurations. In fact, in the self-crossing of each singular curve in $\mathcal{C}$, the mechanism is unable to chose between the two segments in the neighborhood of O, E smoothly passes the coincident singularities and V_1 and V_2 are free of singularities even though they are related to singular curves $\mathscr{C}_1$ and $\mathscr{C}_2$. Despite V_1 and V_2 are disjoint, they are connected through the spherical 4R motion branch related to the coincident singularities. For the evolved spherical 4R linkage two opposite links have the same twist angle, θ, while the other two links have twist angles $2|\gamma_A|$ and $2|\gamma_B|$.

Suppose E lies on $\mathscr{C}_1$ and approaches O, once the linkage starts working in the spherical 4R branch axes $\mathbf{S}_{A2}$ and $\mathbf{S}_{B2}$ can move until the secondary circles are both tangent to $\mathscr{C}_2$ and E can escape from the coincident singularities allowing the mechanism to enter the V_2 branch. Since there are two singular curves crossing O, there are in total four different directions in which E can move to escape from O. Two of these will reconfigure a spherical 4R branch into the same plane-symmetric Bricard branch related to $\mathscr{C}_1$, while the other two will reconfigure to the branch related to $\mathscr{C}_2$. In each of these configurations the evolved spherical 4R linkage must be in a plane-symmetric configuration since such configuration also belongs to a Bricard branch. Fig. 4.9 shows a plane-symmetric mechanism in a spherical 4R branch with $E = O$, the linkage is about to escape to V_1 since the secondary circles C_{2A} and C_{2B} are both tangent to $\mathscr{C}_1$ at O.

However, it is known that the configuration space of the spherical 4R mechanisms may include two branches which may or may not intersect. It is possible that the two configurations that allow to escape to V_1 (E escaping from O to $\mathscr{C}_1$) belong to the same branch of the 4R mechanism, while the other two configurations to escape to V_2 (E escaping from O to $\mathscr{C}_2$) belong to the other branch of the 4R mechanism. In such case, in order to reconfigure the linkage from V_1 to V_2 it is necessary to disassemble it if the two spherical 4R branches

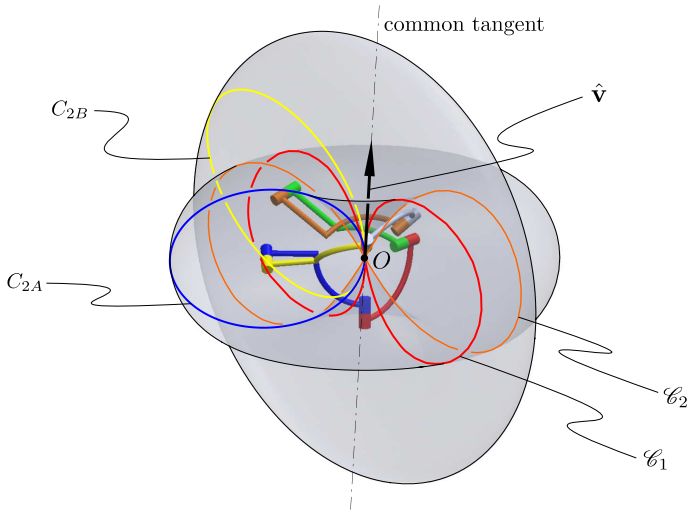

FIGURE 4.9: A reconfigurable Bricard plane-symmetric linkage in its spherical 4R operation mode, with its two secondary circles tangent to each other and to curve $\mathscr{C}_1$ and the mechanism is about to escape to V_1.

.

are disjoint. Therefore, the following paragraphs investigate the two spherical 4R branches and the four escape configurations in order to establish the restrictions that ensure that the mechanism can reconfigure through all of its branches. We begin by analyzing the rotability of the evolved spherical 4R mechanisms since branch identification is different depending on the rotability of the links. However, we restrict this analysis to the cases in which the toroid generators are built using $|\gamma| = \gamma^*$

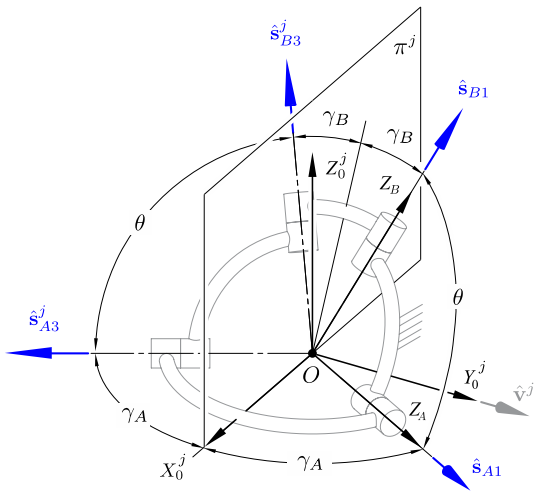

FIGURE 4.10: A plane-symmetric configuration of a spherical 4R linkage with two opposite links of the same angle.

.

Proposition 4.8.1 *The spherical 4R linkages obtained as a behavior of Bricard plane-symmetric linkages that generate two concentric toroids intersecting in two curves are either crank-rocker or change-point.*

Proof: Let the twist angles of the spherical four-bar linkage evolved from the Bricard plane-symmetric linkage be $\alpha_{A1,A3} = 2|\gamma_A|$, $\alpha_{A3,B3} = \alpha_{B1,A1} = \theta$ and $\alpha_{B3,B1} = 2|\gamma_B|$ (Fig. 4.10).

From the second condition in Eq. (4.12): $\theta+\gamma_A+\gamma_B<\pi \Rightarrow 2\theta+2\gamma_A+2\gamma_B<2\pi$, then $\Sigma\alpha_i<2\pi$. According to Gupta and Ma [120], if the sum of twist angles is less that 2π, the full rotability criterion is quite similar to that for the planar case: if $\alpha_{\min}+\alpha_{\max}<\alpha_{\rm p}+\alpha_{\rm q}$, then at least one of the links is fully rotatable.

From the second condition in Eq. (4.12), $\gamma_A+\gamma_B<\theta \Rightarrow \frac{1}{2}(\alpha_{A1,A3}+\alpha_{B3,B1})<\alpha_{A3,B3}=\alpha_{B1,A1}$ and $\alpha_{\min}\neq\alpha_{A3,B3}=\alpha_{B1,A1}$. By contradiction consider that none of the links is fully rotatable. Then, if $\alpha_{\max}=\alpha_{A3,B3}=\alpha_{B1,A1}=\theta$, from the criterion it follows:

$$\alpha_{\min}+\theta>\theta+\alpha_{\rm q} \Rightarrow \alpha_{\min}>\alpha_{\rm q}$$

which is a contradiction. In a similar way, now consider $\alpha_{\rm p}=\alpha_{\rm q}=\alpha_{A3,B3}=\alpha_{B1,A1}=\theta$:

$$\alpha_{\min}+\alpha_{\max}>2\theta \Rightarrow \alpha_{A1,A3}+\alpha_{B3,B1}>2\theta$$

which contradicts the second condition in Eq. (4.12). Hence, it is proved that at least one of the links is fully rotatable. This link is the one whose twist angle is $\alpha_{\min}$. In Fig. 4.10 it can be seen that the twist angle for the coupler and fixed links is θ, which is proved to be different to $\alpha_{\min}$. Therefore, the smallest twist angle corresponds to either the input or output links. Hence, all the linkages are crank-rocker or, if $\alpha_{A1,A3}=\alpha_{B3,B1}\Rightarrow\gamma_A=\gamma_B$, change-point. ■

It is known [121] that in crank-rocker (or rocker-crank) 4R mechanisms both branches are disjoint. Therefore, from proposition 4.8.1 it is concluded that the only way to have a special configuration joining the two branches is the spherical equivalent of a parallelogram mechanism. In such a very special case the criterion for branch change is simply the parallel- or anti-parallelism of the links. For crank-rockers (or rocker-cranks), the following two propositions allow the identification of branch change.

Proposition 4.8.2 *A spherical 4R linkage with two opposite links of the same twist angle can reach four plane-symmetric configurations, two of them belong to the same branch while the other two belong to the other branch.*

Proof: Refer to Fig. 4.10, which shows the spherical 4R linkage with two opposite links of the same twist angle, θ, the angle of the other two links are $2\gamma_A$ and $2\gamma_B$. The mechanism is shown in a plane-symmetric configuration. $\hat{\mathbf{s}}_{A1}$, $\hat{\mathbf{s}}_{A3}$, $\hat{\mathbf{s}}_{B3}$ and $\hat{\mathbf{s}}_{B1}$ are the unit vectors parallel to the axes of the revolute joints. A coordinate system $X_0Y_0Z_0$ is placed fixed to the symmetry plane π, so that π coincides with the plane X_0Z_0 and X_0 bisects the angle between $\hat{\mathbf{s}}_{A1}$ and $\hat{\mathbf{s}}_{A3}$.

The linkage is symmetric with respect to π when ${}^0\hat{\mathbf{s}}_{i1}\cdot\hat{\mathbf{j}}=-{}^0\hat{\mathbf{s}}_{i3}\cdot\hat{\mathbf{j}}$ while ${}^0\hat{\mathbf{s}}_{i1}\cdot\hat{\mathbf{i}}={}^0\hat{\mathbf{s}}_{i3}\cdot\hat{\mathbf{i}}$ and ${}^0\hat{\mathbf{s}}_{i1}\cdot\hat{\mathbf{k}}={}^0\hat{\mathbf{s}}_{i3}\cdot\hat{\mathbf{k}}$, $i=A,B$. Adding this restriction, the following four solutions are found for ${}^0\hat{\mathbf{s}}_{B1}$:

$$\begin{aligned}
{}^0\hat{\mathbf{s}}^1_{B1} &= \left(\frac{\cos\theta}{\cos\gamma_B}-\frac{K_1}{2\cos^2\gamma_B},\frac{K_1}{\cos\gamma_B\sin\gamma_B},\sqrt{\frac{K_2+K_1\cos\theta}{\cos^3\gamma_B}}\right)\\
{}^0\hat{\mathbf{s}}^2_{B1} &= \left(\frac{\cos\theta}{\cos\gamma_B}-\frac{K_1}{2\cos^2\gamma_B},\frac{K_1}{\cos\gamma_B\sin\gamma_B},-\sqrt{\frac{K_2+K_1\cos\theta}{\cos^3\gamma_B}}\right)\\
{}^0\hat{\mathbf{s}}^3_{B1} &= \left(\frac{\cos\theta}{\cos\gamma_B}+\frac{K_1}{2\cos^2\gamma_B},-\frac{K_1}{\cos\gamma_B\sin\gamma_B},\sqrt{\frac{K_2-K_1\cos\theta}{\cos^3\gamma_B}}\right)\\
{}^0\hat{\mathbf{s}}^4_{B1} &= \left(\frac{\cos\theta}{\cos\gamma_B}+\frac{K_1}{2\cos^2\gamma_B},-\frac{K_1}{\cos\gamma_B\sin\gamma_B},-\sqrt{\frac{K_2-K_1\cos\theta}{\cos^3\gamma_B}}\right)
\end{aligned} \tag{4.13}$$

where $K_1=|\cos\gamma_B\sin\gamma_B|\sqrt{2(1-\cos\gamma_A)}$ and $K_2=\frac{1}{2}\cos\gamma_B(2\cos^2\gamma_B-2\cos^2\theta+\cos\gamma_A-1)$. ${}^0\hat{\mathbf{s}}^k_{B3}$, $k=1,\ldots,4$ can be obtained from ${}^0\hat{\mathbf{s}}^k_{B1}$ by simply changing the sign of the Y_0 component

of each vector. ${}^0\hat{\mathbf{s}}_{A1}$ and ${}^0\hat{\mathbf{s}}_{A3}$ are the same for all configurations since they are fixed to plane π.

According to [122], if the mechanism is crank-rocker (or rocker-crank), all the configurations for which $\eta_k := {}^0\hat{\mathbf{s}}_{A1} \times {}^0\hat{\mathbf{s}}^k_{B3} \cdot {}^0\hat{\mathbf{s}}^k_{A3}$ has the same sign belong to the same branch. Upon calculation it is found that, $\text{sign}(\eta_1) = \text{sign}(\eta_3) = \text{sign}(\cos\gamma_B \sin\gamma_B)$ and $\text{sign}(\eta_2) = \text{sign}(\eta_4) = -\text{sign}(\cos\gamma_B \sin\gamma_B)$. Hence, it is concluded that plane-symmetric configurations 1 and 3 lie in the same branch, while configurations 2 and 4 lie in the other branch. ■

From the previous proposition it can be seen that the two different Bricard branches may reconfigure to spherical 4R modes in different branches, making impossible to move from one Bricard branch to the other. Each of the four plane-symmetric configurations presented in the previous proposition is a bifurcation configuration between Bricard branches and spherical 4R branches. Therefore, a vector $\hat{\mathbf{v}}^j$ tangent to the curve of intersection at O can be calculated for each of these configurations. For the sake of simplicity we call these vectors *escape directions*

Proposition 4.8.3 *Given a plane-symmetric Bricard linkage generated from the intersection of two concentric singular toroids with the axis of one rotated about the Y axis from the other, the escape directions lying on the same side of the plane XZ correspond to configurations lying in the same spherical 4R branch.*

Proof: From the geometry of the plane-symmetric mechanisms obtained from the intersection of two concentric singular toroids it can be proved that the escape directions $\hat{\mathbf{v}}_j$ are parallel to[4] $(\hat{\mathbf{s}}_{B3} \times \hat{\mathbf{s}}_{B1}) \times (\hat{\mathbf{s}}_{A3} \times \hat{\mathbf{s}}_{A1}) || \hat{\mathbf{j}}_0$, where $\hat{\mathbf{j}}_0$ is the unit vector in the direction of Y_0 in Fig. 4.10. Each of the four configurations obtained in Proposition 4.8.3 lead to a escape direction $\hat{\mathbf{v}}_j$. We are interested in obtaining such vectors in the coordinate system A, which is fixed, while coordinate system 0 moves from one configuration to another. Therefore, for coordinate system A, vectors ${}^A\hat{\mathbf{s}}_{A1}$ and ${}^A\hat{\mathbf{s}}_{B1}$ are fixed, while there are four sets of vectors ${}^A\hat{\mathbf{s}}^j_{A3}$ and ${}^A\hat{\mathbf{s}}^j_{B3}$.

The escape directions are calculated by finding the bases $\left\{ {}^0\hat{\mathbf{i}}^j_A, {}^0\hat{\mathbf{j}}^j_A, {}^0\hat{\mathbf{k}}^j_A \right\}$:

$$ {}^A\hat{\mathbf{v}}_j = {}^A\hat{\mathbf{j}}^j_0 = {}^A_0\mathbf{T}_j \, {}^0\hat{\mathbf{j}}_0 = \text{aug}\left({}^0\hat{\mathbf{i}}^j_A, {}^0\hat{\mathbf{j}}^j_A, {}^0\hat{\mathbf{k}}^j_A \right)^{-1} \hat{\mathbf{j}} $$

The following four escape directions are found, each related to each of the symmetric configurations found in Proposition 4.8.2:

$$
\begin{aligned}
{}^A\hat{\mathbf{v}}_1 &= \left(\frac{-2\cos\theta\cos\gamma_B\sin^2\gamma_B + K_1}{2|\sin\theta|\cos\gamma_B\sin\gamma_B}, -\frac{\cos\gamma_B\sqrt{2K_2+K_1}}{|\sin\theta|\sqrt{\cos^3\gamma_B}}, \sin\gamma_B \right) \\
{}^A\hat{\mathbf{v}}_2 &= \left(\frac{-2\cos\theta\cos\gamma_B\sin^2\gamma_B + K_1}{2|\sin\theta|\cos\gamma_B\sin\gamma_B}, \frac{\cos\gamma_B\sqrt{2K_2+K_1}}{|\sin\theta|\sqrt{\cos^3\gamma_B}}, \sin\gamma_B \right) \\
{}^A\hat{\mathbf{v}}_3 &= \left(\frac{-2\cos\theta\cos\gamma_B\sin^2\gamma_B - K_1}{2|\sin\theta|\cos\gamma_B\sin\gamma_B}, -\frac{\cos\gamma_B\sqrt{2K_2-K_1}}{|\sin\theta|\sqrt{\cos^3\gamma_B}}, \sin\gamma_B \right) \\
{}^A\hat{\mathbf{v}}_4 &= \left(\frac{-2\cos\theta\cos\gamma_B\sin^2\gamma_B - K_1}{2|\sin\theta|\cos\gamma_B\sin\gamma_B}, \frac{\cos\gamma_B\sqrt{2K_2-K_1}}{|\sin\theta|\sqrt{\cos^3\gamma_B}}, \sin\gamma_B \right)
\end{aligned}
$$

[4] The radius of the secondary circles are the common perpendiculars between axes $\mathbf{S}_{i1}$ and $\mathbf{S}_{i2}$, $i = A, B$. In the spherical 4R branches this line segment coincides with the common perpendicular of $\mathbf{S}_{i2}$ and $\mathbf{S}_{i3}$. Therefore, $\hat{\mathbf{s}}_{i1} \times \hat{\mathbf{s}}_{i3}$ must be parallel to the radius of C_{2i}. Since the circles are tangent to each other in the escape configurations and this tangent is perpendicular to the radii of both circles, it follows that the tangent is parallel to $(\hat{\mathbf{s}}_{B3} \times \hat{\mathbf{s}}_{B1}) \times (\hat{\mathbf{s}}_{A3} \times \hat{\mathbf{s}}_{A1})$

It can be seen that ${}^A\hat{\mathbf{v}}_1$ and ${}^A\hat{\mathbf{v}}_2$ (${}^A\hat{\mathbf{v}}_3$ and ${}^A\hat{\mathbf{v}}_4$) are symmetric with respect to the X_AZ_A plane as the only difference between them is the sign of the Y component. The sign of the Y components of ${}^A\hat{\mathbf{v}}_1$ and ${}^A\hat{\mathbf{v}}_3$ (${}^A\hat{\mathbf{v}}_2$ and ${}^A\hat{\mathbf{v}}_4$) is the same, namely $-\text{sign}(\cos\gamma_B)$ ($\text{sign}(\cos\gamma_B)$), hence they lie in the same side of the X_AZ_A plane. In addition, all these vectors lie in the same side of the X_AY_A plane as their Z components are the same, namely $-\text{sign}(\sin\gamma_B)$. From Proposition 4.8.2 it is known that configurations 1 and 3 (2 and 4) lie in the same branch, therefore it can be concluded that the escape directions lying in the same side of the X_AZ_A plane belong to the same branch of the spherical 4R linkage. ■

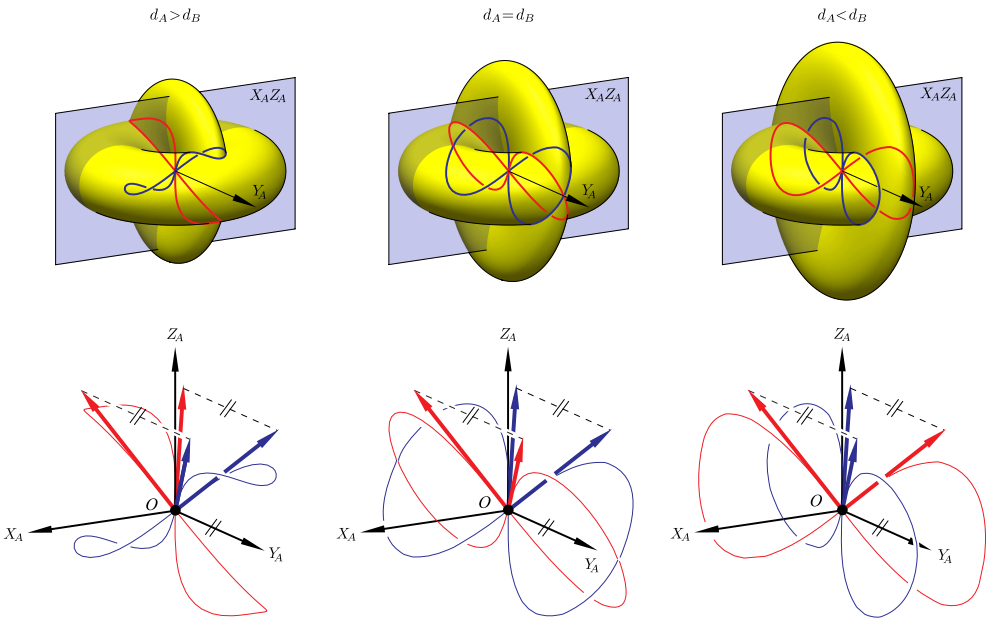

FIGURE 4.11: Tangent vectors to the intersection curves at the coincident singularities, for the three possible cases: $r_A > r_B$, $r_A = r_B$ and $r_A < r_B$

Fig. 4.11 shows three possible cases of intersection composed by two curves: $r_A > r_B$, $r_A = r_B$ and $r_A < r_B$. In each case the tangent vector to the curves at O, the coincident singularities point, are shown. These tangent vectors are the same that were calculated in Proposition 4.8.3, in which it was proven that if these 4 vectors have Z_A component of the same sign, then: when the vectors lie in the same side of the X_AZ_A plane the configurations of the spherical 4R linkage lie in the same branch. From Fig. 4.11 it can be seen that for the case $r_A > r_B$ the vectors lying on the same side of the X_AZ_A plane are tangent to the same curve, and since these configurations belong to the same spherical 4R branch reconfiguration to the other curve is impossible and the two spherical 4R branches cannot be reached without disassembling the linkage. For $r_A = r_B$ and $r_A < r_B$ the two vectors lying on the same side of the X_AZ_A are tangent to different curves, this means that it is possible to reconfigure the disjoint spherical 4R branches without disassembling the linkage as both branches are connected through a Bricard branch related to each of the two curves.

It can be proved[5] that for the change-point evolved spherical 4R mechanisms the escape directions that are symmetric with respect to the plane X_AZ_A belong to the same branch. Therefore, from Fig. 4.11, if $r_A > r_B$ the same Bricard branch can be reconfigured to parallel or anti-parallel branches of change-point spherical 4R mechanism.

Fig. 4.12 shows the reconfiguration diagrams for two cases of reconfigurable plane-symmetric mechanism obtained from the toroids intersection. The diagram in Fig. 4.12a is

[5]Such a proof, as mentioned above, is based on the parallelism or anti-parallelism of the links. The proof is not presented due to space reasons.

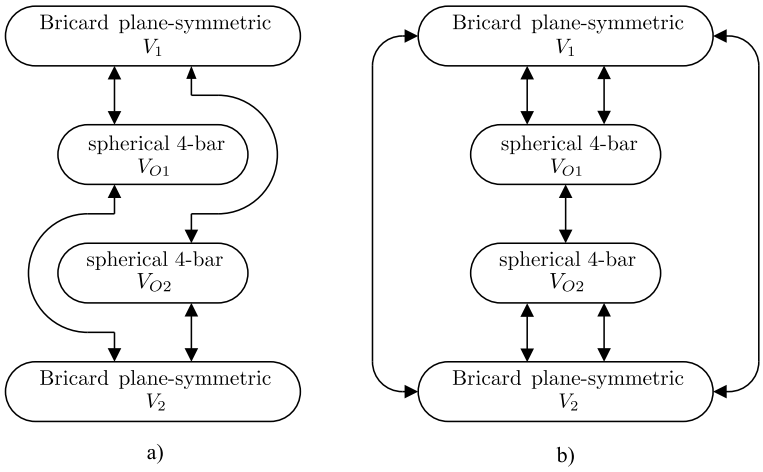

FIGURE 4.12: Two cases of branch reconfiguration diagrams when the intersection of concentric singular toroids is composed of two singular curves: a) $r_A < r_B$ and $\gamma_A \neq \gamma_B$ (example presented in this subsection); b) $r_A = r_B$ and $|\gamma_A| = |\gamma_B|$.

.

related to a case with two crank-rocker spherical 4R branches, it is known that these branches are disjoint, but it is possible to reach both branches without disassembling the linkage since they are communicated through two different Bricard plane-symmetric branches. Fig. 4.12b shows a more complicated case in which $r_A = r_B$ and $|\gamma_A| = |\gamma_B|$, leading to a plane- and line-symmetric linkage for which the toroids are tangent to each other in two points in the Y axis, these singularities communicate the two Bricard branches, furthermore, since $|\gamma_A| = |\gamma_B|$ the evolved spherical 4R linkage is change-point, allowing a direct reconfiguration between its two branches through the special configuration.

4.9 An example with two spherical 4R branches connected through two Bricard plane-symmetric branches

Consider the plane-symmetric linkage shown in fig. 4.13 which has the following DH parameters:

$$\begin{array}{lll} \alpha_{A1,A2} = \frac{1}{3}\pi, & \alpha_{B2,B1} = \frac{23}{12}\pi, & \alpha_{B1,A1} = \frac{17}{36}\pi, \\ a_{A1,A2} = 5, & a_{B2,B1} = 6, & a_{B1,A1} = 0 \\ \alpha_{A2,A3} = \frac{5}{3}\pi, & \alpha_{B3,B2} = \frac{1}{12}\pi, & \alpha_{A3,B3} = \frac{55}{36}\pi, \\ a_{A2,A3} = 5, & a_{B3,B2} = 6, & a_{A3,B3} = 0 \end{array} \tag{4.14}$$

then the mechanism generates the intersection of two concentric singular toroids, such that $\gamma_A = \frac{1}{3}\pi$, $r_A = 5$, $\gamma_B = -\frac{15}{180}\pi$, $r_B = 6$ and $\theta = \frac{85}{180}\pi$. These construction parameters satisfy the conditions in Eq. 4.12, therefore $\mathcal{C} = \mathscr{C}_1 \cup \mathscr{C}_2$ such that $\mathscr{C}_1 \cap \mathscr{C}_2 = \{O\}$. Since E can reach the coincident singularities O the mechanism has four motion branches: two Bricard branches and two spherical 4R branches. In addition, since $r_A < r_B$ and $\gamma_A \neq \gamma_B$ the mechanism should be able to move through the two spherical 4R branches without disassembling it.

Fig. 4.14 shows the mechanism in several configurations in each motion branch. Observe that the two configurations belonging to V_1 (V_2) for which $E = O$ are different as expected. None of these four symmetric configurations coincide since V_1 and V_2 are disjoint. However, each of these is singular in V, allowing the reconfiguration to V_{O1} and V_{O2}, the spherical 4R branches, for which $E(\mathbf{q}) = O, \forall \mathbf{q} \in V_{O1} \cup V_{O2}$. The reconfiguration between branches is presented in the diagram in Fig. 4.12a, which shows how the two branches of the evolved

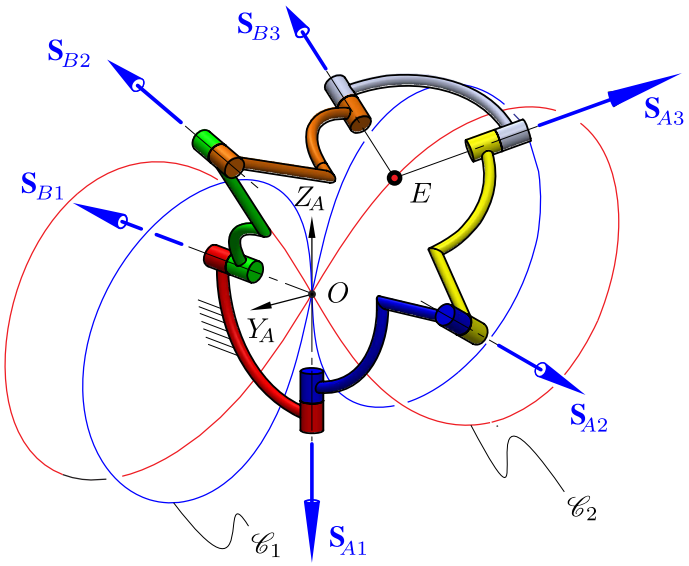

FIGURE 4.13: A reconfigurable Bricard plane-symmetric linkage that allows the reconfiguration between two spherical 4R branches through two Bricard branches. The intersection of the concentric singular toroids is composed of two singular curves.

.

spherical 4R linkage are connected through plane-symmetric Bricard branches allowing reconfigurability without disassembling.

Chapter conclusions

The plane-symmetric case of Bricard loops was analyzed using the intersection of two concentric singular toroids, allowing the design of reconfigurable linkages with several motion branches which can be either plane-symmetric 6R branches or spherical 4R branches. The conditions for having two singular curves in the intersection set were presented. Each of these curves is related to a plane-symmetric 6R branch of motion. The phenomenon of coincident singularities leads to kinematotropy when the two surface generators are joined by a spherical pair or a reduction of this to a pair of revolute joints each being parallel to the axis of rotation of surfaces of revolution. However, in the case of overconstrained plane-symmetric linkages it was found that such coincident singularities leads to a spherical 4R branch.

The study of the escape directions, which are the tangents to the intersection curves at the coincident singularities revealed the existence of linkages whose evolved crank-rocker spherical 4R mechanism can work in its two branches without disassembling it. To the knowledge of the author, this is the first time that a mechanism with this property is presented. These interesting results, along with those for the line-symmetric case, presented in chapter 3, shed light on whether it is possible to design more overconstrained linkages that can be reconfigured between different branches using the method of generated surfaces.

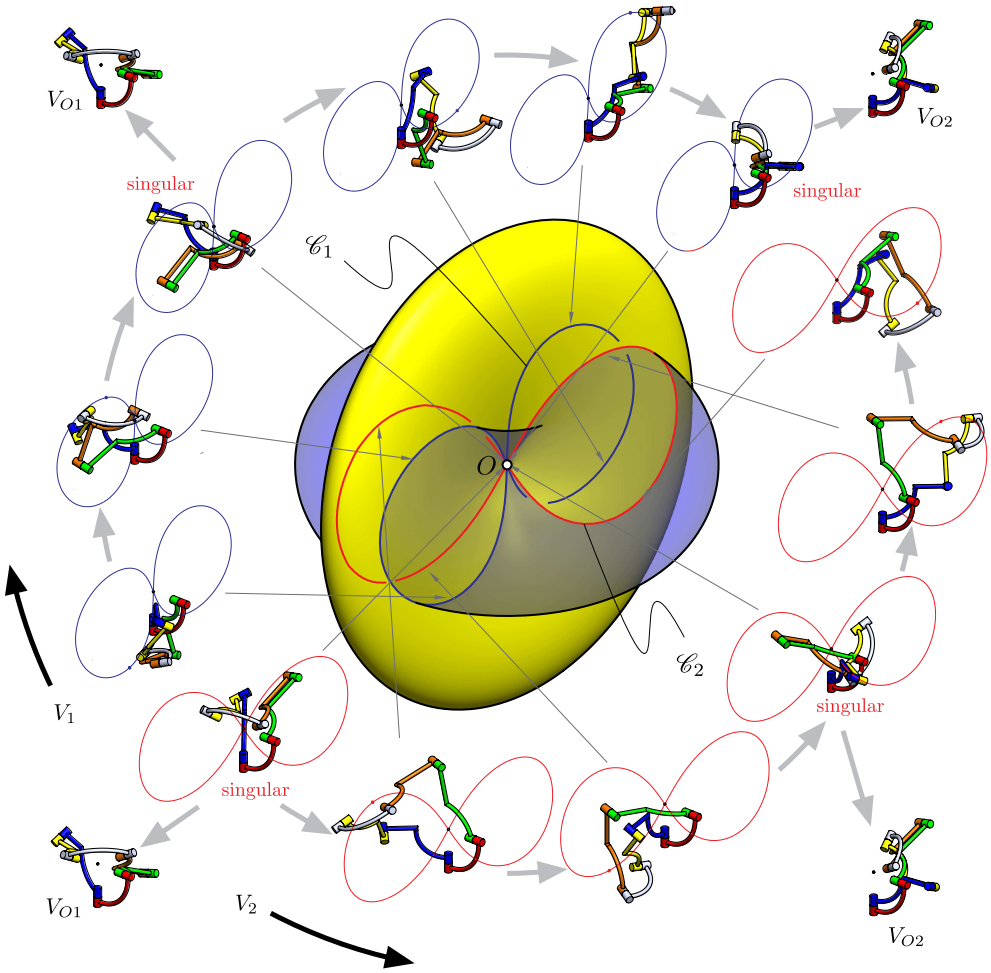

FIGURE 4.14: Several configurations of the plane-symmetric Bricard linkage when the intersection of concentric toroids contains two singular curves.

.

Chapter 5

Design of kinematotropic mechanisms using coincident surfaces: the Bohemian dome

Although the method of generated surfaces has been used effectively in the previous chapters for designing reconfigurable mechanisms, most of these linkages cannot change their number of finite degrees of freedom. In this chapter, a new method is presented for the design of linkages that can change their mobility based on 2-DOF kinematic chains that generate more than one surface. As an example of the proposed method, a kinematotropic linkage is obtained by studying a special case of Bohemian dome which has two different parametrizations constructed by translation of circles and, therefore, two different hybrid kinematic chains can be designed to generate the same Bohemian dome. Each of these hybrid kinematic chains can generate two different surfaces and, thus, can be used in the proposed method. Parametrizations for the secondary surfaces are then obtained and studied. A total of 27 motion branches are found in the configuration space of this kinematotropic linkage. The singularities in the configuration space are further determined using the properties of the surfaces. The resultant linkage offers an explanation of Wholhart's queer-square linkage other than its original paper folding.

As part of the analysis of this example, the relationship between the properties of self-intersections in generated surfaces and the configuration space of the generator linkage is studied leading to a description of motion branches related to self-intersections of generated surfaces.

This chapter is based on the journal publication:

> [37] P.C. López-Custodio and J.S. Dai, "Design of a variable-mobility linkage using the Bohemian dome," *ASME Journal of Mechanical Design*, vol. 141, no. 9, pp. 092303-1–092303-12, 2018. DOI:10.1115/1.4042845.

5.1 Background

Notwithstanding the plethora of kinematotropic linkages in the literature, only a handful of general methods for the design of these devices have been reported. The first of these being proposed by Galletti and Fanghella [13] who used group theory to design single-loop kinematotropic linkages. After Galletti and Fanghella's paper very few articles proposing design methods were published, including [83] where 7R one-loop kinematotropic mechanisms are designed, [14] in which the type synthesis of kinematotropic parallel mechanisms is presented for the first time and [123] which deals with the synthesis of kinematotropic deployable mechanisms. Due to this shortage of methods for the design of kinematotropic linkages, the purpose of this chapter is to present a different method, based in generated

surfaces, to design mechanisms with a very complex configuration space and with variable number of degrees of freedom.

Although Hunt [1] explained that any 2-DOF kinematic chain can be used to generate surfaces, in most of publications only dyads are considered as surface generators leading to a limited number of shapes of surfaces. In this chapter, closed-loop and hybrid surface generators are used in the design of kinematotropic linkages. The use of 2-DOF hybrid surfaces generators will not only bring a large number of new surfaces that have not been investigated yet, but it will also lead to the possibility of kinematic chains that generate more than one surface, this allows reconfiguration through a phenomenon that is different from the traditional tangency between surfaces [11]. In addition, this chapter proves that motion branches in the configuration space of linkages can appear as a consequence of self-intersections in the generated surfaces.

The method for designing kinematotropic linkages proposed in this chapter is applied to a special type of Bohemian dome which can be obtained through two different parametrizations based on the translation of a circle through another circle. The Bohemian dome was used by Tale Masouleh et al. [124] to describe the constant-orientation working space of a parallel robot. In this chapter, the Bohemian dome is generated by a hybrid kinematic chain which also generates a different surface. The resultant linkage is similar to Wohlhart's queer-square mechanism [12] which was later analyzed in its linkage form by Gogu [16] and Qin et al. [15]. Wohlhart [12] noted that a point of the queer-square linkage moves in the upper hemisphere of a quadratic surface obtained by sweeping a circle through another circle and also explained that when the linkage works in 1-DOF mode such point describes a line. In this chapter it is proved that such a line segment corresponds to a self-intersection of the surface. Wohlhart only described two branches of motion of the linkage, probably due to the fact that his model was a foldable carton mechanism which did not allow to see other configurations without interference of the links. Qin et al. [15] proved that after converting it from a foldable carton to a linkage it can reach 14 motion branches, in this chapter it is proved that such motion branches correspond to 3 of the 4 cases of surface intersections that can be obtained from the designed linkage from which the queer-square linkage can be seen as a special case. It is found that the configuration space of the linkage designed in this chapter presents a total of 27 branches of motion. All singularities in this configuration space are also detected from the properties of the generated surfaces.

This chapter is organized as follows: First, the method is introduced in Section 5.2. In Section 5.3 the properties of the Bohemian dome, its parametrizations and their mechanical generators are discussed, the reconfigurability of these generators is also discussed and parametrizations for the secondary surfaces are presented. In Section 5.4 the designed linkage is presented and its similarities with Wohlhart's queer-square linkage are discussed. In Section 5.5 an analysis of how the surfaces and heir intersections are related to the configuration space of the linkage is presented. In Section 5.6 the intersection curves in the four different cases of surface intersections are determined. In 5.7 these intersection curves are used to determine the motion branches in the configuration space of the linkage. Finally, in Section 5.8 the singularities in the configuration space are detected by means of the properties of surfaces.

5.2 A method for designing kinematotropic mechanisms based on coincidence of surfaces

As seen in previous chapters, a point E of the end-effector of any 2-DOF kinematic chain generates a surface with the exception of degenerate cases, like doubly-covered curves. When two surface generators A and B are connected by means of a spherical pair whose center of

rotation E coincides with the points that draw the surfaces E_A and E_B, a 1-DOF mechanism is obtained in the general case that the surfaces intersect in a curve in which E is confined to move. This mechanism can be reconfigurable if the intersection features several curves, all branches of motion are 1-DOF with the exception of coincident conic singularities which turn into rather trivial 2-DOF motions [11].

A more complex case happens when at least one of the surface generators has more than one 2-DOF branch of motion on its own, i.e. the same kinematic chain generates at least two different surfaces. In this case E can move through the intersection of all possible combinations of generated surfaces. The interesting phenomenon occurs when one of these surfaces is the same as the surface generated by the other kinematic chain, in such a situation the mechanism is no longer a 1-DOF chain since the intersection is no longer a curve, but a surface. However, when, in the same mechanism, the surfaces are not the same, the mechanism has 1 DOF again. Therefore, this mechanism can change its number of finite degrees of freedom. The idea just explained can be summarized in the following method for the design of kinematotropic mechanisms:

1. Find a 2-DOF kinematic chain that can generate two different surfaces. For example, a very simple way of doing this is taking a planar or spherical 1-DOF mechanism with at least two motion branches and then attaching a P or R joint to the coupler bar to obtain a 2-DOF hybrid kinematic chain.

2. Find a different 2-DOF kinematic chain that generates one of the surfaces generated by the other kinematic chain.

3. Join the end-effectors of both kinematic chains using an S joint whose center of rotation coincides with the points that draw both surfaces. This S joint can be reduced in some cases to a U joint or a single R joint.

Fig. 5.1 shows a simple example of the kinematotropic mechanisms that can be obtained with the proposed method. In this artifact, surface generator A is a 1-loop CCCC kinematic chain with three 2-DOF branches of motion [50]: point E_A can move through a cylinder with axis coincident with the axis of C joint $A1$, through a cylinder with axis coincident with the axis of C joint $A4$ or through the plane spanned by both axes. Surface generator B is a C chain that allows E_B to move through a cylinder with axis coincident with the axis of $A1$ joint. When chain A generates the same cylinder as generator B the whole mechanism has 2 DOF with E free to move through that cylinder, see fig. 5.1b. However, when A generates the cylinder with axis coincident with the axis of joint $A4$, its intersection with the cylinder generated by B consists of two ellipses each leading to a 1-DOF branch of motion. In the case where A generates a plane, the intersection with cylinder B is two lines, however these configurations are singularities in the generator A though which it can reconfigure from generating the plane to generating the cylinder with axis coincident with the axis of join $A1$, therefore this situation does not lead to a separate branch of motion of the kinematotropic mechanism.

This is a rather simple example because, considering the joint variables as parameters, the parametrizations of both coincident cylinders are the same, i.e., the joint variables of $A1$ and $B1$ in the 2-DOF branch of motion are the same. A much more interesting case could be obtained if the surface had two different parametrizations and none of the parameters in both parametrizations were measured about the same axis, this means that there would be no joints with coincident axes in the 2-DOF branch of motion. A special case of Bohemian dome is an example of a surface with such a property. The remaining of the chapter is dedicated to the kinematotropic linkage obtained applying this method by using the Bohemian dome and its two generators.

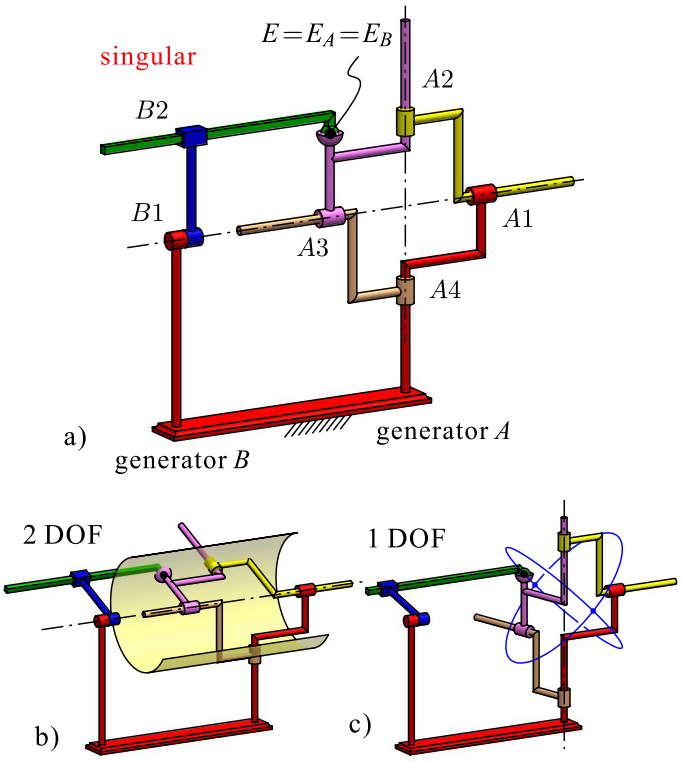

FIGURE 5.1: A kinematotropic mechanism obtained from coincident cylinders: a) singular configuration, b) 2-DOF regular configuration and c) 1-DOF regular configuration

5.3 The symmetric Bohemian dome and its two generators

5.3.1 The symmetric Bohemian dome

Consider the special case of Bohemian dome shown in fig. 5.2a. Such a quartic surface is constructed by translating a *secondary* circle, C_2, through a fixed *base* circle C_1, the normals to the planes that contain the circles, $\hat{\mathbf{n}}_2$ and $\hat{\mathbf{n}}_1$, respectively, always being perpendicular. In this special case of Bohemian dome, the radii of the circles C_1 and C_2 are the same and equal to l_1. A parametrization $\sigma : \mathbb{T}^2 \to \mathbb{R}^3$ with respect to the coordinate system shown in fig. 5.2a for the Bohemian dome is given as follows:

$$\sigma(u,v) := (l_1 \cos u,\, l_1(\sin u + \sin v),\, l_1 \cos v) \tag{5.1}$$

and the Bohemian dome is the set $\mathcal{B} = \mathrm{im}(\sigma(\mathbb{T}^2)) \subset \mathbb{R}^3$. With such parametrization the isoparametric curves in every point are two circles of radius l_1. Parameters $(u,v) \in \mathbb{T}^2$ are measured as shown in fig. 5.2b. It can be seen that $\mathcal{B}$ is invariant to a rotation of $n\pi/2$, $n \in \mathbb{Z}$, radians about the Y-axis. Therefore, we call this special Bohemian dome the *symmetric* Bohemian dome, since it is not only symmetric with respect to the three planes of the coordinate system (as any general Bohemian dome), but also to both planes obtained by rotating the XY plane $\pi/4$ radians about the Y axis. Since $\mathcal{B}$ is invariant to rotations of $\pi/2$ radians about the Y-axis there is a second parametrization $\sigma_B : \mathbb{T}^2 \to \mathcal{B}$ such that $\mathrm{im}(\sigma_A(\mathbb{T}^2)) = \mathrm{im}(\sigma_B(\mathbb{T}^2)) = \mathcal{B}$, where $\sigma_A(u_A, v_A) := \sigma(u_A, v_A)$ and $\sigma_B(u_B, v_B) := \mathrm{Rot}(\hat{\mathbf{j}}, \pi/2)\sigma_A(u_B, v_B)$. The four circles drown by this pair of parametrizations are shown in fig. 5.2c.

An important property of the symmetric Bohemian dome is that it self-intersects in two segments of lines, $\mathscr{L}_1 = \{(l_1 \cos u, 0, l_1 \cos u) : u \in \mathbb{T}\}$ and $\mathscr{L}_2 = \{(l_1 \cos u, 0, -l_1 \cos u) : u \in \mathbb{T}\}$. Since the self-intersections have ends $(l_1, 0, l_1)$, $(l_1, 0, -l_1)$, $(-l_1, 0, l_1)$ and $(-l_1, 0, -l_1)$, the

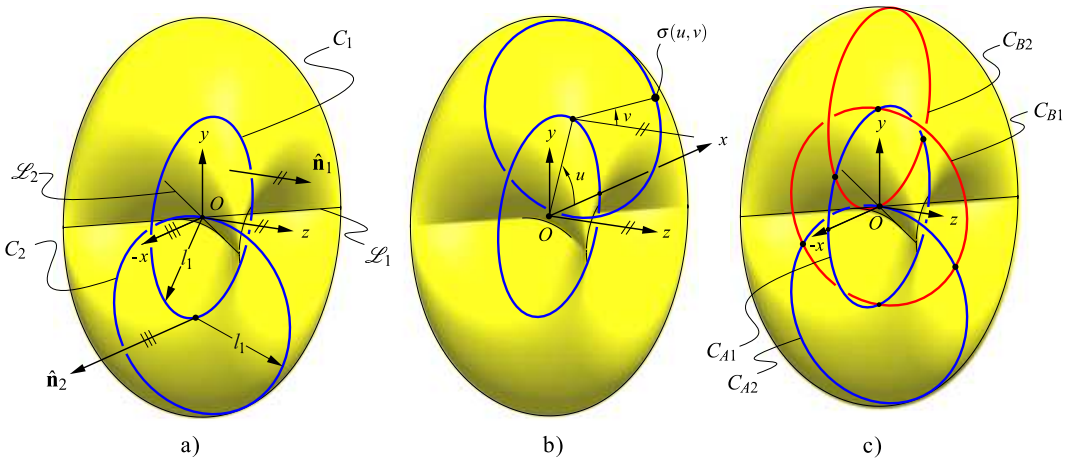

FIGURE 5.2: The symmetric Bohemian dome, a) construction, b) two different sets of circles that generate the same surface

two segments of the surface that meet in the self-intersections become one at these four points. Hence, these four points are conic singularities of $\mathcal{B}$. This is easily verified for singular point $\sigma(0,0) = (l_1, 0, l_1)$, by checking $\partial\sigma/\partial u|_{(u,v)=(0,0)} \times \partial\sigma/\partial v|_{(u,v)=(0,0)} = \mathbf{0}$.

5.3.2 Two different generators for the same Bohemian dome

Since any Bohemian dome is generated by translating a circle through another fixed circle, this type of surface can be generated by a 2-DOF hybrid kinematic chain. *Hybrid* means, in this chapter, that the kinematic chain features both open loops and closed loops. A Bohemian dome can be generated by a kinematic chain that allows the direction of the axis of the second revolute joint to remain fixed while translating through a fixed base circle. This property can be achieved by means of a planar 4-bar parallelogram, since in such a linkage the coupler bar undergoes pure translation and any point of it describes a circle. Hence, by attaching a revolute joint to the coupler link its axis will translate through a circle without changing its orientation. Finally, a point in the end-effector of the hybrid kinematic chain will generate the Bohemian dome. Fig. 5.3a, shows such a hybrid kinematic chain generating a symmetric Bohemian dome. The parallelogram is conformed by the revolute joints with axes $\mathbf{S}_{A1}$, $\mathbf{S}_{A2}$, $\mathbf{S}_{A3}$ and $\mathbf{S}_{A4}$, these axes being parallel to the Z-axis. In the parallelogram $a_{A1,A2} = a_{A3,A4} = l_1$, and the other link length of the parallelogram, $a_{A1,A4} = a_{A2,A3} = l_2$, is arbitrary, however it will be important in the following sections. The coupler point, P_A, is used to draw C_{A1}, and the revolute joint axis $\mathbf{S}_{A5}$ passes through this point and is always parallel to the X-axis. The point E_A, attached to the end-effector, describes $C_{A2}(u_A)$, therefore $d(P_A, E_A) = l_1$.

Since the parametrization in Eq. (5.1) has circles as isoparametric curves at every point, parameters (u_A, v_A) are equal to joint variables q_{A1} and q_{A5}, respectively, with $u_A \in \mathbb{T}$ being the angle between the $X-$axis and the common perpendicular between $\mathbf{S}_{A4}$ and $\mathbf{S}_{A3}$, and $v_A \in \mathbb{T}$, the angle between $\overline{P_A E_A}$ and the $Z-$axis.

Another hybrid kinematic chain can be used to generate the same surface considering parametrization σ_B. It was discussed previously, from Eq. (5.1), that $\mathcal{B} = \text{im}(\sigma_A(\mathbb{T}^2)) = \text{im}(\text{Rot}(\hat{\mathbf{j}}, n\pi/2)\sigma_A(\mathbb{T}^2))$, $n \in \mathbb{Z}$, therefore the second hybrid kinematic chain that generates the same Bohemian dome is obtained by rotating the axes of the generator in fig. 5.3a $\pi/2$ radians about the Y-axis. Hence, it follows that $\mathbf{S}_{Bi} = \text{Adj}(\text{Rot}(\hat{\mathbf{j}}, \pi/2))\mathbf{S}_{Ai}$, $i = 1\ldots,5$, resulting on $\mathbf{S}_{Bi}$, $i = 1,\ldots,4$ being parallel to the X-axis and generating C_{B1} and $\mathbf{S}_{B5}$ always parallel to the Z-axis and generating $C_{B2}(u_B)$.

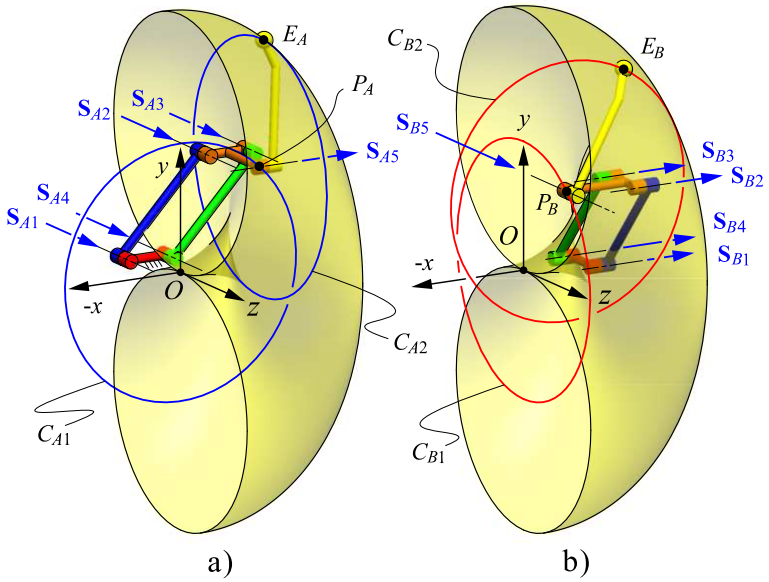

FIGURE 5.3: Two mechanical generators for the symmetric Bohemian dome: a) generator A with base circle C_{A1} on $xy-$plane, b) generator B with base circle C_{B1} on $yz-$plane

We define $V_A \subset \mathbb{T}^5$ and $V_B \subset \mathbb{T}^5$ as the configuration spaces of hybrid kinematic chains A and B, and consider $\mathbf{q}_A := (q_{A1}, \ldots, q_{A5}) \in V_A$ and $\mathbf{q}_B := (q_{B1}, \ldots, q_{B5}) \in V_B$ as the vectors of joint variables.

5.3.3 The two branches of motion of the Bohemian dome generator

Any parallelogram 4-bar linkage has two branches of motion: parallel and anti-parallel mode, thus V_A and V_B are composed of two manifolds. Both branches are connected by two singular flattened configurations in which $u_i = 0, \pi$ for generator $i = A, B$. In parallel mode the coupler draws a circle and the generated surface is a Bohemian dome. However, in the antiparallel mode $E_A(\mathbf{q}_A)$ generates a different surface, $\mathcal{S}_A \subset E^2$. Fig. 5.4 shows generator A in antiparallel mode and the generated surface $\mathcal{S}_A$.

Three parameters of the hybrid kinematic chain that do not affect the generation of the Bohemian dome now affect the shape of $\mathcal{S}_A$ when working in antiparallel mode, namely the distance from fixed axes $\mathbf{S}_{A1}$ and $\mathbf{S}_{A2}$ to the Z-axis, the coupler length l_2 and the choice of the coupler point P_A. As shown in fig. 5.4, for the sake of simplicity, we consider that the fixed link is centered with respect to the Z axis and that P_A lies in the line that joins $\mathbf{S}_{A2}$ and $\mathbf{S}_{A3}$ in the XY plane, and that it is located a distance l_3 from $\mathbf{S}_{A2}$ to $\mathbf{S}_{A3}$.

With such an arrangement it is easy to obtain two parametrization $\varsigma_A^1, \varsigma_A^2 : \mathbb{T}^2 \to \mathbb{R}^3$ for this surface using two different sets of parameters, (u_A, v_A) and (t_A, v_A), respectively, such that $\mathcal{S}_A = \mathrm{im}(\varsigma_A^i(\mathbb{T}^2))$, $i = 1, 2$.

First parameterization of $\mathcal{S}_A$

The parallelogram 4-bar linkage in generator A is shown in fig. 5.5. Points P_1 and P_4 are fixed and $d(O, P_1) = l_2/2$, the orientation of the bars is determined by angles u_A, q_{A2} and q_{A4} which are measured as shown in fig. 5.5. It can be seen that, for a given value of u_A, there are two possible ways of assembling the linkage as the circle of radius l_2 and center at P_2 intersects the circle of radius l_1 and center at P_4 at two points, P_3 and P_3', we are interested in the antiparallel solution, in which $q_{A4} \neq u_A$.

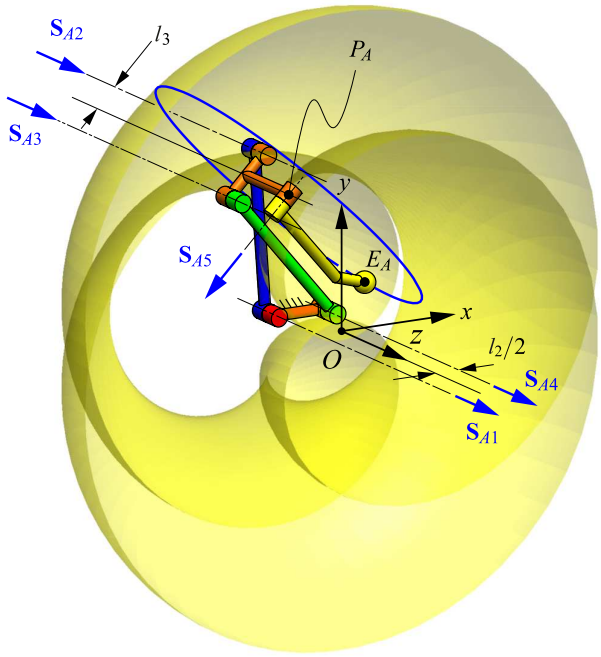

FIGURE 5.4: Bohemian dome hybrid generator in an antiparallel configuration.

Position of point P_3 is given by $\mathbf{r}_{P_3}(u_A, q_{A2}) = (-l_2/2 + l_1 \cos u_A + l_2 \cos q_{A2}, l_1 \sin u_A + l_2 \sin q_{A2}, 0)$, however P_3 is also confined to the circle of radius l_1 and center at P_4, therefore $\mathbf{r}_{P_3}(q_{A4}) = (l_2/2 + l_1 \cos q_{A4}, l_1 \sin q_{A4})$. By considering both possibilities two scalar equations in terms of the 3 joint variables are obtained. The equations are solved to obtain two solutions, the first one corresponds to the parallel case, namely $q_{A2} = 0$ and $q_{A4} = u_A$, for the second solution the following result is obtained:

$$\begin{aligned} \sin(q_{A2}(u_A)) &= \frac{2l_1 \sin u_A (l_1 \cos u_A - l_2)}{l_1^2 + l_2^2 - 2l_1 l_2 \cos u_A} \\ \cos(q_{A2}(u_A)) &= \frac{2l_1 \cos u_A (l_1 \cos u_A - l_2) - l_1^2 + l_2^2}{l_1^2 + l_2^2 - 2l_1 l_2 \cos u_A} \end{aligned} \tag{5.2}$$

Since $d(P_2, P_A) = l_3$, it follows that $\mathbf{r}_{P_A}(u_A) = \mathbf{r}_{P_2}(u_A) + l_3 \hat{\mathbf{n}}(u_A)$, where $\hat{\mathbf{n}}(u_A) = (\cos(q_{A2}(u_A)), \sin(q_{A2}(u_A)), 0)$. $\mathcal{S}_A$ is generated by point E_A which describes a circle of radius l_1, center at P_A and contained in a plane with normal $\hat{\mathbf{n}}$, with respect to the coupler. It follows that:

$$\begin{aligned} \mathbf{r}_{E_A}(u_A, v_A) &= \mathbf{r}_{P_A}(u_A) + \mathrm{Rot}(q_{A2}(u_A), \hat{\mathbf{k}})(0, \cos v_A, \sin v_A), \\ &= \Big(l_1 \cos u_A - \frac{l_2}{2} + l_3 \cos q_{A2} - l_1 \sin q_{A2} \sin v_A, \\ &\qquad l_1 \sin u_A + l_3 \sin q_{A2} + l_1 \cos q_{A2} \sin v_A, l_1 \cos v_A \Big) \end{aligned} \tag{5.3}$$

by substitution of Eq. (5.2) in Eq. (5.3) position of point E_A is found in terms of (u_A, v_A). Since E_A describes $\mathcal{S}_A$, then $\varsigma_A^1(u_A, v_A) := \mathbf{r}_{E_A}(u_A, v_A)$:

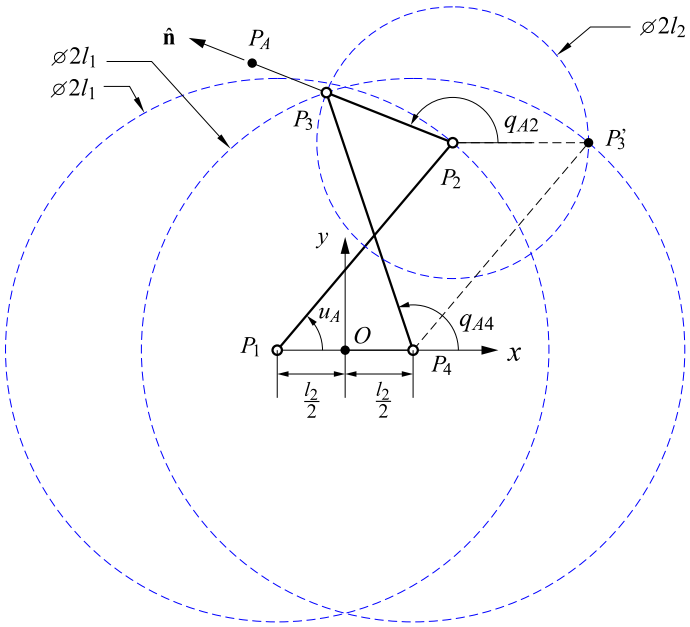

FIGURE 5.5: Two solutions for the parallelogram 4-bar linkage.

$$\varsigma_A^1(u_A, v_A) := \left(l_1 \cos u_A - \frac{l_2}{2} + K_2 l_3 - K_1 l_1 \sin v_A,\, l_1 \sin u_A + l_3 K_1 + l_1 K_2 \sin v_A,\, l_1 \cos v_A \right) \tag{5.4}$$

where,

$$\begin{aligned} K_1 &:= \frac{2 l_1 \sin u_A (l_1 \cos u_A - l_2)}{l_1^2 + l_2^2 - 2 l_1 l_2 \cos u_A} \\ K_2 &:= \frac{2 l_1 \cos u_A (l_1 \cos u_A - l_2) - l_1^2 + l_2^2}{l_1^2 + l_2^2 - 2 l_1 l_2 \cos u_A} \end{aligned}$$

Second parameterization of $\mathcal{S}_A$

An alternative parametrization $\varsigma_A^2 : \mathbb{T}^2 \to \mathbb{R}^3$ which uses a parameter $t_A \in \mathbb{T}$ instead of u_A can be obtained as follows.

In the anti-parallel mode, point F, the point where the input bar, $\overline{P_1P_2}$, and the output bar, $\overline{P_3P_4}$, intersect, draws an ellipse, $\mathscr{E} := \{\mathbf{r}_F(u_A) : u_A \in \mathbb{T}\}$, as shown in fig. 5.6. Points P_1 and P_4 are the foci of $\mathscr{E}$. F describes an ellipse since $d(P_4, F) + d(P_1, F) = l_1$, which is constant. $\mathscr{E}$ can be parametrized by:

$$\mathbf{r}_F(t_A) := \frac{1}{2} \left(l_1 \cos t_A,\, \sqrt{l_1^2 - l_2^2} \sin t_A, 0 \right), t_A \in \mathbb{T}$$

In $\mathscr{E}$, as in any ellipse, the normal line at any point F, $\mathscr{L}(\hat{\mathbf{m}}, F)$, bisects the angle P_1FP_4, therefore the tangent line at F, $\mathscr{L}(\hat{\mathbf{t}}, F)$, is the line of symmetry of the 4-bar mechanism. A vector $\mathbf{t}$, parallel to $\hat{\mathbf{t}}$ is given by $\mathbf{t}(t_A) = \mathrm{d}\mathbf{r}_F(t_A)/\mathrm{d}t_A$. Using this vector it follows that:

$$\hat{\mathbf{m}}(t_A) = \frac{1}{\sqrt{l_1^2 - l_2^2 \cos^2 t_A}} \left(\sqrt{l_1^2 - l_2^2} \cos t_A,\, l_1 \sin t_A, 0 \right)$$

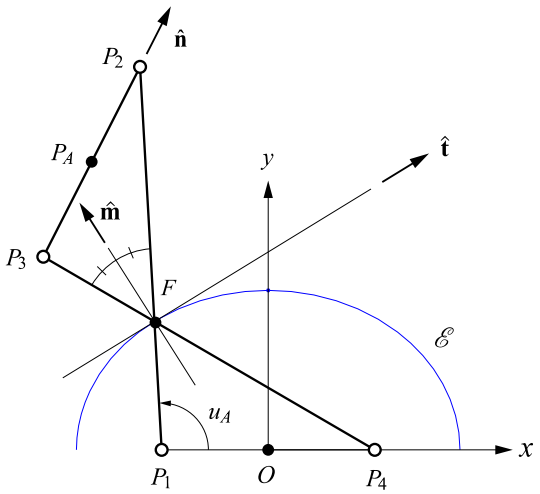

FIGURE 5.6: The intersection of antiparallel bars drawing an ellipse.

For this parametrization we consider $l_3 = l_2/2$, therefore, it follows that:

$$\begin{aligned}\mathbf{r}_{P_A}(t_A) &= \mathbf{r}_F(t_A) + \text{Ref}(\hat{\mathbf{m}}(t_A))(-\mathbf{r}_F(t_A)) \\ &= \frac{1}{l_1^2 - l_2^2\cos^2 t_A}\left((l_1^2 - l_2^2)l_1\cos t_A,\, l_1^2\sqrt{l_1^2 - l_2^2}\sin t_A,\, 0\right)\end{aligned}$$

The circle generated by joint $A5$ lies on a plane with normal $\hat{\mathbf{n}}$ and center at P_A, therefore:

$$\mathbf{r}_{E_A/P_A}(t_A, v_A) = l_1\left(\sin v_A \text{Ref}(\hat{\mathbf{m}}(t_A))(-\hat{\mathbf{j}}) + \cos v_A\hat{\mathbf{k}}\right)$$

Finally, $\mathbf{r}_{E_A}(t_A, v_A) = \mathbf{r}_{E_A/P_A}(t_A, v_A) + \mathbf{r}_{P_A}(t_A)$, which leads to:

$$\begin{aligned}\varsigma_A^2(t_A, v_A) := -l_1\Bigg(&\frac{(2K_3 l_1 \sin v_A \sin t_A + K_3^2)\cos t_A}{l_2^2\cos^2 t_A - l_1^2}, \\ &\frac{K_3 l_1 \sin t_A + ((l_2^2 - 2l_1^2)\cos^2 t_A + l_1^2)\sin v_A}{l_2^2\cos^2 t_A - l_1^2}, \cos v_A\Bigg)\end{aligned} \tag{5.5}$$

where $K_3 := \sqrt{l_1^2 - l_2^2}$, and $l_1 > l_2$ is considered.

Some remarks on the shape of $\mathcal{S}_A$

An example of the resulting surface $\mathcal{S}_A$ is shown in fig. 5.7. $\mathcal{S}_A$ features several self-intersections, some of these lying on the XZ plane. It is straightforward to prove that these self-intersections lead to conic singularities at its endings in a similar way to $\mathscr{L}_1$ and $\mathscr{L}_2$ in $\mathcal{B}$. These singularities turn out to have the same coordinates as the singularities of $\mathcal{B}$. In general, $\mathcal{S}_A$ is not symmetric with respect to the YZ plane, it becomes symmetric when $l_3 = l_2/2$, such case is shown in fig. 5.7. It is important to note that $\mathcal{S}_A \neq \text{im}(\text{Rot}(\hat{\mathbf{j}}, \pi/2)\varsigma_A^2(\mathbb{T}^2))$, therefore, while working in anti-parallel mode, the hybrid kinematic chain B generates a different surface $\mathcal{S}_B \neq \mathcal{S}_A$. $\mathcal{S}_B$ is a rotated version of $\mathcal{S}_A$, obtained after rotating $\mathcal{S}_A$ $\pi/2$ radians about the $y-$axis, hence, a parametrization for $\mathcal{S}_B$ is given by $\varsigma_B^2 := \text{Rot}(\hat{\mathbf{j}}, \pi/2)\varsigma_A^2(u_B, v_B)$.

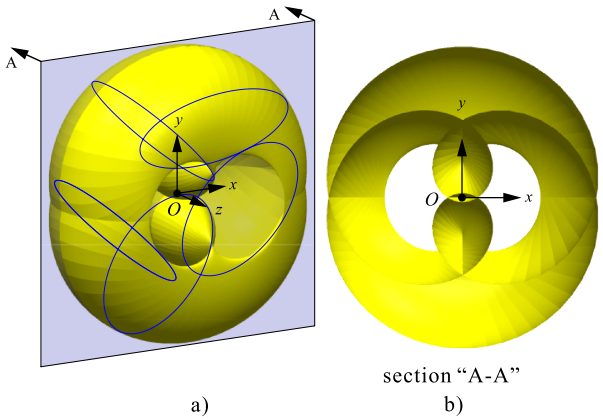

FIGURE 5.7: Surface $\mathcal{S}_A$ generated by the Bohemian dome generator in antiparallel mode, for a case with $l_3 = l_2/2$. a) Surface showing several circles drawn on it, b) cut view showing self-intersections

5.4 A kinematotropic linkage that generates coincident Bohemian domes

Following the idea in section 5.2, a kinematotropic mechanism can be built using the symmetric Bohemian dome by joining generators A and B in fig. 5.3 with a spherical pair. For example, if generator A generates $\mathcal{B}$ and generator B generates $\mathcal{S}_B$, E will move in $\mathcal{B} \cap \mathcal{S}_B$ which consist of several curves and the mechanism will have 1 DOF, while if both generators generate $\mathcal{B}$, E moves in $\mathcal{B} \cap \mathcal{B} = \mathcal{B}$ and the mechanism has 2 DOF.

The obtained linkage is shown in fig. 5.8, we consider $l_3 = l_2/2$ in both hybrid chains. Points E_A and E_B are joined through a spherical pair with center of rotation coincident with E, this spherical pair is represented by $\{\mathbf{S}_X, \mathbf{S}_Y, \mathbf{S}_Z\}$.

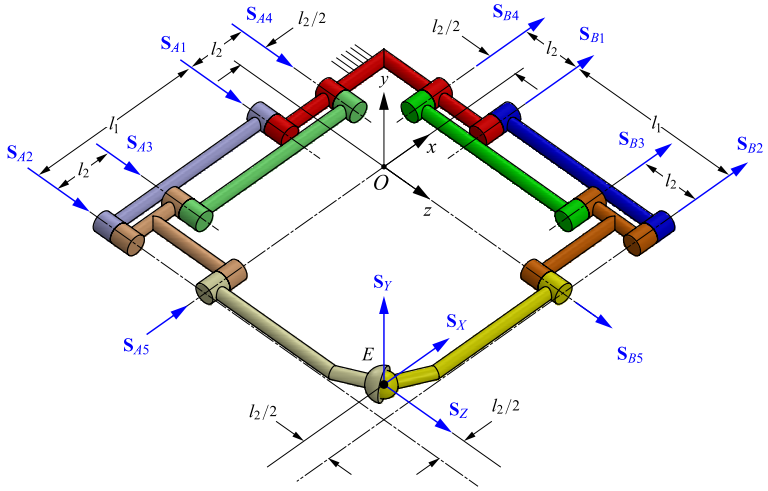

FIGURE 5.8: A kinematotropic linkage that generates coincident Bohemian domes.

It can be noted that the linkage presented in fig. 5.8 is similar to Wohlhart's queer-square mechanism [12], [15], [16]. However, such a linkage does not present the symmetry held by the linkage in fig. 5.8, as l_3 is different to $l_2/2$ in one of the generators. Nonetheless, the most important difference is that in the queer-square mechanism the spherical pair is not included, instead, $\mathbf{S}_{A5}$ is followed by another revolute joint with axis containing E and parallel to the $\mathbf{S}_{A5}$. In a similar manner, a revolute joint parallel to $\mathbf{S}_{B5}$ is inserted at E. Following

the method presented in [11] for spherical pair reduction, when both hybrid chains generate Bohemian domes the axis $\mathbf{S}_{A5}$ ($\mathbf{S}_{B5}$) does not change its orientation, therefore a revolute joint parallel to $\mathbf{S}_{A5}$ ($\mathbf{S}_{B5}$) can cancel this rotation and the mechanism is movable. Without loss of generality, now consider the case when A generates $\mathcal{B}$ and B generates $\mathcal{S}_B$, the rotation due to A can be canceled by a a revolute joint with axis parallel to $\mathbf{S}_{A5}$, on the other hand, B generates rotations parallel to the X-axis and another rotation about $\mathbf{S}_{B5}$, a revolute joint adjacent to $\mathbf{S}_{B5}$ cancels the second rotation, and the remaining first rotation is canceled by the revolute joint with axis parallel to $\mathbf{S}_{A5}$ which is always parallel to the X-axis while generating $\mathcal{B}$ and the linkage is movable again. Nevertheless, when both surfaces generate $\mathcal{S}_A$ and $\mathcal{S}_B$, generator A demands two revolute joints, with axes parallel to $\mathbf{S}_{A5}$ and the Z-axis, while B requires revolute joints with axes parallel to $\mathbf{S}_{B5}$ and the X-axis. It is concluded that the spherical pair is required to ensure motion in all the possible branches that can appear from the intersection of the surfaces. The queer-square linkage cannot work in the motion branches related to the curves in intersection $\mathcal{S}_A \cap \mathcal{S}_B$.

5.5 Relationship between the intersection of generated surfaces and motion branches

We now define $V \subset \mathbb{T}^{13}$ as the configuration space of this linkage, with a vector of joint variables defined as $\mathbf{q} := (u_A, q_{A2}, q_{A3}, q_{A4}, v_A, q_X, q_Y, q_Z, u_B, q_{B2}, q_{B3}, q_{B4}, v_B) \in V$. The linkage has 1 degree of freedom whenever $E(\mathbf{q})$ is confined to move in a curve since, ignoring conic singularities, σ_A and ς_A are bijections from $\mathbb{T}^2$ to $\mathcal{B}$ and $\mathcal{S}_A$, respectively, hence, no passive degrees of freedom are expected. Every curve in the intersection represents a 1-DOF assembly mode of the linkage, if these curves can be reached by $E(\mathbf{q})$ without disassembling the linkage, then the linkage can reconfigure from one motion branch to another. It is known that if the two surfaces are tangent to each other at a point then a bifurcation is expected at such point, however, intersection curves can present branching at points where one of the surfaces present self-intersection, in [30] it was proved that such points do not represent bifurcations in the configuration space.

In the cases when both surfaces present a conic singularity coinciding in the same point, and such conic singularity is not mapped by an isolated pair of parameters, it is known [11] that the linkage presents a 2-DOF motion with partitioned mobility [125]. On the other hand, if there is an isolated (regular) point in the intersection set, then the linkage has 0-DOF when assembled with E coincident at such point.

When the two kinematic chains generate the same surface the intersection is two-dimensional (in non-singular points) and the linkage has 2 degrees of freedom. However, an interesting phenomenon occurs in the self-intersections of such coincident surfaces. This results is presented in the following proposition:

Proposition 5.5.1 *When the two generators of a linkage designed using the surfaces intersection method generate the same surface, a 1-DOF branch appears as a consequence of the self-intersections of the surface.*

Proof: Taking as an example our case, $\mathcal{B}$, which is generated by two different parametrizations, σ_A and σ_B, let (u_A^1, v_A^1) and (u_A^2, v_A^2) ((u_B^1, V_B^1) and (u_B^2, v_B^2)) be two different points in $\mathbb{T}^2$ that map to the same point in the self-intersection $\mathscr{B} = \mathscr{L}_1 \cup \mathscr{L}_2$, each of these points correspond to two different configurations in V_A (V_B) that bring E_A (E_B) to the same point in $\mathscr{B}$. Then, $\sigma_A(u_A^1, v_A^1) = \sigma_A(u_A^2, v_A^2)$ and $\sigma_B(u_B^1, v_B^1) = \sigma_A(u_B^2, v_B^2)$, in addition, since $E_A = E_B$ in the closed-loop linkage, it follows that $\sigma_A(u_A^i, v_A^i) = \sigma_B(u_B^i, v_B^i)$, $i = 1, 2$. Let $\mathcal{N}_A^i$ ($\mathcal{N}_B^i$) be a

neighborhood around $(u_A^i, v_A^i) \in \mathbb{T}^2$ ($(u_B^i, v_B^i) \in \mathbb{T}^2$), $i = 1, 2$. W.l.o.g. let

$$\mathrm{im}(\sigma_A(\mathcal{N}_A^1)) \cap \mathrm{im}(\sigma_B(\mathcal{N}_B^1)) \not\subset \mathscr{B}, \tag{5.6}$$

then, if the configurations of the surface generators A and B correspond to (u_A^1, v_A^1) and (u_B^1, v_B^1), respectively, the local mobility is equal to 2, since E can move out the intersection through one of the sheets intersecting at $\mathscr{B}$. If (5.6) is not true, then $\mathrm{im}(\sigma_A(\mathcal{N}_A^1)) \cap \mathrm{im}(\sigma_B(\mathcal{N}_B^2)) \subset \mathscr{B}$, which means that if the configurations of the surface generators A and B correspond to (u_A^1, v_A^1) and (u_B^2, v_B^2), respectively, the local mobility is equal to 1, E is confined to move in $\mathscr{B}$ since one of the generators can take E through one of the sheets intersecting at $\mathscr{B}$, while the other generator can move E through the other sheet intersecting at $\mathscr{B}$.

This proves that in a linkage designed with the method of generated surfaces, in which both generators generate the same surface, an additional branch of motion appears in its configuration space for every self-intersection curve in the generated surface. ■

5.6 Intersection curves

Since we can describe the motion branches of the linkage by means of the intersection set of the generated surface, the nature of such intersection curves is analyzed in this section. Since both hybrid kinematic chains can generate two different surfaces, the following combinations have to be consider:

- Case 1: Generator A: $\mathcal{B}$. Generator B: $\mathcal{B}$
- Case 2: Generator A: $\mathcal{B}$. Generator B: $\mathcal{S}_B$
- Case 3: Generator A: $\mathcal{S}_A$. Generator B: $\mathcal{B}$
- Case 4: Generator A: $\mathcal{S}_A$. Generator B: $\mathcal{S}_B$

Case 1 is trivial since $\mathcal{B} \cap \mathcal{B} = \mathcal{B}$ and case 2 can be obtained from case 3 by $\mathcal{B} \cap \mathcal{S}_B = \{\mathrm{Rot}(\hat{\mathbf{j}}, \pi/2)\mathbf{r}_P : P \in \mathcal{S}_A \cap \mathcal{B}\}$. Therefore, it is only necessary to analyze cases 3 and 4. In every case the corresponding parametrizations are transformed into polynomial equations to setup a system of 3 equations in 4 unknowns. The system of polynomial equations is solved by Maple. In finding the intersections we consider $l_1 = 3$ and $l_2 = 1$.

5.6.1 Case 3: $\mathcal{S}_A \cap \mathcal{B}$

This case is shown in fig. 5.9. Taking Eqs. (5.1) and (5.4), consider $\mathbf{f}(u_A, v_A, u_B, v_B) := \varsigma_A^1(u_A, v_B) - \sigma_B(u_B, v_B)$. By solving $\mathbf{f}(u_A, v_A, u_B, v_B) = \mathbf{0}$ a total of 10 curves, $\mathscr{C}_{SB1}, \ldots, \mathscr{C}_{SB10}$, are identified:

$$
\begin{aligned}
\mathscr{C}_{SB1} &= \{3(-1,\sin v_A,\cos v_A)\,|\,v_A\in\mathbb{T}\},\\
\mathscr{C}_{SB2} &= \left\{P\in\mathbb{R}^3\,|\,\mathbf{r}_P=\mathrm{Ref}(\hat{\mathbf{i}})\mathbf{r}_Q, Q\in\mathscr{C}_{SB1}\right\},\\
\mathscr{C}_{SB3} &= \left\{\left(\frac{3\sqrt{2}(3\cos u_A-1)}{2K_4},\frac{9\sqrt{2}\left(\cos u_A-\frac{1}{3}\right)^2(\cos u_A-3)K_4}{2\sin u_A(3\cos u_A-5)K_6}+\right.\right.\\
&\quad \left.\left.\frac{-57\cos^3 u_A+131\cos^2 u_A-63\cos u_A+5}{2\sin u_A(3\cos u_A-5)K_6},-\frac{K_5}{2|\sin u_A|}\right)\,\middle|\,u_A\in\mathbb{T}\right\}\\
\mathscr{C}_{SB4} &= \left\{P\in\mathbb{R}^3\,|\,\mathbf{r}_P=\mathrm{Ref}(\hat{\mathbf{k}})\mathbf{r}_Q, Q\in\mathscr{C}_{SB3}\right\},\\
\mathscr{C}_{SB5} &= \left\{\left(\pm\frac{3\sqrt{1296\cos^4 v_B-1368\cos^2 v_B+73}}{36\cos^2 v_B-37},3\sin v_B-\frac{108\sin v_B}{36\sin^2 v_B+1},3\cos v_B\right)\right.\\
&\quad \left.\,\middle|\,v_B\in\left[\arccos\left(\frac{\sqrt{19-12\sqrt{2}}}{6}\right),\pi-\arccos\left(\frac{\sqrt{19-12\sqrt{2}}}{6}\right)\right]\right\}\\
\mathscr{C}_{SB6} &= \left\{P\in\mathbb{R}^3\,|\,\mathbf{r}_P=\mathrm{Ref}(\hat{\mathbf{j}})\mathbf{r}_Q, Q\in\mathscr{C}_{SB5}\right\},\\
\mathscr{C}_{SB7} &= \left\{\left(\frac{36\cos^2 v_B+3K_7-36}{36\cos^2 v_B-37},\frac{3\sin v_B(36\cos^2 v_B+6K_7-35)}{36\cos^2 v_B-37},3\cos v_B\right)\,\middle|\,v_B\in\mathbb{T}\right\}\\
\mathscr{C}_{SB8} &= \left\{P\in\mathbb{R}^3\,|\,\mathbf{r}_P=\mathrm{Ref}(\hat{\mathbf{i}})\mathbf{r}_Q, Q\in\mathscr{C}_{SB7}\right\},\\
\mathscr{C}_{SB9} &= \left\{\left(\frac{36\cos^2 v_B-3K_7-36}{36\cos^2 v_B-37},\frac{3\sin v_B(36\cos^2 v_B-6K_7-35)}{36\cos^2 v_B-37},3\cos v_B\right)\,\middle|\,v_B\in\mathbb{T}\right\}\\
\mathscr{C}_{SB10} &= \left\{P\in\mathbb{R}^3\,|\,\mathbf{r}_P=\mathrm{Ref}(\hat{\mathbf{i}})\mathbf{r}_Q, Q\in\mathscr{C}_{SB9}\right\},
\end{aligned}
\tag{5.7}
$$

where,

$$
\begin{aligned}
K_4 &:= \sqrt{5-3\cos(u_A)},\\
K_5 &:= \sqrt{12\cos u_A-37\cos^2 u_A-2\sqrt{2}(\cos u_A-3)K_1+17},\\
K_6 &:= \sqrt{\cos^2 u_A+(2\sqrt{2}K_1\cos u_A-12)-6\sqrt{2}K_1+19},\\
K_7 &:= \sqrt{33-32\cos^2 v_B}
\end{aligned}
$$

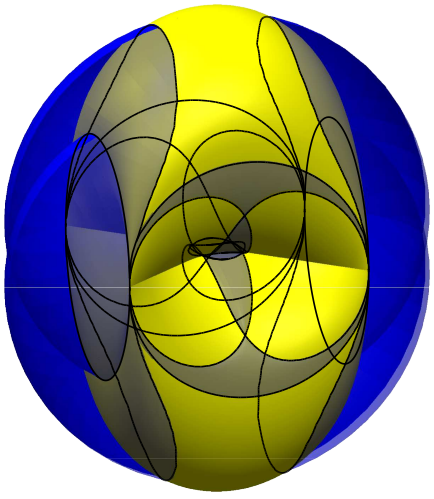

FIGURE 5.9: Case 3: $\mathcal{S}_A\cap\mathcal{B}$.

The intersection curves are shown in fig. 5.10, where they were plotted in SolidWorks using the intersection curve tool, parametric equations (5.7) can be plotted to obtain the same result. It can be seen that four curves are always intersecting in points $Q_1,\ldots,Q_4$, which correspond to the points $(3,0,3)$, $(-3,0,3)$, $(3,0,-3)$ and $(-3,0,-3)$. From Eq. (5.7) it can be concluded that although $\mathscr{C}_{SB3}$ and $\mathscr{C}_{SB4}$ look like circles in fig. 5.10, they are non-planar curves, whilst $\mathscr{C}_{SB1}$ and $\mathscr{C}_{SB2}$ are perfect circles lying on planes parallel to the YZ.

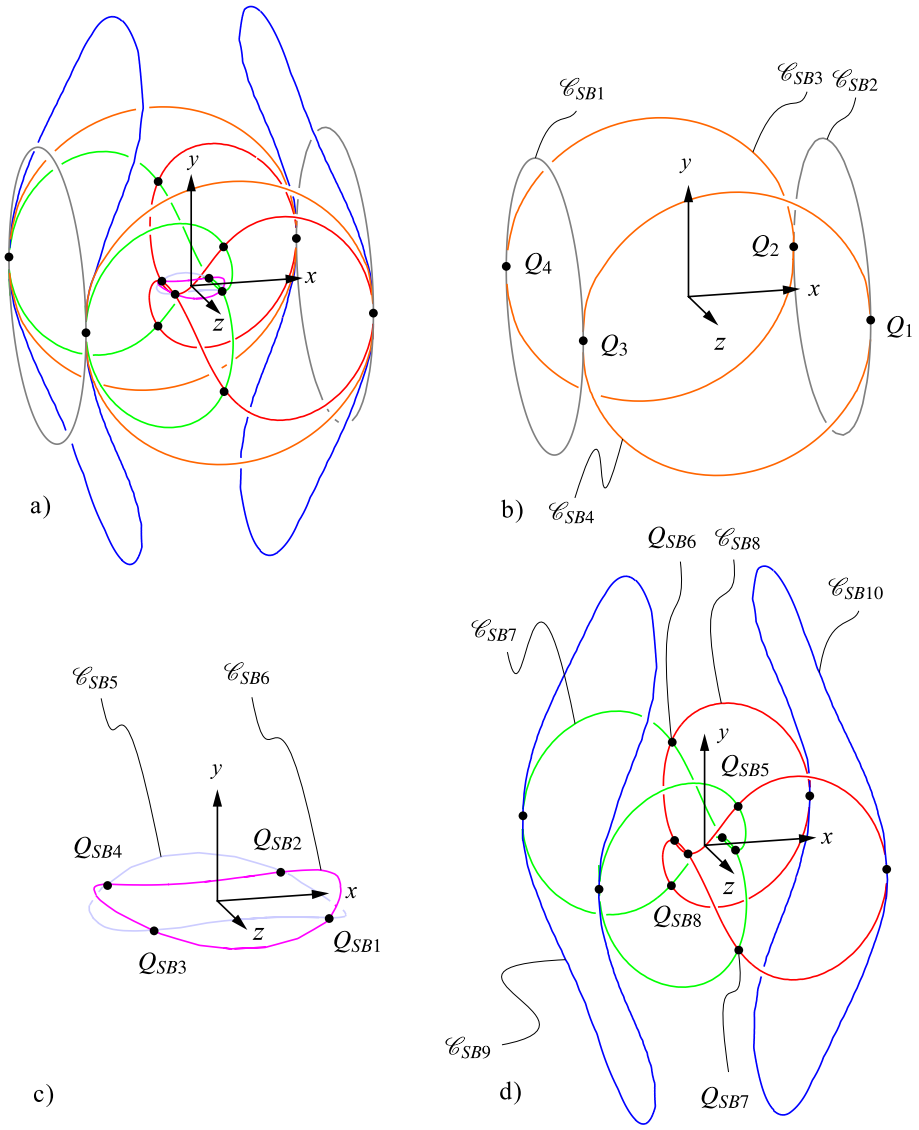

FIGURE 5.10: Intersection curves obtained in SolidWorks in case 3: a) whole set of curves, b) curves $SB1,\ldots,SB4$, c) curves $SB5$ and $SB6$, d) $SB7,\ldots,SB10$

The ten curves $\mathscr{C}_{BSi}\subset\mathbb{R}^3$, $i=1,\ldots,10$, corresponding to case 2 are easily obtained from parametrizations in Eq. (5.7) by:

$$\mathscr{C}_{BSi}=\{P\in\mathbb{R}^3\,|\,\mathbf{r}_P=\mathrm{Rot}(\hat{\mathbf{j}},\pi/2)\mathbf{r}_Q,\,Q\in\mathscr{C}_{SBi}\},\,i=1,\ldots,10$$

5.6.2 Case 4: $\mathcal{S}_A\cap\mathcal{S}_B$

This case is shown in fig. 5.11. Taking Eq. (5.4), consider $\mathbf{f}(u_A,v_A,u_B,v_B):=\varsigma_A^1(u_A,v_A)-\mathrm{Rot}(\hat{\mathbf{j}},\pi/2)\varsigma_A^1(u_B,v_B)$. However, in this case $\mathbf{f}$ is a much more complicated expression. An

alternative method will be applied.

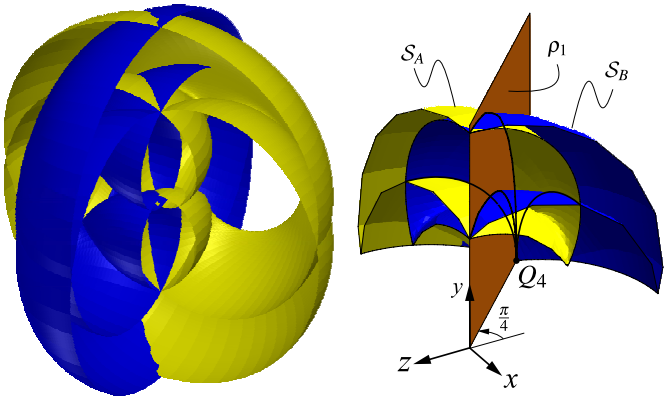

FIGURE 5.11: a) Case 4: $\mathcal{S}_A \cap \mathcal{S}_B$. b) Four curves meeting at Q_4 in case 4.

Observe that $\text{Rot}(\hat{\mathbf{j}}, \pi/2) = \text{Ref}((\sqrt{2}/2, 0, \sqrt{2}/2)) = \text{Ref}((-\sqrt{2}/2, 0, \sqrt{2}/2))$, therefore $\mathcal{S}_B$ can also be obtained by mirroring $\mathcal{S}_A$ through any of the two planes that contain the Y axis and make a $\pi/4$ angle with the XY plane. Moreover, it is known, from the analysis made in Section 2, that these surfaces have self-intersections with end at points Q_i, $i = 1, \ldots, 4$, therefore it is expected that a total of 4 sheets meet at the Q_i points. One part of the intersection happens between sheets from a surface and their mirrored versions and, therefore, it is expected that their intersection is lying on the reflection plane containing the analyzed Q_i point. Hence, this part of the intersection can be computed by intersecting $\mathcal{S}_A$ with planes, ρ_1 and ρ_2, with normals $(\sqrt{2}/2, 0, \sqrt{2}/2)$ and $(-\sqrt{2}/2, 0, \sqrt{2}/2)$, respectively. However, another part of the intersection corresponds to a sheet from a surface and a sheet which is not the mirror of the other. This second part of the intersection is not contained in ρ_1 or ρ_2. Using the alternative parametrization for $\mathcal{S}_A$ and $\mathcal{S}_B$ in Eq. (5.5) it is possible to compute this part of the intersection, however the resulting expression is too long to be presented in this chapter. It is found that such part of the intersection is composed of four curves intersecting at the points Q_i. Fig. 5.11b shows the expected 4 curves passing through Q_4, two of these curves lie on ρ_1 and the other two are spatial curves corresponding to non-mirrored sheets intersections.

Since $\mathcal{S}_A$ is symmetric with respect to the 3 planes spanned by the axes of the coordinate system, it follows that $\mathcal{S}_A \cap \rho_2 = \{P \in \mathbb{R}^3 : \mathbf{r}_P = \text{Rot}(\hat{\mathbf{j}}, \pi/2)\mathbf{r}_Q, Q \in \mathcal{S}_A \cap \rho_1\}$, and it is only necessary to compute $\mathcal{S}_A \cap \rho_1$. After solving the corresponding system of equations, the following two curves are found:

$$\begin{aligned} \mathscr{C}_{SS1} &= \left\{ \text{Rot}\left(\hat{\mathbf{j}}, \frac{\pi}{4}\right) \left(3\sqrt{2}\frac{K_8 - K_9}{K_{10}}, \frac{K_{11} - K_{12}}{K_{13}}, 0 \right) \middle| u_A \in \mathbb{T} \right\} \\ \mathscr{C}_{SS2} &= \left\{ \text{Rot}\left(\hat{\mathbf{j}}, \frac{\pi}{4}\right) \left(3\sqrt{2}\frac{K_8 + K_9}{K_{10}}, \frac{K_{11} + K_{12}}{K_{13}}, 0 \right) \middle| u_A \in \mathbb{T} \right\} \end{aligned} \tag{5.8}$$

where,

$$\begin{aligned}
K_8 &:= 729\cos^7 u_A - 3159\cos^6 u_A + 1620\cos^5 u_A + 4860\cos^4 u_A - 2115\cos^3 u_A \\
&\quad -2211\cos^2 u_A - 746\cos u_A + 510, \\
K_9 &:= 3(3\cos u_A - 1)\sin^2 u_A K_{14} K_{15} \\
K_{10} &:= 13122\cos^8 u_A - 32076\cos^6 u_A + 20250\cos^4 u_A - 3096\cos^2 u_A + 2312 \\
K_{11} &:= 19683\sin^2 u_A \left(\cos u_A - \frac{1}{3}\right)(\cos u_A - 3)\left(\cos^4 u_A + \frac{2}{3}\cos^3 u_A - \cos^2 u_A \right. \\
&\quad \left. -\frac{28}{27}\cos u_A - \frac{34}{81}\right)\left(\cos^2 u_A - \cos u_A + \frac{2}{3}\right) \\
K_{12} &:= \sin^2 u_A (3\cos u_A - 1)(27\cos^2 u_A - 9\cos u_A - 12) K_{14} K_{15} \\
K_{13} &:= 2\sin u_A (3\cos u_A - 1)(81\cos^4 u_A - 54\cos^3 u_A - 81\cos^2 u_A + 84\cos u_A - 34) K_{14}
\end{aligned}$$

where,

$$\begin{aligned}
K_{14} &:= 81\cos^4 u_A + 54\cos^3 u_A - 81\cos^2 u_A - 84\cos u_A - 34 \\
K_{15} &:= \sqrt{333\cos^2 u_A - 276\cos u_A + 127}
\end{aligned}$$

Parametrizations for curves lying on ρ_2 are then obtained using Eq. (5.8):

$$\begin{aligned}
\mathscr{C}_{SS3} &= \left\{ \mathrm{Rot}\left(\hat{\mathbf{j}}, \frac{3}{4}\pi\right)\left(3\sqrt{2}\frac{K_8 - K_9}{K_{10}}, \frac{K_{11} - K_{12}}{K_{13}}, 0\right) \middle| u_A \in \mathbb{T} \right\} \\
\mathscr{C}_{SS4} &= \left\{ \mathrm{Rot}\left(\hat{\mathbf{j}}, \frac{3}{4}\pi\right)\left(3\sqrt{2}\frac{K_8 + K_9}{K_{10}}, \frac{K_{11} + K_{12}}{K_{13}}, 0\right) \middle| u_A \in \mathbb{T} \right\}
\end{aligned}$$

Let $\mathscr{C}_{SS5}, \ldots, \mathscr{C}_{SS8}$ be the four curves that are not lying on ρ_1 or ρ_2 and whose parametrizations are not presented here due to its length, then, fig. 5.12, shows all the 8 curves of intersection case 4, obtained from the intersection of surfaces tool in SolidWorks. A total of 8 curves are obtained from the intersection of case 4.

5.7 Summary of motion branches

Since the intersection sets between the different generated surfaces have been described, it is possible to make a summary of all the motion branches of the linkage. However, note that curves $\mathscr{C}_{BS1}$, $\mathscr{C}_{BS2}$, $\mathscr{C}_{SB1}$ and $\mathscr{C}_{SB2}$ are circles described by a 4-bar loop in parallel mode and the other inactive in its flattened configuration, since in any configuration $\mathbf{q}$ such that $E(\mathbf{q})$ is in any of these four circles, the linkage can escape to the 2-DOF branch V_{BB1} since the inactive loop can move to parallelogram mode, therefore $\mathbf{q} \in V_{BB1}$ and there is no branch of motion related to these circles, the configurations that map to them are just curves in the 2-DOF manifold V_{BB1}. All other curves are related to motion branches in V:

- **Case 1:** Generator A: $\mathcal{B}$. Generator B: $\mathcal{B}$. A 2-DOF branch of motion, V_{BB1}, and two 1-DOF branches, V_{BB2} and V_{BB3}, which are related to the two self-intersections $\mathscr{B}_1$ and $\mathscr{B}_2$.
- **Case 2:** Generator A: $\mathcal{B}$. Generator B: $\mathcal{S}_B$. Eight 1-DOF branches of motion, $V_{BS3}, \ldots,$ V_{BS10}, each related to the eight curves $\mathscr{C}_{BS3}, \ldots, \mathscr{C}_{BS10}$.
- **Case 3:** Generator A: $\mathcal{S}_A$. Generator B: $\mathcal{B}$. Eight 1-DOF branches of motion, $V_{SB3}, \ldots,$ V_{SB10}, each related to the ten curves $\mathscr{C}_{SB3}, \ldots, \mathscr{C}_{SB10}$.

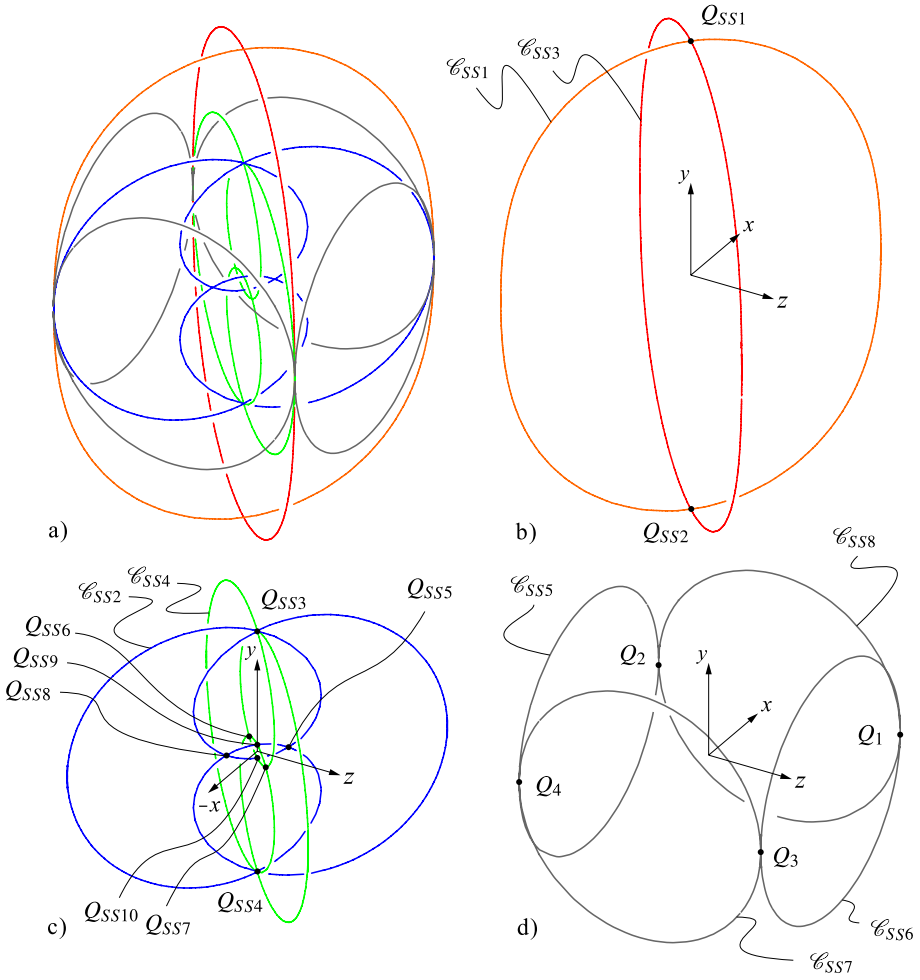

FIGURE 5.12: Intersection curves obtained in SolidWorks for case 4: a) whole set of curves, b) curves $SS1$ and $SS3$, c) curves $SS2$ and $SS4$, d) curves $SS5, \ldots, SS8$

- **Case 4:** Generator A: $\mathcal{S}_A$. Generator B: $\mathcal{S}_B$. Eight 1-DOF branches of motion, $V_{SS1},\ldots,$ V_{SS8}, each related to the ten curves $\mathscr{C}_{SS1},\ldots,\mathscr{C}_{SS8}$.

A total of 27 branches of motion are detected. The linkage is shown in several configurations belonging to different branches in figures 5.13 to 5.16. In figures 5.14 and 5.16 it can be seen that motion branches V_{SS7} and V_{BS4} are very similar. However, although apparently 4-bar loop in generator A is in flattened configuration in both branches, it is not and all joints are active. While in V_{BS4} the angle between the input and the output bars of the 4-bar loop is zero, in V_{SS7} there is a small angle, this agrees with the expected parallel and antiparallel modes of generator A in V_{BS4} and V_{SS7}, respectively.

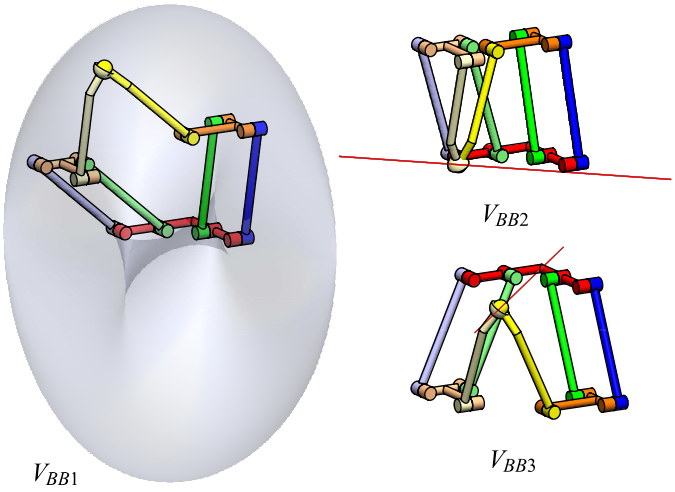

FIGURE 5.13: The linkage in different configurations belonging to three branches of the Case 1.

5.8 Singularities in the configuration space

Taking information from the intersection curves and the surfaces it is possible to detect the singularities in V and determine how the 27 components of V are connected between them through these singularities. As previously discussed, we know that 4 flattened configurations of the linkage ($u_A \in \{0,\pi\}$, $u_B \in \{0,\pi\}$) represent singular configurations since the hybrid kinematic chains can switch the generated surface from $\mathcal{B}$ to $\mathcal{S}_A$ or $\mathcal{S}_B$. Let these four points in V be $\mathbf{q}_1,\ldots,\mathbf{q}_4$, so that $E(\mathbf{q}_i) = Q_i$, $i = 1,\ldots,4$, as shown in figures 5.10 and 5.12, $Q_1 = (3,0,3)$, $Q_2 = (3,0,-3)$, $Q_3 = (-3,0,3)$ and $Q_4 = (-3,0,-3)$. Since such points are contained in all the surfaces and since the switch between generated surfaces happens when E coincides with these points, every curve found in all the intersection sets that intersects any of these points can be reached by E, and thus the corresponding components of V are intersecting at the flattened configurations.

5.8.1 Singularities occurring in case 1

In case 1, since self intersections $\mathscr{L}_1$ and $\mathscr{L}_2$ have ends at the Q_i points, the linkage can enter the 2-DOF branch V_{BB1} from such configurations. It follows that $V_{BB1} \cap V_{BB2} = \{\mathbf{q}_1,\mathbf{q}_4\}$ and $V_{BB1} \cap V_{BB3} = \{\mathbf{q}_2,\mathbf{q}_3\}$. In addition, $\mathscr{L}_1 \cap \mathscr{L}_2 = \{O\}$ but since there are two self-intersections meeting at O, there are actually two configurations, $\mathbf{q}_{O1}$ and $\mathbf{q}_{O2}$, such that $E(\mathbf{q}_{O1}) = E(\mathbf{q}_{O2}) = O$, therefore $V_{BB2} \cap V_{BB3} = \{\mathbf{q}_{O1},\mathbf{q}_{O2}\}$.

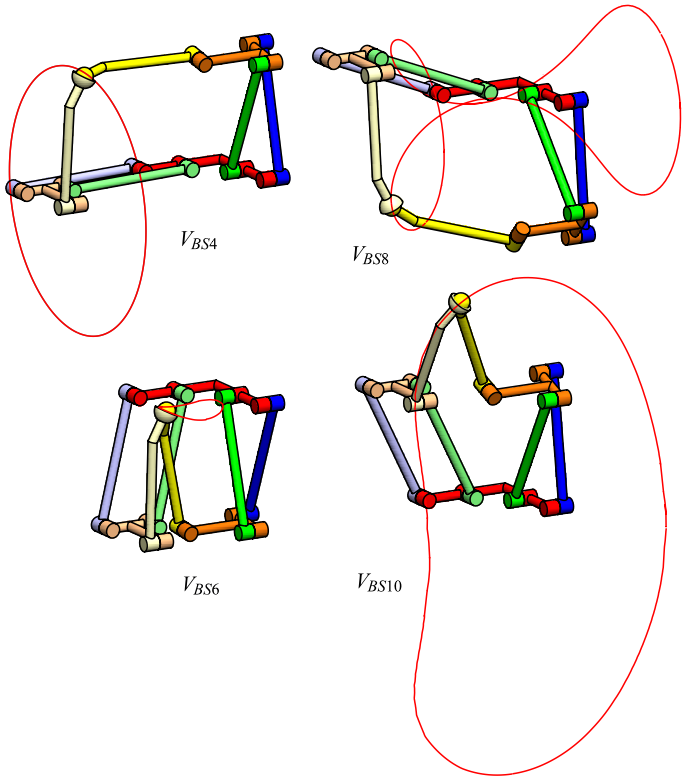

FIGURE 5.14: The linkage in different configurations belonging to four branches of the Case 2.

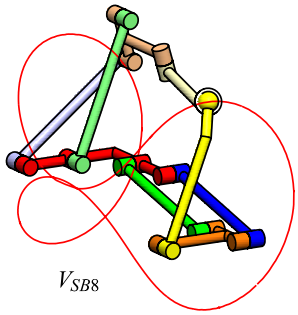

FIGURE 5.15: The linkage in a configurations belonging to V_{SB8} in Case 3.

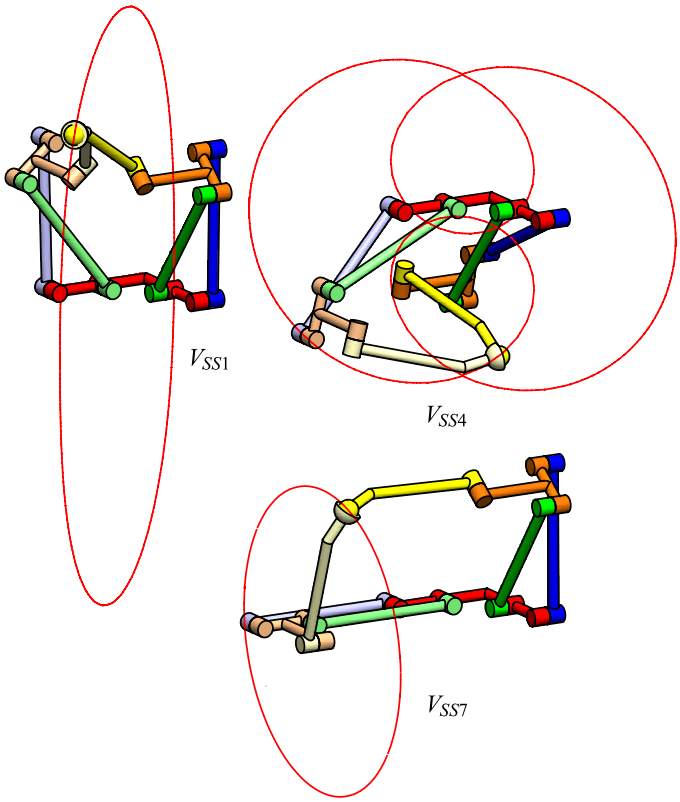

FIGURE 5.16: The linkage in different configurations belonging to three branches of the Case 4.

5.8.2 Singularities occurring in cases 2 and 3

For cases 2 and 3, the analysis is carried out considering only case 3 and the results can be extended to case 2 with rotated versions of the points in the intersection. Refer to fig. 5.10 where the points of intersection between curves are shown. Using the parametrizations in Eq. (5.7), it is found that $\mathscr{C}_{SB5} \cap \mathscr{C}_{SB6} = \{Q_{SB1}, \ldots, Q_{SB4}\} = \{(1/2, 0, 1/2), (1/2, 0, -1/2), (-1/2,\ 0, 1/2), (-1/2, 0, -1/2)\}$, it is also confirmed that such points correspond to the self-crossings of $\mathscr{C}_{SB7}$ and $\mathscr{C}_{SB8}$. Due to symmetry, we consider only one point, $Q_{SB3} = (-1/2, 0, 1/2)$, it is found that $\varsigma_A^1(\text{atan}(4\sqrt{35}/13),\ \arccos(1/6)) = Q_{SB3}$ and that $\sigma_B(\pi - \text{atan}(1/6), -\text{acos}(1/6)) = Q_{SB3}$. The normal to any surface with parametrization $\zeta : U \to \mathbb{R}^3$, at $(u, v) = (p_u, p_v) \in U \subset \mathbb{R}^2$, is obtained by:

$$\mathbf{n}_\zeta(u, v) := \left.\frac{\partial \zeta}{\partial u}\right|_{(u,v)=(p_u,p_v)} \times \left.\frac{\partial \zeta}{\partial v}\right|_{(u,v)=(p_u,p_v)} \tag{5.9}$$

If $\mathcal{B}$ and $\mathcal{S}_A$ are tangent to each other at a point $P = \varsigma_A(p_{u_A}, p_{v_A}) = \sigma_B(p_{u_B}, p_{v_B})$, then $\mathbf{n}_{\varsigma_A^1}(p_{u_A}, p_{v_A}) \times \mathbf{n}_{\sigma_B}(p_{u_B}, p_{v_B}) = \mathbf{0}$. Using Eq. (5.9), it is found that:

$$\mathbf{n}_{\varsigma_A^1}\left(\arctan\left(\frac{4\sqrt{35}}{13}\right), \arccos\left(\frac{1}{6}\right)\right) = \left(\frac{13\sqrt{35}}{16}, \frac{35}{4}, -\frac{9\sqrt{35}}{32}\right),$$

$$\mathbf{n}_{\sigma_B}\left(\pi-\arctan\left(\frac{1}{6}\right),-\arccos\left(\frac{1}{6}\right)\right) = \left(-\frac{\sqrt{35}}{4},\frac{35}{4},-\frac{9\sqrt{35}}{4}\right),$$
$$\left(\frac{13\sqrt{35}}{16},\frac{35}{4},-\frac{9\sqrt{35}}{32}\right) \times \left(-\frac{\sqrt{35}}{4},\frac{35}{4},-\frac{9\sqrt{35}}{4}\right) \neq \mathbf{0}$$

Therefore, the point presents self-intersection in some of the two surfaces and thus it is not mapped by a singularity in V. Due to symmetry, it is concluded that V is perfectly regular at $\mathbf{q}_{SB1},\ldots,\mathbf{q}_{SB4}$. This also means that, although $\mathscr{C}_{SB5}\cap\mathscr{C}_{SB5}\neq\emptyset$, it is not possible to move E from one curve to the other without disassembling the linkage and $V_{SB5}\cap V_{SB6}=\emptyset$. In fact, although these two curves intersect $\mathscr{C}_{SB7}$ and $\mathscr{C}_{SB8}$, V_{SB5} and V_{SB6} are isolated regions of V.

In a similar manner, intersecting points $Q_{SB5},\ldots,Q_{SB8}=\mathscr{C}_{SB7}\cap\mathscr{C}_{SB8}$, are tested for self-intersection presence. The points are found to have coordinates: $Q_{SB5}=(0,3/2,3\sqrt{3}/2)$, $Q_{SB6}=(0,3/2,-3\sqrt{3}/2)$, $Q_{SB7}=(0,-3/2,3\sqrt{3}/2)$ and $Q_{SB8}=(0,-3/2,-3\sqrt{3}/2)$. Following the same procedure it is found that the normals to the surfaces at such points are not parallel and thus, the points present self-intersection in some surface. It is then concluded that V is regular at $\mathbf{q}_{SB5},\ldots,\mathbf{q}_{SB5}$ and $V_{SB7}\cap V_{SB8}=\emptyset$.

As shown in fig. 5.10, $\mathscr{C}_{SB3},\mathscr{C}_{SB4},\mathscr{C}_{SB7},\ldots,\mathscr{C}_{SB10}$ are communicated through $Q_1,\ldots,Q_4$. in every of these points 4 curves are intersecting only in this Case 3. It can be concluded that, for example for Q_1, $V_{SB4}\cap V_{SB8}\cap V_{SB10}=\{\mathbf{q}_1\}$. In addition, it is easy to prove that the unit tangent vectors to $\mathscr{C}_{SB3},\mathscr{C}_{SB4},\mathscr{C}_{SB7},\ldots,\mathscr{C}_{SB10}$ at any of these four points are always parallel to each other and equal to $\hat{\mathbf{j}}$, thus all the curves are tangent to each other at the intersection points.

5.8.3 Singularities occurring in case 4

For case 4 refer to fig. 5.12 where the points of intersection between curves are shown. Using the parametrizations in Eq. (5.8) it is found that $\{Q_{SS1},Q_{SS2}\}=\mathscr{C}_{SS1}\cap\mathscr{C}_{SS3}$ are given by $(0,\pm(2\sqrt{2}+3),0)$. For example, for the positive case $\varsigma_A^1(\arccos(1/3),3\pi/2)=(0,2\sqrt{2}+3,0)$, where $\mathbf{n}_{\varsigma_A^1}(\arccos(1/3),3\pi/2)||\hat{\mathbf{k}}$, due to the symmetry of the surface it is impossible to have a second normal vector at the same point and, hence, the surface is regular at Q_{SS1} and Q_{SS2}. It is concluded that $V_{SS1}\cap V_{SS3}=\{\mathbf{q}_{SS1},\mathbf{q}_{SS2}\}$.

In the case of curves $\mathscr{C}_{SS2}$ and $\mathscr{C}_{SS4}$, let $\alpha:\mathbb{T}\to\mathscr{C}_{SS2}$ be the parametrization of $\mathscr{C}_{SS2}$ used in Eq. (5.8). It is found that $Q_{SS5}=(1/2,0,1/2)$ and $Q_{SS8}=(-1/2,0,-1/2)$ and that $\alpha(\arctan(\sqrt{35}))=\alpha(-\arctan(\sqrt{35}))=Q_{SS5}$. Since there are two different values of u_A that map to Q_{SS5}, such point presents self-intersection in both surfaces. Hence, V is regular in $\mathbf{q}_{SS5},\ldots,\mathbf{q}_{SS8}$. In a similar manner, it is found that $Q_{SS3}=(0,3,0)$ and $Q_{SS4}=(0,-3,0)$ and that:

$$Q_{SS3}=\alpha\left(\arctan\left(\frac{18-2\sqrt{7}}{3+12\sqrt{7}}\right)\right)=\alpha\left(\arctan\left(\frac{18-2\sqrt{7}}{3+12\sqrt{7}}\right)+\pi\right)$$

Since there are two different values of u_A that map to Q_{SS3}, such point presents self-intersection in both surfaces. Hence, V is regular in $\mathbf{q}_{SS3}$ and $\mathbf{q}_{SS4}$. However, for $Q_{SS9}=(0,3-2\sqrt{2},0)$ and $Q_{SS10}=(0,-3+2\sqrt{2},0)$, one only value of u_A for each point is found so that $\alpha(-\arctan(2\sqrt{2}))=Q_{SS9}$ and $\alpha(\text{atan}(2\sqrt{2}))=Q_{SS10}$, it is also found that the normal at such points are parallel to $\hat{\mathbf{k}}$, therefore Q_{SS9} and Q_{SS10} are regular in $\mathcal{S}_A$ and $\mathcal{S}_B$ and are mapped by singularities in V, such that $V_{SS2}\cap V_{SS4}=\{\mathbf{q}_{SS9},\mathbf{q}_{SS10}\}$.

As shown in fig. 5.12, in each of the points $Q_1,\ldots,Q_4$ four different curves are intersecting only in case 4, therefore case 4 contributes with 4 branches of motion intersecting in

the flattened configurations of the linkage. For example, for Q_1, we have $V_{SS1} \cap V_{SS2} \cap V_{SS6} \cap V_{SS8} = \{\mathbf{q}_1\}$.

Fig. 5.17 shows the connections between the 27 motion branches through the ten singular configurations. It can be seen that in every configuration $\mathbf{q}_1, \ldots, \mathbf{q}_4$ a total of 12 branches are intersecting, therefore, if the mechanism is in any of these four singular configurations, it can escape to 12 different branches of motion.

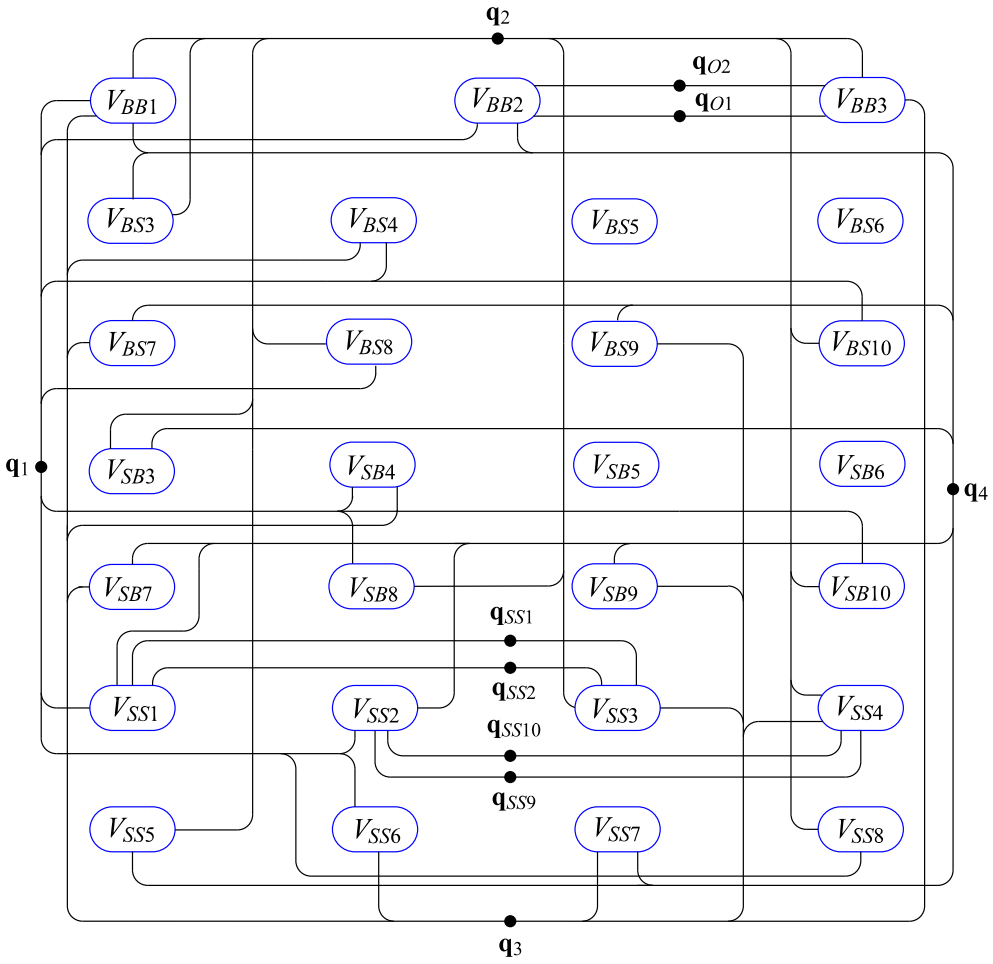

FIGURE 5.17: Connections between motion branches through singular configurations of the linkage.

5.9 Chapter conclusions

A new method for the design of linkages that change its number of finite degrees of freedom was presented. The method is based on the use of 2-DOF kinematic chains that generate more than one surface. The property of double parametrization in a kind of Bohemian dome was used for applying this new method. This was possible since both parametrizations are based on the translation of a circle through another circle. The change in the number of degrees of freedom is a consequence of a case of intersection where both generators draw the same surface. The two hybrid kinematic chains that generate this Bohemian dome also generate a different surface which was described in this chapter. The switch between surfaces gave a new way of reconfiguration which is different from the typical tangency between surfaces, a phenomenon that also appears in this linkage.

The designed new linkage is in a way similar to Wohlhart's queer-square linkage whose mobility and reconfiguration can be explained with the theory developed in this chapter, but has more motion branches than the linkage version of Wohlhart's queer-square analyzed by Qin et al. in [15]. In addition, it was proved that the queer-square linkage can work in three of the four cases of surfaces intersections presented in this chapter.

Chapter 6

A Kinematotropic parallel manipulator with three motion branches, each of different mobility

In the previous chapter it was shown that linkages that can change the surface they generate can be used to design kinematotropic mechanisms. Using a similar approach, in this chapter a reconfigurable parallel manipulator whose number of finite degrees of freedom are constant is added an extra surface generator to obtain a kinematotropic parallel manipulator.

The configuration space of most of the reported kinematotropic mechanisms consists of several subvarieties whose dimension varies between two values. Therefore, most of the reported kinematotropic mechanisms can change their number of degrees of freedom between two values only. The parallel manipulator presented in this chapter has a configuration space with at least three subvarieties of different dimension. These subvarieties intersect at at least two singular points, which allow the mechanism to reconfigure between the three branches without disassembling it and, therefore, the proposed mechanism can change its number of degrees of freedom between three values. The mobility of this mechanism is proven in this chapter by means of geometry and the use of the kinematic tangent cone to the configuration space at both singular configurations.

This chapter is based on the conference publication:

[38] P.C. López-Custodio, A. Müller and J.S. Dai, "A Kinematotropic Parallel Mechanism Reconfiguring Between Three Motion Branches of Different Mobility," In: Uhl T. (eds) *Advances in Mechanism and Machine Science. IFToMM WC 2019. Mechanisms and Machine Science*, vol 73. Springer, Cham. 2611-2620, (2019) DOI:10.1007/978-3-030-20131-9_258.

6.1 Background

Kinematotropic parallel mechanisms (or parallel kinematic machines, PKMs) are of particular interest among spatial kinematotropic mechanisms. These have been investigated since the Wren platform was presented by Wohlhart [12] as a typical example of kinematotropic mechanism. Other examples of reconfigurable and kinematotropic parallel mechanisms have been presented in recent years [14], [72], while mobility-variable metamorphic parallel mechanisms have also been presented [23], [76], [126].

Nevertheless, all these publications deal with kinematotropic mechanisms that can shift between two different numbers of degrees of freedom, i.e., even though they may present many branches of motion, the dimension of these vary only between two values. Examples of kinematotropic mechanisms with more than two different number of degrees of freedom are mostly reported in degenerated cases of more general mechanisms. For example, it is known

that a degenerate case of Wunderlich linkage, in which all bars have the same length, can change between 1, 2 and 3 degrees of freedom, being the 1- and 2-dimensional branches the typical ones displayed by any Wunderlich mechanism and the 3-dimensional one occurring when all links overlap [81]. However, noteworthy is the case of Wohlhart's "star cube" [17], [34], which stands out for having branches of dimension 1, 2 and 3 among its tens of branches of motion. In this chapter a fully parallel mechanism with three branches of motion each of different dimension is presented. Denote by R, C, U and G, a revolute joint, cylindrical joint, universal joint and a RRR chain where all the joint axes are parallel, respectively. The 3-RGR-1-CU parallel mechanism proposed here can change from having 1 DOF, to 2 DOF and 3 DOF, DOF standing for degrees of freedom.

This chapter is organized as follows: In Section 6.2 the geometry of the 3-RGR-1-CU parallel mechanism is explained, in Section 6.3 the motion of the moving platform when leg CU is removed is studied, these results are used in Section 6.4 to investigate the motion of the whole kinematotropic 3-RGR-1-CU mechanism. In Section 6.5 the bifurcations are proved by means of tangent cone analysis. Finally, in Section 6.6 conclusions are presented.

6.2 Geometry of the parallel mechanism

The parallel mechanism to be analyzed is presented in fig. 6.1. The mechanism consists of a fixed platform connected to a moving platform by means of four legs, labeled in fig. 6.1 as leg 1, leg 2, leg 3 and leg C. Legs 1, 2 and 3 are identical.

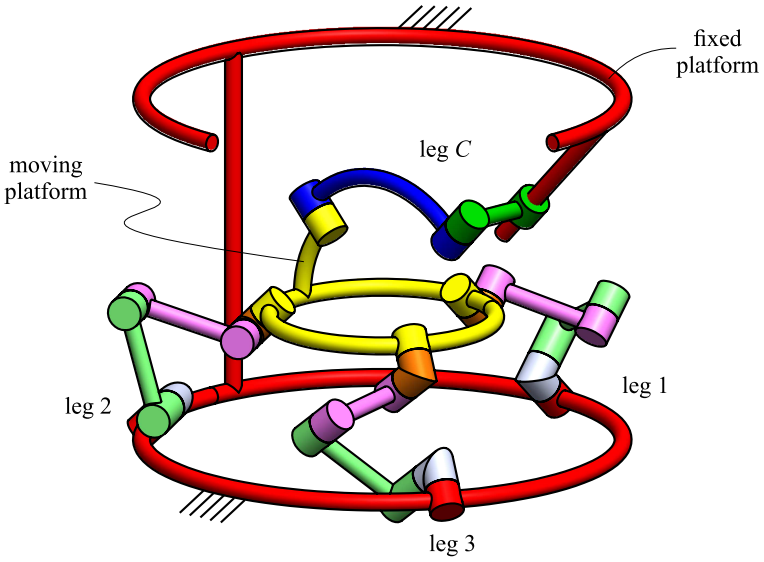

FIGURE 6.1: The kinematotropic parallel mechanism to be analyzed.

Fig. 6.2 shows leg 1 in more detail, the relationship between the joints in this leg are also applied to legs 2 and 3. Leg i ($i = 1,2,3$) consist of five R joints, labeled as $i1,\ldots,i5$. In this chapter R, P and C stand for revolute, prismatic and cylindrical joints, respectively. Axes $\mathbf{S}_{i1}$ and $\mathbf{S}_{i2}$ intersect at point A_i and are perpendicular to each other, forming a U joint. Similarly, $\mathbf{S}_{i4}$ and $\mathbf{S}_{i5}$ intersect perpendicularly at point B_i. In addition, the adjacent axes $\mathbf{S}_{i2}$, $\mathbf{S}_{i3}$ and $\mathbf{S}_{i4}$ are parallel, constituting a mechanical generator of the group of general planar displacements, denoted in this chapter as G. It can also be seen in fig. 6.2 that axes $\mathbf{S}_{i5}$ intersect at point P of the moving platform.

As shown in fig. 6.2 points A_i create an equilateral triangle in the base of the parallel mechanism. Similarly, in the moving platform, points B_i are the nodes of an equilateral triangle. A fixed coordinate system is defined with origin at the center of the triangle $A_1A_2A_3$,

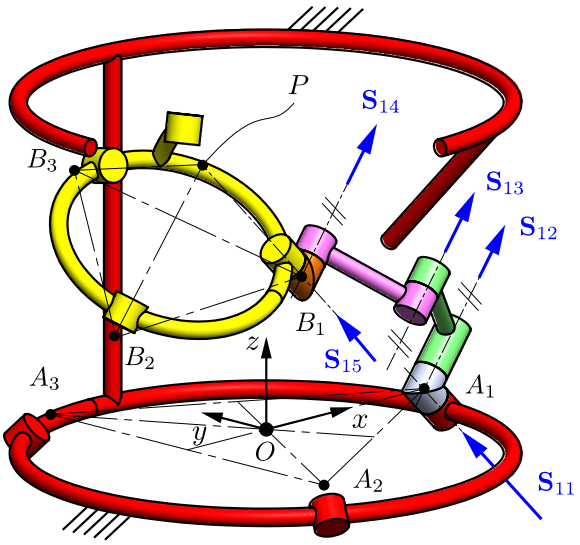

FIGURE 6.2: Leg 1 of the parallel mechanism.

O. The $x-$axis of this coordinate system is pointing in the direction of $\mathbf{r}_{A_1/O}$, while the $z-$axis is perpendicular to the plane that contains $A_1A_2A_3$ and is pointing upwards.

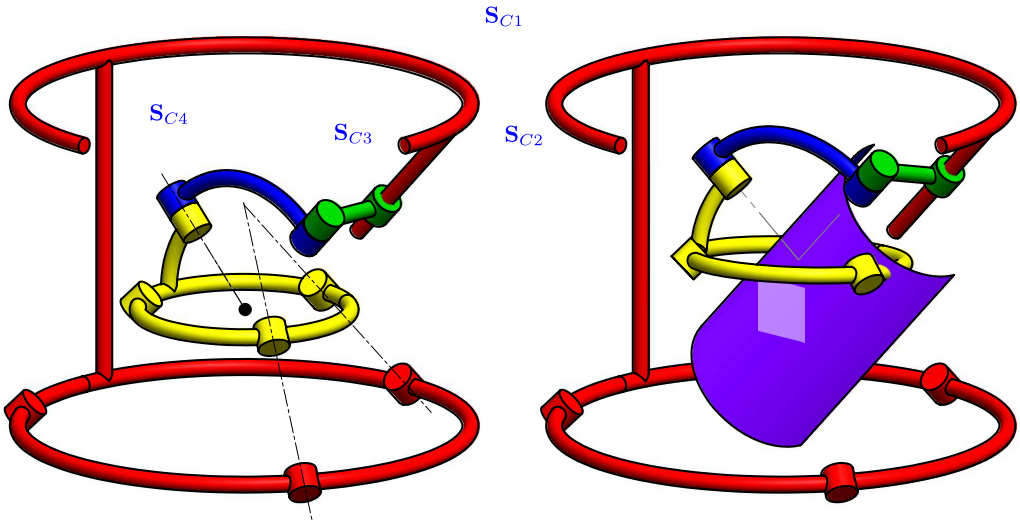

FIGURE 6.3: Leg C of the parallel mechanism.

Fig. 6.3 shows leg C in detail. This leg consists of a C joint (axis $\mathbf{S}_{C1}$ for rotation and $\mathbf{S}_{C2}$ for translation) followed by two R joints (axes $\mathbf{S}_{C3}$ and $\mathbf{S}_{C4}$). The axes of the C joint and $\mathbf{S}_{C3}$ are parallel, while $\mathbf{S}_{C3}$ and $\mathbf{S}_{C4}$ intersect at point E but the angle between them is arbitrary. The geometry of the moving platform must allow the configuration shown in fig. 6.3a, where the axes of joints $\mathbf{S}_{1i}$ and $\mathbf{S}_{5i}$, $i = 1,2,3$, are coincident and $P = P_0$. At such configuration point E lies on the $z-$axis and coincides with point E_0.

An additional condition must be fulfilled by leg C: As shown in fig. 6.3b, point E draws a right cylinder $\mathcal{S}_C$ of radius $a_{C1,C3}$ (which stands for the (shortest) distance between the axes of joints $C1$ and $C3$), $\mathcal{S}_C$ must be tangent to the $z-$axis at point E_0. In the example shown in fig. 6.3b, $T_{E_0}\mathcal{S}_C$ coincides with the $yz-$plane. This condition on $\mathcal{S}_C$ restrict the position and orientation of the C joint.

6.3 Motion of point E when leg C is disconnected

In this section the motion of the moving platform, especially focusing on point E, is analyzed when leg C is removed. In the next section, these results will be used to make sure the parallel mechanism can reconfigure from one branch of motion to another once leg C is connected.

It can be seen in fig. 6.1 that, if leg C is disconnected, legs 1, 2 and 3 constitute a 3-RGR parallel module, which was described in [127]. This module is similar to the DYMO manipulator [64], in which the extra condition of $\mathbf{S}_{i5}$ axes being coplanar is added. The 3-RGR module is designed so that the displacements of its moving platform can lie in either the subgroup of pure rotations in 3 dimensions, SO(3), or the subgroup of pure translations in the 3 dimensions, T(3). It was proved in [127] that both 3-dimensional branches of motion are connected through another 3-dimensional branch which is passive to the moving platform and in which $\mathbf{S}_{i1}$ and $\mathbf{S}_{i5}$ are coincident while the three legs spin about the common axes $\mathbf{S}_{i1} = \mathbf{S}_{i5}$ in a partitioned mobility branch [125]. When working as a translational manipulator, axes $\mathbf{S}_{i1}$ and $\mathbf{S}_{i5}$ are parallel, while when working as a rotational manipulator, axes $\mathbf{S}_{i1}$ and $\mathbf{S}_{i5}$ intersect at P_0 and $P = P_0$ remains fixed during the motion.

From the previous discussion it can be seen that, if leg C remains disconnected, point E in the moving platform moves in the 3-dimensional space when the 3-RGR manipulator works as in translational mode, moves on a sphere, $\mathcal{S}_S$, with center at P_0 and radius $d(P_0, E_0)$ when the manipulator works in pure rotational mode, and will remain fixed in the partitioned mobility branch of motion.

When analyzing the motion of point E, it may look like the module has 2 DOF in the rotational mode, as E lies on the fixed sphere $\mathcal{S}_S$. However, if E is fixed on $\mathcal{S}_S$, the moving platform is still able to rotate with 1 DOF about the line $\overline{P_0E}$, showing the presence of the 3 rotational degrees of freedom.

Let $V^{\mathrm{G}} \subset \mathbb{T}^{15}$ be the configuration space of the 3-RGR module which includes all vectors of joint variables $\mathbf{q}^{\mathrm{G}} := (q_{11}, q_{12}, \ldots, q_{15}, q_{21}, \ldots, q_{25}, q_{31}, \ldots, q_{35}) \in \mathbb{T}^{15}$, and let $V_{\mathrm{T}}^{\mathrm{G}}$, $V_{\mathrm{R}}^{\mathrm{G}}$ and $V_{\mathrm{P}}^{\mathrm{G}}$ be the 3-dimensional subvarieties corresponding to the branches of motion of pure translation, pure rotation and partitioned mobility, respectively. In [127], the singular configurations $\mathbf{q}_{\mathrm{PT}}^{\mathrm{G}} := V_{\mathrm{P}}^{\mathrm{G}} \cap V_{\mathrm{T}}^{\mathrm{G}}$ and $\mathbf{q}_{\mathrm{PR}}^{\mathrm{G}} := V_{\mathrm{P}}^{\mathrm{G}} \cap V_{\mathrm{R}}^{\mathrm{G}}$ were found:

- Configuration $\mathbf{q}_{\mathrm{PT}}^{\mathrm{G}}$: axes $\mathbf{S}_{12}$, $\mathbf{S}_{22}$ and $\mathbf{S}_{32}$ are parallel to the $xy-$plane, while in leg i axes $\mathbf{S}_{i1}$ and $\mathbf{S}_{i5}$ are coincident. Fig. 6.4a shows leg 1 in this configuration.
- Configuration $\mathbf{q}_{\mathrm{PR}}^{\mathrm{G}}$: axes $\mathbf{S}_{i1}$ and $\mathbf{S}_{i5}$ are coincident in leg i and $\mathbf{S}_{i1}$ and $\mathbf{S}_{i2}$ span a plane that is perpendicular to the $xy-$plane. Fig. 6.4b shows leg 1 in this configuration.

It was also found that $V_{\mathrm{R}}^{\mathrm{G}} \cap V_{\mathrm{T}}^{\mathrm{G}} = \emptyset$, i.e. the mechanism cannot transit directly from pure translation pure rotation mode.

The angular velocity of the moving platform and the velocity of point E attached to it are now analyzed in both singularities. In both analyses the following fundamental loop cycles are considered:

$$\begin{aligned} \Lambda_1 &= \{11, 12, 13, 14, 15, 25, 24, 23, 22, 21\}, \\ \Lambda_2 &= \{11, 12, 13, 14, 15, 35, 34, 33, 32, 31\}, \end{aligned}$$

which indicate the sequence of joints considered in the closure equations for the higher order analyses.

Configuration $\mathbf{q}_{\mathrm{PT}}^{\mathrm{G}}$: This point is a transition configuration from partitioned mobility to pure translation mode. The screw coordinates for this configuration are the following:

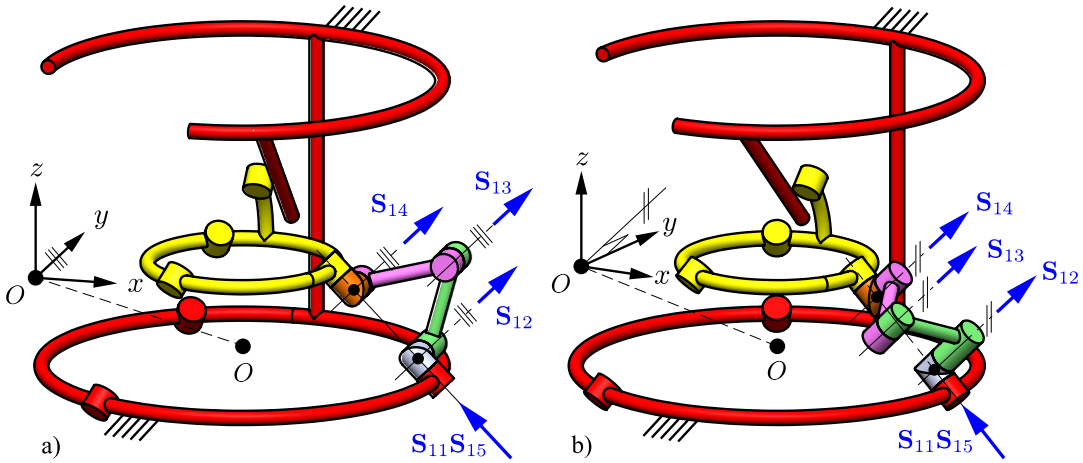

FIGURE 6.4: Leg 1 in singular configuration a) $\mathbf{q}^{\mathrm{G}}_{\mathrm{PT}}$ and b) $\mathbf{q}^{\mathrm{G}}_{\mathrm{PR}}$.

$$
\begin{aligned}
\mathbf{S}_{11}(\mathbf{q}^{\mathrm{G}}_{\mathrm{PT}}) &= \left(-\frac{\sqrt{2}}{2}, 0, \frac{\sqrt{2}}{2}; 0, -\frac{3\sqrt{2}}{2}, 0\right),\\
\mathbf{S}_{12}(\mathbf{q}^{\mathrm{G}}_{\mathrm{PT}}) &= (0,1,0;0,0,3),\\
\mathbf{S}_{13}(\mathbf{q}^{\mathrm{G}}_{\mathrm{PT}}) &= (0,1,0;-2,0,3),\\
\mathbf{S}_{14}(\mathbf{q}^{\mathrm{G}}_{\mathrm{PT}}) &= (0,1,0;-2,0,1),\\
\mathbf{S}_{15}(\mathbf{q}^{\mathrm{G}}_{\mathrm{PT}}) &= \mathbf{S}_{11}(\mathbf{q}^{\mathrm{G}}_{\mathrm{PT}}),\\
\mathbf{S}_{2j}(\mathbf{q}^{\mathrm{G}}_{\mathrm{PT}}) &= \mathrm{Adj}\left(\mathrm{Rot}\left(\frac{2}{3}\pi, \hat{\mathbf{k}}\right), \mathbf{0}\right)\mathbf{S}_{1j}(\mathbf{q}^{\mathrm{G}}_{\mathrm{PT}}),\ j=1,\ldots,5\\
\mathbf{S}_{3j}(\mathbf{q}^{\mathrm{G}}_{\mathrm{PT}}) &= \mathrm{Adj}\left(\mathrm{Rot}\left(\frac{4}{3}\pi, \hat{\mathbf{k}}\right), \mathbf{0}\right)\mathbf{S}_{1j}(\mathbf{q}^{\mathrm{G}}_{\mathrm{PT}}),\ j=1,\ldots,5
\end{aligned}
\tag{6.1}
$$

where $\mathrm{Adj}(\mathbf{R},\mathbf{t}) \in \mathbb{R}^{6\times 6}$ is the adjoint representation of SE(3) [128], [129] given by a rotation $\mathbf{R} \in SO(3)$ and a translation $\mathbf{t} \in \mathbb{R}^3$, and $\mathrm{Rot}(a,\hat{\mathbf{u}}) \in SO(3)$ is a rotation matrix representing a rotation of a radians about an axis that contains the origin and is parallel to $\hat{\mathbf{u}} \in S^2$.

Using higher order analysis it is found that the kinematic tangent cone to V^{G} at $\mathbf{q}^{\mathrm{G}}_{\mathrm{PT}}$ is given by $C^{\mathrm{K}}_{\mathbf{q}^{\mathrm{G}}_{\mathrm{PT}}} V^{\mathrm{G}} = K^2_{\mathbf{q}^{\mathrm{G}}_{\mathrm{PT}}}$ which is, as expected, the union of two 3-dimensional vector spaces $K^2_{\mathbf{q}^{\mathrm{G}}_{\mathrm{PT}}} = K^{2,P}_{\mathbf{q}^{\mathrm{G}}_{\mathrm{PT}}} \cup K^{2,T}_{\mathbf{q}^{\mathrm{G}}_{\mathrm{PT}}}$, where:

$$
\begin{aligned}
K^{2,P}_{\mathbf{q}^{\mathrm{G}}_{\mathrm{PT}}} &= \{(u,0,0,0,-u,v,0,0,0,-v,w,0,0,0,-w) \,|\, u,v,w \in \mathbb{R}\},\\
K^{2,T}_{\mathbf{q}^{\mathrm{G}}_{\mathrm{PT}}} &= \{(u,0,v,-v,-u,w,0,-v,v,-w,w-u,0,v,-v,u-w) \,|\, u,v,w \in \mathbb{R}\}.
\end{aligned}
$$

It can be seen that $K^{2,P}_{\mathbf{q}^{\mathrm{G}}_{\mathrm{PT}}}$ corresponds to the partitioned mobility branch, while $K^{2,T}_{\mathbf{q}^{\mathrm{G}}_{\mathrm{PT}}}$ corresponds to the pure translational operation mode.

The instant velocity of the moving platform of the 3-RGR manipulator, with respect to the fixed coordinate system with origin at O, is described by the twist $\mathbf{V}^{\mathrm{G}}_{\mathrm{mp}}(\mathbf{q}^{\mathrm{G}}_{\mathrm{PT}}) := \sum_{j=1}^{5} \dot{q}_{ij}\mathbf{S}^{\mathrm{G}}_{ij}(\mathbf{q}^{\mathrm{G}}_{\mathrm{PT}})$, where i can be 1, 2 or 3 and $\dot{q}_{ij}$ is the $(5(i-1)+j)$−th coordinate of vector $\dot{\mathbf{q}}^{\mathrm{G}} \in C^{\mathrm{K}}_{\mathbf{q}^{\mathrm{G}}_{\mathrm{PT}}} V^{\mathrm{G}}$. Since $\mathbf{q}^{\mathrm{G}}_{\mathrm{PT}}$ is a branching point of V^{G}, there are two possible velocities that correspond to finite motions of the moving platform at such configuration: $\dot{\mathbf{q}}^{\mathrm{G}} \in K^{2,P}_{\mathbf{q}^{\mathrm{G}}_{\mathrm{PT}}}$ and $\dot{\mathbf{q}}^{\mathrm{G}} \in K^{2,T}_{\mathbf{q}^{\mathrm{G}}_{\mathrm{PT}}}$.

In the case of partitioned mobility, $K^{2,P}_{\mathbf{q}^{\mathrm{G}}_{\mathrm{PT}}}$, $\mathbf{V}^{\mathrm{G}}_{\mathrm{mp}}(\mathbf{q}^{\mathrm{G}}_{\mathrm{PT}}) = \mathbf{0}$, which was expected as the platform is not moving in this branch. Since there is no rotation, the velocity of point E fixed to the moving platform is the same as that of point O' which is fixed to the moving platform and at the analyzed configuration coincides with O: $\mathbf{v}_E = \mathbf{v}_{O'} = \mathbf{0}$. In fact, $E(\mathbf{q}^{\mathrm{G}}) = E_0, \forall \mathbf{q}^{\mathrm{G}} \in V^{\mathrm{G}}_{\mathrm{P}}$. In the case of pure translation mode $\mathbf{V}^{\mathrm{G}}_{\mathrm{mp}}(\mathbf{q}^{\mathrm{G}}_{\mathrm{PT}}) = (0,0,0,0,0,2v)$, which indicates that the angular velocity of the moving platform is $\boldsymbol{\omega}_{\mathrm{mp}} = \mathbf{0}$ and $\mathbf{v}_{O'} = (0,0,2v)$, therefore $\mathbf{v}_E = (0,0,2v)$.

Configuration $\mathbf{q}^{\mathrm{G}}_{\mathrm{PR}}$: This is the transition configuration from partitioned mobility to pure rotation mode. The screw coordinates for this configuration are the following:

$$
\begin{aligned}
\mathbf{S}_{11}(\mathbf{q}^{\mathrm{G}}_{\mathrm{PR}}) &= \left(-\frac{\sqrt{2}}{2}, 0, \frac{\sqrt{2}}{2}; 0, -\frac{3\sqrt{2}}{2}, 0\right),\\
\mathbf{S}_{12}(\mathbf{q}^{\mathrm{G}}_{\mathrm{PR}}) &= \left(\frac{\sqrt{2}}{2}, 0, \frac{\sqrt{2}}{2}; 0, -\frac{3\sqrt{2}}{2}, 0\right),\\
\mathbf{S}_{13}(\mathbf{q}^{\mathrm{G}}_{\mathrm{PR}}) &= \left(\frac{\sqrt{2}}{2}, 0, \frac{\sqrt{2}}{2}; 1, -\frac{\sqrt{2}}{2}, -1\right),\\
\mathbf{S}_{14}(\mathbf{q}^{\mathrm{G}}_{\mathrm{PR}}) &= \left(\frac{\sqrt{2}}{2}, 0, \frac{\sqrt{2}}{2}; 0, \frac{\sqrt{2}}{2}, 0\right),\\
\mathbf{S}_{15}(\mathbf{q}^{\mathrm{G}}_{\mathrm{PR}}) &= \mathbf{S}_{11}(\mathbf{q}^{\mathrm{G}}_{\mathrm{PR}}),\\
\mathbf{S}_{2j}(\mathbf{q}^{\mathrm{G}}_{\mathrm{PR}}) &= \mathrm{Adj}\left(\mathrm{Rot}\left(\frac{2}{3}\pi, \hat{\mathbf{k}}\right), \mathbf{0}\right)\mathbf{S}_{1j}(\mathbf{q}^{\mathrm{G}}_{\mathrm{PR}}),\ j = 1,\ldots,5\\
\mathbf{S}_{3j}(\mathbf{q}^{\mathrm{G}}_{\mathrm{PR}}) &= \mathrm{Adj}\left(\mathrm{Rot}\left(\frac{4}{3}\pi, \hat{\mathbf{k}}\right), \mathbf{0}\right)\mathbf{S}_{1j}(\mathbf{q}^{\mathrm{G}}_{\mathrm{PR}}),\ j = 1,\ldots,5
\end{aligned}
\tag{6.2}
$$

It is found that $C^{\mathrm{K}}_{\mathbf{q}^{\mathrm{G}}_{\mathrm{RT}}} V^{\mathrm{G}} = K^{2}_{\mathbf{q}^{\mathrm{G}}_{\mathrm{RT}}}$ which is, as expected, the union of two 3-dimensional vector spaces $K^{2}_{\mathbf{q}^{\mathrm{G}}_{\mathrm{RT}}} = K^{2,P}_{\mathbf{q}^{\mathrm{G}}_{\mathrm{RT}}} \cup K^{2,R}_{\mathbf{q}^{\mathrm{G}}_{\mathrm{PR}}}$, where:

$$
\begin{aligned}
K^{2,P}_{\mathbf{q}^{\mathrm{G}}_{\mathrm{PT}}} &= \{(u,0,0,0,-u,v,0,0,0,-v,w,0,0,0,-w) \mid u,v,w \in \mathbb{R}\},\\
K^{2,R}_{\mathbf{q}^{\mathrm{G}}_{\mathrm{PT}}} &= \left\{\left(u, \frac{1}{3}(v-u-w), 0, u-v+w, \frac{1}{3}(2w-u-2v), v, \frac{1}{3}(u-v+w), 0, v-u-w,\right.\right.\\
&\qquad \left.\left.\frac{1}{3}(-2u-v-2w), w, \frac{1}{3}(-u+v-w), 0, u-v+w, \frac{1}{3}(2u-2v-w)\right) \,\middle|\, u,v,w \in \mathbb{R}\right\}
\end{aligned}
$$

It can be seen that $K^{2,P}_{\mathbf{q}^{\mathrm{G}}_{\mathrm{PT}}}$ corresponds to the partitioned mobility branch, while $K^{2,R}_{\mathbf{q}^{\mathrm{G}}_{\mathrm{PT}}}$ corresponds to the pure rotational operation mode.

Again, in the case of partitioned mobility, $\mathbf{V}^{\mathrm{G}}_{\mathrm{mp}}(\mathbf{q}^{\mathrm{G}}_{\mathrm{RT}}) = \mathbf{0}$ and $\mathbf{v}_E = \mathbf{0}$. In the case of pure rotation mode $\mathbf{V}^{\mathrm{G}}_{\mathrm{mp}}(\mathbf{q}^{\mathrm{G}}_{\mathrm{PR}}) = (0,0,(2\sqrt{2}/3)(u-v+w),0,0,0)$, which indicates that $\boldsymbol{\omega}_{\mathrm{mp}} = (0,0,\dot{\theta}_z)$ and $\mathbf{v}_{O'} = \mathbf{0}$, where $\dot{\theta}_z := (2\sqrt{2}/3)(u-v+w)$. Therefore, $\mathbf{v}_E = \mathbf{v}_{O'} + \boldsymbol{\omega}_{\mathrm{mp}} \times \mathbf{r}_{E/O'} = \mathbf{0}$.

6.4 Description of the motion of the parallel mechanism when leg C is connected

As mentioned in Section 6.2 and shown in fig. 6.3b, if legs 1, 2 and 3 are now disconnected and the moving platform is connected to the fixed platform only by leg C, point E will move on a cylinder $\mathcal{S}_C$. When all legs are connected point E is constrained by both, the 3-RGR mechanism and leg C. Thus, if $V \subset \mathbb{T}^{18} \times \mathbb{R}$ is the configuration space of the 3-RGR-1-CU parallel mechanism which consists of vectors $\mathbf{q} := (q_{11}, \ldots, q_{15}, q_{21}, \ldots, q_{25}, q_{31}, \ldots, q_{35}, q_{C1}, \ldots, q_{C4})$, the following branches of motion are expected:

- Branch 1, $V_1 \subset V$: $E \in \mathcal{S}_C \cap \mathcal{S}_S$. E moves through the intersection curve of the cylinder and the sphere. If the rotation about line $\overline{P_0E}$ is not allowed by leg C, then $\dim(V_1) = 1$ and the mechanism has 1 DOF.
- Branch 2, $V_2 \subset V$: $E \in \mathcal{S}_C \cap E^3 = \mathcal{S}_C$. E moves through the cylinder while the parallel platform undergoes pure translation. Leg C allows pure translation of the moving platform as, since $\mathbf{S}_{C1} || \mathbf{S}_{C3}$, it is possible to get $\dot{q}_{C1} + \dot{q}_{C3} = \dot{q}_{C4} = 0$. It follows that $\dim(V_2) = 2$ and the mechanism has 2 DOFs.
- Branch 3, $V_3 \subset V$: $E \in \mathcal{S}_C \cap E_0 \Rightarrow E = E_0$. E remains fixed and leg C is idle while legs 1, 2 and 3 spin about their axes leading to a total of 3 DOFs, and $\dim(V_3) = 3$.

Fig. 6.5 shows $\mathcal{S}_S$, $\mathcal{S}_C$ and their intersection being generated by the 3-RGR-1-CU parallel mechanism.

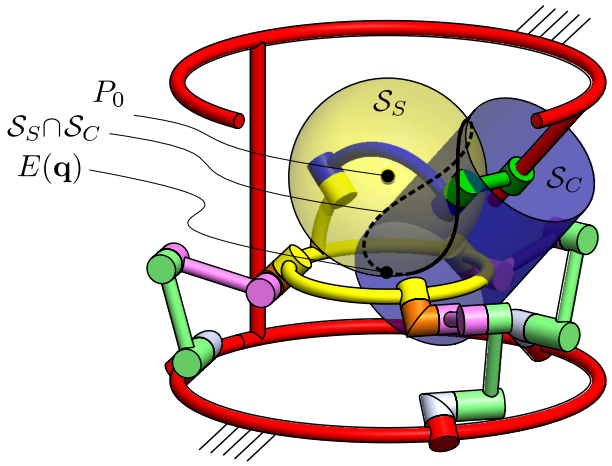

FIGURE 6.5: The two surfaces generated by the 3-RGR-1-CU parallel mechanism.

The constraints added by leg C in the 3-RGR-1-CU kinematotropic mechanism must allow the reconfiguration happening in configurations $\mathbf{q}^{\mathrm{G}}_{\mathrm{PT}}$ and $\mathbf{q}^{\mathrm{G}}_{\mathrm{PR}}$ when leg C is not connected, as described in the previous section. E is the connecting point between the 3-RGR mechanism and leg C, therefore it is used to check whether reconfigurations from V_3 to V_1 and from V_3 to V_2.

Reconfiguration from V_3 to V_2: The 3-RGR mechanism is in the partitioned mobility branch in V_3 and in translational branch in V_2. In Section 6.3 it was discussed that $\boldsymbol{\omega}_{\mathrm{mp}} = \mathbf{0}$ and $\mathbf{v}_E = (0, 0, 2v)$ at the bifurcation. This suggests that in order to move to this branch of motion, leg C must allow (at least instantaneously) translation of point E in the $z-$direction. In section 6.2 it was indicated that leg C must be designed so that the cylinder $\mathcal{S}_C$ is tangent to

the $z-$axis, this will allow reconfiguration of the 3-RGR-1-CU mechanism between V_3 and V_2.

Reconfiguration from V_3 to V_1: The 3-RGR mechanism is in the partitioned mobility branch in V_3 and in rotational branch in V_2. In Section 6.3 it was discussed that $\boldsymbol{\omega}_{\text{mp}} = (0,0,\dot{\theta}_z)$ and $\mathbf{v}_E = \mathbf{0}$. Point E is in a dead point position and, therefore, there is no restriction on the design of $\mathcal{S}_C$ generated by leg C, as long as $E_0 \in \mathcal{S}_C$. On the other hand, $\boldsymbol{\omega}_{\text{mp}} = (0,0,\dot{\theta}_z)$, which suggests that in order to move to V_1, leg C must allow (at least instantaneously) the rotation of the moving platform about the $z-$axis. In section 6.2 (see fig. 6.3) it was indicated that, when axes $\mathbf{S}_{i1}$ and $\mathbf{S}_{i5}$ are coincident, $\mathbf{S}_{C3}$ and $\mathbf{S}_{C4}$ lie on the xz-plane and E lies on the $z-$axis. Clearly, in this configuration $\mathbf{V}^{\text{G}}_{\text{mp}} = (0,0,\dot{\theta}_z,0,0,0) \in \text{span}(\mathbf{S}_{C3},\mathbf{S}_{C4})$, this allows reconfiguration between V_3 and V_1.

In the kinematotropic 3-RGR-1-CRR mechanism working in V_1, it is important to consider that even though $E(\mathbf{q}_1)$, $\mathbf{q}_1 \in V_1$, is confined to move in the curve $\mathcal{S}_S \cap \mathcal{S}_C$ with 1 DOF, if the moving platform is able to spin about $\overline{P_0E(\mathbf{q}_1)}$, E will remain fixed yet the parallel mechanism will undergo motion, leading to a total of 2-DOF. Observe that once $E(\mathbf{q}_1)$ is no longer equal to E_0 it does not lie on the $z-$axis and, in general, $\overline{P_0E(\mathbf{q}_1)} \notin \text{span}(\mathbf{S}_{C3}(\mathbf{q}_1),\mathbf{S}_{C4}(\mathbf{q}_1))$, therefore, leg C does not allow a rotation about $P_0E(\mathbf{q}_1)$ and the kinematotropic 3-RGR-1-CU mechanism has only 1 DOF in this branch.

6.5 Mobility analysis at both singular configurations

In Section 6.4 it was discussed that the design of leg C allows the 3-RGR-1-CU parallel mechanism to reconfigure from V_3 to V_2 and from V_3 to V_1. We now define the singular points in V: $\mathbf{q}_{3,1} := V_3 \cap V_1$ and $\mathbf{q}_{3,2} := V_3 \cap V_2$. Note that $\mathbf{S}_{Cj}(\mathbf{q}_{3,1}) = \mathbf{S}_{Cj}(\mathbf{q}_{3,2})$, $i = 1,\ldots,4$ as $E(\mathbf{q}_{3,1}) = E(\mathbf{q}_{3,2}) = E_0$ for both configurations. In this section, the kinematic tangent cone to V is computed at both $\mathbf{q}_{3,1}$ and $\mathbf{q}_{3,2}$, this will prove the bifurcations and different mobilities of the 3-RGR-1-CU parallel mechanism. In both analyses the following fundamental loop cycles are considered:

$$\begin{aligned}
\Lambda_1 &= \{11,12,13,14,15,-25,-24,-23,-22,-21\}\\
\Lambda_2 &= \{31,32,33,34,35,-25,-24,-23,-22,-21\}\\
\Lambda_3 &= \{31,32,33,34,35,-C4,-C3,-C2,-C1\}
\end{aligned}$$

6.5.1 3 DOF to 2 DOF: singularity $\mathbf{q}_{3,2}$

The singular configuration $\mathbf{q}_{3,2} \in V$ (see fig. 6.6a) is analyzed and is shown to be a transition configuration between a 2-dim and a 3-dimensional motion mode.

The screw coordinate vectors are given by:

$$\begin{aligned}
&\mathbf{S}_{ij}(\mathbf{q}_{3,2}) = \mathbf{S}_{ij}(\mathbf{q}^{\text{G}}_{\text{PT}}),\ i = 1,2,3,\ j = 1,\ldots,5,\\
&\mathbf{S}_{C1}(\mathbf{q}_{3,2}) = \left(0,0,0,0,\frac{\sqrt{2}}{2},\frac{\sqrt{2}}{2}\right),\ \mathbf{S}_{C2}(\mathbf{q}_{3,2}) = \left(0,\frac{\sqrt{2}}{2},\frac{\sqrt{2}}{2},-\sqrt{2},\frac{\sqrt{2}}{3},\frac{\sqrt{2}}{3}\right),\\
&\mathbf{S}_{C3}(\mathbf{q}_{3,2}) = \left(0,\frac{\sqrt{2}}{2},\frac{\sqrt{2}}{2},-\sqrt{2},0,0\right),\ \mathbf{S}_{C4}(\mathbf{q}_{3,2}) = \left(0,-\frac{\sqrt{2}}{2},\frac{\sqrt{2}}{2},\sqrt{2},0,0\right)
\end{aligned}$$

The first-order tangent cone is the 4-dimensional vector space

$$K^1_{\mathbf{q}_{3,2}} = \{\mathbf{x} \in \mathbb{R}^{19} | \quad x_{12} = x_{22} = x_{32} = x_{C4} = 0, x_{11} = s, x_{15} = -s, x_{31} = v, x_{35} = -v, x_{21} = u, \\ x_{25} = -u, x_{13} = x_{23} = x_{33} = w, x_{14} = x_{24} = x_{34} = -w, x_{C1} = \sqrt{2}w, \\ x_{C2} = \tfrac{3}{\sqrt{2}}w, x_{C3} = -\tfrac{3}{\sqrt{2}}w \text{ with } s,u,v,w \in \mathbb{R}\}$$

where $\mathbf{x} := (x_{11}, \ldots, x_{15}, x_{21} \ldots, x_{25}, x_{31}, \ldots, x_{35}, x_{C1}, \ldots, x_{C4}) \in \mathbb{R}^{19}$.

The second order tangent cone is the union of two vector spaces:

$$K^2_{\mathbf{q}_{3,2}} = K^{2,I}_{\mathbf{q}_{3,2}} \cup K^{2,II}_{\mathbf{q}_{3,2}}$$

with

$$K^{2,I}_{\mathbf{q}_{3,2}} = \{\mathbf{x} \in \mathbb{R}^{19} | \quad x_{12} = x_{13} = x_{14} = x_{22} = x_{23} = x_{24} = x_{32} = x_{33} = 0, \\ x_{34} = x_{C1} = x_{C2} = x_{C3} = x_{C4} = 0, x_{11} = s, x_{15} = -s, x_{21} = u, x_{25} = -u, \\ x_{31} = v, x_{35} = -v \text{ with } s,u,v \in \mathbb{R}\}$$

$$K^{2,II}_{\mathbf{q}_{3,2}} = \{\mathbf{x} \in \mathbb{R}^{19} | \quad x_{12} = x_{22} = x_{32} = x_{C4} = 0, x_{25} = s, x_{34} = t, x_{11} = 2s + \tfrac{3}{2}\sqrt{\tfrac{3}{2}}u, x_{13} = -u, \\ x_{14} = u, x_{15} = -2s - \tfrac{3}{2}\sqrt{\tfrac{3}{2}}u, x_{21} = -s, x_{23} = -u, x_{24} = u, \\ x_{31} = -s - \tfrac{3}{2}\sqrt{\tfrac{3}{2}}u, x_{33} = -u, x_{35} = s + \tfrac{3}{2}\sqrt{\tfrac{3}{2}}u, x_{C1} = -\sqrt{2}u, \\ x_{C2} = -\tfrac{3}{\sqrt{2}}u, x_{C3} = \tfrac{3}{\sqrt{2}}u, \text{ with } s,u \in \mathbb{R}\}$$

The third-order tangent cone is the same as the second-order one:

$$K^3_{\mathbf{q}_{3,2}} = K^2_{\mathbf{q}_{3,2}}$$

Further $K^2_{\mathbf{q}_{3,2}} = K^i_{\mathbf{q}_{3,2}}, i \geq 3$ so that $C^{\mathrm{K}}_{\mathbf{q}_{3,2}} V = K^2_{\mathbf{q}_{3,2}}$

$K^{2,I}_{\mathbf{q}_{3,2}}$ is the tangent space to the 3-dimensional manifold V_3 and $K^{2,II}_{\mathbf{q}_{3,2}}$ the tangent space to the 2-dimensional manifold V_2. Fig. 6.6 shows the 3-RGR-2-CU parallel mechanism in the analyzed bifurcation configuration $\mathbf{q}_{3,2}$ and in two regular configurations belonging to the two branches intersecting at such singularity.

6.5.2 3 DOF to 1 DOF: singularity $\mathbf{q}_{3,1}$

The singular configuration $\mathbf{q}_{3,1} \in V$ (see fig. 6.7a) is analyzed and is shown to be a transition configuration between a 1-dim and a 3-dimensional motion mode.

The screw coordinate vectors are given by:

$$\begin{aligned} \mathbf{S}_{ij}(\mathbf{q}_{3,1}) &= \mathbf{S}_{ij}(\mathbf{q}^{\mathrm{G}}_{\mathrm{PR}}), i = 1,2,3, j = 1,\ldots,5, \\ \mathbf{S}_{Cj}(\mathbf{q}_{3,1}) &= \mathbf{S}_{Cj}(\mathbf{q}_{3,2}), j = 1,\ldots,4, \end{aligned}$$

The first-order tangent cone is the 4-dimensional vector space

$$K^1_{\mathbf{q}_{3,1}} = \{\mathbf{x} \in \mathbb{R}^{19} | \quad x_{13} = x_{23} = x_{33} = x_{C1} = x_{C2} = 0, x_{11} = s, x_{12} = -w, x_{14} = 3w, \\ x_{15} = 2w - s, x_{21} = u, x_{22} = w, x_{24} = -3w, x_{25} = -u - 2w, x_{31} = v, \\ x_{32} = -w, x_{34} = 3w, x_{35} = 2w - v, x_{C3} = -2w, x_{C4} = -2w \\ \text{with } s,u,v,w \in \mathbb{R}\}$$

The second-order tangent cone is the union of two vector spaces:

$$K^2_{\mathbf{q}_{3,1}} = K^{2,I}_{\mathbf{q}_{3,1}} \cup K^{2,II}_{\mathbf{q}_{3,1}}$$

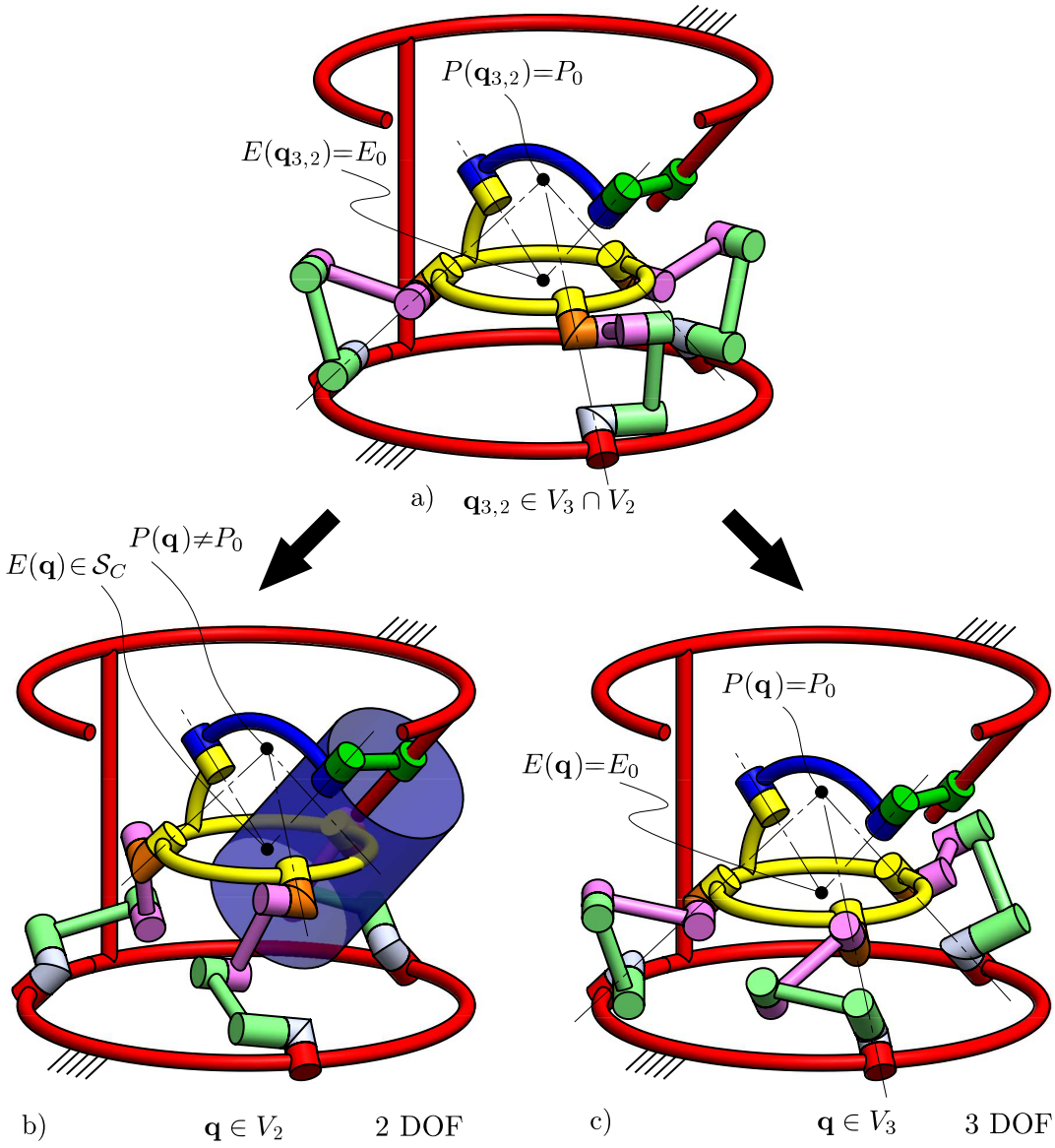

FIGURE 6.6: 3-RGR-1-CU parallel mechanism in a) singular configuration $\mathbf{q}_{3,2} \in V_3 \cap V_2$, b) a regular configuration in V_2 and c) a regular configuration in V_3.

with

$$K^{2,I}_{\mathbf{q}_{3,1}} = \{\mathbf{x} \in \mathbb{R}^{19} | \quad x_{12} = x_{13} = x_{14} = x_{22} = x_{23} = x_{24} = x_{32} = 0,$$
$$x_{33} = x_{34} = x_{C1} = x_{C2} = x_{C3} = x_{C4} = 0$$
$$x_{15} = -s, x_{25} = -w, x_{35} = -u, x_{11} = s, x_{21} = w, x_{31} = u$$
$$\text{with } s,u,w \in \mathbb{R}\}$$
$$K^{2,II}_{\mathbf{q}_{3,1}} = \{\mathbf{x} \in \mathbb{R}^{19} | \quad x_{13} = x_{23} = x_{33} = x_{C1} = x_{C2} = 0, x_{14} = x_{34} = -\frac{6\sqrt{3}}{2\sqrt{3}-3}s,$$
$$x_{11} = x_{15} = x_{22} = -\frac{2\sqrt{3}}{2\sqrt{3}-3}s, x_{12} = x_{32} = \frac{2\sqrt{3}}{2\sqrt{3}-3}s, x_{21} = s, x_{24} = \frac{6\sqrt{3}}{2\sqrt{3}-3}s,$$
$$x_{25} = \frac{(2\sqrt{3}+3)}{2\sqrt{3}-3}s, x_{31} = -\frac{(2\sqrt{3}+3)}{2\sqrt{3}-3}s, x_{35} = -s, x_{C3} = x_{C4} = \frac{4\sqrt{3}}{2\sqrt{3}-3}s,$$
$$\text{with } s \in \mathbb{R}\}$$

The third-order tangent cone is the same as the second-order one:

$$K^3_{\mathbf{q}_{3,1}} = K^2_{\mathbf{q}_{3,1}}$$

Further $K^3_{\mathbf{q}_{3,1}} = K^i_{\mathbf{q}_{3,1}}, i \geq 4$ so that $C^{\mathrm{K}}_{\mathbf{q}_{3,1}} V = K^3_{\mathbf{q}_{3,1}}$

$K^{2,I}_{\mathbf{q}_{3,1}}$ is the tangent space to the 3-dimensional manifold V_3 and $K^{2,II}_{\mathbf{q}_{3,1}}$ the tangent space to the 1-dimensional manifold V_1. Fig. 6.7 shows the 3-RGR-2-CU parallel mechanism in the analyzed bifurcation configuration $\mathbf{q}_{3,1}$ and in two regular configurations belonging to the two branches intersecting at such singularity.

6.6 Chapter conclusions

A novel kinematotropic parallel mechanism was presented. It was proved that the 3-RGR-1-CU mechanism has 3 branches of motion exhibiting 1, 2 and 3 DOF. The proof of bifurcations between branches was made by means of geometric reasoning but also by use of higher order analysis and the computation of the tangent cone to the configuration space at the singularities. These results matched.

It has to be mentioned that the 3-RGR mechanism presented in [127] has a general topology which does not require the perpendicularity between the axes of the R joints and the G group of R joints which is assumed in this chapter for the 3-RGR module of the proposed kinematotropic mechanism. Kong and Gosselin [127] explain that the other branches of motion exhibited by the DYMO parallel mechanism [64] are a consequence of the extra conditions that become the DYMO a special case of their general 3-RGR platform. In a similar manner, the 3-RGR module of the 3-RGR-2-CU kinematotropic mechanism presented in this chapter may exhibit some additional branches of motion due to the perpendicularity between the G group and the R joints in each leg. These would lead to unexplored behavior of the 3-RGR-2-CU kinematotropic mechanism. Other branches of motion not studied here were detected in the solid model of the mechanism. A complete analysis of the architecture of the configuration space of this parallel mechanism is to be developed in future research.

The leg C in the 3-RGR-1-CU mechanism presented here can clearly be replaced by any surface generator as long as this surface is tangent to the $z-$axis. The 3-RGR module can also be replaced by other parallel modules with similar behavior of their moving platform. An extension to other similar mechanisms is to be done in a forthcoming publication.

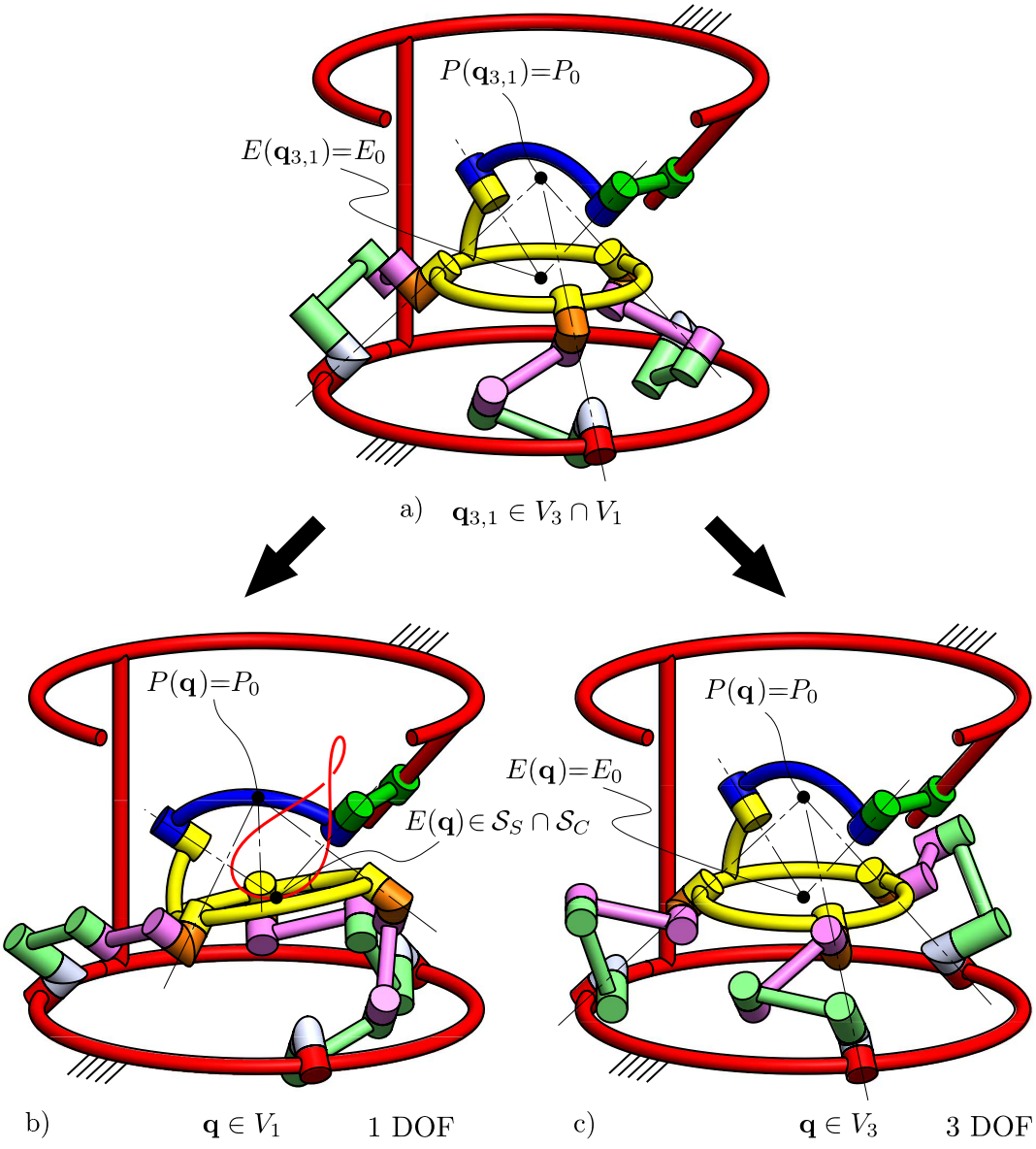

FIGURE 6.7: 3-RGR-1-CU parallel mechanism in a) singular configuration $\mathbf{q}_{3,1} \in V_3 \cap V_1$, b) a regular configuration in V_1 and c) a regular configuration in V_3.

Chapter 7

A synthesis method for 1-DOF mechanisms with a cusp in the configuration space

Significant progress has been made in the study of singularities of mechanisms. This research has, however, exclusively focused on situations where different motion branches intersect, i.e. bifurcation points of the configuration space (c-space). Other types of singularities have not been studied due to lack of mechanisms examples. In particular, mechanisms exhibiting cusp singularities in their c-space are almost unknown, besides a planar linkage presented by Connelly and Servatius, which served as an example where the common definition of rigidity fails. In this chapter, a method for the synthesis of spatial 1-degree-of-freedom (1-DOF) cusp mechanisms is presented. This method consists in synthesizing the mechanical generator of a spatial curve with specific characteristics and then appropriately connecting this module with its mirrored version. Several examples are presented including a kinematotropic linkage, which is characterized by a singularity that is a cusp (1 DOF motion) and a bifurcation of a curve and a surface (2-DOF motion). It is discussed that all available methods for the local analysis of singularities fail at cusp singularities. The presented synthesis method allows for constructing mechanisms that shall initiate the research into the study of cusp singularities.

This chapter is based on the journal publication:

[39] P.C. López-Custodio, A. Müller, J.M. Rico and J.S. Dai, "A synthesis method for 1-DOF mechanisms with a cusp in the configuration space," *Mechanisms and Machine Theory*, vol 132, 154-175, (2019) DOI:10.1016/j.mechmachtheory.2018.09.008.

7.1 Background

Singularities of mechanisms have been widely studied since it was noted that the kinematic properties of a mechanism change suddenly in certain configurations [58], [130]–[132]. In the abundance of research made on the topic, several types of singularities have been identified. Of particular significance are configuration space (c-space) singularities where the differential degrees of freedom (DOF) of a mechanism change, called *increased mobility configurations* by Hunt [58]. At such singularities the c-space ceases to be a smooth manifold. Best known are bifurcation singularities or constraint singularities, i.e. intersection points of different branches which allow for reconfiguration [24], [25] of a mechanism. This type of singularities has been widely studied [60], [64], [133], [134]. However, there is a situation that has not at all been studied thoroughly: the presence of cusp singularities in the c-space. The analysis of such singularities is challenging since at a cusp the tangential aspect does not reveal the local c-space geometry, i.e. possible motions, as it does for bifurcations.

In particular the tangent space and the tangent cone fail to reveal the first-order and local properties, which is a topic of active research in differential geometry that motivated various definitions of tangent cone.

From a kinematic point of view, at a cusp singularity the mechanism is in a dead point, which means that the velocities of all joints are zero (if it is not a bifurcation point at the same time, in which case only some of the joint velocities must be zero) and the only possibility of motion is a reversal. Since at a cusp singularity, the velocities of all joints are zero, and the mechanism is seemingly rigid, the phenomenon attracted the attention in the field of mathematical rigidity theory. In [119] Connelly and Servatius designed a planar mechanism exhibiting a cusp singularity in its c-space in order to bring a case of a movable linkage which is third-order rigid but not rigid, thus it is a counterexample of the traditional definition of *higher-order rigidity*. This will be called the 'double-Watt mechanism' as it is constructed by combining two Watt linkages. To the best knowledge of the author, although a few other papers in the field of rigidity addressed the topic [135]–[139], no other example of cusp mechanism was presented. In addition, from the point of view of kinematics, the problem of cusp singularities was only discussed in [140].

The lack of examples of similar mechanisms whose c-space has a cusp singularity hinders establishing fundamental research into this phenomenon and finding a way to properly analyze such singularities. Therefore, in this chapter a method for the design of spatial 1-DOF mechanisms with cusp singularities is presented as a means to generate test cases facilitating such research. This method is based in the intersection of generated surfaces. In addition, a planar mechanism with a higher-order cusp singularity is presented using the same idea applied by Connelly and Servatius [119] in the design of the double-Watt mechanism. It will be proved that some of the cusp mechanisms presented in this chapter have a complicated c-space in which several regular branches intersect at the cusp singularity, in one of the examples one of these branches is a 2-dimensional manifold which proves that the example is a kinematotropic cusp mechanism. With the exception of the mechanism recently presented by the authors of this thesis in [141], this is the first time that spatial mechanisms featuring cusp singularities are presented and also the first time that reconfiguration is carried out through a cusp singularity.

This chapter is organized as follows: Firstly, in section 7.2, the cusp mechanism presented by Connelly and Servatius is revisited and a new planar cusp mechanism is presented; the method used in planar curves in section 7.2 is extended to spatial curves in section 7.3; the generation of these spatial curves with mechanisms in presented in section 7.4; in section 7.5 some examples are presented and analyzed; finally, conclusions are presented in section 7.6.

7.2 Planar Mechanisms with Cusp Singularities in the C-Space

7.2.1 The Double-Watt Mechanism

In [119] Connelly and Servatius presented the mechanism shown in fig. 7.1 while trying to address the different problems that stem from the concept of *rigidity*. The mechanism is, to the authors' knowledge, the first example which has a configuration space that features a cusp. This linkage is obtained by merging two 4-bar Watt mechanisms, one being a reflection of the other and then joining the centers of both coupler bars (points P_1 and P_2 in fig. 7.1) with another link.

The 4-bar Watt mechanism is a line generator [142] as the middle point of the coupler bar draws an 8-shaped curve that approximates a line up to third order at the self-crossing. The curves generated by the couplers of both Watt mechanisms are drawn in fig. 7.1. It can be seen that the mechanism is built so that the reflection line of the mechanism is parallel to the tangents of these curves at the self-crossing. In the shown configuration P_1 and P_2 coincide

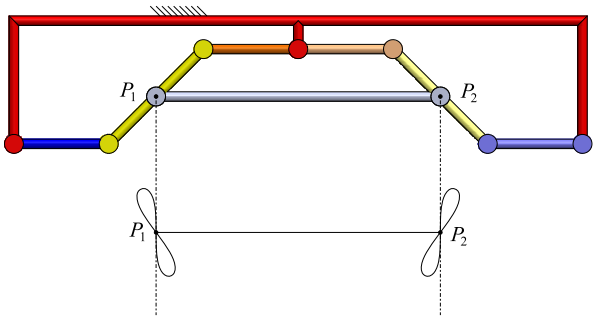

FIGURE 7.1: Double-Watt mechanism presented by Connelly and its generated coupler curves.

with the self-crossing of the coupler curves. Despite the presence of the self-crossing, P_1 and P_2 are only able to move through the branch whose tangent is shown and is parallel to the reflection line. Fig. 7.2 shows these branches from both curves connected by the bar $\overline{P_1P_2}$ of length l. The curves have an inflection point at the self-crossings P_1 and P_2, therefore, the horizontal distance between both curves is longer than l above $\overline{P_1P_2}$, equal to l at $\overline{P_1P_2}$, and shorter than l below $\overline{P_1P_2}$. This implies that a circle of radius l centered at Q_1 on the left-hand curve never intersects the other curve if Q_1 is above P_1. It intersects the other curve in one point if $Q_1 = P_1$. If Q_1 is below P_1 the circle intersects the other curve at two points, Q_2 and Q_2'. Therefore, in the last situation, there are two solutions corresponding to two assembly configurations of the mechanism. Now, as Q_1 gets closer to P_1, Q_2' gets closer to Q_2 until Q_1 reaches P_1 where the two intersections become one and $Q_2' = Q_2 = P_2$ and Q_1 cannot continue moving upwards. This indicates that the mechanism is in a dead point position where all the velocities must be zero since the only possibility of motion is Q_1 moving down again, implying a change in the sign of all joint angles. It can be concluded that the position $Q_1 = P_1$ is a cusp in the configuration space of the double-Watt mechanism. The local higher order analysis of the mechanism at such singularity was presented in [140]. It is important to mention that the length of the coupler bar l is not restricted since the curvature of the drawn curves is zero at the self-crossings, which means that the radius of curvature is infinite. However, the shorter the length l, the better the phenomenon can be appreciated.

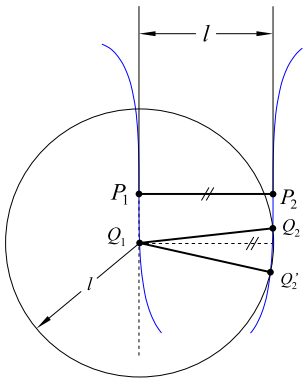

FIGURE 7.2: Curves generated by the coupler bars of both 4-bar Watt loops in the Connelly mechanism.

7.2.2 Generalization to Other Planar Mechanisms

Any planar mechanism that draws a curve with an inflection point can be used to obtain a cusp mechanism following the same idea. Fig. 7.3 shows an example of Evans mechanism

[143] which is a planar 4-bar mechanism whose coupler point P_1 approximates a straight line. In this example of Evans mechanism the coupler curve presents an inflection point where the curve intersects the axis of the revolute joint that connects the fixed link with the input link of length 1. The tangent to the coupler curve at such point is the horizontal line shown in fig. 7.3.

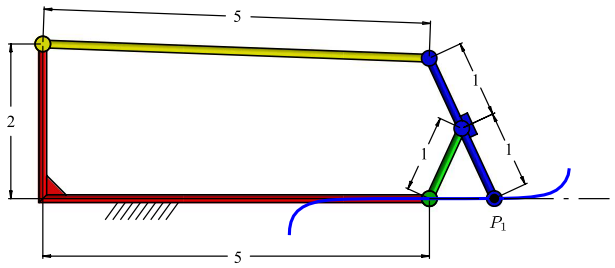

FIGURE 7.3: An example of Evans straight line mechanism.

Since the coupler curve has an inflection point, this Evans mechanism can be used to obtain a planar cusp mechanism like the one shown in fig. 7.4, where the 4-bar mechanism has been mirrored through a line parallel to the tangent to the coupler curve at the inflection point. At the cusp singularity, $\mathbf{q}_0$, the coupler points P_1 and P_2 coincide with the inflection points of the coupler curves as shown in fig. 7.4a).

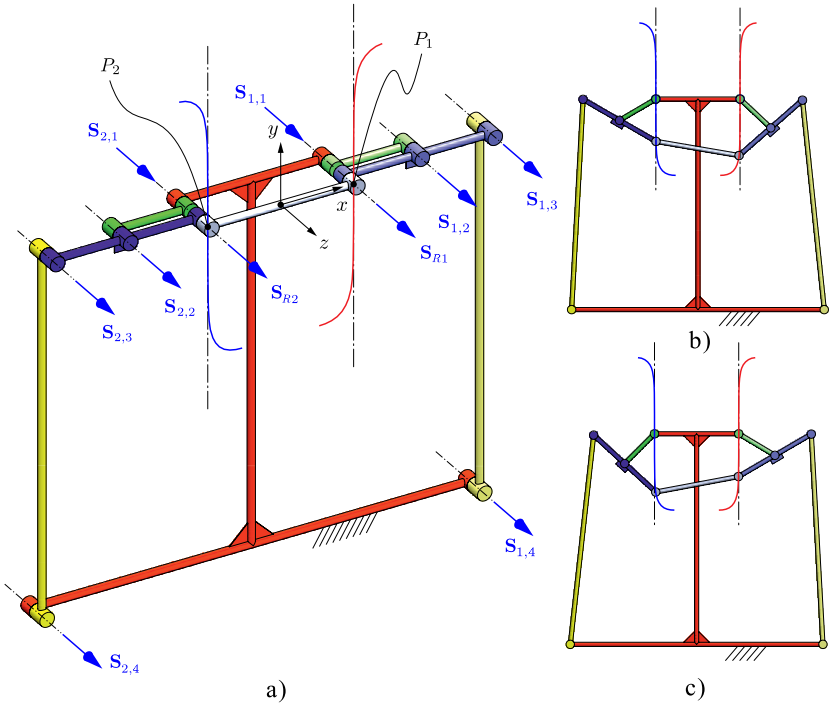

FIGURE 7.4: The double-Evans cusp mechanism: a) Cusp singularity. b) and c) two configurations near the cusp.

Cusp singularities of algebraic curves correspond to multiple solutions of the defining algebraic equations. In the above construction, the c-space is defined by the constitutive constraint equations of the two individual linkages and by the additional constraint due to the connecting link. With this construction it is clear that the order of tangency at the cusp (and thus the multiplicity of the solution) depends on the order up to which the coupler curves resemble a straight line. In the example in section 7.2.1, the double-Watt mechanism, the

coupler curves are second-order approximations of straight lines at the inflection point. Consequently, at the cusp, when moving toward and when returning from the cusp, the velocity and acceleration of the Double-Watt linkage must vanish. This observation has led Connelly and Servatius [119] to question the notion of higher-order rigidity as it is established in rigidity theory since the Double-Watt is finitely mobile although it does not allow for second- and third-order motions. The order of tangency of the two coupler curves determine the order of the cusp.

The coupler curve of the Evans mechanism shown in fig. 7.3 approximates a straight line up to the fifth-order. This can be proved by obtaining the higher-order derivatives of the position vector of point P_1 and noting that the first four derivatives are parallel to the approximated straight line and the fifth-order derivative is the first one that is non-parallel. Hence, it is expected that the c-space of the double-Evans mechanism shown in fig. 7.4 features a fifth-order cusp. This can be established by a higher-order approximation of possible finite motions through this configuration, i.e. by computing the tangents to the corresponding curves in c-space. The mathematical framework is the kinematic tangent cone $C^{\mathrm{K}}_{\mathbf{q}_0}V$ that can be determined in terms of the instantaneous joint screw coordinates [62], [140]. The instantaneous joint screws in the configuration $\mathbf{q}_0$ are

$$\begin{aligned}
&\mathbf{S}_{1,1}(\mathbf{q}_0) = (0,0,1;0,-1,0), && \mathbf{S}_{2,1}(\mathbf{q}_0) = (0,0,1;0,1,0)\\
&\mathbf{S}_{1,2}(\mathbf{q}_0) = (0,0,1;0,-2,0), && \mathbf{S}_{2,2}(\mathbf{q}_0) = (0,0,1;0,2,0)\\
&\mathbf{S}_{1,3}(\mathbf{q}_0) = (0,0,1;0,-3,0), && \mathbf{S}_{2,3}(\mathbf{q}_0) = (0,0,1;0,3,0)\\
&\mathbf{S}_{1,4}(\mathbf{q}_0) = (0,0,1;-5,-3,0), && \mathbf{S}_{2,4}(\mathbf{q}_0) = (0,0,1;-5,3,0)\\
&\mathbf{S}_{R1}(\mathbf{q}_0) = (0,0,1;0,-1,0), && \mathbf{S}_{R2}(\mathbf{q}_0) = (0,0,1;0,1,0).
\end{aligned}$$

It is found that there are non-trivial differential motions up to fifth order, whereas $C^{\mathrm{K}}_{\mathbf{q}_0}V = \{\mathbf{0}\}$. Nevertheless, it can be shown that the linkage is finitely mobile with 1 DOF as demonstrated in [144] for Connelly's mechanism.

7.3 Generation of Spatial Curves Whose Projections on Certain Planes Exhibit Inflection Points

7.3.1 The Basic Principle

The phenomenon occurring in the 8-shaped curves generated by the double-Watt mechanism can be obtained for curves in E^3. Consider a curve $\mathscr{C}_1$, which can be projected onto a plane Π in such a way that the resulting projection has an inflection point (fig. 7.5). Trace the tangent to the projected curve at the inflection point, then take a vector $\hat{\mathbf{n}}$ perpendicular to this tangent and fix a plane ρ with normal $\hat{\mathbf{N}}_\rho = \hat{\mathbf{n}}$ and located a distance $l/2$ from the inflection point. Now reflect $\mathscr{C}_1$ through ρ to obtain a curve $\mathscr{C}_2$. It can be seen that the projection of both curves onto Π is similar to the array of curves in fig. 7.2. P_1 and P_2 are the points whose projections onto Π are the inflection points, thus the distance between them is l.

Now, the case of a sphere of radius l whose center Q_1 is moving through $\mathscr{C}_1$ is analyzed. Refer to fig. 7.5b), the points O and O' lie on the curve $\mathscr{C}_1$, such that P_1 lies on the segment of $\mathscr{C}_1$ between O and O'. If Q_1 is located between points O and P_1 in fig. 7.5b), then the projection of the sphere onto Π is a circle of radius l and center lying on the projection of $\mathscr{C}_1$. Such circle does not intersect the projection of $\mathscr{C}_2$, as explained in the section 7.2.1. Therefore, the sphere does not intersect $\mathscr{C}_2$ as their projections do not intersect, the converse is not necessary true. For the case when Q_1 is located between points P_1 and O' in fig. 7.5b), consider the line segment $\overline{Q_1Q_1^r}$, where Q_1^r is the reflection of Q_1 through ρ. Then $\overline{Q_1Q_1^r}$ is parallel to $\hat{\mathbf{N}}_\rho$ and, hence, its projection onto Π has the same length. On Π it is clear that such projected segment is shorter than l, and therefore $d(Q_1,Q_1^r) < l$. Thus Q_1^r is inside the

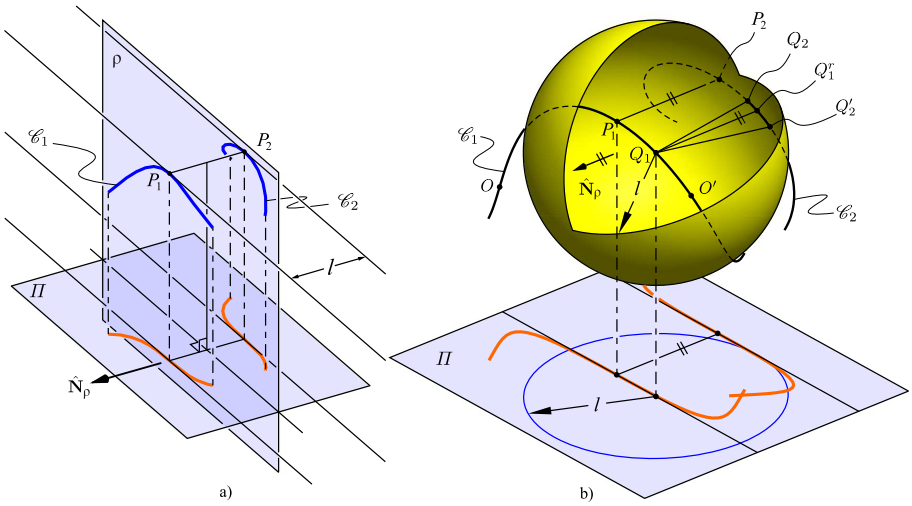

FIGURE 7.5: a) A curve (and its reflection) in 3-space which can be projected onto a plane as a curve with an inflection point. b) A sphere of radius l and center moving through such curve.

sphere with center Q_1 and radius l and $\mathscr{C}_2$ must intersect this sphere at two points Q_2 and Q_2'. As Q_1 gets closer to P_1, Q_2 and Q_2' get closer to each other until $Q_1 = P_1$ when both points coincide, i.e. $Q_2 = Q_2' = P_2$. This indicates that the solution has a cusp.

A well-known fact [145] is that, given a curve in Euclidean 3-space, its projection onto the rectifying plane at a certain point can feature an inflection point. However, this does not apply to every point on the curve, this is proved in Proposition 7.3.1[1].

Proposition 7.3.1 *The projection of a curve onto the rectifying plane at a point P has an inflection point if and only if, it has non-zero torsion at P.*

Proof: Let $\alpha(s) \in \mathbb{R}^3$ be the arc-length parametrization of a curve $\mathscr{C} := \mathrm{im}(\alpha([a,b]))$, $[a,b] \subseteq \mathbb{R}$, then, for any point $s = s_o$ where $\alpha(s)$ is C^2, the following holds:

$$\begin{aligned} \alpha'(s_o) &= \hat{\mathbf{t}}(s_o), \\ \alpha''(s_o) &= \kappa(s_o)\hat{\mathbf{n}}(s_o), \\ \alpha'''(s_o) &= -\kappa(s_o)^2\hat{\mathbf{t}}(s_o) + \kappa(s_o)\hat{\mathbf{n}}(s_o) + \kappa(s_o)\tau(s_o)\hat{\mathbf{b}}(s_o), \end{aligned} \tag{7.1}$$

where $\hat{\mathbf{t}}(s_o)$, $\hat{\mathbf{n}}(s_o)$ and $\hat{\mathbf{b}}(s_o)$ are the tangent, normal and binormal vectors of the Frenet frame at $s = s_o$ and κ and τ, the corresponding curvature and torsion at such point, respectively. Choose[2] $s_o = 0$, using the arc-length derivatives from Eq. (7.1) the Taylor expansion of $\alpha(s)$

[1] In the literature, this proof is usually made considering only the first four terms of the Taylor expansion and approximating the projected curve to a cubic curve.

[2] The proof can be made for $s_o = 0$ without loss of generality since we can always define another arc-length parametrization $\beta : [a,b] \to \mathbb{R}^3$, such that $\beta(s) = \alpha(s + s_o)$, then $\beta(0) = \alpha(s_o)$

around $s_o = 0$ is given by

$$\begin{aligned}\alpha(s) &= s\alpha'(0) + \frac{s^2}{2}\alpha''(0) + \frac{s^3}{6}\alpha'''(0) + \sum_{i=4}^{\infty}\frac{s^i}{i!}\alpha^{(i)}(0), \\ &= \left[s - \frac{1}{6}\kappa(0)^2 s^3 + \sum_{i=4}^{\infty}\frac{s^i}{i!}\alpha^{(i)}(0)\cdot\hat{\mathbf{t}}(0)\right]\hat{\mathbf{t}}(0) + \\ &\quad + \left[\frac{1}{2}\kappa(0)s^2 + \frac{1}{6}\kappa(0)s^3 + \sum_{i=4}^{\infty}\frac{s^i}{i!}\alpha^{(i)}(0)\cdot\hat{\mathbf{n}}(0)\right]\hat{\mathbf{n}}(0) + \\ &\quad + \left[\frac{1}{6}\kappa(0)\tau(0)s^3 + \sum_{i=4}^{\infty}\frac{s^i}{i!}\alpha^{(i)}(0)\cdot\hat{\mathbf{b}}(0)\right]\hat{\mathbf{b}}(0) \qquad (7.2)\end{aligned}$$

Let $\gamma(s) \in \mathbb{R}^2$ be a parametrization of the projection of $\mathscr{C}$ onto the rectifying plane at $s = 0$, which is spanned by the tangent and binormal vectors, then

$$\gamma(s) = \left(s - \frac{1}{6}\kappa(0)^2 s^3 + \sum_{i=4}^{\infty}\frac{s^i}{i!}\alpha^{(i)}(0)\cdot\hat{\mathbf{t}}(0),\ \frac{1}{6}\kappa(0)\tau(0)s^3 + \sum_{i=4}^{\infty}\frac{s^i}{i!}\alpha^{(i)}(0)\cdot\hat{\mathbf{b}}(0)\right) \qquad (7.3)$$

where the $x-$ and $y-$coordinates are taken along $\hat{\mathbf{t}}(0)$ and $\hat{\mathbf{b}}(0)$, respectively.

To prove that $s = 0$ is a potential inflection point, we consider the curvature of $\gamma(s)$, which has to be zero at an inflection point. Zero curvature in a planar parametric curve implies that $f(s) := x'(s)y''(s) - y'(s)x''(s)$ vanishes at $s = 0$. From Eq (7.3), it follows that $\gamma'(0) = (1,0)$ and $\gamma''(0) = (0,0)$, therefore $f(0) = 0$. However, at an inflection point the curvature is not only zero, but it is also changing its sign, thus $f'(s) \neq 0$ at $s = 0$ is required. After derivation it follows that $f'(0) = -\kappa(0)\tau(0)$. Notice that $\kappa(0)$ is the curvature of $\mathscr{C}$ at $s = 0$. In order to define the Frenet apparatus it is required that $\kappa(0) \neq 0$, however $\tau(0) = 0$ is possible and would imply that the projected curve does not present an inflection point at $s = 0$. It is concluded that the projection of a curve onto the rectifying plane at a point has an inflection point if and only if it has non-zero torsion at such point. ■

7.3.2 Generating Curves with Inflection Points by Projecting the Intersection of Surfaces

The manipulation of curves becomes easy when considering them as the intersection of two surfaces. The Frenet apparatus can be computed using the local properties of the surfaces [146]. Hence, it is not required to find a parametrization of the intersection curve as long as the parameterizations or implicit forms of the surfaces are known and local properties, i.e. normal vector, principal directions and principal normal curvatures, are available.

Fig. 7.6a) shows a curve $\mathscr{C}_1$ obtained by intersecting two cylinders, $\mathcal{S}_1^A$ and $\mathcal{S}_1^B$. At the point P_1 with non-vanishing torsion, the Frenet frame is shown. The curve is projected onto a plane Π parallel to the rectifying plane at P_1. The resulting 8-shaped planar curve has an inflection point at the projection of P_1. Thus, following the idea previously explained, $\mathcal{S}_2^A$ and $\mathcal{S}_2^B$ are the reflections of $\mathcal{S}_1^A$ and $\mathcal{S}_1^B$, respectively, and their intersection, $\mathscr{C}_2$ is a reflection of $\mathscr{C}_1$. On the other hand, fig. 7.6b) shows the same curve and its Frenet frame at a zero-torsion point, Q. The projection of $\mathscr{C}_1$ onto the rectifying plane leads to a curve with zero curvature at the projection of Q, however, this is not an inflection point.

An even simpler way of obtaining a projection with an inflection point is using spatial 8-shaped curves or 2-winged curves with two planes of symmetry. These can be easily obtained by intersecting surfaces that become tangent to each other at an isolated point, this point becomes the self-crossing of the 8-shaped curve. Fig. 7.7 shows the Viviani curve, $\mathscr{C}$,

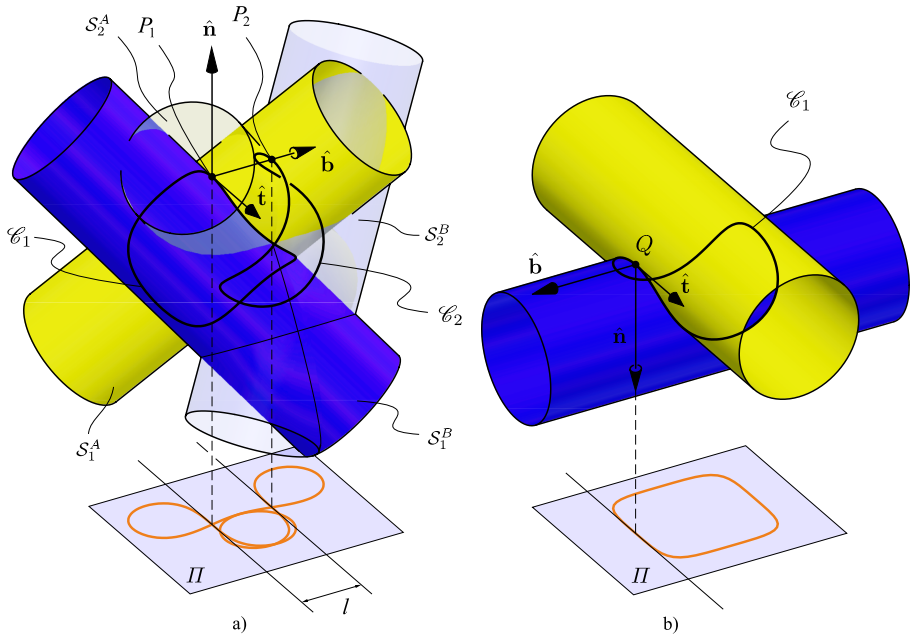

FIGURE 7.6: The curve $\mathscr{C}_1$ as the intersection of two cylinders and its projection onto rectifying plane. a) The projection happens at a non-zero torsion point and the surfaces are reflected. b) The projection occurs at a zero-torsion point.

obtained from the intersection of a cylinder, $\mathcal{S}^A$, and a sphere , $\mathcal{S}^B$, which are tangent to each other at P, and, hence, they have the same normal vector $\hat{\mathbf{N}}$ at such point. $\mathscr{C}$ has two planes of symmetry which contain $\hat{\mathbf{N}}$. Let Π be a plane parallel to $T_P\mathcal{S}^A = T_P\mathcal{S}^B$, and, therefore, having normal $\hat{\mathbf{N}}$, then the projection of $\mathscr{C}$ onto Π is a symmetric 8-shaped planar curve with two branches intersecting at the projection of P onto Π. Each branch has an inflection point and considering the two tangent vectors $\hat{\mathbf{t}}_1$ and $\hat{\mathbf{t}}_2$ there are two possible planes that can be used to reflect both surfaces.

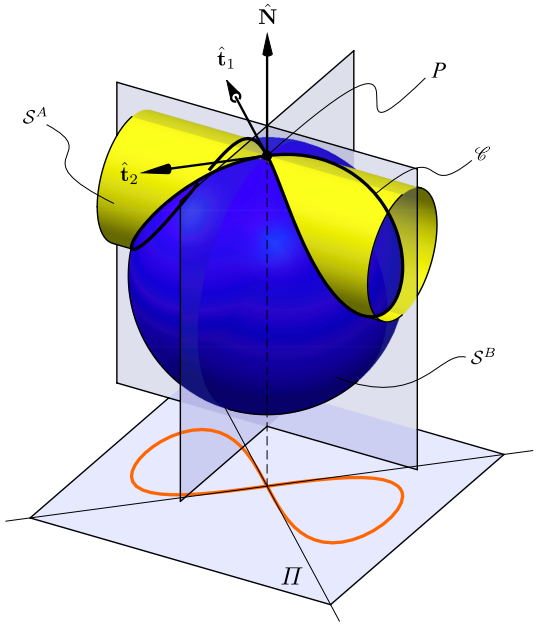

FIGURE 7.7: The Viviani curve as an intersection of surfaces and its projection onto a plane parallel to the tangent plane at the self-crossing.

It is not necessary to calculate a parametrization of $\mathscr{C}$ since $\hat{\mathbf{t}}_1$ and $\hat{\mathbf{t}}_2$ can be obtained from the local properties of $\mathcal{S}_A$ and $\mathcal{S}_B$, namely, the principal curvatures and common normal vector. The normal curvature of both surfaces is the same at P in the $\hat{\mathbf{t}}_1$ and $\hat{\mathbf{t}}_2$ directions, hence, using Euler's formula [147] for normal curvature it follows:

$$\kappa^{\mathrm{n}}_{A,1}\cos^2\phi_A + \kappa^{\mathrm{n}}_{A,2}\sin^2\phi_A = \kappa^{\mathrm{n}}_{B,1}\cos^2\phi_B + \kappa^{\mathrm{n}}_{B,2}\sin^2\phi_B \tag{7.4}$$

where, for $i = A, B$, $\kappa^{\mathrm{n}}_{i,1}$ and $\kappa^{\mathrm{n}}_{i,2}$ are the principal normal curvatures of $\mathcal{S}^i$, and ϕ_i is the angle from the principal direction $\hat{\mathbf{e}}_{i,1}$ to some tangent to the intersection curve. Since all principal directions, $\hat{\mathbf{e}}_{A,1}$, $\hat{\mathbf{e}}_{A,2}$, $\hat{\mathbf{e}}_{B,1}$ and $\hat{\mathbf{e}}_{B,2}$ are expected to be known, a linear restriction $\phi_B(\phi_A)$ is known and can be substituted in Eq. (7.4) to obtain one non-linear equation in the unknown ϕ_A. For this case, two solutions are expected, each related to the respective tangent to the intersection curve. If (7.4) has no solution, the surfaces are touching at P, which is in such case an isolated point (intersection in one point). If (7.4) has a double root, then the intersection of the surfaces is a curve containing P.

7.4 Construction of cusp mechanisms

7.4.1 Mechanical Generators for the Intersection of Surfaces

It is known [148]–[150] that symmetric spatial 8-shaped curves, similar to the Viviani curve, can be traced by coupler points of spherical 4-bar and crank-slider mechanisms. However, from the previous discussion it is clear that the use of intersection curves can ease the design of mechanisms with cusps in the configuration space. The first step is to generate the appropriate surfaces by using two kinematic dyads, and the second step is to appropriately connect them so to form a 1-DOF closed loop mechanism.

A variety of surfaces can be generated by the end link of kinematic dyads. These surfaces can be ruled surfaces (one of the kinematic pairs is a prismatic joint), surfaces of revolution (the first joint is a revolute) or helical surfaces (the first kinematic pair is a helical joint), among other forms.

Let A and B be two kinematic dyads, whose points E_1^A and E_1^B, defined at the end links, generate the surfaces $\mathcal{S}_1^A$ and $\mathcal{S}_1^B$, respectively. If the end links of both dyads are connected so that $E_1 := E_1^A = E_1^B$, then E_1 is confined to move on $\mathcal{S}_1^A \cap \mathcal{S}_1^B$. The end link must be connected by an adequate number of revolute joints with axes meeting E_1 to allow for the necessary relative rotation between the end links. Since the position of E_1^A and E_1^B is enforced to coincide with E_1, no further kinematic joints are required to ensure the 1-DOF motion of the closed loop mechanism.

Fig. 7.8 shows the four possible cases depending on the number of revolute joints intersecting E_1 that are required to make the linkage mobile. If the number of these revolute joints is three, the resulting mechanism has seven kinematic pairs and it is non-overconstrained. However, if less than three revolute joints are required to join E_1 and E_2, then the mechanism is overconstrained. The number of these revolute joints is always 2 or 1 for the intersection of ruled surfaces as well as in cases when one of the surfaces is a plane. In some other cases where certain constraints between the construction parameters of the surfaces lead to special symmetries, the number of revolute joints intersecting at E_1 (respectively E_2) can be reduced to 2 or 1, and the mechanism becomes a paradoxical mechanism [44], [151], [152]. An example is shown in Section 7.5 where the intersection of two toroids leads to a Bricard plane-symmetric paradoxical 6R mechanism.

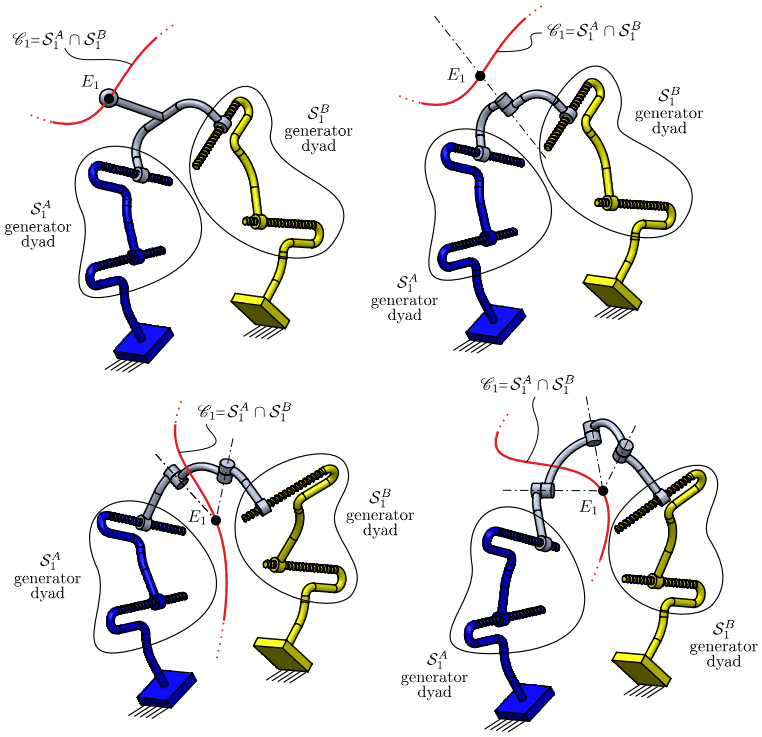

FIGURE 7.8: The four different cases of one-loop mechanisms obtained from the intersection of surfaces.

7.4.2 Interconnection of the Curve Generator with its Mirrored Copy

Once a mechanism is defined whose coupler curve $\mathscr{C}_1 \subseteq \mathcal{S}_1^A \cap \mathcal{S}_1^B$ can be projected onto a plane such that at certain point P_1 the projected curve has an inflection, this mechanism is mirrored so that the new generated surfaces, $\mathcal{S}_2^A$ and $\mathcal{S}_2^B$, are reflections of $\mathcal{S}_1^A$ and $\mathcal{S}_1^B$, as explained in Section 7.3. The reflected closed-loop kinematic chain consist of two dyads joined by an adequate number of revolute joints with axes meeting at point E_2 that generates the intersection curve $\mathscr{C}_2$. Finally, points E_1 and E_2 are joined with a coupler bar of length l. The length l is not restricted as explained in section 7.2.1. This bar is connected to the two curve generator mechanisms by means of a spherical pair (S) at one of its ends and a universal joint (U) at the other end. These allow unlimited relative rotations of the curve generators, while the U joint eliminates a passive degree of freedom that would be present if both ends of the coupler bar were connected by S joints. Namely, the bar could spin about its longitudinal axis. It is also possible to connect the two curve generator mechanisms by means of a URU kinematic chain where the axis of the R joint intersects the centers of the U joints.

With the above described construction, the generated mechanism possesses three topologically independent loops as shown in fig. 7.9.

7.4.3 Summary of the Proposed Method

The procedure discussed in the previous section can be summarized as a set of steps to obtain spatial mechanisms with a cusp in the configuration space.

1. Find two surfaces, $\mathcal{S}_1^A$ and $\mathcal{S}_1^B$, that can be generated by kinematic dyads and whose intersection curve $\mathscr{C}_1$ can be projected onto a plane Π to obtain an inflection point. Fix $P_1 \in \mathscr{C}_1$ at the point whose projection is the inflection point.

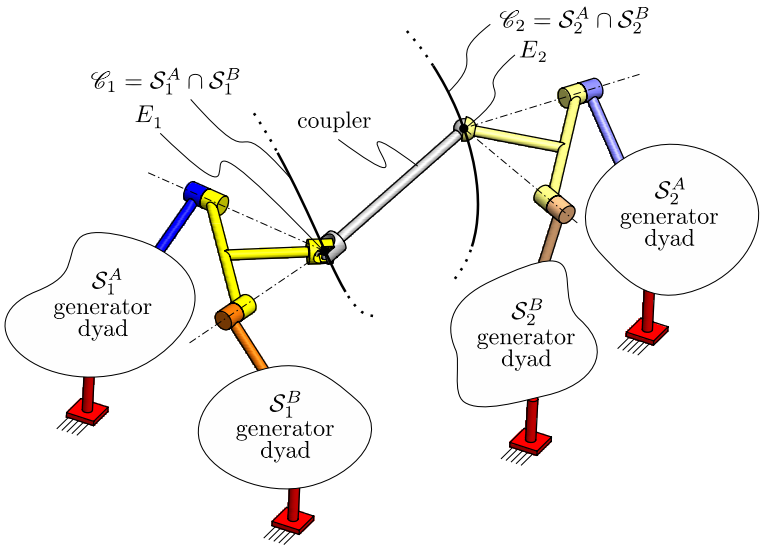

FIGURE 7.9: The general form of a cusp mechanism in the case in which two revolute joints allow the motion about E_1 and E_2 at $\mathscr{C}_1$ and $\mathscr{C}_2$, respectively.

2. Find the tangent vector $\hat{\mathbf{t}}$ to the curve at P_1.

3. Define a reflection plane ρ perpendicular to Π, with normal being perpendicular to $\hat{\mathbf{t}}$ and placed a distance $l/2$ from P_1.

4. Design a 1-loop mechanism that generates $\mathscr{C}_1$: obtain kinematic dyads that generate $\mathcal{S}_1^A$ through E_1^A and $\mathcal{S}_1^B$ through E_1^B, join their end-links so that $E_1 = E_1^A = E_1^B$ with the required number of revolute joints with axes intersecting E_1.

5. Mirror the mechanism through ρ. The point E_2 in the reflected mechanism generates $\mathscr{C}_2$.

6. Join points E_1 and E_2 with a coupler bar of length l with a spherical (S) joint at one of its endings and a universal joint (U) in the other. The result is a 1-DOF 3-loop cusp mechanism. The coupler bar is connected via S and U joints in order to avoid a passive motion of the bar (spinning about its longitudinal axis that would be introduced if two *S* joints were used). In the case that the generated curves are planar the coupler bar is connected to the two curve generators by means of revolute joints with axes that are perpendicular to the plane that contains the curves.

7.5 Examples

In this section three examples of spatial cusp mechanisms are presented. Each step from section 7.4.3 is described. The screws of the joints in the mechanism are presented for the cusp configuration $\mathbf{q}_0 \in V$. For that aim, a coordinate frame 0 is fixed with origin in the middle point of $\overline{P_1P_2}$ and with y_0-axis perpendicular to the reflection plane ρ. At the cusp configuration, the joint screw coordinate vectors of the mechanism generating $\mathscr{C}_1$ are determined in coordinate frame 0, denoted with ${}^0\mathbf{S}_{1,i} := ({}^0\hat{\mathbf{s}}_{1,i};\, {}^0\mathbf{r}_{1,i} \times {}^0\hat{\mathbf{s}}_{1,i} + h_{1,i}\,{}^0\hat{\mathbf{s}}_{1,i})$, $i = 1,\ldots,5$. Finding ${}^0\mathbf{S}_{2,i}$, $i = 1,\ldots,5$ becomes easy since ${}^0\hat{\mathbf{s}}_{2,i} = \mathrm{Ref}(\hat{\mathbf{j}})\,{}^0\hat{\mathbf{s}}_{1,i}$, ${}^0\mathbf{r}_{2,i} = \mathrm{Ref}(\hat{\mathbf{j}})\,{}^0\mathbf{r}_{1,i}$ and $h_{2,i} = -h_{1,i}$. Since screw coordinates are always represented in the coordinate frame 0, the reference to this frame is omitted: ${}^0\mathbf{S} = \mathbf{S}$.

7.5.1 A Spatial Mechanism Generating Planar Curves

Step 1: Two frames, A_1 and B_1, are defined as shown in fig. 7.10a). $\mathcal{S}_1^A := \text{im}(\sigma_1^A(\mathbb{R}^2))$, where ${}^{A_1}\sigma_1^A(u,v) := (u,v,0)$, is a plane. $\mathcal{S}_1^B := \text{im}(\sigma_1^B(\mathbb{R}^2))$, where ${}^{B_1}\sigma_1^B(u,v) := (d\cos u, v, hu)$, is the result of extruding a cosine curve in the $x_1^B z_1^B$ plane through the y_1^B axis. This surface looks like a corrugated roof. The origins of frames A_1 and B_1 coincide and ${}^{A_1}_{B_1}\mathbf{R} := \text{Rot}\left(\pi/6, \hat{\mathbf{i}}\right)$ as shown in fig. 7.10a). $\mathscr{C}_1 = \text{im}(\alpha(\mathbb{R}))$, where ${}^{A_1}\alpha(u) := (d\cos u, 2hu, 0)$ is a cosine function in the $x_1^A y_1^A$ plane. Such planar curve has an inflection point whenever it crosses the y_1^A-axis. We can choose any of these points and fix P_1 there, as shown in fig. 7.10c). In this example we consider $d = 10$ and $h = 5/(2\pi)$.

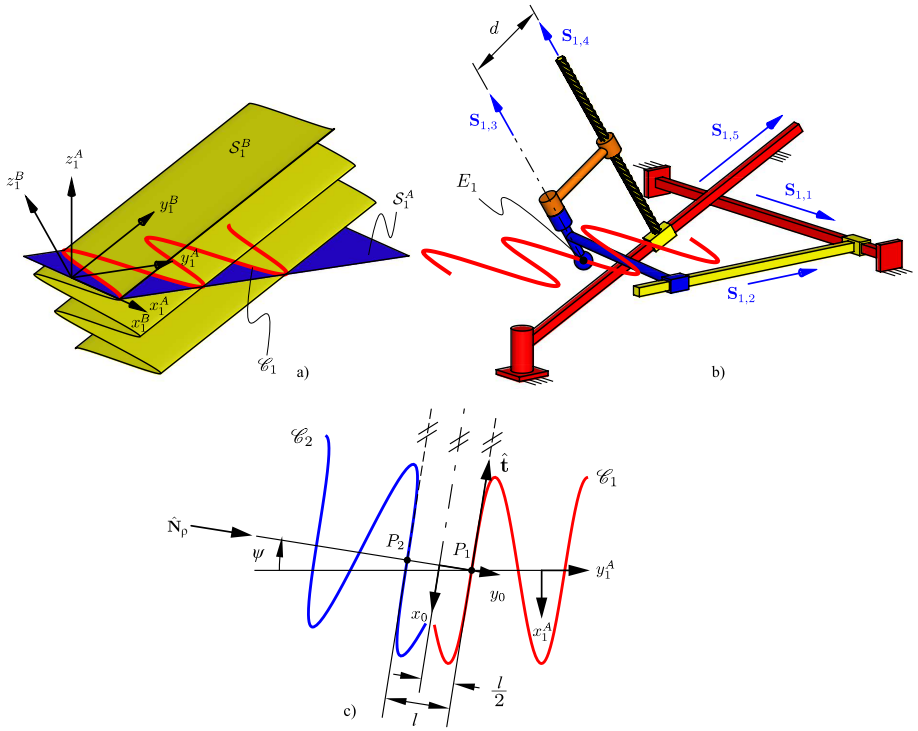

FIGURE 7.10: The intersection of two surfaces that leads to a planar curve with inflection points. a) Surfaces setup. b) Overconstrained mechanism that generates such curve. c) Reflection of the intersection curve

Step 2: ${}^{A_1}\hat{\mathbf{t}} = (1/k, -2\pi/k, 0)$, where $k = \sqrt{1+4/\pi^2}$.

Step 3: $\hat{\mathbf{N}}_\rho$ lies on $x_1^A y_1^A$ and is perpendicular to $\hat{\mathbf{t}}$ as shown in fig. 7.10c). The orientation of coordinate system 0 with respect to A_1 is given by ${}^{A_1}_{0}\mathbf{R} = \text{Rot}(\psi, \hat{\mathbf{k}})$, with $\psi = \arctan(2\pi)$.

Step 4: $\mathcal{S}_1^A$ is generated by a pair of prismatic joints with axes parallel to any non-parallel vectors in $x_1^A y_1^A$ plane. $\mathcal{S}_1^B$ is generated by $\{\mathbf{S}_{1,5}, \mathbf{S}_{1,4}\}$ (see fig. 7.10b), where $\mathbf{S}_{1,5}$ represents a prismatic joint with axis parallel to y_1^B and $\mathbf{S}_{1,4}$ represents a helical joint of pitch h and axis perpendicular to $\mathbf{S}_{1,5}$. $\mathcal{S}_1^B$ is generated by a point E_1 fixed to the end link and located a distance d from $\mathbf{S}_{1,4}$ (see [1]). E_1^A and E_1^B are joined by a single revolute joint with axis $\mathbf{S}_{1,3}$ passing through E_1. This revolute joint compensates the rotation of the helical joint, so that $\mathrm{d}^n q_{1,4}/\mathrm{d}t^n = -\mathrm{d}^n q_{1,3}/\mathrm{d}t^n, \forall n \in \mathbb{Z}$.

Steps 5 and 6: Fig. 7.11a) shows the 3-loop mechanism obtained after mirroring the overconstrained linkage, obtained in step 4, through a plane perpendicular to the z-axis and containing the origin O. The two mechanisms are connected through a coupler bar of length $l = 7$. Since $\mathscr{C}_1$ and $\mathscr{C}_2$ are planar curves, the coupler bar is attached via revolute joints with axes $\mathbf{S}_{R1}$ and $\mathbf{S}_{R2}$ parallel to z_1^A. The topological graph is shown in fig. 7.11b).

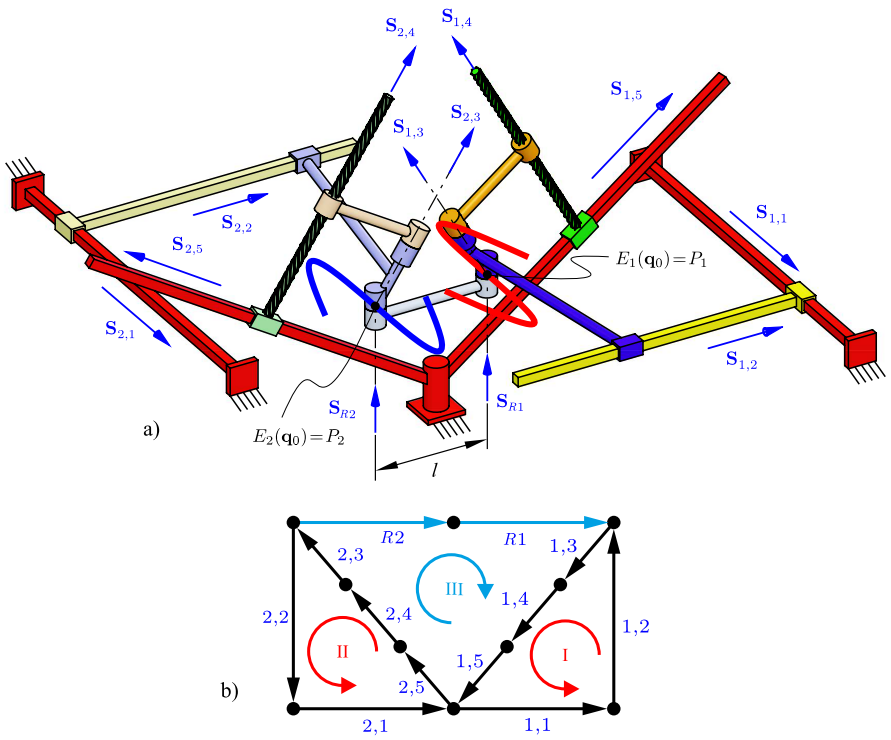

FIGURE 7.11: a) A mechanism that generates two planar curves of the cosine form in a cusp configuration. b) Topological graph

Analysis of smooth motions through $\mathbf{q}_0$: The screw coordinates at the cusp are

$$
\begin{aligned}
\mathbf{S}_{1,1}(\mathbf{q}_0) &= (0,0,0;1,0,0),\\
\mathbf{S}_{1,2}(\mathbf{q}_0) &= (0,0,0;0,1,0),\\
\mathbf{S}_{1,3}(\mathbf{q}_0) &= \left(\frac{1}{2k},-\frac{\pi}{k},\frac{\sqrt{3}}{2};\frac{7\sqrt{3}}{2},0,-\frac{7}{4k}\right),\\
\mathbf{S}_{1,4}(\mathbf{q}_0) &= \left(\frac{1}{2k},-\frac{\pi}{k},\frac{\sqrt{3}}{2};\frac{7\pi\sqrt{3}k+80\pi^2+5}{4\pi k},\frac{15}{2k},\frac{20\sqrt{3}\pi^2-7\pi k+5\sqrt{3}}{16\pi^3+4\pi}\right),\\
\mathbf{S}_{1,5}(\mathbf{q}_0) &= \left(0,0,0;-\frac{\sqrt{3}}{2k},\frac{\sqrt{3}\pi}{k},\frac{1}{2}\right),\\
\mathbf{S}_{2,1}(\mathbf{q}_0) &= (0,0,0;1,0,0),\\
\mathbf{S}_{2,2}(\mathbf{q}_0) &= (0,0,0;0,1,0),\\
\mathbf{S}_{2,3}(\mathbf{q}_0) &= \left(\frac{1}{2k},\frac{\pi}{k},\frac{\sqrt{3}}{2};-\frac{7\sqrt{3}}{4},0,\frac{7}{4k}\right),
\end{aligned}
$$

$$\mathbf{S}_{2,4}(\mathbf{q}_0) = \left(\frac{1}{2k}, \frac{\pi}{k}, \frac{\sqrt{3}}{2}; \frac{-7\pi\sqrt{3}k - 80\pi^2 - 5}{4\pi k}, \frac{15}{2k}, \frac{-20\sqrt{3}\pi^2 + 7\pi k - 5\sqrt{3}}{16\pi^3 + 4\pi}\right),$$

$$\mathbf{S}_{2,5}(\mathbf{q}_0) = \left(0, 0, 0; -\frac{\sqrt{3}}{2k}, -\frac{\sqrt{3}\pi}{k}, \frac{1}{2}\right),$$

$$\mathbf{S}_{R1}(\mathbf{q}_0) = \left(0, 0, 1; \frac{7}{2}, 0, 0\right),$$

$$\mathbf{S}_{R2}(\mathbf{q}_0) = \left(0, 0, 1; -\frac{7}{2}, 0, 0\right).$$

The kinematic tangent cone is therewith found to be $C^{\mathrm{K}}_{\mathbf{q}_0} V = \{\mathbf{0}\}$. That is, there is no smooth curve passing through the singular reference configuration.

7.5.2 A Double-Koenigs Mechanism

Step 1: $\mathcal{S}_1^A := \mathrm{im}(\sigma_1^A(\mathbb{T}\times\mathbb{R}))$, where ${}^{A_1}\sigma_1^A(u,v) := (v, d\cos u, d\sin u)$, is a right cylinder (with axis being perpendicular to the plane that contains the circle) of radius d and with axis along x_1^A and $\mathcal{S}_1^B := \mathrm{im}(\sigma_1^B(\mathbb{T}\times\mathbb{R}))$, where ${}^{B_1}\sigma_1^B(u,v) := (v, (d/2)\cos u, (d/2)\sin u)$, is another right cylinder with radius $d/2$ and axis along x_1^B. The origin of frame B_1 with respect to the origin of frame A_1 is displaced by ${}^{A_1}\mathbf{r}_{B_1/A_1} = (0,0,d/2)$ and their relative orientation is given by ${}^{A_1}_{B_1}\mathbf{R} := \mathrm{Rot}(\pi/2, \hat{\mathbf{k}})$ as shown in figure 7.12a). $\mathscr{C}_1$ is an 8-shaped curve with two planes of symmetry. Therefore, its projection onto the $x_1^A y_1^A$ plane has an inflection point at the projection of the self-crossing. We set P_1 at the self crossing, as shown in fig. 7.12c). For this example we consider $d = 2$.

Step 2: $\hat{\mathbf{t}}_1$ and $\hat{\mathbf{t}}_2$ are obtained using Eq. (7.4). Since the cylinders are surfaces of revolution, the principal curvatures are the curvatures of the meridians and parallels passing through the point. Hence, $\kappa^{\mathrm{n}}_{A,1} = d$, $\kappa^{\mathrm{n}}_{A,2} = 0$ and $\kappa^{\mathrm{n}}_{B,1} = d/2$ and $\kappa^{\mathrm{n}}_{B,2} = 0$. Two solutions are found for equations (7.4): $\phi_{A,1} = \pi/2 - \arccos(\sqrt{6}/3)$ and $\phi_{A,2} = 3\pi/2 - \arccos(\sqrt{6}/3)$. We choose $\psi = \phi_{A,1}$, the angle between $\hat{\mathbf{t}}_1$ and the x_1^A axis, as shown in fig. 7.12c). Then, ${}^{A_1}\mathbf{t}_1 = (\cos\psi, \sin\psi, 0)$.

Step 3: $\hat{\mathbf{N}}_\rho$ lies on $x_1^A y_1^A$ and is perpendicular to $\hat{\mathbf{t}}_1$ as shown in fig. 7.12c). The orientation of coordinate system 0 with respect to A_1 is given by ${}^{A_1}_{0}\mathbf{R} = \mathrm{Rot}(\psi, \hat{\mathbf{k}})$.

Step 4: $\mathcal{S}_1^A$ and $\mathcal{S}_1^B$ are generated by RP dyads that allow permutation. In fig. 7.12b) $\mathcal{S}_1^A$ is generated by the dyad $\{\mathbf{S}_{1,1}, \mathbf{S}_{1,2}\}$ and $\mathcal{S}_1^B$ is generated by $\{\mathbf{S}_{1,6}, \mathbf{S}_{1,5}\}$. To join the end links of both dyads, two revolute joints with axes parallel to the axes of the cylinders and intersecting at E_1 are required. The result is the overconstrained mechanism shown in fig. 7.12b) which is known as the Koenigs joint [8], [86]. At $E_1 = P_1$ its coupler curve has a bifurcation.

Steps 5 and 6: Fig. 7.13 shows the 3-loop mechanism obtained after reflecting the overconstrained linkage obtained in step 4 and adding a coupler bar of length $l = 2$.

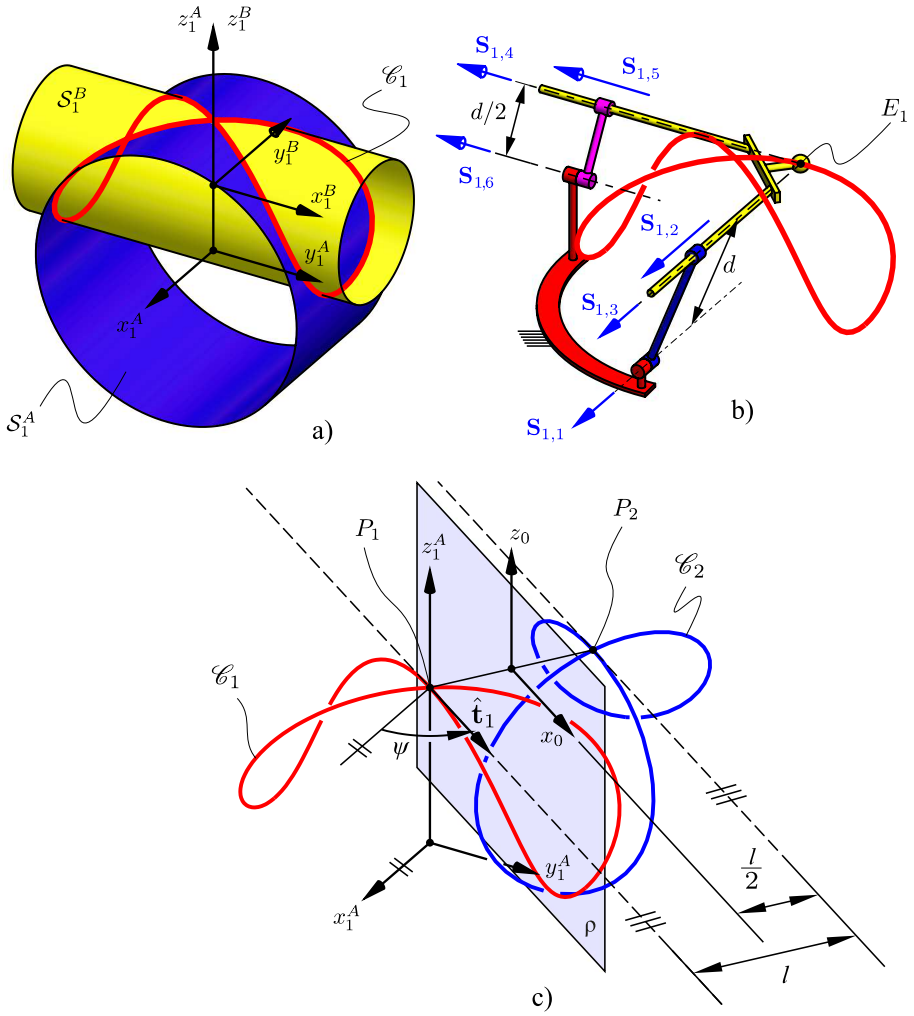

FIGURE 7.12: The intersection of two cylinders that has a projection with an inflection point. a) Surfaces setup. b) The Koenigs joint that generates such intersection. c) reflection of the intersection curve

Analysis of smooth motions through $\mathbf{q}_0$: The screw coordinates at the cusp are

$$
\begin{aligned}
\mathbf{S}_{1,1}(\mathbf{q}_0) &= \left(\frac{\sqrt{3}}{3}, -\frac{\sqrt{6}}{3}, 0; -\frac{2\sqrt{6}}{3}, -\frac{2\sqrt{3}}{3}, \frac{\sqrt{3}}{3}\right),\\
\mathbf{S}_{1,2}(\mathbf{q}_0) &= \left(0, 0, 0; \frac{\sqrt{3}}{3}, -\frac{\sqrt{6}}{3}, 0\right),\\
\mathbf{S}_{1,3}(\mathbf{q}_0) &= \left(\frac{\sqrt{3}}{3}, -\frac{\sqrt{6}}{3}, 0; 0, 0, \frac{\sqrt{3}}{3}\right),\\
\mathbf{S}_{1,4}(\mathbf{q}_0) &= \left(\frac{\sqrt{6}}{3}, \frac{\sqrt{3}}{3}, 0; 0, 0, \frac{\sqrt{6}}{3}\right),\\
\mathbf{S}_{1,5}(\mathbf{q}_0) &= \left(0, 0, 0; \frac{\sqrt{6}}{3}, \frac{\sqrt{3}}{3}, 0\right),\\
\mathbf{S}_{1,6}(\mathbf{q}_0) &= \left(\frac{\sqrt{6}}{3}, \frac{\sqrt{3}}{3}, 0; \frac{\sqrt{3}}{3}, -\frac{\sqrt{6}}{3}, \frac{\sqrt{6}}{3}\right),\\
\mathbf{S}_{2,1}(\mathbf{q}_0) &= \left(\frac{\sqrt{3}}{3}, \frac{\sqrt{6}}{3}, 0; \frac{2\sqrt{6}}{3}, -\frac{2\sqrt{3}}{3}, -\frac{\sqrt{3}}{3}\right),
\end{aligned}
$$

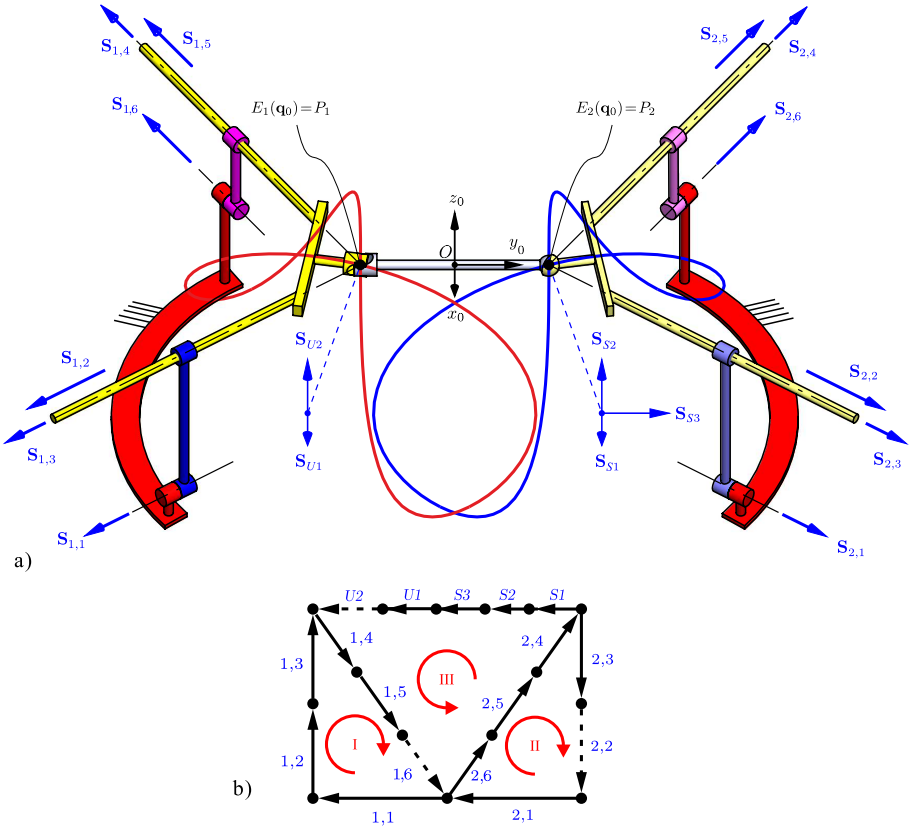

FIGURE 7.13: A double-Koenigs mechanism in a cusp configuration.

$$
\begin{aligned}
\mathbf{S}_{2,2}(\mathbf{q}_0) &= \left(0,0,0;\frac{\sqrt{3}}{3},\frac{\sqrt{6}}{3},0\right),\\
\mathbf{S}_{2,3}(\mathbf{q}_0) &= \left(\frac{\sqrt{3}}{3},\frac{\sqrt{6}}{3},0;0,0,-\frac{\sqrt{3}}{3}\right),\\
\mathbf{S}_{2,4}(\mathbf{q}_0) &= \left(\frac{\sqrt{6}}{3},-\frac{\sqrt{3}}{3},0;0,0,-\frac{\sqrt{6}}{3}\right),\\
\mathbf{S}_{2,5}(\mathbf{q}_0) &= \left(0,0,0;\frac{\sqrt{6}}{3},-\frac{\sqrt{3}}{3},0\right),\\
\mathbf{S}_{2,6}(\mathbf{q}_0) &= \left(\frac{\sqrt{6}}{3},-\frac{\sqrt{3}}{3},0;-\frac{\sqrt{3}}{3},-\frac{\sqrt{6}}{3},-\frac{\sqrt{6}}{3}\right),\\
\mathbf{S}_{U1}(\mathbf{q}_0) &= (1,0,0;0,0,1),\\
\mathbf{S}_{U2}(\mathbf{q}_0) &= (0,0,1;-1,0,0),\\
\mathbf{S}_{S1}(\mathbf{q}_0) &= (1,0,0;0,0,-1),\\
\mathbf{S}_{S2}(\mathbf{q}_0) &= (0,1,0;0,0,0),\\
\mathbf{S}_{S3}(\mathbf{q}_0) &= (0,0,1;1,0,0),
\end{aligned}
$$

With these screw coordinates, the kinematic tangent cone is determined as $C^{\mathrm{K}}_{\mathbf{q}_0}V = C^{\mathrm{K}}_{\mathbf{q}_0}V_1 \cup C^{\mathrm{K}}_{\mathbf{q}_0}V_2 \cup C^{\mathrm{K}}_{\mathbf{q}_0}V_3$ where

$$
\begin{aligned}
C^{\mathrm{K}}_{\mathbf{q}_0}V_1 &= \Big\{ \mathbf{x} \;\Big|\; x_{11}=x_{12}=x_{13}=x_{14}=x_{15}=x_{16}=0, x_{U1}=x_{S1}=x_{S2}=0, x_{21}=\frac{1}{\sqrt{2}}s, \\
&\qquad x_{22}=10s, x_{23}=-\frac{1}{\sqrt{2}}s, x_{24}=-s, x_{25}=-10\sqrt{2}s, x_{26}=s, x_{U2}=-\frac{\sqrt{3}}{2}s, \\
&\qquad x_{S3}=\frac{\sqrt{3}}{2}s \text{ with } s\in\mathbb{R}\Big\} \\
C^{\mathrm{K}}_{\mathbf{q}_0}V_2 &= \Big\{ \mathbf{x} \;\Big|\; x_{11}=\frac{1}{\sqrt{2}}s, x_{12}=-10s, x_{13}=-\frac{1}{\sqrt{2}}s, x_{14}=-s, x_{15}=10\sqrt{2}s, x_{U2}=\frac{\sqrt{3}}{2}s, \\
&\qquad x_{S3}=-\frac{\sqrt{3}}{2}s, x_{16}=s, x_{21}=x_{22}=x_{23}=x_{24}=x_{25}=x_{26}=0, \\
&\qquad x_{U1}=x_{S1}=x_{S2}=0 \text{ with } s\in\mathbb{R}\Big\} \\
C^{\mathrm{K}}_{\mathbf{q}_0}V_3 &= \Big\{ \mathbf{x} \;\Big|\; x_{11}=\frac{1}{\sqrt{2}}s, x_{12}=-10s, x_{13}=-\frac{1}{\sqrt{2}}s, x_{14}=-s, x_{15}=10\sqrt{2}s, x_{21}=\frac{1}{\sqrt{2}}s, \\
&\qquad x_{22}=10s, x_{23}=-\frac{1}{\sqrt{2}}s, x_{24}=-s, x_{25}=-10\sqrt{2}s, x_{26}=s, x_{16}=s, \\
&\qquad x_{U1}=x_{U2}=x_{S1}=x_{S2}=x_{S3}=0 \text{ with } s\in\mathbb{R}\Big\}. \qquad (7.5)
\end{aligned}
$$

Each $C^{\mathrm{K}}_{\mathbf{q}_0}V_i, i=1,2,3$ is a 1-dimensional vector space. These are the tangent spaces to the manifolds V_i intersecting at $\mathbf{q}_0$, shown in fig. 7.14. The motion branches V_4 and V_5 shown in the figure are not smooth manifolds and curves in V_4 and V_5 are not smooth at $\mathbf{q}_0$. Therefore, their tangent aspects are not revealed by the kinematic tangent cone, which consists of tangents to smooth curves.

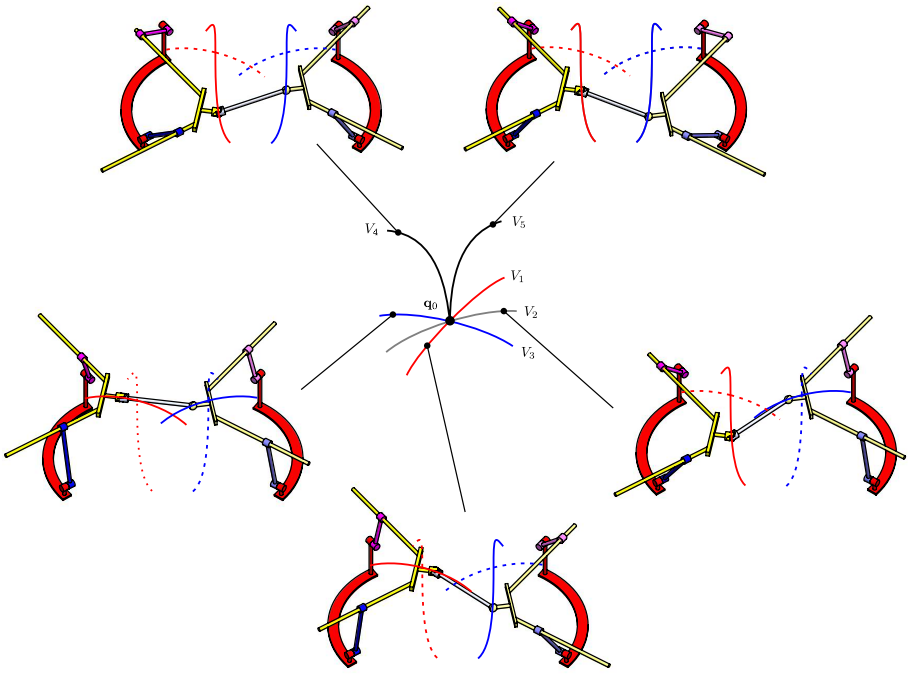

FIGURE 7.14: Different branches of the configuration space intersecting at $\mathbf{q}_0$.

Discussion on branches: $\mathbf{q}_0 \in V$ is a cusp in the configuration space of the double-Koenigs mechanism when $E_1(\mathbf{q}_0) = P_1$ and $E_2(\mathbf{q}_0) = P_2$. Refer to fig. 7.14. There are two branches, V_1 and V_2, in the configuration space which are cut off at $\mathbf{q}_0$, each related to each of the two solutions explained in Section 7.3. However, since the self crossing of $\mathscr{C}_i$ is regular in both $\mathcal{S}_i^A$ and $\mathcal{S}_i^B$, $i = 1,2$, points E_1 and E_2 are able to move through the other branches of the self-crossings. As a consequence of this, three regular curves, V_1, V_2 and V_3, are intersecting at $\mathbf{q}_0$. These three curves represent smooth motions of E_1 and E_2 through different combination of the branches intersecting at the self-crossings of $\mathscr{C}_1$ and $\mathscr{C}_2$. Fig. 7.14 shows a (regular) configuration of the mechanism in each branch.

7.5.3 A Kinematotropic Double-Bricard Mechanism

Step 1: Consider the following parametrization:

$$\sigma(u,v) := d\Big((\cos v+1)\cos u - \cos\gamma\sin v\sin u,\ \cos\gamma\sin v\cos u + \sin u\cos v + \sin u,\ \sin\gamma\sin v\Big),$$

so that $\mathcal{S} := \mathrm{im}(\sigma(\mathbb{T}^2))$ is a toroid in which the radius of both the base circle and the secondary circle are d. Thus, it has a conic singularity at the center of the base circle. The tilting angle between the planes containing the secondary circle and the base circle is γ and the axis of the toroid is the $z-$axis. Consider the toroids $\mathcal{S}_1^A := \mathrm{im}(\sigma_1^A(\mathbb{T}^2))$, where ${}^{A_1}\sigma_1^A(u,v) := \sigma(u,v)$ with $d = 3$ and $\gamma = \pi/4$, and $\mathcal{S}_1^B := \mathrm{im}(\sigma_1^B(\mathbb{T}^2))$, where ${}^{B_1}\sigma_1^B(u,v) := \sigma(u,v)$ with $d = 4$ and $\gamma = \pi/6$. The origins of frames A_1 and B_1 coincide and their relative orientation is given by ${}^{A_1}_{B_1}\mathbf{R} := \mathrm{Rot}(\pi/4,\hat{\mathbf{j}})$ as shown in fig. 7.15a). $\mathscr{C}_1$ is an 8-shaped curve that is symmetric with respect to the $x_1^A z_1^A$ plane. Moreover, one of the two wings is obtained by rotating the other wing π radians about the $y_1^A = y_1^B$ axis. Therefore, its projection onto the $y_1^A z_1^A$ plane[3] has an inflection point at the projection of the self-crossing. We set P_1 at the self crossing, as shown in fig. 7.15c).

Step 2: Since P_1 is a singularity in $\mathcal{S}_1^A$ and $\mathcal{S}_1^B$ there is no local information available. $\hat{\mathbf{t}}_1$ and $\hat{\mathbf{t}}_2$ can, however, be easily obtained by finding the intersection of two right cones with half angles $\pi/2 - \alpha_{1,1-1,2} = \pi/4$ and $\pi/2 - \alpha_{1,6-1,5} = \pi/3$ and the same axes of revolution as $\mathcal{S}_1^A$ and $\mathcal{S}_1^B$, respectively. Since a toroid with a singularity at the origin is tangent to a cone whose singularity coincides with that of the toroid and whose half angle is $\pi/2$ minus the tilting angle between the base and secondary circle, the intersection of two toroids of this kind is tangent to the lines obtained by intersecting the cones that are tangent to the toroids at the singularity. The two tangents are ${}^{A_1}\hat{\mathbf{t}}_1 = (0,-\sqrt{2}/2,\sqrt{2}/2)$ and $\hat{\mathbf{t}}_2 = (0,\sqrt{2}/2,\sqrt{2}/2)$. We choose $\hat{\mathbf{t}}_1$, to perform the reflection.

Step 3: $\hat{\mathbf{N}}_\rho$ lies in the $y_1^A z_1^A$ plane and is perpendicular to $\hat{\mathbf{t}}_1$ as shown in fig. 7.15c). The orientation of coordinate system 0 with respect to A_1 is given by ${}^{A_1}_{0}\mathbf{R} = \mathrm{Rot}(\psi,\hat{\mathbf{i}})$, where $\psi = \pi/4$ is obtained from $\hat{\mathbf{t}}_1$.

Step 4: Fig. 7.15b) shows the mechanism that generates such intersection. $\mathcal{S}_1^A$ is generated by the point E_1 of the dyad $\{\mathbf{S}_{1,1},\mathbf{S}_{1,2}\}$, while $\mathcal{S}_1^B$ is generated by the point E_1 of the dyad $\{\mathbf{S}_{1,1},\mathbf{S}_{1,2}\}$. $\mathbf{S}_{1,1}$ and $\mathbf{S}_{1,6}$ are along z_1^A and z_1^B, so they can generate the base circles (see [6]). Observe that since the radii of the secondary and base circles are the same, the distance between E_1 and $\mathbf{S}_{1,2}$ (E_1 and $\mathbf{S}_{1,5}$) is the same as the link length $a_{11,12} = 3$ ($a_{16,15} = 4$), where $a_{1i,1j}$ is the normal distance between the axes of $\mathbf{S}_{1,i}$ and $\mathbf{S}_{1,j}$. This symmetry allows the assembling of a plane-symmetric Bricard mechanism [85], [86], [90] in

[3] A parametrization of $\mathscr{C}$ is not difficult to be obtained due to the symmetries of the surfaces. With such parametrization it can be proved that $\mathscr{C}$ has zero curvature at P_1 and, hence, the Frenet apparatus is not defined. Due to such anomaly, a plane onto which $\mathscr{C}$ can be projected to obtain an inflection point is not unique. In this case the projection onto any plane containing $\hat{\mathbf{t}}_1$ has an inflection point.

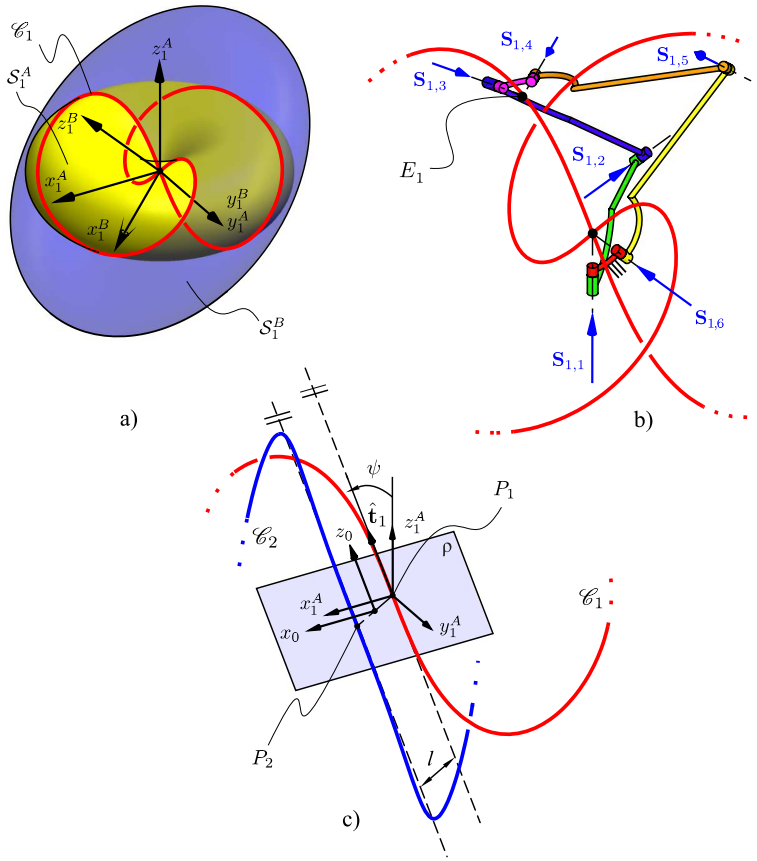

FIGURE 7.15: The intersection of two toroids that has a projection with an inflection point. a) Surfaces setup. b) The Bricard plane-symmetric 6R mechanism that generates such intersection. c) reflection of the intersection curve.

fig. 7.16 where the spherical joint at E_1 is reduced to a pair of revolute joints $\mathbf{S}_{1,3}$ and $\mathbf{S}_{1,4}$. The plane of symmetry is that containing the permanently intersecting axes $\mathbf{S}_{1,2}$ and $\mathbf{S}_{1,5}$. The twist angles $\alpha_{1,1-1,2} = \pi/4$ and $\alpha_{1,6-1,5} = \pi/6$ are the value of γ for $\mathcal{S}_1^A$ and $\mathcal{S}_1^B$, respectively. $a_{1,1-1,2} = a_{1,2-1,3} = 3$ and $a_{1,6-1,5} = a_{1,5-1,4} = 4$ are the radii of both the base and the secondary circles of $\mathcal{S}_1^A$ and $\mathcal{S}_1^B$, respectively. The twist angle $\alpha_{1,1-1,6} = \pi/4$ is the angle between the axes of the toroids (angle between z_1^A and z_1^B), and, due to symmetry, $\alpha_{1,3-1,4} = \alpha_{1,1-1,6}$. The Denavit-Hartenberg (DH) parameter [153] for axial displacement is zero for all joints, therefore, the toroids are symmetric with respect to the plane containing their base circles. Observe that when E_1 coincides with the singularities of the toroids, the revolute joints with axes $\mathbf{S}_{1,1}$, $\mathbf{S}_{1,2}$, $\mathbf{S}_{1,3}$ and $\mathbf{S}_{1,4}$ constitute a spherical 4-bar mechanism. Once this mechanism starts moving the plane symmetry is broken and revolute joints with axes $\mathbf{S}_{1,2}$ and $\mathbf{S}_{1,5}$ become idle. The mechanism enters in a spherical 4-bar operation mode with E_1 remaining coincident with the singularities of the toroids during this motion. A special line- and plane-symmetric Bricard mechanism presenting the same reconfiguration to a spherical 4-bar linkage was presented in [97]. The line-symmetric Bricard linkages obtained as the intersection of two toroids was first analyzed in [36].

It is important to mention, that since $P_1 \in \text{sing}(\mathcal{S}_1^A) \cap \text{sing}(\mathcal{S}_1^B)$, E_1 is unable to move from one branch to another at P_1, see [36] for an in-depth analysis of this singularity. Therefore, unlike in the Koenigs joint, in this Bricard mechanism the two branches of the configuration space, V, related to the two branches of $\mathscr{C}_1$ intersecting at P_1 are not intersecting when $E_1 = P_1$ and, thus, $\exists \mathbf{q}_1, \mathbf{q}_2 \in V$ such that $\mathbf{q}_1 \neq \mathbf{q}_2$ and $E_1(\mathbf{q}_1) = E_1(\mathbf{q}_2) = P_1$.

Steps 5 and 6: Fig. 7.16 shows the 3-loop mechanism obtained after reflecting the overconstrained linkage obtained in step 4 and adding the coupler bar.

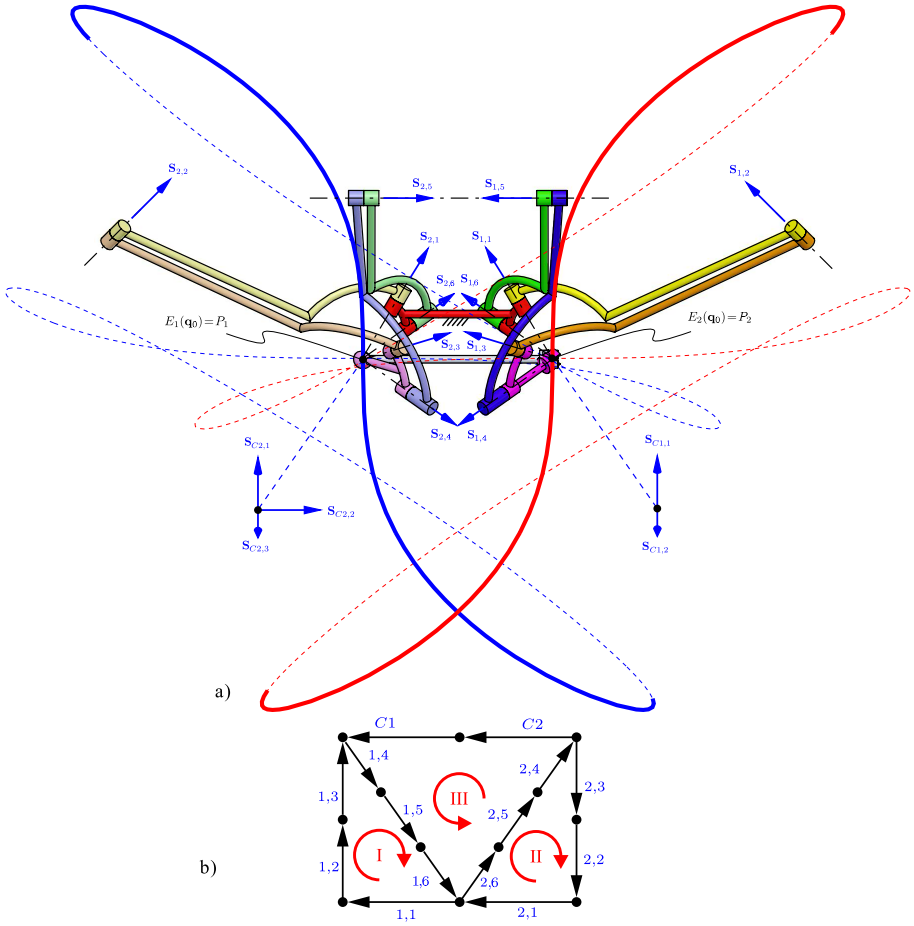

FIGURE 7.16: A double-Bricard mechanism in a cusp configuration.

Analysis of smooth motions through $\mathbf{q}_0$: The screw coordinates at the cusp are

$$
\begin{aligned}
\mathbf{S}_{1,1}(\mathbf{q}_0) &= \left(0, \frac{\sqrt{2}}{2}, \frac{\sqrt{2}}{2}; 5\sqrt{2}, 0, 0\right), \\
\mathbf{S}_{1,2}(\mathbf{q}_0) &= (0, 1, 0; 0, 0, -30), \\
\mathbf{S}_{1,3}(\mathbf{q}_0) &= \left(0, \frac{\sqrt{2}}{2}, -\frac{\sqrt{2}}{2}; -5\sqrt{2}, 0, 0\right), \\
\mathbf{S}_{1,4}(\mathbf{q}_0) &= \left(\frac{\sqrt{2}}{2}, \frac{1}{2}, -\frac{1}{2}; -5, 0, -5\sqrt{2}\right), \\
\mathbf{S}_{1,5}(\mathbf{q}_0) &= \left(\frac{\sqrt{6}}{3}, \frac{\sqrt{3}}{3}, 0; 0, 0, -40 - \frac{10\sqrt{6}}{3}\right), \\
\mathbf{S}_{U1}(\mathbf{q}_0) &= (1, 0, 0; 0, 0, -10), \\
\mathbf{S}_{U2}(\mathbf{q}_0) &= (0, 0, 1; 10, 0, 0),
\end{aligned}
$$

$$
\begin{aligned}
\mathbf{S}_{1,6}(\mathbf{q}_0) &= \left(\frac{\sqrt{2}}{2}, \frac{1}{2}, \frac{1}{2}; 5, 0, -5\sqrt{2}\right), \\
\mathbf{S}_{2,1}(\mathbf{q}_0) &= \left(0, -\frac{\sqrt{2}}{2}, \frac{\sqrt{2}}{2}; -5\sqrt{2}, 0, 0\right), \\
\mathbf{S}_{2,2}(\mathbf{q}_0) &= (0, -1, 0; 0, 0, 30), \\
\mathbf{S}_{2,3}(\mathbf{q}_0) &= \left(0, -\frac{\sqrt{2}}{2}, -\frac{\sqrt{2}}{2}; 5\sqrt{2}, 0, 0\right), \\
\mathbf{S}_{2,4}(\mathbf{q}_0) &= \left(\frac{\sqrt{2}}{2}, -\frac{1}{2}, -\frac{1}{2}; 5, 0, 5\sqrt{2}\right), \\
\mathbf{S}_{2,5}(\mathbf{q}_0) &= \left(\frac{\sqrt{6}}{3}, -\frac{\sqrt{3}}{3}, 0; 0, 0, 40 + \frac{10\sqrt{6}}{3}\right), \\
\mathbf{S}_{2,6}(\mathbf{q}_0) &= \left(\frac{1}{2}\sqrt{2}, -\frac{1}{2}, \frac{1}{2}; -5, 0, 5\sqrt{2}\right), \\
\mathbf{S}_{S1}(\mathbf{q}_0) &= (1, 0, 0; 0, 0, 10), \\
\mathbf{S}_{S2}(\mathbf{q}_0) &= (0, 1, 0; 0, 0, 0), \\
\mathbf{S}_{S3}(\mathbf{q}_0) &= (0, 0, 1; -10, 0, 0).
\end{aligned} \tag{7.6}
$$

With these screw coordinates, the kinematic tangent cone is determined as

$$
\begin{aligned}
C^{\mathrm{K}}_{\mathbf{q}_0} V = \Big\{ \mathbf{x} \;\Big|\; & x_{11} = \frac{1}{\sqrt{2}}s, x_{12} = 0, x_{13} = -\frac{1}{\sqrt{2}}s, x_{14} = s, x_{15} = 0, x_{16} = -s, x_{21} = -\frac{1}{\sqrt{2}}t, \\
& x_{22} = 0, x_{23} = \frac{1}{\sqrt{2}}t, x_{24} = -t, x_{25} = 0, x_{26} = t, x_{U1} = 0, x_{U2} = s, x_{S1} = 0, \\
& x_{S2} = 0, x_{S3} = -t \;\text{ with }\; s,t \in \mathbb{R} \Big\}.
\end{aligned} \tag{7.7}
$$

This is the tangent space to the manifold V_3 shown in fig. 7.16. The branches V_1 and V_2 shown in the figure are not smooth manifolds and curves in V_1 and V_2 are not smooth at $\mathbf{q}_0$.

Discussion on branches: Since, in the cusp configuration presented in fig. 7.16 $E_1 = P_1$ and $E_2 = P_2$ both Bricard loops are able to enter the spherical 4-bar operation mode explained above. During this motion, E_1 and E_2 remain coincident with P_1 and P_2, respectively. The coupler bar restricting the position of E_1 and E_2 remains static and there is no restriction between the motion of loops I and II. Hence, from $\mathbf{q}_0$ the mechanism can enter a 2-DOF branch of motion with partitioned mobility [125]. Fig. 7.17 shows a 3-dimensional section of the c-space near the cusp.

7.6 Chapter conclusions

This chapter presented a method for the design of spatial 1-DOF mechanisms that exhibit a cusp in their configuration space. The method was obtained by extending the idea presented by Connelly and Servatius in their double-Watt linkage which is a planar cusp mechanism. Such a linkage takes advantage of the inflection point of the curve drawn by the middle point of the coupler link of each of the two 4-bar Watt linkages. In this chapter, this idea was extended to the spatial case in order to design spatial 1-DOF cusp mechanisms. It was found that a simple way of dealing with curves traced by spatial mechanisms is the use of intersection of surfaces generated [2], [11], [35], [36] by kinematic dyads. Using this method,

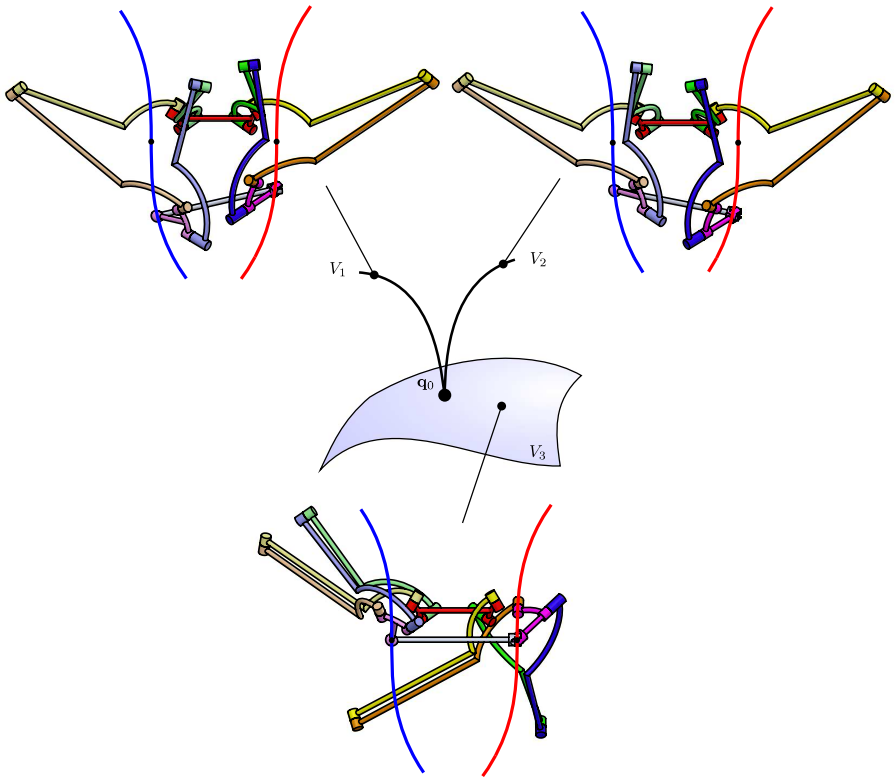

FIGURE 7.17: Different branches of the configuration space intersecting at $\mathbf{q}_0$.

three examples were presented. It was shown that the c-spaces of two of these examples not only present the cusp singularity, but also have other motion branches intersecting at such a singularity, leading to very complex c-spaces that are difficult to analyze. For every example, a local approximation of smooth motions was computed by means of the kinematic tangent cone. While this provides a sufficient local description at non-cuspidal c-space singularities (bifurcations), it is shown that this is not true at cusps. The presented analysis thus shows the need for additional research into the singularity analysis. The development of such analysis methods has not been a topic of research simply because the phenomenon is widely unknown, given that only Connelly and Servatius have presented an example. The presented synthesis method and examples are aimed to provide spatial 1-DOF test cases. A straight-forward approach to the cusp singularity analysis is the local approximation of the c-space using Taylor series expansion of the constraints. This can be formalized [144] in the framework of screw theory.

The existence of mechanisms with higher-order cusps in their configuration space was further discussed in this chapter by providing a planar example. Such a mechanism (a double-Evans linkage) was designed by noting that a 4-bar Evans mechanism can draw a curve that approximates a straight line up to the fifth order at an inflection point.

To the knowledge of the author the examples presented in this chapter are the first cusp mechanisms presented after Connelly's double-Watt linkage and the mechanism recently presented by the author in [141]. All the examples presented in this chapter can be used in the study of cusp singularities and as challenges for proposed methods of local analysis of mechanisms.

Chapter 8

Tangential intersection of branches of motion

In the previous chapter, intersection curves were used to design linkages with a peculiar type of singularity, the cusp. In this chapter, another rather uncommon type of singularity is explored, the tangent intersection.

In the vast majority of reported linkages whose configuration spaces contain multiple branches of motion the intersection happens transversally, allowing local methods, like the computation of its tangent cone, to identify different branches by means of their tangents. However, if these branches are of the same dimension and they intersect tangentially, it is not possible to identify them by means of the tangent cone at the singularity as the tangent spaces to the branches are the same. Although this possibility has been mentioned by a few researchers, whether linkages with this kind of tangent intersection of branches of motion exist is still an open question. In this chapter, it is shown that the answer to this question is yes: A local method is proposed for the effective identification of branches of motion intersecting tangentially, and a method for the type synthesis of linkages that exhibit this particular type of singularity is presented.

This chapter is based on the journal publication:

[40] P.C. López-Custodio, A. Müller and J.S. Dai, "Tangential intersection of branches of motion," *Mechanisms and Machine Theory*, vol 147, 103730, (2020) DOI:10.1016/j.mechmachtheory.2019.103730.

8.1 Background

The study of singularities is nothing short of crucial in the analysis, design and control of mechanisms and robots. This is a topic that has been thoroughly investigated since researchers noted that the properties of linkages dramatically change in certain configurations. Of particular importance are the singularities occurring in the configuration space of the mechanism [64], [65], where its smoothness is lost. Hunt [58] called these singularities *uncertainty configurations* and used a planar 4-bar mechanism in a flattened configuration as an example (see also [66]), pointing out that from such configuration it is possible to unfold the mechanism "in two essentially different ways". These two different ways are two branches of motion in the configuration space of the mechanism. An example of a 4-bar mechanism with opposite links of the same length is shown in fig. 8.1. It can be seen that from a flattened configuration $\mathbf{q}_0$ the mechanism can be unfolded in two different ways: a parallelogram ($\mathbf{q}_2$) and an anti-parallelogram ($\mathbf{q}_1$).

Although singularities in the configuration space have been investigated rigorously through decades, most of this research has focused on transversal intersection of motion branches of

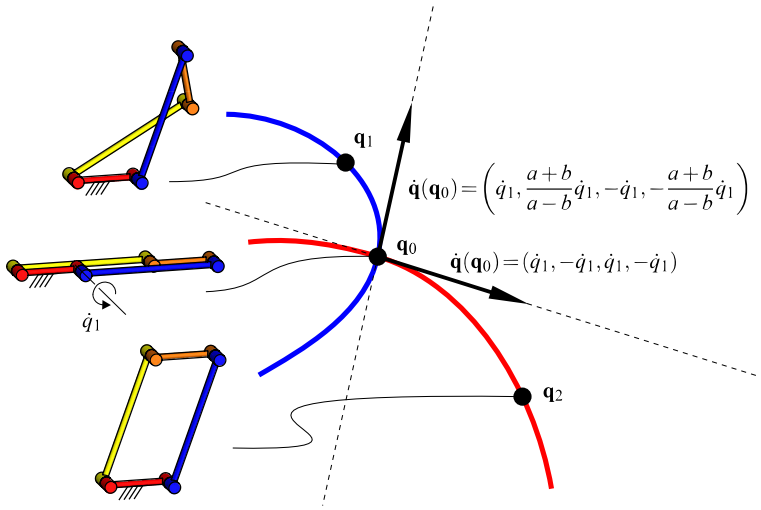

FIGURE 8.1: A 4-bar mechanism and a singularity in its configuration space.

the same and of different dimensions. In a *transversal* intersection, the two manifolds intersecting have non-parallel tangents at the intersection point. The intersection in the configuration space of the 4-bar mechanism shown in 8.1 happens transversally. In fig. 8.1, the entries of the tangent vectors $\dot{\mathbf{q}} \in \mathbb{R}^4$ are given by the angular velocities of the four revolute joints. At the intersection, $\mathbf{q}_0$, the vectors that are tangent to the branch of motion related to parallelogram configurations are non-parallel to the tangent vectors to the branch of motion with anti-parallel configurations. This is depicted in fig. 8.1, where a and b are the two different link lengths and $\dot{q}_1 \in \mathbb{R}$ is the angular velocity of the input joint.

In the case of transversal intersections, the concept of tangent cone works perfectly as it reveals the number of motion branches intersecting as well as their dimension, i.e., the number of finite degrees of freedom of the mechanism in each branch. However, there are several other situations of intersections of branches of motion that have remained rather obscure mainly due to the lack of examples of mechanisms exhibiting these types of singularities. Table 8.1 shows seven different cases of intersections of motion branches, it has to be warned that this table is not meant to be exhaustive.

It can be seen that cases 1 and 2 of Table 8.1 are common singularities with many examples being reported. In these types of singularities, the tangents to the subvarieties span different vector spaces and they can be recognized by means of the computation of the tangent cone. Cases 5, 6 and 7 involve a cusp. These cases were analysed in chapter 7

Using algebraic geometry, Piiponen et al. [156] discussed the possibility of branches of motion intersecting not transversally, but *tangentially* i.e. the tangents at the intersection are parallel, as in cases 3 and 4 in Table 8.1. However, Piiponen et al. [156] did not present any example to prove the existence of these mechanisms and this type of singularity.

It is clear that in the case of tangent intersections, the tangent cone analysis would fail in detecting the bifurcations as the tangents are either the same vector space or one is a subspace of the other.

This opened the question of whether there exist mechanisms with tangential intersections of motion branches in their configuration space[1]. In addition, no technique for the analysis of this singularity has been proposed. In this chapter, we show that the answer to this question

[1] In [157] it was suggested that a classic kinematotropic linkage, the Wunderlich mechanism [12], [158], presented a tangential intersection between its 2-dimensional branch and one of its 1-dimensional branches. This result was used in [40] to explain the phenomenon. However, some time later, the author of this thesis together with the authors of [157] would prove this result was incorrect and such a 1-dimensional branch was simply a subvariety of the 2-dimensional branch.

TABLE 8.1: Different types of intersections between motion branches. (*Examples of mechanisms exhibiting singularities of the cases 1 and 2 are very common. The references cited here are just a sample of publications focusing exclusively in this kind of mechanisms.)

Singularity	Examples reported	Tangent cone can identify branches
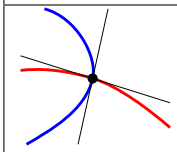 1. Same dimension, transversal	✓ [11], [20], [27], [35], [36], [63], [64], [68], [73], [78], [79], [110], [126], [127], [154], [155]*	✓
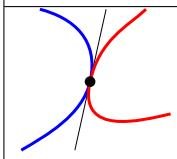 3. Same dimension, tangential	✗	✗
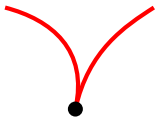 5. Cusp	✓ [39], [119]	✗
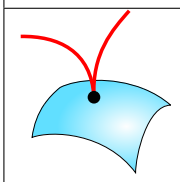 7. Cusp and surface	✓ [39]	✗

Singularity	Examples reported	Tangent cone can identify branches
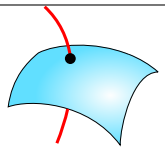 2. Different dimension, transversal	✓ [12]–[16], [34], [37], [83], [123]*	✓
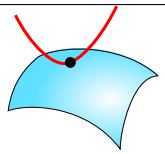 4. Different dimension, tangential	✗	✗
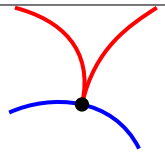 6. Cusp and curve	✓ [39]	✗

is yes. Examples of mechanisms with this type of singularity are presented for the first time and an extension to the tangent cone analysis method is proposed which effectively detects these motion branches.

It is important to mention that the case of tangential intersection of motion branches is of particular interest since the mechanism can move from one motion branch to another through a C^{n_C} curve, i.e. a curve whose first n_C derivatives exist, while in a typical reconfiguration through a transversal intersection of motion branches the mechanism has to move through a non-differentiable C^0 curve, in which not even the first derivative exists, forcing the mechanism to stop at the singularity. This will make reconfiguration technically easier, although it is not exactly a smooth motion, which would imply a curve in C^∞, therefore the terms *smooth reconfiguration* and *smooth kinematotropy* (or *regular* reconfiguration and kinematotropy) used in [156], [157] are not adopted in this chapter.

This chapter is organized as follows: In Section 8.2 a representation of a configuration space is used to explain the phenomenon of tangential intersection of motion branches. In Section 8.3 a method for detecting and analyzing tangential intersections in the configuration space is presented. Section 8.4 explains how to design mechanisms with this type of singularity and two examples are presented and analyzed in Section 8.5. Finally, conclusions are drawn in Section 8.6.

8.2 Transversal and tangential intersections in the configuration space

Fig. 8.2 shows a representation of a configuration space, V, with three branches of motion, V_1, V_2 and V_3, intersecting at singularity $\mathbf{q}_0$. With V_1 being of dimension 2 and V_2 and V_3 of dimension 1.

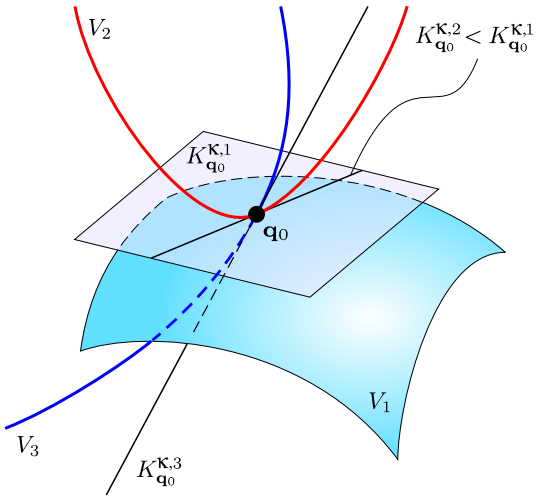

FIGURE 8.2: A configuration space with a tangential and a transversal intersection at $\mathbf{q}_0$.

It can be seen in fig. 8.2 that 1-dimensional branch V_3 intersects transversally V_1 and V_2, while V_1 and V_2 intersect tangentially. The kinematic tangent cone to V at $\mathbf{q}_0$ is the union of the three tangent spaces to the three subvarieties intersecting at $\mathbf{q}_0$: $C^{\mathrm{K}}_{\mathbf{q}_0}V = \cup_{i=1}^{3} K^{\kappa,i}_{\mathbf{q}_0}$, where $\dim(K^{\kappa,1}_{\mathbf{q}_0}) = 2$ and $\dim(K^{\kappa,2}_{\mathbf{q}_0}) = \dim(K^{\kappa,3}_{\mathbf{q}_0}) = 1$. However, since $T_{\mathbf{q}_0}V_2 < T_{\mathbf{q}_0}V_1$, we have $K^{\kappa,2}_{\mathbf{q}_0} < K^{\kappa,1}_{\mathbf{q}_0}$ and, therefore:

$$C^{\mathrm{K}}_{\mathbf{q}_0}V = \cup_{i=1}^{3} K^{\kappa,i}_{\mathbf{q}_0} = K^{\kappa,1}_{\mathbf{q}_0} \cup K^{\kappa,3}_{\mathbf{q}_0}$$

This tangent cone suggest that there are only two components intersecting at $\mathbf{q}_0$, 2-dimensional branch V_1 and 1-dimensional branch V_3. Therefore, the kinematic tangent cone approach fails in revealing the local structure of V around $\mathbf{q}_0$.

Now consider the intersection of two 1-dimensional branches of motion. Fig. 8.3a shows the typical case in which the branches intersect transversally at $\mathbf{q}_0$. If a κ_1th-order approximation is required to compute the tangent cone to V at $\mathbf{q}_0$, then $C^{\mathrm{K}}_{\mathbf{q}_0}V = K^{\kappa_1,1}_{\mathbf{q}_0} \cup K^{\kappa_1,2}_{\mathbf{q}_0}$, where $K^{\kappa_1,1}_{\mathbf{q}_0}$ and $K^{\kappa_1,2}_{\mathbf{q}_0}$ are two non-parallel lines, and $C^{\mathrm{K}}_{\mathbf{q}_0}V$ describes perfectly the local structure of V around $\mathbf{q}_0$. In the case of intersections of higher-dimensional subvarieties, $C^{\mathrm{K}}_{\mathbf{q}_0}V$ is the union of two different vector spaces of the same dimension.

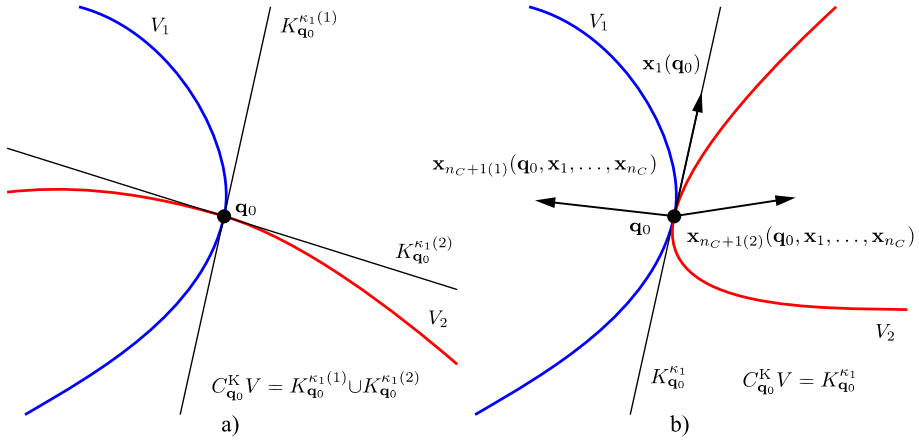

FIGURE 8.3: Intersection of 1-dimensional subvarieties: a) transversal case and b) tangential case.

However, if curves V_1 and V_2 intersect tangentially as shown in fig. 8.3b, then $T_{\mathbf{q}_0}V_1 = T_{\mathbf{q}_0}V_2$ and, hence, $K^{\kappa_1,1}_{\mathbf{q}_0} = K^{\kappa_1,2}_{\mathbf{q}_0}$, which means that the tangent cone, rather than being the union of two vector spaces is a sole vector space: $C^{\mathrm{K}}_{\mathbf{q}_0}V = K^{\kappa_1}_{\mathbf{q}_0}$, with $K^{\kappa_1}_{\mathbf{q}_0} := K^{\kappa_1,i}_{\mathbf{q}_0}$, $i = 1,2$. This means that $C^{\mathrm{K}}_{\mathbf{q}_0}V$ is not giving us enough information as it fails to indicate that there are two branches intersection at the analysis point, it rather suggests that there is only one tangent space to V at such point, which could lead to the incorrect conclusion that there is no branching at $\mathbf{q}_0$. It is also important to mention that although this is a c-space singularity and, as such, the rank of the Jacobian matrix will drop at such configuration, this rank decrement is a necessary but not sufficient condition for having a bifurcation in V and, therefore, having a rank decrement and a tangent cone that is only one vector space is not sufficient to prove a tangent bifurcation. In [62] an example of a Goldberg 6R linkage in a configuration with a rank decrement but no bifurcation in the c-space was found.

In order to find out whether $\mathbf{q}_0$ is a tangent intersection further analysis is required. As shown in fig. 8.3b, all vectors $a\mathbf{x}_1(\mathbf{q}_0)$, $a \in \mathbb{R}$, which are joint velocity vectors at $\mathbf{q}_0$, are parallel and lie in $C^{\mathrm{K}}_{\mathbf{q}_0}V$, which is spanned by such vectors as $\{a\mathbf{x}_1 : a \in \mathbb{R}\}$. However, it is possible that the joint acceleration vectors $\mathbf{x}_2(\mathbf{q}_0, \mathbf{x}_1)$, are no longer parallel. If these vectors are still parallel they are again not useful in detecting the two branches intersecting at $\mathbf{q}_0$. There must exist some number $n_C \in \mathbb{Z}$ called *order of contact*, for which the $(n_C + 1)$th order derivatives $\mathbf{x}_{(n_C+1)}(\mathbf{q}_0, \mathbf{x}_1, \ldots, \mathbf{x}_{(n_C)})$ span two different vector spaces allowing the identification of both branches. It is then said that all tangential intersections exhibit at least a 1st-order contact. It can be seen that, with this approach, the higher-order analysis is the only required tool to prove a tangent intersection. In the following section, a formal methodology that allows identifying any kind of intersection is presented.

8.3 Identification of tangential intersections of branches of motion of the same dimension

A tangential intersection at a configuration $\mathbf{q} \in V$ is characterized by the fact that there are smooth curves through $\mathbf{q}$ having the same tangents. If the intersecting branches are of the same dimension, the first-order aspect, and hence the kinematic tangent cone (any other definition of tangent cone [33]) is insufficient to identify such intersection. However, the solution set of higher-order constraints can be used to this end.

The solution set of the ith-order constraints is

$$\begin{aligned} \overline{K}^i_{\mathbf{q}} := \{(\mathbf{x}_1, \mathbf{x}_2, \ldots, \mathbf{x}_i) \in \mathbb{R}^{i\times n} : \quad & \mathbf{H}^{(1)}(\mathbf{q}, \mathbf{x}_1) = \mathbf{0}, \\ & \mathbf{H}^{(2)}(\mathbf{q}, \mathbf{x}_1, \mathbf{x}_2) = \mathbf{0}, \\ & \mathbf{H}^{(3)}(\mathbf{q}, \mathbf{x}_1, \mathbf{x}_2, \mathbf{x}_3) = \mathbf{0}, \\ & \qquad \ldots \\ & \mathbf{H}^{(i)}(\mathbf{q}, \mathbf{x}_1, \mathbf{x}_2, \mathbf{x}_3, \ldots, \mathbf{x}_i) = \mathbf{0}\}. \end{aligned} \tag{8.1}$$

Denote with $\pi_k : \mathbb{R}^{i\times n} \to \mathbb{R}^n$ the projection to the kth factor of $\overline{K}^i_{\mathbf{q}}$ according to

$$\pi_k(\overline{K}^i_{\mathbf{q}}) := \{\mathbf{x}_k \in \mathbb{R}^n | \, (\mathbf{x}_1, \ldots, \mathbf{x}_k, \ldots, \mathbf{x}_i) \in \overline{K}^i_{\mathbf{q}}\}. \tag{8.2}$$

The ith-order cone is then given by

$$K^i_{\mathbf{q}} = \pi_1(\overline{K}^i_{\mathbf{q}}) \tag{8.3}$$

At a singularity, $\overline{K}^i_{\mathbf{q}}$ splits into the union of s_i solution sets

$$\overline{K}^i_{\mathbf{q}} = \overline{K}^{i,1}_{\mathbf{q}} \cup \ldots \cup \overline{K}^{i,s_i}_{\mathbf{q}}. \tag{8.4}$$

where $i > n_C$ and n_C is the order of contact between the motion branches intersecting tangentially at $\mathbf{q}$.

Different motion branches meeting at $\mathbf{q} \in V$ can be separated by investigating higher-order motions, which is not taken into consideration in (2.14). At a tangential intersection there are different higher-order motions, according to the motion branch, which have the same tangents.

Proposition 8.3.1 *A point $\mathbf{q} \in V$ is a tangential intersection if and only if $\pi_1(\overline{K}^{i,j}_{\mathbf{q}}) \leq \pi_1(\overline{K}^{i,l}_{\mathbf{q}})$ and $\pi_i(\overline{K}^{i,j}_{\mathbf{q}}) \neq \pi_i(\overline{K}^{i,l}_{\mathbf{q}}), j \neq l$ for some $i > n_C$. If the branches of motion are of the same dimension the equal symbol is fulfilled in the first condition.*

The necessary order i may be different from κ_1 in Eq. (XX). Notice that $\mathbf{q}$ may additionally be a singularity due to non-smoothness of V (e.g. cusp), i.e. when $\mathbf{q}$ is a boundary point of a motion branch.

Similarly to $\dim\left(K^i_{\mathbf{q}_0}\right)$, $\dim\left(\pi_i\left(\overline{K}^k_{\mathbf{q}}\right)\right)$, $k > i$, decreases as k increases, until at order κ_i one has $\dim\left(\pi_i\left(\overline{K}^{\kappa_i}_{\mathbf{q}}\right)\right) = i\dim\left(K^{\kappa_1}_{\mathbf{q}}\right)$, which will no longer decrease and it can be concluded that the set of $\mathbf{x}_i$ vectors has been computed.

8.4 Design of 1-DOF linkages with a tangential intersection in the configuration space

A mechanism with two motion branches intersecting tangentially can be designed taking a linkage that is known to have at least two motion branches and then forcing the two branches to have the same joint velocities at their intersection configuration. Following this idea, a procedure for the design of these mechanisms is presented for the 1-DOF case.

Consider a 1-DOF mechanism that is known to have two branches of motion, α and β, which are intersecting at a singular configuration $\mathbf{q}_0 \in V_\alpha \cap V_\beta$. One way to make sure the joint velocities, $\mathbf{x}_1$, are the same in both branches at $\mathbf{q}_0$ is to have one joint that is idle in branch α, which implies that its velocity is 0 not only at $\mathbf{q}_0$ but at any point in V_α, while in branch β the same joint is in a *stationary configuration* [58] at $\mathbf{q}_0$, i.e., its velocity is 0 in that configuration but it is different from 0 in the neighborhood of $\mathbf{q}_0$, it is also usual to say that the joint is in a *dead-point* or *transitionally inactive* [58]. A simple way to design a mechanism with such a property in one of its joins is now explained. We start by taking an overconstrained 6R linkage in which the axes of four of its joins, $\mathbf{S}_{\Pi 1}, \ldots, \mathbf{S}_{\Pi 4}$, lie on a plane Π in the configuration $\mathbf{q}_0$. The other two joint axes, $\mathbf{S}_{\Lambda 1}$ and $\mathbf{S}_{\Lambda 2}$, are perpendicular to Π at $\mathbf{q}_0$. This arrangement is shown in fig. 8.4. It is also required that in this configuration the 6R mechanism is not in a singular configuration.

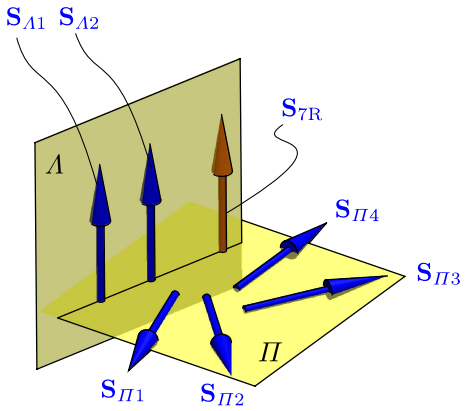

FIGURE 8.4: Joint axes of a 1-DOF mechanism with tangential intersections in the configuration space.

Define $\mathscr{S}_\Pi := \text{span}(\mathbf{S}_{\Pi 1}(\mathbf{q}_0), \ldots, \mathbf{S}_{\Pi 4}(\mathbf{q}_0))$ and $\mathscr{S}_{6R} := \text{span}(\mathscr{S}_\Pi, \mathbf{S}_{\Lambda 1}(\mathbf{q}_0), \mathbf{S}_{\Lambda 2}(\mathbf{q}_0))$, clearly $\{\mathbf{S}_{\Lambda 1}(\mathbf{q}_0), \mathbf{S}_{\Lambda 2}(\mathbf{q}_0)\} \nsubseteq \mathscr{S}_\Pi$, and since the 6R mechanism is not in a singular configuration and $\mathscr{S}_\Pi$ is a 3-system, $\dim(\mathscr{S}_{6R}) = 5$. This implies that, in the equation $\sum_{i=1}^{4} \dot{q}_{\Pi i} \mathbf{S}_{\Pi i} + \sum_{i=1}^{2} \dot{q}_{\Lambda i} \mathbf{S}_{\Lambda i} = \mathbf{0}$, the solution includes $\dot{q}_{\Lambda 1}(\mathbf{q}_0) = \dot{q}_{\Lambda 2}(\mathbf{q}_0) = 0$, therefore, these joins are transitionally inactive. This conclusion can be taken as a corollary to Theorem 2 of Section 2.2 in [58].

In order to design a reconfigurable mechanism based on this 6R overconstrained mechanism, let us insert a seventh R joint with axis $\mathbf{S}_{7R}$. This 7R mechanism has a branch of motion α in which the joint with axis $\mathbf{S}_{7R}$ is idle if $\mathbf{S}_{7R}$ is different to all the axes in the 6R mechanism, which means the 7R mechanism is still 1-DOF and follows the same motion as it was the 6R linkage. Another branch of motion, β, appears as a non-overconstrained motion with all seven R joints being active, since this is a non-overconstrained motion the branch is also 1-DOF.

In order to have $\dot{q}_{7R}(\mathbf{q}_0) = 0$ in branch β so that both branches intersect tangentially, it is necessary to have $\mathbf{S}_{7R}(\mathbf{q}_0)$ parallel to $\mathbf{S}_{\Lambda 1}(\mathbf{q}_0)$ and $\mathbf{S}_{\Lambda 2}(\mathbf{q}_0)$. It is also required that the 7R mechanism is in a singular configuration as subvarieties V_α and V_β are intersecting at

$\mathbf{q}_0$. Therefore we need $\mathbf{S}_{7R}(\mathbf{q}_0) \in \mathscr{S}_{6R}$, this is fulfilled by placing $\mathbf{S}_{7R}(\mathbf{q}_0)$ in Λ, the plane containing $\mathbf{S}_{\Lambda 1}(\mathbf{q}_0)$ and $\mathbf{S}_{\Lambda 2}(\mathbf{q}_0)$ (see fig. 8.4).

For this 7R mechanism in configuration $\mathbf{q}_0$, it can be seen that $\dim(\text{span}(\mathscr{S}_{6R}, \mathbf{S}_{7R}(\mathbf{q}_0))) = 5$, therefore $\mathbf{q}_0$ is singular as we know both branches of motion are 1-dimensional. In addition, due to the geometry of the joint axes belonging to perpendicular planes, $\dot{q}_{7R}(\mathbf{q}_0)$, $\dot{q}_{\Lambda 1}(\mathbf{q}_0)$ and $\dot{q}_{\Lambda 2}(\mathbf{q}_0)$ cannot be written in terms of any velocity of the joints whose axes lie on Π, therefore, $\dot{q}_{7R}(\mathbf{q}_0) = \dot{q}_{\Lambda 1}(\mathbf{q}_0) = \dot{q}_{\Lambda 2}(\mathbf{q}_0) = 0$.

It is important to mention that the above procedure makes sure the 7R linkage is in a singular configuration and the angular velocities of the joints with axes lying on plane Λ are 0. However, there is still a possibility of obtaining a rather strange situation in which the mechanism cannot work as a non-overconstrained 7R mechanism without inactive joints. In this situation, there is only one branch of motion passing through $\mathbf{q}_0$ in which the inserted seventh joint is always inactive, however the dimension of the screw system spanned by all 7 joints is 5 only at $\mathbf{q}_0$. This kind of singularity in which there is no bifurcation is rather strange, see example 7.4 of [62] for a case of this type. Nevertheless, this situation can be identified when using the analysis method described in Section 8.3, not only does the method reveal the branching at the solution set of the order higher than the order of contact, it also shows that the time derivative of this order of the joint variable q_{7R} is different to 0, indicating that the joint is not inactive.

8.5 Examples

In this section two examples of reconfigurable mechanisms with two branches of motion intersecting tangentially are presented. Both examples are obtained using the method discussed in Section 8.4. The tangential intersection is identified using the concepts discussed in Section 8.3. See [48], [50], [53], [54], [159] for more detailed examples of the computation of the solutions to the higher-order kinematic analyses.

8.5.1 Case 1: A line-symmetric-based 7R mechanism

Fig. 8.5a shows a 7R mechanism in which joints with axes $\mathbf{S}_{\Pi 1}$, $\mathbf{S}_{\Pi 2}$ $\mathbf{S}_{\Lambda 1}$, $\mathbf{S}_{\Pi 3}$, $\mathbf{S}_{\Pi 4}$ and $\mathbf{S}_{\Lambda 2}$ constitute a Bricard line-symmetric 6R linkage [86], [90]. As shown in fig. 8.5b, in the configuration $\mathbf{q}_0 \in V$, axes $\mathbf{S}_{\Pi 1}, \ldots, \mathbf{S}_{\Pi 4}$ lie on plane Π, while axes $\mathbf{S}_{\Lambda 1}$ and $\mathbf{S}_{\Lambda 2}$ lie on Λ and are perpendicular to Π. A seventh R joint is inserted between joints with axes $\mathbf{S}_{\Pi 1}$ and $\mathbf{S}_{\Lambda 2}$. At $\mathbf{q}_0$, the axis of the seventh joint, $\mathbf{S}_{7R}$, is parallel to $\mathbf{S}_{\Lambda 1}$ and also lies on Λ.

The screw coordinates with respect to the coordinate system with origin at O shown in fig. 8.5a are the following:

$$
\begin{aligned}
\mathbf{S}_{\Pi 1}(\mathbf{q}_0) &:= (0, -1, 0; 0, 0, 0), \\
\mathbf{S}_{\Pi 2}(\mathbf{q}_0) &:= (-1, 0, 0; 0, 0, 0), \\
\mathbf{S}_{\Lambda 1}(\mathbf{q}_0) &:= (0, 0, 1; 1, 0, 0), \\
\mathbf{S}_{\Pi 3}(\mathbf{q}_0) &:= (0, 1, 0; 0, 0, 2), \\
\mathbf{S}_{\Pi 4}(\mathbf{q}_0) &:= (1, 0, 0; 0, 0, -1), \\
\mathbf{S}_{\Lambda 2}(\mathbf{q}_0) &:= (0, 0, 1; 0, -2, 0), \\
\mathbf{S}_{7R}(\mathbf{q}_0) &:= \left(0, 0, 1; \frac{1}{2}, -1, 0\right),
\end{aligned}
$$

Define $\mathbf{x}_i := (x_i^1, \ldots, x_i^7) \in \mathbb{R}^7$, where $x_i^1 := \mathrm{d}^i q_{\Pi 1}/\mathrm{d}t^i$, $x_i^2 := \mathrm{d}^i q_{\Pi 2}/\mathrm{d}t^i$, $x_i^3 := \mathrm{d}^i q_{\Lambda 1}/\mathrm{d}t^i$, $x_i^4 := \mathrm{d}^i q_{\Pi 3}/\mathrm{d}t^i$, $x_i^5 := \mathrm{d}^i q_{\Pi 4}/\mathrm{d}t^i$, $x_i^6 := \mathrm{d}^i q_{\Lambda 2}/\mathrm{d}t^i$ and $x_i^7 := \mathrm{d}^i q_{7\mathrm{R}}/\mathrm{d}t^i$. The solution set for the first order constraints is:

$$\overline{K}^1_{\mathbf{q}_0} = K^1_{\mathbf{q}_0} = \left\{ \left(x_1^1, 2x_1^1, x_1^3, x_1^1, 2x_1^1, x_1^3, -2x_1^3\right) \,\middle|\, x_1^1, x_1^3 \in \mathbb{R} \right\}.$$

The solution set for the second order constraints is:

$$\begin{aligned} \overline{K}^2_{\mathbf{q}_0} = \big\{ (\mathbf{x}_1, \mathbf{x}_2) \,\big|\, \quad \mathbf{x}_1 &= \left(x_1^1, 2x_1^1, 0, x_1^1, 2x_1^1, 0, 0\right), \\ \mathbf{x}_2 &= \left(x_2^1, 2x_2^1, x_2^3, x_2^1, 2x_2^1, x_2^3, 4(x_1^1)^2 - 2x_2^3\right), x_1^1, x_2^1, x_2^3 \in \mathbb{R} \big\}, \end{aligned}$$

from which the second order approximation to the tangent cone is:

$$K^2_{\mathbf{q}_0} = \pi_1\left(\overline{K}^2_{\mathbf{q}_0}\right) = \left\{ \left(x_1^1, 2x_1^1, 0, x_1^1, 2x_1^1, 0, 0\right) \,|\, x_1^1 \in \mathbb{R} \right\}$$

Since $\dim\left(K^2_{\mathbf{q}_0}\right) = 1$ it is concluded that $\kappa_1 = 2$ and $C^{\mathrm{K}}V = K^2_{\mathbf{q}_0}$ as we know this is a 1-DOF mechanism. It can be seen that the tangent cone is only one vector space failing to reveal the bifurcation at $\mathbf{q}_0$.

The solution set for the third order constraints is:

$$\begin{aligned} \overline{K}^3_{\mathbf{q}_0} = \Bigg\{ (\mathbf{x}_1, \mathbf{x}_2, \mathbf{x}_3) \quad \Bigg| \quad & \mathbf{x}_1 \in \pi_1\left(\overline{K}^2_{\mathbf{q}_0}\right), \mathbf{x}_2 \in \pi_2\left(\overline{K}^2_{\mathbf{q}_0}\right), \\ & \mathbf{x}_3 = \left(x_3^1, 12(x_1^1)^3 - 12x_1^1x_2^3 + 2x_3^1, x_3^3, 12(x_1^1)^3 - 6x_1^1x_2^3 + x_3^1, \right. \\ & \left. 6(x_1^1)^3 - 9x_1^1x_2^3 + 2x_3^1, x_3^3, 12x_1^1x_2^1 - 2x_3^3\right) \text{ with } x_1^1, x_2^1, x_2^3, x_3^1, x_3^3 \in \mathbb{R} \Bigg\} \end{aligned}$$

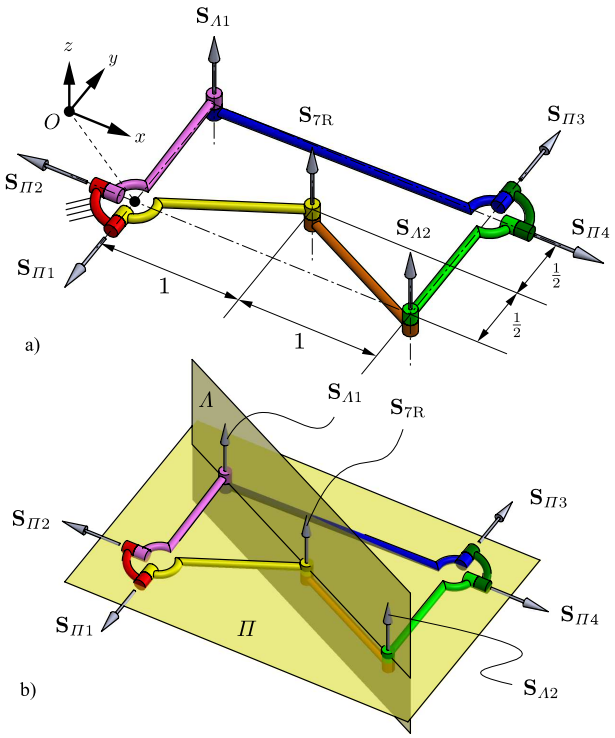

FIGURE 8.5: A line-symmetric-based 7R mechanism with a tangential intersection in the configuration space.

The solution set for the forth order constraints is:

$$\overline{K}^4_{\mathbf{q}_0} = \overline{K}^{4,\alpha}_{\mathbf{q}_0} \cup \overline{K}^{4,\beta}_{\mathbf{q}_0}$$

where,

$$\begin{aligned}
\overline{K}^{4,\alpha}_{\mathbf{q}_0} \quad = \quad & \left\{ (\mathbf{x}_1,\mathbf{x}_2,\mathbf{x}_3,\mathbf{x}_4) \,\middle|\, \mathbf{x}_1 \in \pi_1\left(\overline{K}^2_{\mathbf{q}_0}\right), \right. \\
& \mathbf{x}_2 = \left(x_2^1,\, 2x_2^1,\, 2(x_1^1)^2,\, x_2^1,\, 2x_2^1,\, 2(x_1^1)^2,\, 0\right) \\
& \mathbf{x}_3 = \left(x_3^1,\, -12(x_1^1)^3+2x_3^1,\, x_3^3,\, x_3^1,\, -12(x_1^1)^3+2x_3^1,\, x_3^3,\, 12x_1^1x_2^1-2x_3^3\right), \\
& \mathbf{x}_4 = \left(x_4^1,\, 24(x_1^1)^2x_2^1-16x_1^1x_3^3+2x_4^1,\, x_4^3,\, 48(x_1^1)^2x_2^1-8x_1^1x_3^3+x_4^1,\, -12x_1^1x_3^3+2x_4^1,\, x_4^3,\right. \\
& \left. \left. -28(x_1^1)^4+12(x_2^1)^2+16x_1^1x_3^1-2x_4^3\right) \text{ with } x_1^1,x_2^1,x_3^1,x_3^3,x_4^1,x_4^3 \in \mathbb{R} \right\}
\end{aligned}$$

and

$$\begin{aligned}
\overline{K}^{4,\beta}_{\mathbf{q}_0} \quad = \quad & \left\{ (\mathbf{x}_1,\mathbf{x}_2,\mathbf{x}_3,\mathbf{x}_4) \,\middle|\, \mathbf{x}_1 \in \pi_1\left(\overline{K}^2_{\mathbf{q}_0}\right), \right. \\
& \mathbf{x}_2 = \left(x_2^1,\, 2x_2^1,\, -\frac{6}{5}(x_1^1)^2,\, x_2^1,\, 2x_2^1,\, -\frac{6}{5}(x_1^1)^2,\, \frac{32}{5}(x_1^1)^2\right), \\
& \mathbf{x}_3 = \left(x_3^1,\, \frac{132}{5}(x_1^1)^3+2x_3^1,\, x_3^3,\, \frac{96}{5}(x_1^1)^3+x_3^1,\, \frac{84}{5}(x_1^1)^3+2x_3^1,\, x_3^3,\, 12x_1^1x_2^1-2x_3^3\right), \\
& \mathbf{x}_4 = \left(x_4^1,\, \frac{504}{5}(x_1^1)^2x_2^1-16x_1^1x_3^3+2x_4^1,\, x_4^3,\, \frac{432}{5}(x_1^1)^2x_2^1-8x_1^1x_3^3+x_4^1,\right. \\
& \left. \frac{288}{5}(x_1^1)^2a_2^1-12x_1^1x_3^3+2x_4^1,\, \frac{1632}{25}(x_1^1)^4+x_4^3,\, \frac{2948}{25}(x_1^1)^4+12(x_2^1)^2+16x_1^1x_3^1-2x_4^3\right) \\
& \left. \text{with } x_1^1,x_2^1,x_3^1,x_3^3,x_4^1,x_4^3 \in \mathbb{R} \right\}
\end{aligned}$$

It can be seen that although $\pi_1\left(\overline{K}^{4,\alpha}_{\mathbf{q}_0}\right) = \pi_1\left(\overline{K}^{4,\beta}_{\mathbf{q}_0}\right)$, $\pi_2\left(\overline{K}^{4,\alpha}_{\mathbf{q}_0}\right) \neq \pi_2\left(\overline{K}^{4,\beta}_{\mathbf{q}_0}\right)$, therefore it is concluded that $\mathbf{q}_0$ is a tangential intersection of V_α and V_β. It is also concluded that $n_C = 1$. Note that $\dim\left(\pi_2\left(\overline{K}^{4,j}_{\mathbf{q}_0}\right)\right) = 2 = 2\dim\left(\pi_1\left(\overline{K}^{4,j}_{\mathbf{q}_0}\right)\right)$, $j = \alpha,\beta$, therefore $\kappa_2 = 4$ and $\dim\left(\pi_2\left(\overline{K}^{4,j}_{\mathbf{q}_0}\right)\right)$ will no longer decrease and the vector $\mathbf{x}_2$ will remain unchanged through the solution sets of any order. Observe that $\ddot{q}_{7\mathrm{R}}(\mathbf{q}_0,\mathbf{x}_1) = x_2^7 = 0$ in branch α and $\ddot{q}_{7\mathrm{R}}(\mathbf{q}_0,\mathbf{x}_1) = x_2^7 = (32/5)(x_1^1)^2 \neq 0$ in branch β, which proves that the seventh R joint is active in β. Fig. 8.6 shows the 7R mechanism in two configurations each belonging to each motion branch.

8.5.2 Case 2: A Schatz-based 7R mechanism

Fig. 8.7a shows a 7R mechanism in which joints with axes $\mathbf{S}_{\Pi 1}$, $\mathbf{S}_{\Pi 2}$ $\mathbf{S}_{\Lambda 1}$, $\mathbf{S}_{\Pi 3}$, $\mathbf{S}_{\Lambda 2}$ and $\mathbf{S}_{\Pi 4}$ constitute a Schatz 6R linkage [160], [161]. As shown in fig. 8.7b, in the configuration $\mathbf{q}_0 \in V$, axes $\mathbf{S}_{\Pi 1},\ldots,\mathbf{S}_{\Pi 4}$ lie on plane Π, while axes $\mathbf{S}_{\Lambda 1}$ and $\mathbf{S}_{\Lambda 2}$ lie on Λ and are perpendicular to Π. A seventh R joint is inserted between joints with axes $\mathbf{S}_{\Pi 3}$ and $\mathbf{S}_{\Lambda 2}$. At $\mathbf{q}_0$, the axis of the seventh joint, $\mathbf{S}_{7\mathrm{R}}$, is parallel to $\mathbf{S}_{\Lambda 1}$ and also lies on Λ.

The screw coordinates with respect to the coordinate system with origin at O shown in fig. 8.7a are the following:

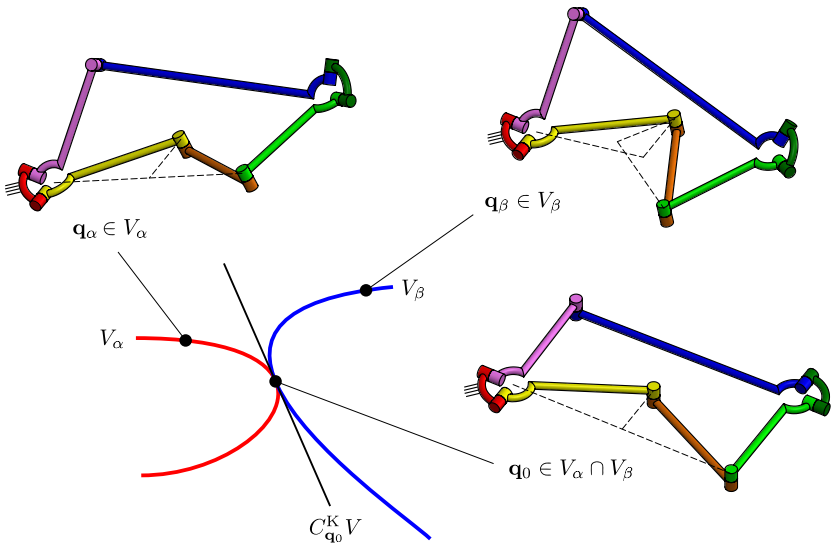

FIGURE 8.6: Branches of motion of the line-symmetric-based 7R mechanism.

$$
\begin{aligned}
\mathbf{S}_{\Pi 1}(\mathbf{q}_0) &:= (0,-1,0;0,0,0),\\
\mathbf{S}_{\Pi 2}(\mathbf{q}_0) &:= (-1,0,0;0,0,0),\\
\mathbf{S}_{\Lambda 1}(\mathbf{q}_0) &:= (0,0,1;2,0,0),\\
\mathbf{S}_{\Pi 3}(\mathbf{q}_0) &:= \left(\frac{1}{2},\frac{\sqrt{3}}{2},0;0,0,1\right),\\
\mathbf{S}_{7\mathrm{R}}(\mathbf{q}_0) &:= \left(0,0,1;\frac{1}{2},-\frac{3\sqrt{3}}{2},0\right),\\
\mathbf{S}_{\Lambda 2}(\mathbf{q}_0) &:= (0,0,1;0,-2\sqrt{3},0),\\
\mathbf{S}_{\Pi 4}(\mathbf{q}_0) &:= \left(0,-1,0;0,0,-2\sqrt{3}\right),
\end{aligned}
$$

Define $\mathbf{x}_i := (x_i^1,\ldots,x_i^7) \in \mathbb{R}^7$, where $x_i^1 := \mathrm{d}^i q_{\Pi 1}/\mathrm{d}t^i$, $x_i^2 := \mathrm{d}^i q_{\Pi 2}/\mathrm{d}t^i$, $x_i^3 := \mathrm{d}^i q_{\Lambda 1}/\mathrm{d}t^i$, $x_i^4 := \mathrm{d}^i q_{\Pi 3}/\mathrm{d}t^i$, $x_i^5 := \mathrm{d}^i q_{7\mathrm{R}}/\mathrm{d}t^i$, $x_i^6 := \mathrm{d}^i q_{\Lambda 2}/\mathrm{d}t^i$ and $x_i^7 := \mathrm{d}^i q_{\Pi 4}/\mathrm{d}t^i$. The solution set for the first order constraints is:

$$
\overline{K}^1_{\mathbf{q}_0} = K^1_{\mathbf{q}_0} = \left\{ \left(x_1^1, \frac{\sqrt{3}}{2}x_1^1, -\frac{1}{4}x_1^5, \sqrt{3}x_1^1, x_1^5, -\frac{3}{4}x_1^5, \frac{1}{2}x_1^1 \right) \,\middle|\, x_1^1, x_1^5 \in \mathbb{R} \right\}.
$$

The solution set for the second order constraints is:

$$
\begin{aligned}
\overline{K}^2_{\mathbf{q}_0} = \Bigg\{ (\mathbf{x}_1,\mathbf{x}_2) \;\Bigg|\; & \mathbf{x}_1 = \left(x_1^1, \frac{\sqrt{3}}{2}x_1^1, 0, \sqrt{3}x_1^1, 0, 0, \frac{1}{2}x_1^1 \right),\\
& \mathbf{x}_2 = \left(x_2^1, \frac{\sqrt{3}}{2}x_2^1, \frac{\sqrt{3}}{2}(x_1^1)^2 - \frac{1}{4}x_2^5, \sqrt{3}x_2^1, x_2^5, \frac{\sqrt{3}}{4}(x_1^1)^2 - \frac{3}{4}x_2^5, \frac{1}{2}x_2^1 \right)\\
& \text{with } \; x_1^1, x_2^1, x_2^5 \in \mathbb{R} \Bigg\},
\end{aligned}
$$

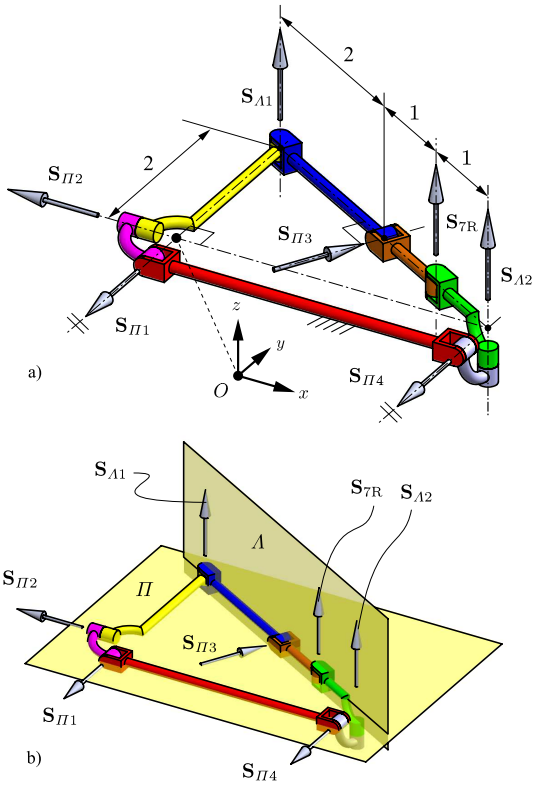

FIGURE 8.7: A Schatz-based 7R mechanism with a tangential intersection in the configuration space.

from which the second order approximation to the tangent cone is:

$$K^2_{\mathbf{q}_0} = \pi_1\left(\overline{K}^2_{\mathbf{q}_0}\right) = \left\{ \left(x^1_1, \frac{\sqrt{3}}{2}x^1_1, 0, \sqrt{3}x^1_1, 0, 0, \frac{1}{2}x^1_1 \right) \,\middle|\, x^1_1 \in \mathbb{R} \right\}$$

Since $\dim\left(K^2_{\mathbf{q}_0}\right) = 1$ it is concluded that $\kappa = 2$ and $C^{\mathrm{K}}V = K^2_{\mathbf{q}_0}$ as we know this is a 1-DOF mechanism. It can be seen that the tangent cone is only one vector space failing to reveal the bifurcation at $\mathbf{q}_0$.

The solution set for the third order constraints is:

$$\begin{aligned}\overline{K}^3_{\mathbf{q}_0} = \Bigg\{ (\mathbf{x}_1, \mathbf{x}_2, \mathbf{x}_3) \;\Bigg|\; & \mathbf{x}_1 \in \pi_1\left(\overline{K}^2_{\mathbf{q}_0}\right), \mathbf{x}_2 \in \pi_2\left(\overline{K}^2_{\mathbf{q}_0}\right), \\ & \mathbf{x}_3 = \Bigg(x^1_3, \frac{\sqrt{3}}{8}\left(4x^1_3 - (x^1_1)^3\right) + \frac{9}{8}x^1_1x^5_2, \frac{3\sqrt{3}}{2}x^1_1x^1_2 - \frac{1}{4}x^5_3, \frac{\sqrt{3}}{4}\left(4x^1_3 \right. \\ & \left. -(x^1_1)^3\right), x^5_3, \frac{3\sqrt{3}}{4}x^1_1x^1_2 - \frac{3}{4}x^5_3, -\frac{3\sqrt{3}}{8}x^1_1x^5_2 + \frac{3}{4}(x^1_1)^3 + \frac{1}{2}x^1_3 \Bigg) \\ & \text{with } x^1_1, x^1_2, x^5_2, x^1_3, x^5_3 \in \mathbb{R} \Bigg\},\end{aligned}$$

The solution set for the forth order constraints is:

$$\overline{K}^4_{\mathbf{q}_0} = \overline{K}^{4,\alpha}_{\mathbf{q}_0} \cup \overline{K}^{4,\beta}_{\mathbf{q}_0}$$

where,

$$\overline{K}^{4,\alpha}_{\mathbf{q}_0} = \Bigg\{ (\mathbf{x}_1,\mathbf{x}_2,\mathbf{x}_3,\mathbf{x}_4) \;\Bigg|\; \mathbf{x}_1 \in \pi_1\left(\overline{K}^2_{\mathbf{q}_0}\right),$$
$$\mathbf{x}_2 = \left(x_2^1, \frac{\sqrt{3}}{2}x_2^1, \frac{\sqrt{3}}{2}(x_1^1)^2, \sqrt{3}x_2^1, 0, \frac{\sqrt{3}}{4}(x_1^1)^2, \frac{1}{2}x_2^1\right)$$
$$\mathbf{x}_3 = \Bigg(x_3^1, \frac{\sqrt{3}}{8}\left(4x_3^1 - (x_1^1)^3\right), \frac{3\sqrt{3}}{2}x_1^1x_2^1 - \frac{1}{4}x_3^5, \frac{\sqrt{3}}{4}\left(4x_3^1 - (x_1^1)^3\right),$$
$$x_3^5, \frac{3\sqrt{3}}{4}x_1^1x_2^1 - \frac{3}{4}x_3^5, \frac{3}{4}(x_1^1)^3 + \frac{1}{2}x_3^1\Bigg),$$
$$\mathbf{x}_4 = \Bigg(x_4^1, \frac{\sqrt{3}}{4}\left(2x_4^1 - 3(x_1^1)^2x_2^1\right) + \frac{3}{2}x_1^1x_3^5, \frac{\sqrt{3}}{4}\left(7(x_1^1)^4 + 6(x_2^1)^2 +$$
$$8x_1^1x_3^1\right) - \frac{1}{4}x_4^5, -\frac{\sqrt{3}}{2}\left(3(x_1^1)^2x_2^1 - 2x_4^1\right), x_4^5, \frac{\sqrt{3}}{8}\left(7(x_1^1)^4 + 6(x_2^1)^2 +$$
$$8x_1^1x_3^1\right) - \frac{3}{4}x_4^5, -\frac{\sqrt{3}}{2}x_1^1x_3^5 + \frac{9}{2}(x_1^1)^2x_2^1 + \frac{1}{2}x_4^1\Bigg)$$
$$\text{with } x_1^1,x_2^1,x_3^1,x_3^5,x_4^1,x_4^5 \in \mathbb{R}\Bigg\}$$

and

$$\overline{K}^{4,\beta}_{\mathbf{q}_0} = \Bigg\{ (\mathbf{x}_1,\mathbf{x}_2,\mathbf{x}_3,\mathbf{x}_4) \;\Bigg|\; \mathbf{x}_1 \in \pi_1\left(\overline{K}^2_{\mathbf{q}_0}\right),$$
$$\mathbf{x}_2 = \left(x_2^1, \frac{\sqrt{3}}{2}x_2^1, 0, \sqrt{3}x_2^1, 2\sqrt{3}(x_1^1)^2, -\frac{5\sqrt{3}}{4}(x_1^1)^2, \frac{1}{2}x_2^1\right),$$
$$\mathbf{x}_3 = \Bigg(x_3^1, \frac{\sqrt{3}}{8}\left(4x_3^1 + 17(x_1^1)^3\right), \frac{3\sqrt{3}}{2}x_1^1x_2^1 - \frac{1}{4}x_3^5,$$
$$\frac{\sqrt{3}}{4}\left(4x_3^1 - (x_1^1)^3\right), x_3^5, \frac{3\sqrt{3}}{4}x_1^1x_2^1 - \frac{3}{4}x_3^5, -\frac{3}{2}(x_1^1)^3 + \frac{1}{2}x_3^1\Bigg),$$
$$\mathbf{x}_4 = \Bigg(x_4^1, \frac{\sqrt{3}}{4}\left(15(x_1^1)^2x_2^1 + 2x_4^1\right) + \frac{3}{2}x_1^1x_3^5, \frac{\sqrt{3}}{4}\left(16(x_1^1)^4 +$$
$$6(x_2^1)^2 + 8x_1^1x_3^1\right) - \frac{1}{4}x_4^5, -\frac{\sqrt{3}}{2}\left(3(x_1^1)^2x_2^1 - 2x_4^1\right), x_4^5,$$
$$\frac{\sqrt{3}}{8}\left(25(x_1^1)^4 + 6(x_2^1)^2 + 8x_1^1x_3^1\right) - \frac{3}{4}x_4^5, -\frac{\sqrt{3}}{2}x_1^1x_3^5 + \frac{1}{2}x_4^1\Bigg)$$
$$\text{with } x_1^1,x_2^1,x_3^1,x_3^5,x_4^1,x_4^5 \in \mathbb{R}\Bigg\}$$

It can be seen that $\pi_1\left(\overline{K}^{4,\alpha}_{\mathbf{q}_0}\right) = \pi_1\left(\overline{K}^{4,\beta}_{\mathbf{q}_0}\right)$ and $\pi_2\left(\overline{K}^{4,\alpha}_{\mathbf{q}_0}\right) \neq \pi_2\left(\overline{K}^{4,\beta}_{\mathbf{q}_0}\right)$, therefore $\mathbf{q}_0$ is a tangential intersection of V_α and V_β with $n_C = 1$. Since $\dim\left(\pi_2\left(\overline{K}^{4,j}_{\mathbf{q}_0}\right)\right) = 2 = 2\dim\left(\pi_1\left(\overline{K}^{4,j}_{\mathbf{q}_0}\right)\right)$, $j = \alpha,\beta$, therefore $\kappa_2 = 4$. Observe that $\ddot{q}_{7R}(\mathbf{q}_0,\mathbf{x}_1) = x_2^5 = 0$ in branch α and $\ddot{q}_{7R}(\mathbf{q}_0,\mathbf{x}_1) = x_2^5 = 2\sqrt{3}(x_1^1)^2 \neq 0$ in branch β, which proves that the seventh R joint is active in β. Fig. 8.8 shows the 7R mechanism in two configurations each belonging to each motion branch, where geometric constraints lead to metamorphic behavior that limits the motion of links.

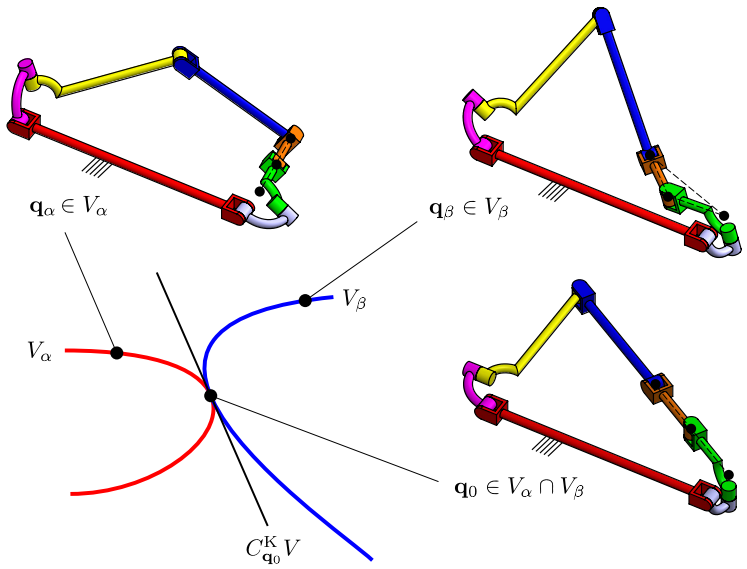

FIGURE 8.8: Branches of motion of the Schatz-based 7R mechanism.

8.6 Chapter conclusions

This chapter presented the first examples of reconfigurable mechanisms whose configuration space contains tangent intersections of two branches of motion. It was pointed out that these singularities cannot be analyzed by computation of the kinematic tangent cone. In these examples, the dimension of both branches is one. There is no theoretical restriction for designing mechanisms with this property and with mobility higher than one, however, this is out of the scope of the presented design method. A method for detecting branches of motion that intersect tangentially was also presented. This local method effectively detects the branches with common tangents at their intersection by considering solutions of the higher-order kinematic analyses, which are normally not considered in bifurcation analysis.

Chapter 9

Solutions for IKP and FKP of an Exechon parallel robot using a generated toroid

An example of a simpler, more typical application of generated surfaces is presented in this last chapter. A toroid is used to simplify the process of finding the solution to the inverse and forward kinematics of an Exechon parallel robot.

An Exechon robot with offsets between the axes of the joints that connect the legs to the fixed platform is analyzed in this chapter. Ideally these axes intersect constituting two universal and one spherical joint. The introduction of imperfections in these universal and spherical joints leads to more complex forward and inverse kinematics which are solved in this chapter. It is proved that the equations used for the kinematics of the ideal Exechon robot are no longer applicable when these offsets are added. When a perfect spherical joint is considered in the ideal case, a specific point to be considered in the analysis remains fixed to the ground. However, when this spherical joint is no longer considered perfect and error offsets are included, such a point is no longer fixed, but it lies on a generated toroid.

The constraint system of this Exechon robot with offsets is also obtained and it is found to be different to the one of the ideal case. Finally, the combination of offsets that lead to the largest deviation in the position of the parallel platform is determined.

This chapter is based on the journal publication:

[41] P.C. López-Custodio, J.S. Dai, R. Fu, and Y. Jin, "Kinematics and constraints of the Exechon robot accounting offsets due to errors in the base joint axes," *ASME. J. Mechanisms Robotics*, vol 12, no 2, 021109, (2020) DOI:10.1115/1.4045942.

9.1 Background

Since the Stewart platform was developed in the sixties [162], [163], applications for parallel kinematic machines (PKM) of parallel robots [164], [165] have been expanding in industry. Nevertheless, the use of PKMs in manufacturing is relatively recent. It was until 1996 that Boing incorporated the Tricept technology [166], [167] in their production lines. Since then, the use of PKMs in manufacturing became a topic of interest of many researchers.

The big advantage of the Tricept robot is its topology, which is *hybrid*, this means that the robot consists of a parallel module with a serial module attached to the moving platform of the parallel one. This combination of characteristics allows to get the benefits from both worlds: a hybrid robot has the high stiffness which can be obtained from any parallel robot, but at the same time, the hybrid robot overcomes the important drawback of a parallel robot which is workspace limitations.

However, the topology of the Tricept robot has an important problem: it has many passive joints, leading to control problems and costly manufacturing. The Tricept has a completely unactuated leg which is in addition prone to high torsion and tension stresses. To overcome this, the same team which developed the Tricept and which is led by Neumann, designed in 2004 a new hybrid robot with a reduced number of passive joints but with all the advantages brought by the Tricept. The result is the Exechon robot [168], [169] which again a 5-DOF robot with a serial module attached to the moving platform of a fully parallel mechanism. The Exechon has been already used in several applications, particularly, the Exechon is been used in aircraft manufacturing [170].

In addition to the applications of the Exechon robot, its striking topology has called the attention of many researchers who have worked in studying its kinematics [171]–[173], stiffness [174]–[177], constraint space and singularities [178], [179], dimensional synthesis [172], equivalent PKMs [180].

In the material provided by the developer of the Exechon, the diagram introducing the dimensions of the Exechon robot presents a more general topology [168]. The diagram is shown in fig. 9.1, it can be seen that the revolute joints that connect the legs to the fixed platform are not intersecting as in the ideal model, where the nominal lengths of the common perpendiculars between these axes is zero.

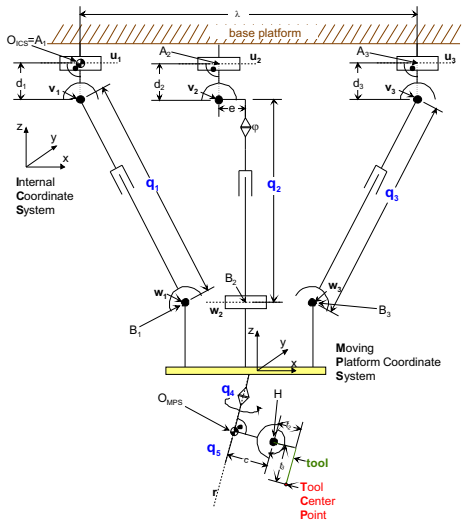

FIGURE 9.1: Diagram of a more general Exechon robot, taken from [168].

The error propagation in the structure of the Exechon robot is currently being studied in a research carried out in conjunction between King's College London and Queen's University Belfast. As part of this research this chapter aims to kinematically analyze for the first time the Exechon robot considering the geometric imperfection [181] of the joint axes connecting the legs to the fixed platform. The equations applied to solve both the inverse and the forward kinematics of the ideal Exechon robot will no longer hold when accounting these offsets. The study only considers the five offsets of the ideally intersecting axes in the base of the robot. The analysis presented in this chapter is valid for Exechon models in which the serial module is a spherical wrist. We consider the joint axes in this spherical wrist as perfect, i.e., they intersect. Models with offset wrists are also available and their coupled kinematics will be analyzed in future research. In addition, the study presented in this chapter only considers offsets between axes that nominally should be equal to zero, however it considers all revolute joints as perfect, the clearance in them is not a topic addressed in this chapter.

The study will reveal the forward and inverse kinematics of the robot, its system of constraints which will also turn out to be different to that of the ideal Exechon robot and finally it

will shortly study the effects of these offsets in the position of the moving platform, revealing also which combination of errors produces the largest deviation in position.

This chapter is organized as follows: Section 9.2 describes the geometry of the ideal Exechon robot, this one is then compared in section 9.3 to the geometry of the Exechon robot with offsets to be studied in the chapter, in section 9.4 the inverse kinematics of the Exechon robot with offsets is solved, followed by its forward kinematics in section 9.5 and the computation of its constraint system 9.6. The results of the forward kinematics problem are used in section 9.7 in order to determine the deviation of the position of the parallel platform of the robot due to the introduction of offsets. Finally, some conclusions are drawn in section 9.8.

9.2 Geometry of the ideal Exechon robot

Fig. 9.2 shows a representation of the ideal Exechon hybrid robot. The hybrid robot is conformed by a 3-DOF parallel module and a 3-DOF serial module. The parallel module consists of a moving platform and a fixed platform connected by three legs. Legs 1 and 3 are UPR serial chains, while leg 2 is an SPR kinematic chain. In the ideal model joint axes $\mathbf{S}_{l1}$ and $\mathbf{S}_{l2}$ intersect in point A_l, $l = 1,3$ and $\mathbf{S}_{21}$, $\mathbf{S}_{22}$ and $\mathbf{S}_{23}$ intersect in A_2. In addition, $\mathbf{S}_{l3} \perp \mathbf{S}_{l2}$, $l = 1,3$, $\mathbf{S}_{24} \perp \mathbf{S}_{22}$ and $\mathbf{S}_{24} || \mathbf{S}_{23}$.

Refer to fig. 9.3, points A_1, A_2 and A_3 constitute the vertices of an isosceles triangle with base $2d_{A1} := d(A_1, A_3)$ and height $d_{A2} := d(A_2, \mathbf{S}_{11})$. Points B_1, B_2 and B_3 also form an isosceles triangle with base $2d_{B1} := d(B_1, B_3)$ and height $d_{B2} := d(B_2, \overline{B_1 B_2})$. Points A_1, A_3, B_1 and B_3 are coplanar, we call the plane that these point lie on Π, while plane Λ is the one containing B_1, B_2 and B_3. The joint variables of the actuated joints of each leg are measured as follows: $q_{l3} := d(A_l, B_l)$, $l = 1,3$, and $q_{24} := d(A_2, B_2)$.

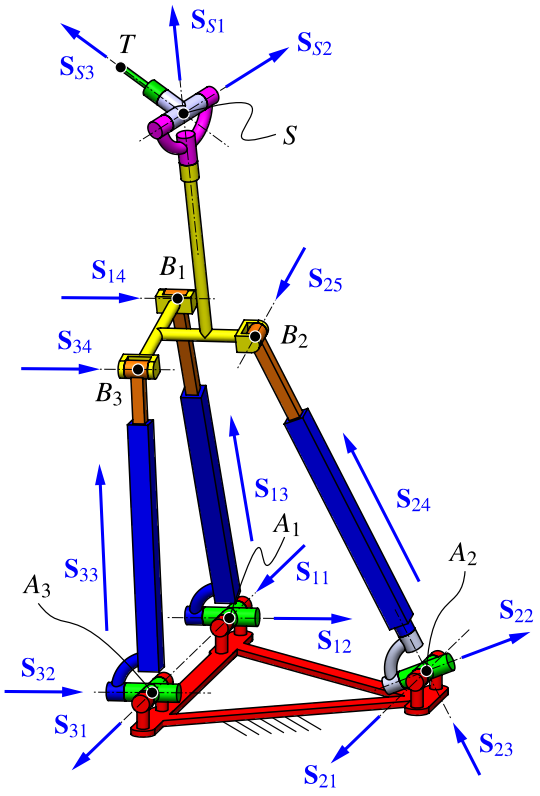

FIGURE 9.2: The ideal Exechon hybrid robot

The serial module is mounted on the moving platform. This module is a serial 3R chain with its three axes $\mathbf{S}_{S1}$, $\mathbf{S}_{S2}$ and $\mathbf{S}_{S3}$ intersecting at point S. Revolute joint with axis $\mathbf{S}_{S3}$ represents the rotation of the tool, the tip of the tool is the point T. Point S is located a distance $h_z := d(S,\Lambda)$ from plane Λ and a distance $h_x := d(S,\Pi)$ from plane Π. Axis $\mathbf{S}_{S1}$ is perpendicular to Λ and the three axes constituting the serial module are perpendicular to each other. The distance between T and S is $d_T := d(T,S)$.

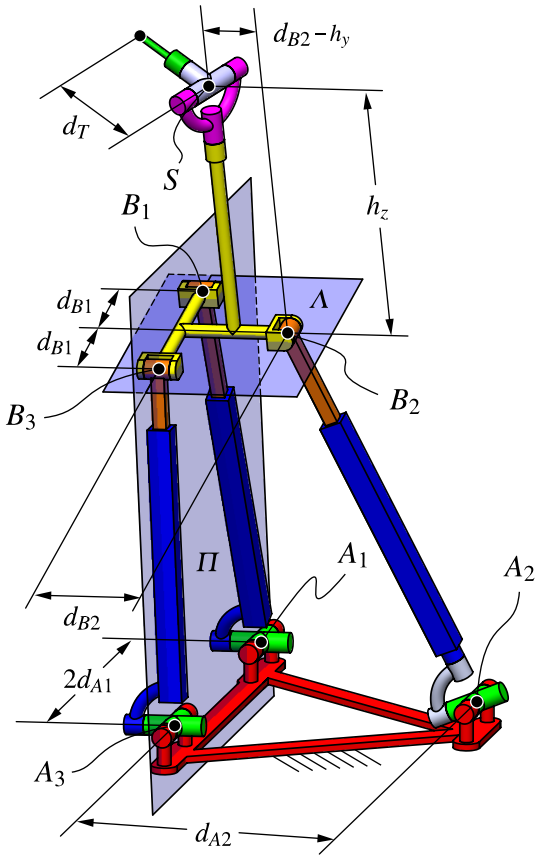

FIGURE 9.3: Structural dimensions of the ideal Exechon hybrid robot and planes Π and Λ

9.3 The Exechon robot with offset errors in the base revolute joints

9.3.1 Geometry of the inserted offsets

Fig. 9.4 shows an Exechon hybrid robot in which offsets were introduced between the axes of the revolute joints connecting the fixed platform. The condition of having axes intersecting at points A_i, $i = 1,2,3$, no longer holds. In the model shown in fig. 9.4, former points A_i, $i = 1,2,3$, have been renamed as A_{ia}, $i = 1,2,3$. Error E_4 is the length of the common perpendicular between now skew axes $\mathbf{S}_{11}$ and $\mathbf{S}_{12}$, this common perpendicular intersects $\mathbf{S}_{11}$ at A_{1a} and $\mathbf{S}_{12}$ at A_{1b}. Similarly, the common perpendicular between $\mathbf{S}_{31}$ and $\mathbf{S}_{32}$ intersects these axes at A_{3a} and A_{3b}, respectively, and has a length of E_5. The joint variable of the actuated prismatic joint in legs $i = 1,3$ is defined as $q_{i3} := d(A_{ia},B_i)$. In summery, if $E_{l1} := E_4$ and $E_{l3} := E_5$, the DH parameters for legs $i = 1,3$ are given by:

$$
\begin{array}{llll}
a_{i1,i2} = E_{li}, & \alpha_{i1,i2} = \frac{\pi}{2}, & d_{i1} = 0, & \theta_{i1} = q_{i1}, \\
a_{i2,i3} = 0, & \alpha_{i2,i3} = \frac{\pi}{2}, & d_{i2} = 0, & \theta_{i2} = q_{i2}, \\
a_{i3,i4} = 0, & \alpha_{i3,i4} = -\frac{\pi}{2}, & d_{23} = q_{i3}, & \theta_{i3} = 0, \\
 & & d_{25} = 0, & \theta_{25} = q_{i4}.
\end{array}
$$

E_4 and E_5 are considered in the kinematic analysis carried out in [173], however the rest of joints are considered ideal. It is seen in [173], that the introduction of E_4 and E_5 does not really affect the analysis which is basically the same as that for the wholly ideal Exechon.

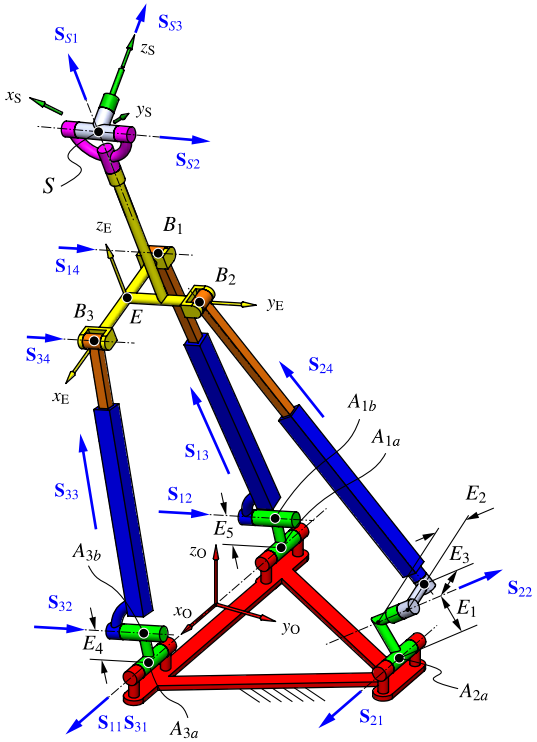

FIGURE 9.4: Exechon robot with offset errors in the base R joints

E_1 and E_3 are the lengths of the common perpendiculars between adjacent axes $\mathbf{S}_{21}$ and $\mathbf{S}_{22}$, and $\mathbf{S}_{22}$ and $\mathbf{S}_{23}$, respectively, and the distance between these two common perpendiculars is E_2. The common perpendicular between $\mathbf{S}_{21}$ and $\mathbf{S}_{22}$ intersects $\mathbf{S}_{21}$ at A_{2a}.

For leg 2, the common perpendicular between adjacent axes $\mathbf{S}_{21}$ and $\mathbf{S}_{22}$ has a length of E_1 and intersects $\mathbf{S}_{21}$ at A_{2a}. Similarly, the common perpendicular between adjacent axes $\mathbf{S}_{22}$ and $\mathbf{S}_{23}$ has a length of E_3 and intersects $\mathbf{S}_{23}$ at A_{2b}. The distance between these two common perpendiculars is E_2. Joint variable of the actuated prismatic joint is defined as $q_{24} := d(A_{2b}, B_2)$. In summary, the DH parameters of leg 2 in the distal convention are:

$$
\begin{array}{llll}
a_{21,22} = E_1, & \alpha_{21,22} = -\frac{\pi}{2}, & d_{21} = 0, & \theta_{21} = q_{21}, \\
a_{22,23} = E_3, & \alpha_{22,23} = \frac{\pi}{2}, & d_{22} = E_2, & \theta_{22} = q_{22}, \\
a_{23,24} = 0, & \alpha_{23,24} = 0, & d_{23} = 0, & \theta_{23} = q_{23}, \\
a_{24,25} = 0, & \alpha_{24,25} = \frac{\pi}{2}, & d_{24} = q_{24}, & \theta_{24} = -\frac{\pi}{2}, \\
 & & d_{25} = 0, & \theta_{25} = q_{25}.
\end{array}
$$

Plane Λ is defined the same as for the ideal Exechon robot, whilst plane Π is now defined as the plane containing points A_{1b}, A_{3b}, B_1 and B_3. Three coordinate systems that will be useful throughout the analysis are defined as shown in fig. 9.4: Coordinate system O, is fixed to the fixed platform with origin at point O, the middle point of segment $\overline{A_{1a}A_{3a}}$, so that $d(O,A_{3a}) = d(O,A_{1a}) = d_{A1}$ and $d(O,A_{2a}) = d_{A2}$, axes x_O and y_O are parallel to $\overline{A_{1a}A_{3a}}$ and

$\overline{OA_{2a}}$, respectively. Frame E is fixed to the moving platform, its origin, point E, is the middle point of segment $\overline{B_1B_3}$ so that $d(E,B_3) = d(E,B_1) = d_{B1}$ and $d(E,B_2) = d_{B2}$, axes x_{E} and y_{E} are parallel to $\overline{B_1A_3}$ and $\overline{EB_2}$, respectively. Finally, a frame S is fixed to the end-effector tool, with origin at S, the center of the spherical wrist of the serial module, axis z_{S} is coincident with $\mathbf{S}_{S3}$, so that ${}^{\mathrm{S}}\mathbf{r}_{T/S} = (0,0,d_T)$.

9.3.2 Mobility of the parallel module of the Exechon robot with offsets

The mobility of the modified Exechon robot is the same as that of the ideal Exechon robot. A very simple way to prove this mobility is described. Considering legs $i = 1,3$ and locking joints $i1$, the result is a planar mechanism, since $\mathbf{S}_{i2}$, $\mathbf{S}_{i3}$ and $\mathbf{S}_{i4}$ constitute a generator of the group of general planar displacements $G(\hat{\mathbf{u}}_\Pi)$, where $\hat{\mathbf{u}}_\Pi$ is the normal vector to Π, the moving platform undergoes general planar motions in this situation. Therefore, both legs can be replaced by any kinematic chain that can generate $G(\hat{\mathbf{u}}_\Pi)$ connected to the fixed platform by means of an R joint with axis $\mathbf{S}_{11}$. In fig. 9.5a, legs 1 and 3 have been replaced by a single 4R leg, with axes $\mathbf{S}_{11}$, $\mathbf{S}_{G1}$, $\mathbf{S}_{G2}$ and $\mathbf{S}_{G3}$, where $\mathbf{S}_{Gj}$, $j = 1\ldots3$ are a generator of $G(\hat{\mathbf{u}}_\Pi)$. Since the only conditions for these three axes is them being non-coincident to each other and being parallel to $\hat{\mathbf{u}}_\Pi$, we can choose $\mathbf{S}_{G3}$ to intersect B_2.

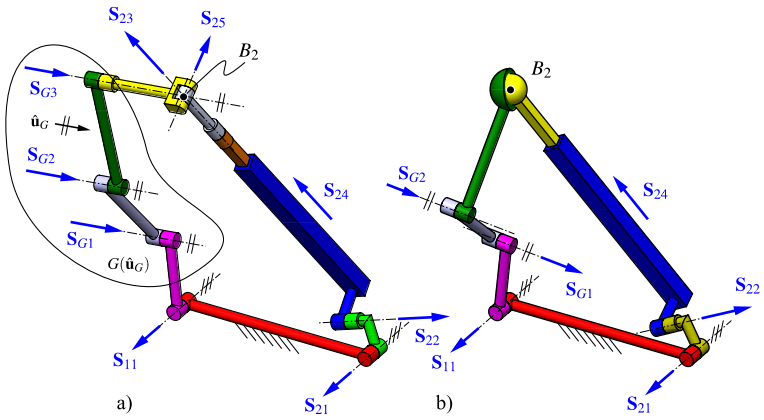

FIGURE 9.5: Equivalent mechanisms obtained by reducing the parallel module of the Exechon robot with offsets inserted.

It can be seen that in leg 2 $\mathbf{S}_{23}||\mathbf{S}_{24}$ and since these two joints are adjacent, they represent a generator of the group of cylindrical displacements $C(\mathbf{r}_{B_2/A_{2b}}/|\mathbf{r}_{B_2/A_{2b}}|, B_2)$, and as such, permutation of these joints is allowed. In fig. 9.5a joints 23 and 24 have been permuted.

The moving platform of the equivalent mechanism shown in fig. 9.5a undergoes exactly the same motion pattern than the moving platform of the Exechon robot with offsets in fig. 9.4. It can be seen that in such a mechanism axes $\mathbf{S}_{G3}$, $\mathbf{S}_{23}$ and $\mathbf{S}_{25}$ intersect at B_2, and since they are the axes of three adjacent R joints, they generate the group of spherical motions $S(B_2)$, as such, they can be replaced an S joint with center at $B2$. Fig. 9.5b shows the equivalent mechanism with the S joint included.

For the equivalent mechanism shown in fig. 9.5b, note that if joints 21, 22 and 24 are disconnected, point B_2 can move to any point in the three dimensional space as it can reach any point in Π, by means of joints $G1$ and $G2$, but then Π can be rotated about $\mathbf{S}_{11}$, allowing B_2 to visit any point in space. In a similar manner, now disconnect joints 11, $G1$ and $G2$, point B_2 can reach any point in the plane perpendicular to $\mathbf{S}_{22}$ by means of joints 22 and 24, however, this plane can also rotate about $\mathbf{S}_{21}$, allowing B_2 to visit any point in space. It can be seen that when all joints are connected point B_2 still can reach any point in space, having 3 DOFs and since there are no passive degrees of freedom when positioning B_2 in space, the whole mechanism, has 3 DOFs. This mechanism is in fact non-overconstrained

[93]. Since this is an equivalent mechanism, the Exechon robot has the same mobility. In addition, observe that this analysis is not compromised by removing of the errors, therefore, these steps also prove the mobility of the ideal Exechon mechanism.

9.4 Inverse kinematics of the Exechon robot with offsets in the base revolute joints

The following information is known in the inverse kinematic problem (IKP): ${}^{\mathrm{O}}\mathbf{r}_T$, the position of the tip of the tool, point T, with respect to the fixed coordinate system, and ${}^{\mathrm{O}}_{\mathrm{S}}\mathbf{R}$, the orientation of coordinate system S attached to the tool with respect to the fixed coordinate system. The purpose of the IKP is to determine the screw coordinates of all joint axes in the robot with respect to the fixed coordinate system: ${}^{\mathrm{O}}\mathbf{S}_{1i}$, ${}^{\mathrm{O}}\mathbf{S}_{3i}$, ${}^{\mathrm{O}}\mathbf{S}_{2j}$ and ${}^{\mathrm{O}}\mathbf{S}_{Sk}$, $i = 1,\ldots,4$, $j = 1,\ldots,5$, $k = 1,2,3$.

In the Exechon robot the parallel module is used to control position, while the serial module allows control of the orientation of the tool. Clearly, the motion of the moving platform of the 3-DOF parallel module is not pure translation, the parasitic rotation obtained after positioning the tool is compensated by the serial module, which allows to obtain the desired orientation of the tool. The IKP can, thus, be split in determining the joint axes of the parallel module for a desired position and then using these results to calculate the screw coordinates of the joint axes of the serial module for the desired orientation.

In the case of the analysis of the parallel module it is convenient to have as input the position of a point that is fixed to the moving platform. Note that known point T has relative motion with respect to the moving platform. However, from the input information of the IKP it is possible to determine the position of point S, which is fixed with respect to the moving platform: ${}^{\mathrm{O}}\mathbf{r}_S = {}^{\mathrm{O}}\mathbf{r}_T + {}^{\mathrm{O}}_{\mathrm{S}}\mathbf{R}(0,0,-d_T)$. Hence, we have the following input and output information for the analysis of each module:

- **Parallel module.** Input: ${}^{\mathrm{O}}\mathbf{r}_S := (S_x, S_y, S_z)$. Output: ${}^{\mathrm{O}}\mathbf{S}_{1i}$, ${}^{\mathrm{O}}\mathbf{S}_{3i}$, ${}^{\mathrm{O}}\mathbf{S}_{2j}$, ${}^{\mathrm{O}}_{\mathrm{E}}\mathbf{R}$.
- **Serial module.** Input: ${}^{\mathrm{O}}_{\mathrm{E}}\mathbf{R}$, ${}^{\mathrm{O}}_{\mathrm{T}}\mathbf{R}$. Output: ${}^{\mathrm{O}}\mathbf{S}_{Sk}$

9.4.1 Analysis of the parallel module for the IKP

To start this analysis we first attempt to follow the steps presented in [171], [173] for the IKP of the parallel module of the ideal Exechon robot and it will be seen that there is an equation that no longer is fulfilled in the Exechon robot with offsets in the joint variables.

The idea is to fully determine frame E with respect to O, i.e. computing ${}^{\mathrm{O}}\hat{\mathbf{i}}_{\mathrm{E}}$, ${}^{\mathrm{O}}\hat{\mathbf{j}}_{\mathrm{E}}$, ${}^{\mathrm{O}}\hat{\mathbf{k}}_{\mathrm{E}}$ and ${}^{\mathrm{O}}\mathbf{r}_{\mathrm{E}}$. If this frame is known then points B_1, B_2 and B_3 are known and computing the screw coordinates of the joint axes becomes straightforward (at least for the ideal parallel module).

Refer to fig. 9.6a, ${}^{\mathrm{O}}\hat{\mathbf{j}}_{\mathrm{E}}$ can be find by computation of $\alpha := \hat{\mathbf{u}}_{\Pi} \cdot \hat{\mathbf{j}}_{\mathrm{O}}$, the angle between planes Π and $x_{\mathrm{O}}z_{\mathrm{O}}$. The angle is still computable from the input information and the geometry in fig. 9.6a. It is easy to obtain:

$$\alpha = \arctan\left(\frac{-S_y\sqrt{S_y^2+S_z^2-h_y^2} \pm S_z h_y}{S_z\sqrt{S_y^2+S_z^2-h_y^2} \pm S_y h_y}\right) \tag{9.1}$$

then ${}^{\mathrm{O}}\hat{\mathbf{j}}_{\mathrm{E}} = \mathrm{Rot}(\alpha, {}^{\mathrm{O}}\hat{\mathbf{i}}_{\mathrm{O}})(0,1,0)$.

We now introduce a new point, C (see fig. 9.6a), which is given by ${}^{\mathrm{O}}\mathbf{r}_C := {}^{\mathrm{O}}\mathbf{r}_S + (d_{B2} - h_y){}^{\mathrm{O}}\hat{\mathbf{j}}_{\mathrm{E}}$. It can be seen that C is fully defined with the information known so far. A new coordinate system, C, is defined with origin at C and orientation given by ${}^{\mathrm{O}}_{\mathrm{C}}\mathbf{R} := \mathrm{Rot}(\alpha, {}^{\mathrm{O}}\hat{\mathbf{i}}_{\mathrm{O}})$,

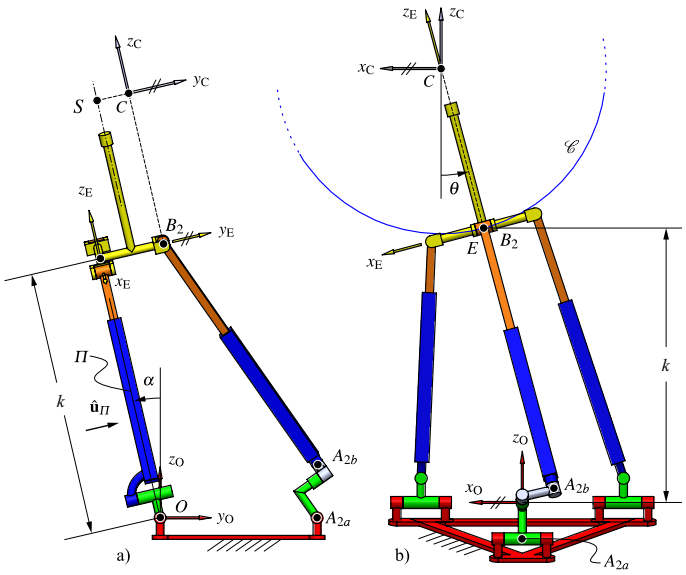

FIGURE 9.6: Definition of coordinate system C and variables a) α and b) θ.

so that $\hat{\mathbf{j}}_C || \hat{\mathbf{j}}_E$ and $\hat{\mathbf{i}}_C || \hat{\mathbf{i}}_O$. Frame C is also known. In Eq. (9.1), the positive sign refers to the typical assembly shown in fig. 9.6, while the negative sign can only be achieved by disassembling the mechanism. This different assembly requires the following transformation between the C and O frames: ${}^O_C\mathbf{R} := \text{Rot}(\alpha, {}^O\hat{\mathbf{i}}_O)\text{Rot}(\pi, {}^O\hat{\mathbf{k}}_O)$.

In order to find ${}^O\hat{\mathbf{i}}_E$, the way to proceed in the case of the ideal Exechon robot is to use the following condition, see fig. 9.2: ${}^O\hat{\mathbf{i}}_E \perp {}^O\mathbf{r}_{S/A_2}$. Since point A_2 is fixed to the ground ${}^O\mathbf{r}_{S/A_2}$ is known and adding the condition $\hat{\mathbf{i}}_E \perp \hat{\mathbf{j}}_E$, ${}^O\hat{\mathbf{i}}_E$ can be obtained.

Unfortunately, the first condition does not hold for the Exechon with offsets in the base joints. It can be seen in fig. 9.6 that ${}^O\hat{\mathbf{i}}_E \not\perp {}^O\mathbf{r}_{S/A_{2a}}$. Instead, our version of the condition is ${}^O\hat{\mathbf{i}}_E \perp {}^O\mathbf{r}_{S/A_{2b}}$. However, unlike $A_{2a} = A_2$, A_{2b} is unknown as it is not fixed to the ground. As a result of this, the analysis becomes much more complicated.

Point A_{2b} which in the ideal Exechon robot is fixed and coincident with A_{2a} is now moving in a toroid $\mathcal{S}$ [6], [35], [36] as shown in fig. 9.7. The common perpendicular between axes $\mathbf{S}_{21}$ and $\mathbf{S}_{22}$ intersects the later at point A_{2c}. This point draws a circle $\mathscr{C}_1$ lying on plane $y_O z_O$ with radius E_1. The common perpendicular between axes $\mathbf{S}_{22}$ and $\mathbf{S}_{23}$ intersects $\mathbf{S}_{22}$ at A_{2d}. Point A_{2b} draws a circle $\mathscr{C}_2$ of radius E_3, with center at A_{2d} and normal parallel to $\mathbf{S}_{22}$. when actuating joint 21 $\mathscr{C}_2(q_{21})$ is swept along $\mathscr{C}_1$ generating a toroid. The axial displacement E_2 gives a banana shape to the cross section of the toroid, see [6].

Point A_{2b} can be located by means of any parametrization of $\mathcal{S}$, here the following is used:

$$
\begin{aligned}
{}^O\boldsymbol{\sigma}(q_{21}, q_{22}) \;:=\; & {}^O\mathbf{r}_{A_{2a}} + \text{Rot}\left(\frac{\pi}{2}, {}^O\hat{\mathbf{j}}_O\right)\text{Rot}\left(q_{21}, {}^O\hat{\mathbf{k}}_O\right)\left(E_1\,{}^O\hat{\mathbf{i}}_O - E_2\,{}^O\hat{\mathbf{j}}_O + \right. \\
& \left. E_3\text{Rot}\left(q_{22}, -{}^O\hat{\mathbf{j}}_O\right){}^O\hat{\mathbf{i}}_O\right) \\
=\; & \left(E_3 \sin q_{22},\, d_{A2} + (E_1 + E_3\cos q_{22})\sin q_{21} - E_2 \cos q_{21},\right. \\
& \left. -(E_1 + E_3\cos q_{22})\cos q_{21} - E_2 \sin q_{21}\right)
\end{aligned}
\tag{9.2}
$$

so that ${}^O\hat{\mathbf{r}}_{A_{2b}} = {}^O\boldsymbol{\sigma}(q_{21}, q_{22})$ and $\mathcal{S} = \text{im}(\boldsymbol{\sigma}(\mathbb{T}^2))$. This parametrization uses the joint variables (q_{21}, q_{22}) as parameters, q_{21} being measured from z_O axis to the common perpendicular of

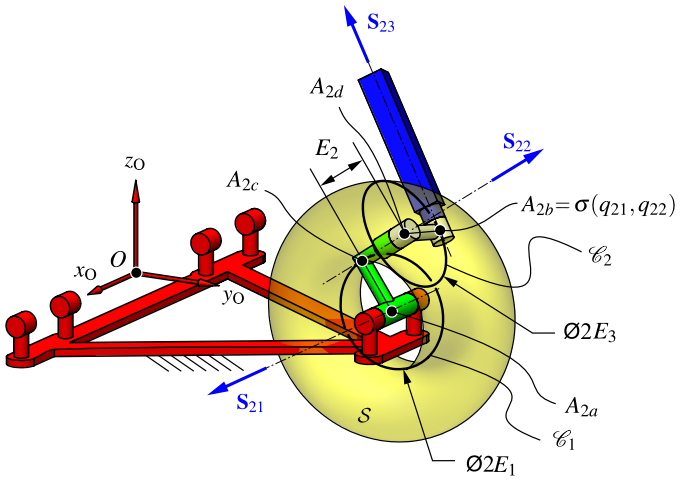

FIGURE 9.7: Point A_{2b} lying on a toroid.

length E_1, about $\mathbf{S}_{21}$ and q_{22} measured from the common perpendicular of length E_1 to the common perpendicular of length E_3 about $-\mathbf{S}_{22}$.

Since $\overline{A_{2d}A_{2b}} \perp \mathbf{S}_{23}$, it follows that $\mathbf{S}_{23}(q_{22},q_{23})$ is tangent to $\mathscr{C}_2(q_{22})$, therefore, the following condition holds:

$$\mathbf{S}_{23}(q_{21},q_{22}) \| \left.\frac{\partial \sigma}{\partial q_{22}}\right|_{(q_{21},q_{22})} \tag{9.3}$$

With the information in hand so far we also know that B_2 lies somewhere in a circle $\mathscr{C}$ of radius h_z, center at C and contained in the $x_C z_C$ plane (see fig. 9.6b). We define the angle θ as the angle from z_C to z_E measured about y_C (or y_E). With this angle, $\mathscr{C}$ is drawn by:

$${}^{O}\mathbf{r}_{B_2/C}(\theta) = h_z \mathrm{Rot}(\alpha, {}^{O}\hat{\mathbf{i}}_O)\mathrm{Rot}(\theta, {}^{O}\hat{\mathbf{j}}_O)(-{}^{O}\hat{\mathbf{k}}_O) \tag{9.4}$$

and the position of B_2 is given by: ${}^{O}\mathbf{r}_{B_2}(\theta) = {}^{O}\mathbf{r}_C + {}^{O}\mathbf{r}_{B_2/C}(\theta)$.

A first condition to consider is that $\mathbf{r}_{B_2/C}$, $\hat{\mathbf{j}}_C$ and $\partial\sigma/\partial q_{22}$ must be coplanar. Therefore:

$$\begin{aligned} \det\left(\mathrm{aug}\left({}^{O}\mathbf{r}_{B_2/C}, \sigma_{q_{22}}, {}^{O}\hat{\mathbf{i}}_O\right)\right) &= 0 \\ \sin q_{q_{22}} \sin\theta(\cos\alpha\cos q_{21} + \sin\alpha\sin q_{21}) - \cos q_{22}\cos\theta &= 0 \end{aligned} \tag{9.5}$$

where $\sigma_{q_{22}} := \partial\sigma/\partial q_{22}$. Eq. (9.5) is in terms of unknowns θ, q_{21} and q_{22}. The computation of these unknowns fully solves the IKP of the parallel module, hence it is required to find more conditions that involve these variables.

Note in fig. 9.6 that $\mathbf{S}_{23}$ must intersect axis y_C, which are the lines given by $\mathscr{L}(\sigma_{q_{22}}, A_{2b})$ and $\mathscr{L}(\hat{\mathbf{j}}_C, S)$, respectively. Therefore, if these two lines intersect the following condition holds:

$$\begin{aligned} \left({}^{O}\sigma_{q_{22}} \times {}^{O}\hat{\mathbf{j}}_C\right) \cdot \left({}^{O}\mathbf{r}_{A_{2b}} - {}^{O}\mathbf{r}_S\right) &= 0 \\ \Big(\big(-E_2\cos q_{21} + E_1\sin q_{21} + d_{A2} - S_y\big)\sin\alpha + \big(E_1\cos q_{21} + E_2\sin q_{21} + \\ S_z\big)\cos\alpha\Big)\cos q_{22} - E_3\big(S_x\sin q_{22} - E_3\big)\big(\cos\alpha\cos q_{21} + \sin\alpha\sin q_{21}\big) &= 0 \end{aligned} \tag{9.6}$$

A third equation to complete the system can be obtained from condition in Eq. (9.3) by considering $\mathbf{r}_{B2/A_{2b}} \| \mathbf{S}_{23}$ then $\mathbf{r}_{B_2/A_{2b}} \| \sigma_{q_{22}}$. Since ${}^{O}\mathbf{r}_{B_2}$ and ${}^{O}\mathbf{r}_{A_{2b}}$ are known in terms of the

three unknowns, the condition can be used as follows:

$$\begin{aligned} {}^{O}\mathbf{r}_{B_2/A_{2b}} \cdot (0,1,0)\,{}^{O}\sigma_{q_{22}} \cdot (0,0,1) - {}^{O}\mathbf{r}_{B_2/A_{2b}} \cdot (0,0,1)\,{}^{O}\sigma_{q_{22}} \cdot (0,1,0) &= 0 \\ \Leftrightarrow & \\ ((d_{B2}-h_y)\cos\alpha + h_z \sin\alpha\cos\theta - d_{A2} + S_y)\cos q_{21} + & \\ (S_z - h_z\cos\alpha\cos\theta + (d_{B2}-h_y)\sin\alpha)\sin q_{21} + E_2 &= 0 \end{aligned} \tag{9.7}$$

Eqs. (9.5-9.7) represent a system of 3 non-linear equations in 3 unknowns. However, note that Eq. (9.6) is only in terms of unknowns q_{21} and q_{22}, and Eq. (9.7) is only in terms θ and q_{21}. It is possible to solve these two equations so that two variables are eliminated.

Eq. (9.6) has the form $K_1\cos q_{22} + K_2 \sin q_{22} + K_3 = 0$, which be solved for q_{22} with two solutions:

$$q_{22}(q_{21}) := \operatorname{atan2}\left(\frac{K_2(K_1(K_1K_3 \mp K_4) - K_3(k_1^2 + K_2^2))}{-K_1K_3 \pm K_4}\right) \tag{9.8}$$

where

$$\begin{aligned} K_1 &:= (-E_2\cos q_{21} + E_1 \sin q_{21} + d_{A2} - S_y)\sin\alpha + (E_1\cos q_{21} + E_2\sin q_{21} + S_z)\cos\alpha, \\ K_2 &:= S_x(\cos\alpha\cos q_{21} + \sin\alpha\sin q_{21}), \\ K_3 &:= E_3(\cos\alpha\cos q_{21} + \sin\alpha\sin q_{21}), \\ K_4 &:= \sqrt{K_1^2K_2^2 + K_2^4 - K_2^2K_3^2}. \end{aligned}$$

Eq. (9.7) can be easily solved for θ to obtain:

$$\begin{aligned} \theta(q_{21}) := \pi \pm \arccos\Big(& (d_{B2}\sin\alpha\sin q_{21} - h_y\sin\alpha\sin q_{21} + d_{B2}\cos\alpha\cos q_{21} \\ & - h_y\cos\alpha\cos q_{21} + S_z\sin q_{21} + (S_y - d_{A2})\cos q_{21} + E_2)(h_z(\sin\alpha\cos q_{21} \\ & - \cos\alpha\sin q_{21})^{-1})\Big) \end{aligned} \tag{9.9}$$

Replacing the expressions for q_{22} and θ from Eqs. (9.8) and (9.9) in Eq. (9.5) the system is reduced to a single equation in a single variable, q_{21}. However, this equation is too complex to obtain a closed form solution and a numerical method has to be applied. There are two solutions in each expression in Eq. (9.8) and (9.9), therefore, at least four solutions can be obtained for the system of equations, however, it is not possible to determine how many solutions can be obtained from Eq. (9.5) once each expression for q_{22} and θ are replaced in it and it is solved numerically.

When the values of q_{21}, q_{22} and θ are defined frame E is determined by ${}^{O}_{E}\mathbf{R} = {}^{O}_{C}\mathbf{R}\mathrm{Rot}(\theta, {}^{C}\hat{\mathbf{j}}_C) = \mathrm{Rot}(\alpha, {}^{O}\hat{\mathbf{i}}_O)\mathrm{Rot}(\theta, {}^{O}\hat{\mathbf{j}}_C)$ and ${}^{O}\mathbf{r}_E = {}^{O}\mathbf{r}_S + \mathrm{Rot}(\theta, {}^{O}\hat{\mathbf{j}}_C)(0, -h_y, -h_z)$. ${}^{O}\mathbf{r}_{B_i}$, $i = 1,2,3$, are also easily obtained now that frame E is known. ${}^{O}\mathbf{r}_{A_{2b}}$ is also known by evaluating parametrization in Eq. (9.2).

The screw coordinates of all joint axes in the parallel module are given by:

Leg $i = 1,3$:

$$\begin{aligned} {}^{O}\mathbf{S}_{i1} &= \left({}^{O}\hat{\mathbf{i}}_O; \mathbf{0}\right), \\ {}^{O}\mathbf{S}_{i2} &= \left({}^{O}\hat{\mathbf{j}}_E; {}^{O}\hat{\mathbf{j}}_E \times ({}^{O}\mathbf{r}_{A_{ia}} + E_l\,{}^{O}\hat{\mathbf{k}}_C)\right), \\ {}^{O}\mathbf{S}_{i3} &= \left(\mathbf{0}; \frac{{}^{O}\mathbf{r}_{B_i} - {}^{O}\mathbf{r}_{A_{ia}} - E_4\,{}^{O}\hat{\mathbf{k}}_C}{|{}^{O}\mathbf{r}_{B_i} - {}^{O}\mathbf{r}_{A_{ia}} - E_l\,{}^{O}\hat{\mathbf{k}}_C|}\right) \\ {}^{O}\mathbf{S}_{i4} &= \left({}^{O}\hat{\mathbf{j}}_E; {}^{O}\hat{\mathbf{j}}_E \times \mathbf{r}_{B_i}\right) \end{aligned}$$

Leg 2:

$$
\begin{aligned}
{}^{O}\mathbf{S}_{21} &= \left({}^{O}\hat{\mathbf{i}}_{O}; d_{A_{2a}}\,{}^{O}\hat{\mathbf{i}}_{O}\times{}^{O}\hat{\mathbf{j}}_{O}\right),\\
{}^{O}\mathbf{S}_{22} &= \mathrm{Adj}\left(\exp(q_{21},{}^{O}\mathbf{S}_{21})\right)\left(-{}^{O}\hat{\mathbf{j}}_{O}; {}^{O}\hat{\mathbf{j}}_{O}\times(-E_1\,{}^{O}\hat{\mathbf{k}}_{O})\right),\\
{}^{O}\mathbf{S}_{23} &= \left(\frac{{}^{O}\boldsymbol{\sigma}_{q_{22}}}{|{}^{O}\boldsymbol{\sigma}_{q_{22}}|}; \frac{{}^{O}\boldsymbol{\sigma}_{q_{22}}}{|{}^{O}\boldsymbol{\sigma}_{q_{22}}|}\times{}^{O}\boldsymbol{\sigma}\right),\\
{}^{O}\mathbf{S}_{24} &= \left(\mathbf{0}; \frac{{}^{O}\boldsymbol{\sigma}_{q_{22}}}{|{}^{O}\boldsymbol{\sigma}_{q_{22}}|}\right)\\
{}^{O}\mathbf{S}_{25} &= \left({}^{O}\hat{\mathbf{i}}_{E}; {}^{O}\hat{\mathbf{i}}_{E}\times\mathbf{r}_{B_2}\right)
\end{aligned}
$$

Joint variables of the actuated joints are given by: $q_{i3} = |{}^{O}\mathbf{r}_{B_i} - {}^{O}\mathbf{r}_{A_{ia}} \mp E_l\,{}^{O}\hat{\mathbf{k}}_{C}|$ and $q_{24} := \mathrm{sign}({}^{O}\hat{\mathbf{s}}_{23}\cdot{}^{O}\mathbf{r}_{B_2/A_{2b}})|{}^{O}\mathbf{r}_{B_2} - {}^{O}\boldsymbol{\sigma}|$, $\{i,l\} = \{1,4\},\{3,5\}$. The negative signs of E_4 and E_5 in q_{13} and q_{33}, respectively, refer to the typical configuration shown in fig. 9.8a, while changing these signs other three configurations shown in fig. 9.8 are obtained. The same situation happens in the ideal case [173]. Observe that these four possibilities only affect the values of q_{13} and q_{33}, therefore, for every solution found another three can be obtained by changing the signs of E_4 and E_5 and without altering any of the other results.

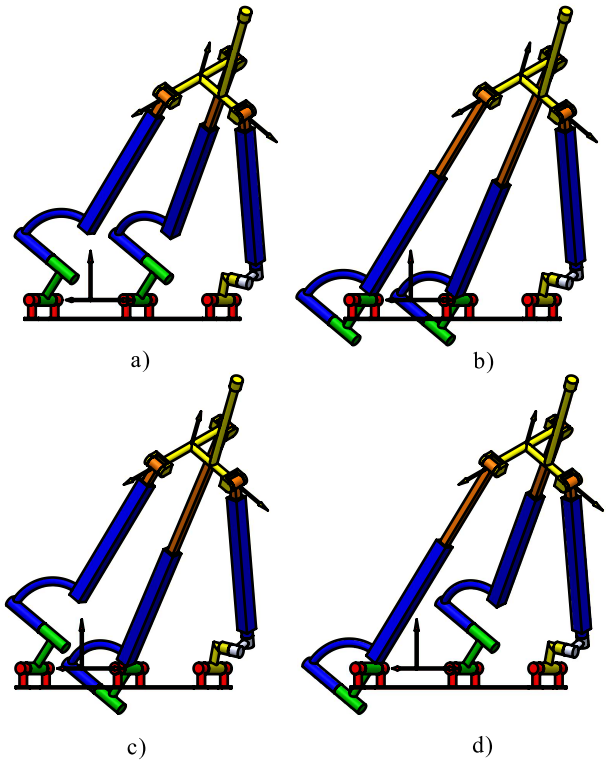

FIGURE 9.8: Four possible configurations of legs 1 and 3 for the same pose of the end-effector and leg 2.

Using the two possible values of α, q_{22} and θ shown in Eqs. (9.1), (9.8) and (9.9), respectively, a total of eight uni-variable equations are obtained. These equations cannot be converted into polynomial expressions due to the presence of multiple square roots which cannot be eliminated. This prevents the straightforward determination of the number of solutions in the complex field. Nevertheless, all possible real solutions were computed for a given position of the end-effector using numerical methods. The results show that each of these 8 equations has two real roots, which give a total of 16 solutions. In addition, considering the four possible configurations of legs 1 and 3 shown in fig. 9.8, there are four cases for each of

the 16 solutions. Then, a total of 64 solutions to the IKP can be obtained. These results are shown in Appendix C . This number of solutions contrasts with the 16 solutions of the ideal case (see [173]) which can be obtained from closed-form solution.

9.4.2 Analysis of the serial module for the IKP

After the analysis of the parallel module the orientation of frame E, ${}^{\mathrm{O}}_{\mathrm{E}}\mathbf{R}$, is known. From the input information of the IKP ${}^{\mathrm{O}}_{\mathrm{S}}\mathbf{R}$ is also known.

It can be seen that ${}^{\mathrm{E}}_{\mathrm{S}}\mathbf{R} = ({}^{\mathrm{O}}_{\mathrm{E}}\mathbf{R}^{\mathrm{t}}){}^{\mathrm{O}}_{\mathrm{S}}\mathbf{R}$. The same transformation must be achieved by actuating the motors of the serial module from an initial configuration $\mathbf{q}_0$ in which frames E and S coincide. Such a configuration is shown in fig. 9.9.

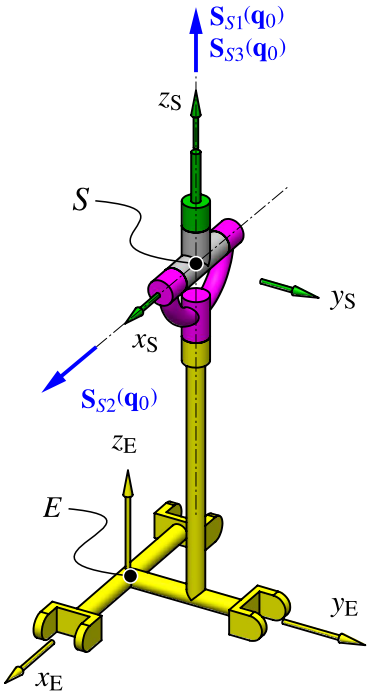

FIGURE 9.9: Initial configuration of the serial module.

After actuation of the three motors of the serial module, the orientation of frame S with respect to E is given by ${}^{\mathrm{E}}_{\mathrm{S}}\mathbf{R} = \mathrm{Rot}(q_{S1}, {}^{\mathrm{E}}\hat{\mathbf{k}}_{\mathrm{E}})\mathrm{Rot}(q_{S2}, {}^{\mathrm{E}}\hat{\mathbf{i}}_{\mathrm{E}})\mathrm{Rot}(q_{S3}, {}^{\mathrm{E}}\hat{\mathbf{k}}_{\mathrm{E}})$. Matching this rotation matrix with ${}^{\mathrm{E}}_{\mathrm{S}}\mathbf{R} = ({}^{\mathrm{O}}_{\mathrm{E}}\mathbf{R}){}^{\mathrm{t}}{}^{\mathrm{O}}_{\mathrm{S}}\mathbf{R}$, the values of q_{Si}, $i = 1,2,3$, are obtained as:

$$\begin{aligned} q_{S2} &= \mathrm{atan2}(\pm R_{2,3}, \pm R_{1,3}), \\ q_{S2} &= \mathrm{atan2}\big(\pm\sqrt{1-R_{3,3}}, R_{3,3}\big), \\ q_{S3} &= \mathrm{atan2}(\pm R_{3,2}, \mp R_{3,1}) \end{aligned}$$

where $R_{i,j}$ is the (i,j) entry of known matrix ${}^{\mathrm{E}}_{\mathrm{S}}\mathbf{R}$. Note that two possible solutions are obtained for a desired orientation of the tool.

The screw coordinates of the joint axes in the serial module are given by ${}^{\mathrm{O}}\mathbf{S}_{Si} = (\hat{\mathbf{s}}_{Si}; \hat{\mathbf{s}}_{Si} \times {}^{\mathrm{O}}\mathbf{r}_S)$, where:

$$\hat{\mathbf{s}}_{S1} = {}^{\mathrm{O}}\hat{\mathbf{k}}_{\mathrm{E}},\ \hat{\mathbf{s}}_{S2} = \mathrm{Rot}(q_{S1}, {}^{\mathrm{O}}\hat{\mathbf{k}}_{\mathrm{E}}){}^{\mathrm{O}}\hat{\mathbf{i}}_{\mathrm{E}},\ \hat{\mathbf{s}}_{S3} = {}^{\mathrm{O}}\hat{\mathbf{k}}_{\mathrm{S}}.$$

9.5 Forward kinematics of the Exechon robot with offsets in the base R joints

In the forward kinematics problem (FKP) of the Exechon robot with offsets the input information are the values of joint variables q_{13}, q_{24}, q_{33}, q_{S1}, q_{S2} and q_{S3} and the outputs are ${}^{\mathrm{O}}_{\mathrm{S}}\mathbf{R}$ and ${}^{\mathrm{O}}\mathbf{r}_T$.

In a similar way to the IKP, it is possible to analyze the parallel and the serial modules separately.

9.5.1 Analysis of the parallel module for the FKP

The FKP of the parallel module consists of finding the position and orientation of the moving platform, i.e. ${}^{\mathrm{O}}_{\mathrm{E}}\mathbf{R}$ and ${}^{\mathrm{O}}\mathbf{r}_E$, respectively, when q_{13}, q_{24} and q_{33} are given. Again, as done with the IKP, the procedure in [171], [173] is first attempted to follow.

Refer to fig. 9.6, a new variable k is introduced and it is defined as $k := {}^{\mathrm{O}}\mathbf{r}_E \cdot {}^{\mathrm{O}}\hat{\mathbf{k}}_C = \mathrm{sign}\left({}^{\mathrm{O}}\mathbf{r}_E \cdot {}^{\mathrm{O}}\hat{\mathbf{k}}_C\right)\sqrt{e_y^2+e_z^2}$, where ${}^{\mathrm{O}}\mathbf{r}_E := (e_x, e_y, e_z)$. If the limits of the actual robot are considered k will always be positive. The following two conditions hold analyzing the projection on plane Π shown in fig. 9.6b:

$$\left(e_x + d_{B1}\cos\theta - d_{A1}\right)^2 + \left(k - d_{B1}\sin\theta \mp E_4\right)^2 - q_{13}^2 = 0 \tag{9.10}$$

$$\left(e_x - d_{B3}\cos\theta + d_{A3}\right)^2 + \left(k + d_{B3}\sin\theta \mp E_5\right)^2 - q_{33}^2 = 0 \tag{9.11}$$

where, as explained in Section 9.4, the signs of E_4 and E_5 determine the four configurations of legs 1 and 3 shown in fig. 9.8, with negative signs for both E_4 and E_5 referring to the typical case in fig. 9.8a. Eqs. (9.10) and (9.11) are in terms of unknowns k, e_x and θ. Two sets of closed-form solutions for k and e_x in terms of θ can be obtained, however the expressions are two long to be presented in this chapter. Considering the 4 possible versions of the system of equations (9.10) and (9.11), a total of 8 sets of closed-form solutions for k and e_x are obtained.

Note that ${}^{\mathrm{O}}\mathbf{r}_E = (e_x, -k\sin\alpha, k\cos\alpha)$, therefore, finding e_x, k and α solves the FKP since α also defines ${}^{\mathrm{O}}\hat{\mathbf{j}}_{\mathrm{E}}$ and using Eqs. (9.10) and (9.11), θ would be obtained which allows the computation of ${}^{\mathrm{O}}\hat{\mathbf{i}}_{\mathrm{E}}$ and ${}^{\mathrm{O}}\hat{\mathbf{k}}_{\mathrm{E}}$.

To obtain equations involving e_x, k and α two expressions for point B_2 are written. The first one describes the vectors from point O to E to B_2:

$$\begin{aligned} {}^{\mathrm{O}}\mathbf{r}_{B_2} &= {}^{\mathrm{O}}\mathbf{r}_E + d_{B2}\mathrm{Rot}(\alpha, {}^{\mathrm{O}}\hat{\mathbf{i}}_{\mathrm{O}})\,{}^{\mathrm{O}}\hat{\mathbf{j}}_{\mathrm{O}} \\ &= (e_x(\theta), -k(\theta)\sin\alpha, k(\theta)\cos\alpha) + d_{B2}\mathrm{Rot}(\alpha, {}^{\mathrm{O}}\hat{\mathbf{i}}_{\mathrm{O}})\,{}^{\mathrm{O}}\hat{\mathbf{j}}_{\mathrm{O}} \end{aligned} \tag{9.12}$$

and the second equation takes the vectors from point O to A_{2a} to B_2:

$${}^{\mathrm{O}}\mathbf{r}_{B_2} = {}^{\mathrm{O}}\mathbf{r}_{A_{2a}} + {}^{\mathrm{O}}\boldsymbol{\sigma}(q_{21}, q_{22}) + q_{24}\frac{{}^{\mathrm{O}}\boldsymbol{\sigma}_{q_{22}}(q_{21}, q_{22})}{|{}^{\mathrm{O}}\boldsymbol{\sigma}_{q_{22}}(q_{21}, q_{22})|} \tag{9.13}$$

Plugging Eqs. (9.12) and (9.13), three scalar equations in terms of 4 unknowns, θ, α, q_{21} and q_{22}, are obtained. In order to get rid of one of the variables, the condition of axis x_{E}

being always perpendicular to joint axes $\mathbf{S}_{23}$ and $\mathbf{S}_{24}$ is considered:

$$\begin{aligned} \sigma_{q_{22}}(q_{21},q_{22})\cdot\hat{\mathbf{i}}_E &= 0 \\ &\Leftrightarrow \\ {}^O\sigma_{q_{22}}(q_{21},q_{22})\cdot \mathrm{Rot}(\alpha,{}^O\hat{\mathbf{i}}_O)\mathrm{Rot}(\theta,{}^O\hat{\mathbf{j}}_O){}^O\hat{\mathbf{i}}_O &= 0 \\ &\Leftrightarrow \\ -\cos q_{21}\sin q_{22}\cos\alpha\sin\theta-\sin q_{21}\sin q_{22}\sin\alpha\sin\theta+\cos q_{22}\cos\theta &= 0 \end{aligned} \quad (9.14)$$

Eq. (9.14) can be solved for q_{22} to obtain two solutions:

$$q_{22}(\theta,\alpha,q_{21}) \in \left\{\arctan\left(\frac{\mathrm{ctg}\theta}{\cos(\alpha-q_{21})}\right),\arctan\left(\frac{\mathrm{ctg}\theta}{\cos(\alpha-q_{21})}\right)-\pi\right\} \quad (9.15)$$

Replacing this solution in Eqs. (9.12) and (9.13) a system of three equations in unknowns three unknowns, θ, α and q_{21}, is obtained. The expressions are large and have to be solved numerically.

When θ, α and q_{21} are known the FKP is solved as: ${}^O_E\mathbf{R}=\mathrm{Rot}(\alpha,{}^O\hat{\mathbf{i}}_O)\mathrm{Rot}(\theta,{}^O\hat{\mathbf{j}}_O)$ and ${}^O\hat{\mathbf{r}}_E=\mathrm{Rot}(\alpha,{}^O\hat{\mathbf{i}}_O)(e_x(\theta),0,k(\theta))$. In addition, the center of the spherical wrist, S, can be easily located by means of: ${}^O\mathbf{r}_S={}^O\mathbf{r}_E+\mathrm{Rot}(\alpha,{}^O\hat{\mathbf{i}}_O)\mathrm{Rot}(\theta,{}^O\hat{\mathbf{j}}_O)(0,h_y,h_z)$.

Using the eight sets of solutions for k and e_x obtained from Eqs. (9.10) and (9.11), along with the two solutions from q_{22} in Eq. (9.15), a total of 16 systems of 3 nonlinear equations in 3 unknowns are obtained. Since these systems cannot be reduced to polynomial expressions it is not possible to obtain the number of solutions in the field of complex numbers in a straightforward way. However, using numerical methods, all possible real solutions of the FKP were obtained for a particular set of actuation values. The results are shown in Appendix C . A total of 57 real solutions were obtained. 16 of these solutions belong to the case of typical configuration of legs 1 and 3 shown in fig. 9.8. To the knowledge of the author, the number of solutions of the FKP of the ideal case is not available in the literature, the reason being that no closed-form solution is available. However, using the same equations presented in this chapter, fixing $E_i=0$, $i=1\ldots5$, all possible solutions of the FKP for the ideal case were obtained numerically for the typical configuration of legs 1 and 3 shown in fig. 9.8. The results show 8 solutions and a duplicate of each one with q_{21} replaced by $q_{21}+\pi$, this simply means that the direction of the axis of revolute joint 22 has been reflected. This change is imperceptible as such joint is part of an arrangement of a spherical joint. For the same configuration of legs 1 and 3.

It is important to mention that the solutions $k(\theta)$ and $e_x(\theta)$, from Eqs. (9.10) and (9.11) do not exist should both $\theta=0$ and $E_4=E_5$ happen. In such a situation, Eqs. (9.10) and (9.11) are reduced to two equations in $k(\theta)$ and $e_x(\theta)$ with the following solutions:

$$\begin{aligned} e_x &= -\frac{q_{13}^2-q_{33}^2}{4(d_{A_1}-d_{B_1})}, \\ k &= \frac{1}{4(d_{A_1}-d_{B_1})}\left(\pm\left(\left(8d_{A_1}^2-16d_{A_1}d_{B_1}+8d_{B1}^2+2q_{13}^2\right)q_{33}^2-q_{33}^4\right.\right. \\ &\quad \left.\left.-16\left(d_{A_1}-d_{B1}-\frac{q_{13}}{2}\right)^2\left(d_{A_1}-d_{B1}+\frac{q_{13}}{2}\right)^2\right)^{\frac{1}{2}}+4E_4(d_{A_1}-d_{B1})\right) \end{aligned} \quad (9.16)$$

Eq. (9.14) now leads to $q_{22}\in\{\pi/2,3\pi/2\}$, replacing the known values of e_x, k and q_{22} in Eqs. (9.12) and (9.13) three equations in unknowns q_{21} and α is obtained. The extra equations gives a necessary condition for $\theta=0$ to happen: $q_{33}=\sqrt{4E_3(d_{A_1}-d_{B_1})+q_{13}^2}$.

It can be seen that in the ideal Exechon robot, i.e. $E_3 = 0$, the parallel module adopts a symmetric configuration with respect to the $y_O z_O$ plane.

9.5.2 Analysis of the serial module for the FKP

After solving the FKP of the parallel module, the values of ${}^{O}\mathbf{r}_E$ and ${}^{O}_{E}\mathbf{R}$ are known. Since ${}^{E}\mathbf{r}_S = (0, h_y, h_z)$ is constant, the position of the center of the spherical wrist, S, w.r.t. frame O is fully determined after solving the FKP of the parallel module as ${}^{O}\mathbf{r}_S = {}^{O}_{E}\mathbf{R}\,{}^{E}\mathbf{r}_S$. The orientation of the tool frame, S, (see Fig. 9.9) with respect to the platform frame E is given by ${}^{E}_{S}\mathbf{R} = \mathrm{Rot}(q_{S1}, {}^{E}\hat{\mathbf{k}}_E)\mathrm{Rot}(q_{S2}, {}^{E}\hat{\mathbf{i}}_E)\mathrm{Rot}(q_{S3}, {}^{E}\hat{\mathbf{k}}_E)$. Therefore, if the input variables of actuation q_{S1}, q_{S2} and q_{S3} are known the orientation of the tool is computed by ${}^{O}_{S}\mathbf{R} = {}^{O}_{E}\mathbf{R}\,{}^{E}_{S}\mathbf{R}$.

9.6 Constraint system

It is desired to know the system of constraints for a given position and orientation of the end-effector. After solving the IKP for such a pose of the tool, it is possible to compute the wrench system of constraints. In this section, the computation of the wrench system of the parallel module is addressed. Note that a basis for the wrench system of the serial module, which is a spherical wrist, simply consists of three linearly independent wrenches of pitch 0 intersecting S, the center of the wrist.

The constraint system of each leg of the parallel module of the Exechon robot with offsets is different from that of the ideal Exechon robot. However, for legs 1 and 3 the wrench system is the same and still can be found by means of geometry as shown in fig. 9.10 for leg 1: Similarly to legs $i = 1, 3$ of the ideal Exechon robot, the wrench system of constraints consists of two wrenches, the first one, $\mathbf{W}_{ci1}$ being a pure moment that is perpendicular to axes $\mathbf{S}_{i1}$ and $\mathbf{S}_{i2}$ and, in consequence, also perpendicular to $\mathbf{S}_{i4}$. Since it is $\mathbf{W}_{ci1}$ is a pure moment, then $\mathrm{Kl}(\mathbf{W}_{ci1}, \mathbf{S}_{i3}) = 0$ is also ensured. The second wrench, $\mathbf{W}_{ci2}$, is a pure force intersecting $\mathbf{S}_{i1}$ and parallel to $\mathbf{S}_{i2}$ and $\mathbf{S}_{i4}$. Since $\mathbf{W}_{ci2} \perp \mathbf{S}_{13}$ their reciprocity is ensured.

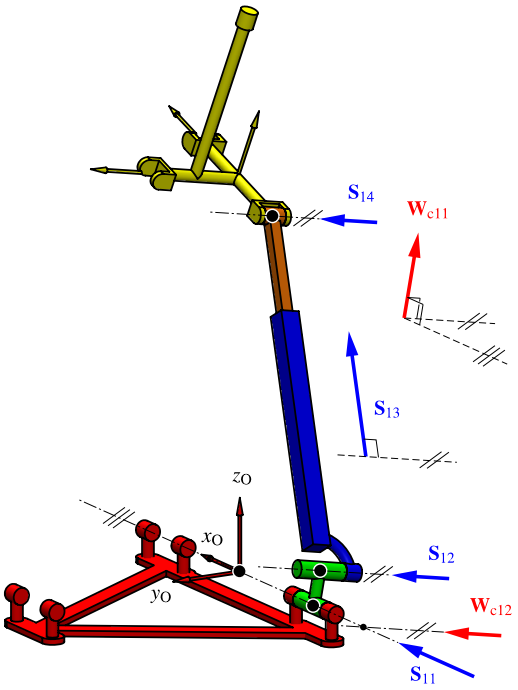

FIGURE 9.10: Constraint system of leg 1.

Since the IKP is considered to be known, the two wrenches for legs $i = 1,3$ can be computed by means of:

$$\begin{aligned} {}^{O}\mathbf{W}_{ci1} &= \left(\mathbf{0}; \mathrm{Rot}(\alpha, {}^{O}\hat{\mathbf{i}}_{O}) {}^{O}\hat{\mathbf{k}}_{O}\right), \\ {}^{O}\mathbf{W}_{ci2} &= \left(\mathrm{Rot}(\alpha, {}^{O}\hat{\mathbf{i}}_{O}) {}^{O}\hat{\mathbf{j}}_{O}; \mathbf{0}\right). \end{aligned}$$

Unfortunately, for leg 2, unlike in the ideal Exechon robot, the sole wrench the spans the system of constraints of the leg is neither 0- nor infinite-pitched, and therefore it cannot be located by means of geometry, at least not easily. $\mathbf{W}_{c21}$, the only wrench in this system, can be found by computation of a basis of $\mathrm{Null}((\mathbf{J}_2(\mathbf{q}))^{t})$, where $\mathbf{J}_2 := \mathrm{aug}({}^{O}\mathbf{S}_{21}, \ldots, {}^{O}\mathbf{S}_{25})$.

Although IKP is solved numerically, it is possible to obtain a closed form solution for ${}^{O}\mathbf{W}_{c21}$ if $\mathbf{J}_2$ is expressed in terms of α, θ, q_{21} and q_{22}. When these values are obtained in the IKP it is easier to evaluate the closed form solution of ${}^{O}\mathbf{W}_{c21}$ than computing $\mathrm{Null}((\mathbf{J}_2(\mathbf{q}))^{t})$ for the given configuration $\mathbf{q}$.

Let $\lambda {}^{O}\tilde{\mathbf{W}}_{c21}$ be the only element of the basis of the computed null space [182] (it is multiplied by λ since it is not necessary a unit screw), then $\mathrm{span}({}^{O}\tilde{\mathbf{W}}_{c21}) = \mathrm{Null}((\mathbf{J}_2^{t}(\mathbf{q}))^{t})$, where, if $\mathbf{W}_{c21} := (\hat{\mathbf{s}}; \mathbf{v})$, then $\tilde{\mathbf{W}}_{c21} := (\mathbf{v}; \mathbf{s})$. Clearly, $\mathrm{Kl}({}^{O}\mathbf{S}_{2j}, {}^{O}\mathbf{W}_{c21}) = 0$, $j = 1, \ldots, 5$, if and only if $({}^{O}\mathbf{S}_{2j})^{t} \tilde{\mathbf{W}}_{c21} = 0$.

Using symbolic algebra software Maple $\mathrm{Null}((\mathbf{J}_2(\mathbf{q}))^{t})$ is computed and a closed-form solution is found in terms of the previously mentioned intermediate variables. The solution is long and is presented in Appendix B.

9.7 Effects of offsets in the position of the moving platform

It is possible that not all five offsets are present in the robot, therefore a total of $2^5 = 32$ situations are possible, depending on which links present error and which are ideal. For example, the link between joints 11 and 12 can be ideal and $E_4 = 0$, while the other offsets are still present. It is possible to check which of these 32 cases produces the biggest error in the position of the moving platform. The 32 cases will be tested in different points of the reachable workspace of the robot, and in each case the deviation of point E in the platform will be compared to its ideal position that would be obtained in the ideal Exechon robot using the same values of the actuated joint variables.

Parameter	Value (mm)
h_y	83
h_z	408.1
d_{A_1}	250
d_{A_2}	400
d_{B_1}	133
d_{B_2}	166
q_{13}, q_{24} and q_{33}, actuator fully contracted	563
Stroke of actuators	300

TABLE 9.1: Dimensions and joint limits of the example.

The comparison is made using the dimensions shown in table 9.1. The stroke of each actuator is split in 11 positions, generating a total of $11^3 = 1331$ configurations to be tested. Since in each configuration 32 different cases of combinations of offsets are to be analyzed, a total of $1331 \times 32 = 42592$ iterations are required.

Fig. 9.11 shows the contour graph approximated using the position of point E in each of the 1331 analyzed configurations in the ideal case. The plot shows a typical shape of workspace in parallel mechanisms.

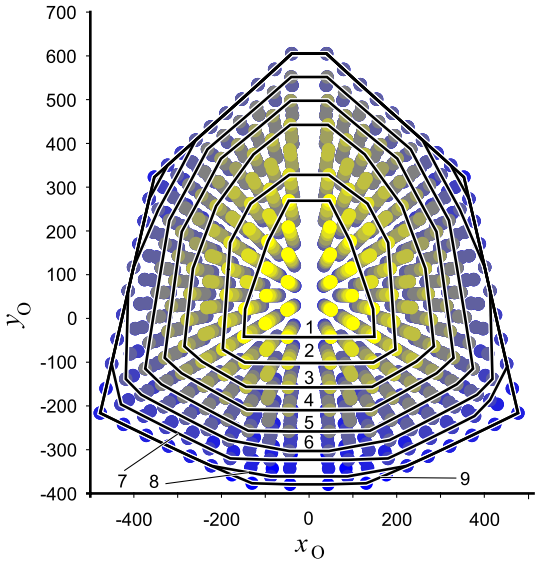

FIGURE 9.11: Contour plot of the workspace of the ideal Exechon robot approximated using the tested configurations. Level 1, $z_0 = 794.1$; level 2, $z_0 = 749.2$; level 3, $z_0 = 704.3$; level 4, $z_0 = 659.4$; level 5, $z_0 = 614.5$; level 6, $z_0 = 569.6$; level 7, $z_0 = 524.7$; level 8, $z_0 = 479.8$; and level 9, $z_0 = 434.9$

In each of the 1331 configurations the case of offsets combinations that produces the biggest deviation of point E is saved. When all the configurations have been analyzed, the number of times that every case of offsets combinations gave the biggest deviation is counted. According to these results, the case that affected the position of E the worst is when all offsets are present except E_5, the length of the common perpendicular between joint axes $\mathbf{S}_{31}$ and $\mathbf{S}_{33}$, which was the worst case in 428 configurations. Note that this non-symmetrical result is a consequence of the loss of symmetry of the parallel module, whose offsets between axes in leg 3 break the symmetry borne by the ideal mechanism.

Fig. 9.12 shows the points reached by the ideal Exechon robot in the 1331 configurations analyzed. In such plots, the clearer the dots are, the larger the deviation of point E in the parallel platform will be when all offsets, except the one in leg 3 are introduced. It can be seen that the safest area is when x_O-coordinate of E is negative, while its y_O-coordinate is positive. These results were obtained using an offset of 1 mm, for which the largest deviation of the position of E with respect to the ideal case was 2.8428193 mm, while the mean was a deviation of 2.216036073 mm.

In order to observe the effects of the same arrangement of offsets on the position and orientation of the end-effector, consider a configuration with actuation values $q_{13} = 800$mm, $q_{24} = 600$mm, $q_{33} = 670$mm, $q_{S1} = 65°$, $q_{S2} = 32°$ and $q_{S3} = 210°$. Table 9.2 compares the ideal case against the case with 1-mm offsets inserted in all base axes except the one in leg 3, which is, according to the previously-discussed results, the worst case. According to the values in table 9.2, the deviation of point E of the moving platform is 2.37549666 mm, while the deviation of point S in the end-effector is 3.278749429 mm.

In regard to the constraint system, in the ideal case, it is spanned by the single element ${}^{O}\mathbf{W}_{c21} = ({}^{O}\hat{\mathbf{s}}_{c21}, {}^{O}\mathbf{v}_{c21})$, which is a pure force parallel to ${}^{O}\hat{\mathbf{s}}_{25} = (0.956434219, -0.120992931, -0.265695869)$ and intersecting point A_2. When the error offsets are considered, the single element in the wrench system is obtained by means of the null space as. This wrench is slightly non-parallel to the axis of joint 25, which is computed as ${}^{O}\hat{\mathbf{s}}_{25} = (0.956867789,$

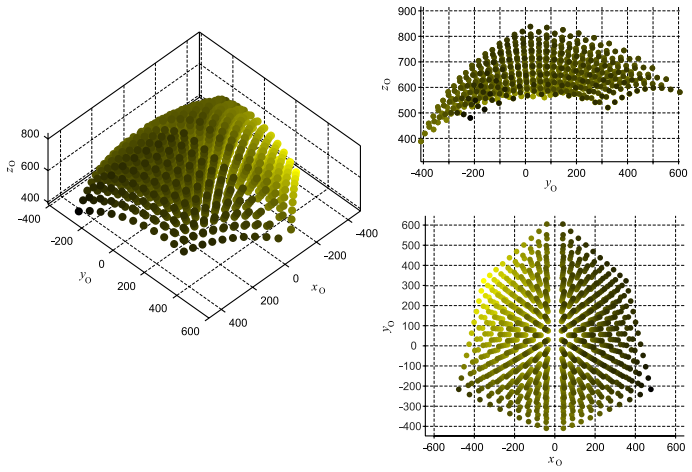

FIGURE 9.12: Workspace of Exechon robot with projections on the $y_O z_O$ and $x_O y_O$ planes (top right and bottom right, respectively). The clearer the dots, the larger the deviation of the moving platform if all offsets are introduced except that of leg 3.

-0.119963676, -0.264599229). This wrench has also a small pitch, $h_{c21} = {}^{O}\hat{\mathbf{s}}_{c21} \cdot {}^{O}\mathbf{v}_{c21} = 0.149887$, which makes it a non-pure force. Finally, its axis does not intersect point A_2, but it is located a distance 1.30615095 mm away from it.

	Ideal case	Offsets inserted
${}^{O}\mathbf{r}_E$	$\begin{pmatrix} 165.352704 \\ 293.201618 \\ 643.859589 \end{pmatrix}$	$\begin{pmatrix} 163.50554 \\ 292.513261 \\ 645.185159 \end{pmatrix}$
${}^{O}\mathbf{r}_S$	$\begin{pmatrix} 284.4966477 \\ 530.5001643 \\ 964.6846679 \end{pmatrix}$	$\begin{pmatrix} 282.0682724 \\ 529.3520278 \\ 966.5648205 \end{pmatrix}$
${}^{O}_{S}\mathbf{R}$	$\begin{pmatrix} -0.05985 & 0.70474 & 0.70693 \\ -0.98463 & -0.15807 & 0.07422 \\ 0.16405 & -0.69162 & 0.70337 \end{pmatrix}$	$\begin{pmatrix} -0.05947 & 0.70577 & 0.70593 \\ -0.98494 & -0.15649 & 0.07349 \\ 0.16234 & -0.69093 & 0.70445 \end{pmatrix}$
${}^{O}\mathbf{W}_{c21}$	$\begin{pmatrix} 0.956434219 \\ -0.12099293 \\ -0.265695869 \\ -106.278348 \\ 0 \\ -382.573688 \end{pmatrix}$	$\begin{pmatrix} 0.956843709 \\ -0.12021105 \\ -0.264574035 \\ -105.829614 \\ 0.887651387 \\ -383.707314 \end{pmatrix}$

TABLE 9.2: Comparison of the position, ${}^{O}\mathbf{r}_S$, and orientation, ${}^{O}_{S}\mathbf{R}$, of the end effector and constraint of leg 2, ${}^{O}\mathbf{W}_{c21}$, between the ideal case and the case with 1mm offset inserted in all base joints except that of leg 3.

9.8 Chapter conclusions

In this chapter the Exechon robot was analyzed considering imperfect joint axes in the joints connecting the legs to the fixed platform. The forward and inverse kinematics of the robot were solved and its constraint system was obtained. It can be concluded that the introduction of these offsets makes the analysis of the robot a much more complex problem which had to be solved numerically, although the systems of equations were reduced from their original form. The constraint system is the same as in the ideal case for legs 1 and 3, however for leg 2 the single wrench that spans the system of constraints of such leg cannot be obtained by geometrical means. The use of the FKP showed that the combination of all offsets except that of leg 1 leads to the largest deviation in the position of the parallel platform. In addition,

eight solutions to the IKP of the parallel module were obtained for a given position of the end-effector. Meanwhile, sixteen solutions to the FKP of the parallel module were obtained. It can be seen that the number of solutions for the IKP was reduced from the original 16 solutions of the ideal case.

The results obtained in this chapter allow a more precise prediction of the position and orientation of the tool once the dimensions of each offset are known. These results are also the first step to the determination of a stiffness model of this robot with imperfections for a more detailed analysis of the errors produced during machining operations.

Chapter 10

General Conclusions

This thesis presented results from the application of the method of generated surfaces to the design and analysis of mechanisms with different purposes. The following conclusions can be drawn from this research:

- Two families of reconfigurable paradoxical Bricard linkages were obtained from the intersection of two toroids, one of this families consists of line-symmetric linkages, while the other includes plane-symmetric linkages. It was shown that in the line-symmetric case, branches of motion in which the linkage behaves like a 4R Bennett mechanism, while the plane-symmetric cases presented branches of motion where the linkage works as a spherical 4R mechanism.
- A method for the design of multi-loop kinematotropic linkages was established using kinematic chains that can change the surface they generate. Therefore, these mechanical generators cannot be dyads, they must be closed or hybrid chains. The Bohemian dome was used as an example and its multiple self-crossings allowed the description of new ways of reconfiguration that had not been used before in the method of generated surfaces.
- A kinematotropic PKM was designed by taking an existing constant-mobility reconfigurable PKM and adding a carefully designed surface generator as an extra leg. The PKM was able to shift between three different values of finite mobility: 1 DOF, 2 DOF and 3 DOF. Although this is a very uncommon property, Wohlhart's Star-Cube is believed to have tens of branches of motions with (at least) the same three different values of finite mobility.
- The first method for the design of spatial cusp mechanisms was presented, this allowed the discovery of two new types of singularities: the intersection of a cusp and a regular curve, and the intersection of a cusp and regular surface. Interestingly, the intersection of a cusp and a surface would force the linkage to change from 1 DOF to 2 DOFs instead of choosing between the branches as normally happens in transverse intersections. This would lead to an easier-to-control reconfiguration.
- The first method for the design of mechanisms with a tangential intersection of branches of motion was presented. In addition, it was presented how to distinguish these branches of motion using only higher order analysis. In a similar way to the previous conclusion, theoretically a tangential intersection would allow a "smoother" transition between working modes, although not really a smooth curve in the formal mathematical sense.
- The FKP and IKP for the Exechon robot with error offsets at the base were solved and the error in the position of a point was modeled as a toroid. It was shown that the closed-form solution that has been reported for the IKP of the ideal Exechon robot is lost when error offsets are added and only numerical solutions can be obtained.

It can be seen that the method of generated surfaces represents a technique that can help the solution of more modern problems in mechanisms theory and robotics. The biggest drawback of the method is determining the intersection set between the surfaces by obtaining a parametrization of each of its components. Several techniques to aid for solving this were applied in this thesis as have been in the literature. This includes plugging parametric equations with implicit forms and changing parameters. However, as it was shown in this thesis, the power of the method of generated surfaces does not require the computation of the intersection set in order to be useful. Local analysis of the intersection can be carried out, the curvatures and other properties of the surfaces can be used and, generally, knowing a general behaviour of the intersection is required. The use of SolidWorks, Maple and Matlab in order to generate these surfaces and intersection curves brings a powerful insight on the behaviour of the linkage. This is one of the most beneficial aspects of the method.

Tentative future work includes:

- Finding a method for the identification and analysis of cusp singularities when only local information is available, this problem was not solved in chapter 7
- In the design of both mechanisms with cusps and with tangential intersection of branches of motion, it is not known yet if these phenomena happen only in 1-DOF linkages, the question is open for higher mobility, e.g., for 2 DOFs, configuration spaces that look like a funnel or surfaces that are tangent to each other.
- In chapter 7, only one PKM was designed, it is straightforward to extend these results to a general method to obtain more examples.
- Several models of the Exechon PKM, e.g. the Exechon XMini, present an offset wrist, instead of a spherical one, as serial component. The kinematics of these robots is no longer decoupled. The results presented in chapter 9 have to be obtained for models featuring an offset wrist.

The solutions to these problems, are still open problems in the literature. However, results for the last two points have already been recently obtained by the author of this thesis.

Appendix A

Solutions for the toroids parameters in the line-symmetric case

In this Appendix the four solutions for the concentric toroid-toroid intersection with line symmetry are listed.
Solution 1:

$$
\begin{aligned}
u_A(v_B) &= \operatorname{atan2}\Bigg(\frac{-1}{\sin\theta\cos\gamma_B}(b_2(b_2+b_1\cos v_B)\sqrt{K_1}-b_1b_2\cos\gamma_A\cos\gamma_B\sin^2 v_B(b_1\sin\gamma_A\cos\theta \\
&\quad -b_2\sin\gamma_B)),\ \frac{-\sin v_B}{\sin\theta\cos\gamma_B}(b_1b_2\cos\gamma_A\sqrt{K_1}+b_2\cos\gamma_B(b_2+b_1\cos v_B)(b_1\sin\gamma_A\cos\theta \\
&\quad +b_2\sin\gamma_B))\Bigg) \\
v_A(v_B) &= v_B \\
u_B(v_B) &= \operatorname{atan2}\Bigg(\frac{-b_2\csc\theta\sec\gamma_B}{b_2^2\sin^2 v_B\cos^2\gamma_B+(b_1+b_2\cos^2 v_B)^2}((b_1+b_2\cos v_B)\sqrt{K_1} \\
&\quad -b_2\cos\gamma_A\cos\gamma_B\sin^2 v_B(b_1\sin\gamma_A-b_2\sin\gamma_B\cos\theta)), \\
&\quad \frac{-\sin v_B\csc\theta\sec\gamma_B}{b_2^2\sin^2 v_B\cos^2\gamma_B+2b_1b_2\cos v_B+b_2^2\cos^2\gamma_B+b_1^2}(b_2\sqrt{K_1}+(b_1 \\
&\quad +b_2\cos v_B)(-b_2\sin\gamma_B\cos\theta+b_1\sin\gamma_A))\Bigg)
\end{aligned}
$$

Solution 2:

$$
\begin{aligned}
u_A(v_B) &= \operatorname{atan2}\Bigg(\frac{-1}{\sin\theta\cos\gamma_B}(-b_2(b_2+b_1\cos v_B)\sqrt{K_1}-b_1b_2\cos\gamma_A\cos\gamma_B\sin^2 v_B(b_1\sin\gamma_A\cos\theta \\
&\quad +b_2\sin\gamma_B)),\ \frac{-\sin v_B}{\sin\theta\cos\gamma_B}(-b_1b_2\cos\gamma_A\sqrt{K_1}+b_2\cos\gamma_B(b_2+b_1\cos v_B)(b_1\sin\gamma_A\cos\theta \\
&\quad -b_2\sin\gamma_B))\Bigg) \\
v_A(v_B) &= v_B \\
u_B(v_B) &= \operatorname{atan2}\Bigg(\frac{-b_2\csc\theta\sec\gamma_B}{b_2^2\sin^2 v_B\cos^2\gamma_B+(b_1+b_2\cos^2 v_B)^2}(-(b_1+b_2\cos v_B)\sqrt{K_1} \\
&\quad -b_2\cos\gamma_A\cos\gamma_B\sin^2 v_B(b_1\sin\gamma_A-b_2\sin\gamma_B\cos\theta)), \\
&\quad \frac{-\sin v_B\csc\theta\sec\gamma_B}{b_2^2\sin^2 v_B\cos^2\gamma_B+2b_1b_2\cos v_B+b_2^2\cos^2\gamma_B+b_1^2}(-b_2\sqrt{K_1}+(b_1 \\
&\quad +b_2\cos v_B)(-b_2\sin\gamma_B\cos\theta+b_1\sin\gamma_A))\Bigg)
\end{aligned}
$$

Solution 3:

$$
\begin{aligned}
u_A(v_B) &= \operatorname{atan2}\Bigg(\frac{-1}{\sin\theta\cos\gamma_B}(b_2(b_2+b_1\cos v_B)\sqrt{K_2}-b_1b_2\cos\gamma_A\cos\gamma_B\sin^2 v_B(b_1\sin\gamma_A\cos\theta \\
&\quad -b_2\sin\gamma_B)),\ \frac{\sin v_B}{\sin\theta\cos\gamma_B}(b_1b_2\cos\gamma_A\sqrt{K_2}+b_2\cos\gamma_B(b_2+b_1\cos v_B)(b_1\sin\gamma_A\cos\theta \\
&\quad +b_2\sin\gamma_B))\Bigg) \\
v_A(v_B) &= -v_B \\
u_B(v_B) &= \operatorname{atan2}\Bigg(\frac{-b_2\csc\theta\sec\gamma_B}{b_2^2\sin^2 v_B\cos^2\gamma_B+(b_1+b_2\cos^2 v_B)^2}((b_1+b_2\cos v_B)\sqrt{K_2} \\
&\quad +b_2\cos\gamma_A\cos\gamma_B\sin^2 v_B(b_1\sin\gamma_A-b_2\sin\gamma_B\cos\theta)), \\
&\quad \frac{-\sin v_B\csc\theta\sec\gamma_B}{b_2^2\sin^2 v_B\cos^2\gamma_B+2b_1b_2\cos v_B+b_2^2\cos^2\gamma_B+b_1^2}(b_2\sqrt{K_2}+(b_1 \\
&\quad +b_2\cos v_B)(-b_2\sin\gamma_B\cos\theta-b_1\sin\gamma_A))\Bigg)
\end{aligned}
$$

Solution 4:

$$
\begin{aligned}
u_A(v_B) &= \operatorname{atan2}\Bigg(\frac{-1}{\sin\theta\cos\gamma_B}(-b_2(b_2+b_1\cos v_B)\sqrt{K_2}-b_1b_2\cos\gamma_A\cos\gamma_B\sin^2 v_B(b_1\sin\gamma_A\cos\theta \\
&\quad -b_2\sin\gamma_B)),\ \frac{\sin v_B}{\sin\theta\cos\gamma_B}(-b_1b_2\cos\gamma_A\sqrt{K_2}+b_2\cos\gamma_B(b_2+b_1\cos v_B)(b_1\sin\gamma_A\cos\theta \\
&\quad +b_2\sin\gamma_B))\Bigg) \\
v_A(v_B) &= -v_B \\
u_B(v_B) &= \operatorname{atan2}\Bigg(\frac{-b_2\csc\theta\sec\gamma_B}{b_2^2\sin^2 v_B\cos^2\gamma_B+(b_1+b_2\cos^2 v_B)^2}(-(b_1+b_2\cos v_B)\sqrt{K_2} \\
&\quad +b_2\cos\gamma_A\cos\gamma_B\sin^2 v_B(b_1\sin\gamma_A-b_2\sin\gamma_B\cos\theta)), \\
&\quad \frac{-\sin v_B\csc\theta\sec\gamma_B}{b_2^2\sin^2 v_B\cos^2\gamma_B+2b_1b_2\cos v_B+b_2^2\cos^2\gamma_B+b_1^2}(-b_2\sqrt{K_2}+(b_1 \\
&\quad +b_2\cos v_B)(-b_2\sin\gamma_B\cos\theta-b_1\sin\gamma_A))\Bigg)
\end{aligned}
$$

where:

$$
\begin{aligned}
K_1 &:= -\cos\gamma_B\big((2b_1b_2\sin\gamma_A\sin\gamma_B\cos\theta-b_2^2\sin^2\gamma_B-b_1^2\sin^2\gamma_A)\cos^2 v_B-2b_1b_2\sin^2\theta\cos v_B \\
&\quad +(b_1^2+b_2^2)\cos^2\theta-2b_1b_2\sin\gamma_A\sin\gamma_B\cos\theta-b_1^2\cos^2\gamma_A-b_2^2\cos^2\gamma_B\big) \\
K_2 &:= -\cos\gamma_B\big((-2b_1b_2\sin\gamma_A\sin\gamma_B\cos\theta-b_2^2\sin^2\gamma_B-b_1^2\sin^2\gamma_A)\cos^2 v_B-2b_1b_2\sin^2\theta\cos v_B \\
&\quad +(b_1^2+b_2^2)\cos^2\theta-2b_1b_2\sin\gamma_A\sin\gamma_B\cos\theta-b_1^2\cos^2\gamma_A-b_2^2\cos^2\gamma_B\big)
\end{aligned}
$$

Appendix B

Wrench of constraints of leg 2 of the Exechon PKM

The following wrench of constraints of leg 2 is computed:

$$\lambda^{O}\mathbf{W}_{c21} = (K_5, K_6, K_7; d_{A_2}, K_8, K_9)$$

where:

$$\begin{aligned} K_5 := {} & ((-S_x(\cos\alpha\cos q_{21} + \sin\alpha\sin q_{21})\sin\theta + (-\cos\theta(b_{B_2} - h_y)\sin\alpha + \cos\alpha h_z \\ & - \cos\theta S_z)\cos q_{21} - \sin q_{21}(((h_y - d_{B2})\cos\alpha + d_{A_2} - S_y)\cos\theta - \sin\alpha h_z))\sin q_{22} + \\ & \sin\theta(-\sin\alpha\cos q_{22}(d_{A_1} - d_{A_2})\cos^2 q_{21} + (\cos q_{22}(d_{A_1} - d_{A_2})\sin q_{21} + \cos q_{22}E_1 + \\ & E_3)\cos\alpha\cos q_{21} + ((\cos q_{22}E_1 + E_3)\sin q_{21} + \cos q_{22}(d_{A_1} - d_{A_2}))\sin\alpha))\sin q_{22} \end{aligned}$$

$$\begin{aligned} K_6 := {} & (-\cos\alpha(\cos q_{22} - 1)(\cos q_{22} + 1)(d_{A_1} - d_{A_2})\cos^3 q_{21} + (-\sin\alpha\sin q_{21}(d_{A_1} \\ & - d_{A_2})\cos^2 q_{22} - E_3\sin\alpha\cos q_{22} + ((d_{A_1} - d_{A_2})\sin q_{21} - E_1)\sin\alpha - E_2\cos\alpha)\cos^2 q_{21} + \\ & ((S_z\sin\alpha + (d_{A_1} - 2d_{A_2} + S_y)\cos\alpha - h_y + d_{B_2})\cos^2 q_{22} + \cos\alpha\sin q_{21}E_3\cos q_{22} + \\ & (-\sin q_{21}E_2 - S_z)\sin\alpha + (E_1\sin q_{21} + d_{A_2} - S_y)\cos\alpha - d_{B_2} + h_y)\cos q_{21} + \\ & (((d_{A1} - d_{A_2})\sin q_{21} + E_1)\cos q_{22} - \sin q_{22}S_x + E_3)\sin\alpha\cos q_{22})\sin\theta + \sin(q_{22})(\sin\alpha h_z - \\ & ((h_y - d_{B_2})\cos\alpha + d_{A2} - S_y)\cos\theta)\cos q_{22} \end{aligned}$$

$$\begin{aligned} K_7 := {} & ((\sin\alpha(d_{A_1} - d_{A2})\cos^3 q_{21} - \cos\alpha\sin q_{21}(d_{A1} - d_{A_2})\cos^2 q_{21} - \sin\alpha(d_{A_1} - d_{A2})\cos q_{21} + \\ & (s_z\sin\alpha + (-d_{A_2} + s_y)\cos\alpha - h_y + d_{B2})\sin q_{21} - \cos\alpha E_1)\cos^2 q_{22} + (-\cos\alpha\cos^2 q_{21}E_3 \\ & - \sin\alpha\sin q_{21}E_3\cos q_{21} + s_x\cos\alpha\sin q_{22})\cos q_{22} - \sin\alpha(d_{A_1} - d_{A_2})\cos^3 q_{21} + \\ & (\cos\alpha\sin q_{21}(d_{A_1} - d_{A_2}) - \cos\alpha E_1 + \sin\alpha E_2)\cos^2 q_{21} + ((-E_2\cos\alpha - \sin\alpha E_1)\sin q_{21} + \\ & \sin\alpha(d_{A_1} - d_{A_2}))\cos q_{21} + (-s_z\sin\alpha + (d_{A_2} - s_y)\cos\alpha + h_y - d_{B_2})\sin q_{21} + \cos\alpha E_1 \\ & - \sin\alpha E_2)\sin\theta - \sin q_{22}\cos q_{22}((h_y - d_{B_2})\cos\theta\sin\alpha + \cos\alpha h_z - s_z\cos\theta) \end{aligned}$$

$$
\begin{aligned}
K_8 := {} & ((\cos\alpha(d_{B_2}-h_y)-d_{A_2}+s_y)\cos\theta+\sin\alpha(-\sin\theta s_x+h_z))(d_{A_1}-d_{A_2})(\cos q_{22}+\\
& 1)(\cos q_{22}-1)\cos^3 q_{21}+(-(d_{A_1}-d_{A_2})\sin q_{21}(((h_y-d_{B_2})\sin\alpha-s_z)\cos\theta+\\
& \cos\alpha(-\sin\theta s_x+h_z))\cos^2 q_{22}+(E_3(\sin\alpha(d_{B_2}-h_y)+s_z)\cos\theta+(((d_{A_2}-s_y)(d_{A_1}\\
& -d_{A2})\sin q_{22}+E_3 s_x)\sin\theta-h_z E_3)\cos\alpha-\sin\theta\sin q_{22}(\sin\alpha s_z-h_y+d_{B_2})(d_{A_1}\\
& -d_{A_2}))\cos q_{22}+(E_2(d_{B_2}-h_y)\cos\alpha-(d_{A_1}-d_{A_2})(\sin\alpha(d_{B2}-h_y)+s_z)\sin q_{21}+\\
& E_1(d_{B_2}-h_y)\sin\alpha-E_2 d_{A_2}+s_z E_1+E_2 s_y)\cos\theta+(((d_{A_1}-d_{A_2})\sin q_{21}-E_1)\cos\alpha+\\
& \sin\alpha E_2)(-\sin\theta s_x+h_z))\cos^3 q_{21}+(-((\cos\alpha(d_{B_2}-h_y)-d_{A_2}+s_y)\cos\theta+\\
& \sin\alpha(-\sin\theta s_x+h_z))(d_{A_1}-d_{A_2})\cos^2 q_{22}-((\cos\alpha(d_{B_2}-h_y)-d_{A_2}+s_y)\cos\theta+\\
& \sin\alpha(-\sin\theta s_x+h_z))\sin q_{21}E_3\cos q_{22}+((d_{B_2}-h_y)(-E_1\sin q_{21}+d_{A_1}-d_{A_2})\cos\alpha+\\
& (E_2(d_{B_2}-h_y)\sin\alpha+E_1 d_{A_2}-s_y E_1+s_z E_2)\sin q_{21}-(d_{A_2}-s_y)(d_{A_1}-d_{A_2}))\cos\theta+\\
& (-\sin q_{21}E_2\cos\alpha+\sin\alpha(-E_1\sin q_{21}+d_{A_1}-d_{A_2}))(-\sin\theta s_x+h_z))\cos q_{21}+((d_{A_1}-\\
& d_{A_2})\sin q_{21}+E_1)(((h_y-d_{B_2})\sin(\alpha)-s_z)\cos\theta+\cos(\alpha)(-\sin\theta s_x+h_z))\cos^2 q_{22}+\\
& (-E_3(\sin\alpha(d_{B_2}-h_y)+s_z)\cos\theta+(-\sin\theta\sin q_{22}E_1(d_{A_1}-s_y)\sin q_{21}+((d_{A_2}{}^2+(-d_{A_1}\\
& -s_y)d_{A_2}+d_{A_1}s_y-E_1{}^2)\sin q_{22}-E_3 s_x)\sin\theta+h_z E_3)\cos\alpha+\sin\theta\sin q_{22}(\sin\alpha s_z-h_y+\\
& d_{B_2})(E_1\sin q_{21}+d_{A_1}-d_{A_2}))\cos q_{22}+E_2((h_y-d_{B_2})\cos\alpha+d_{A2}-s_y)\cos\theta\\
& -\sin q_{22}\sin\theta((d_{A_2}-s_y)\sin q_{21}+E_1)E_3\cos\alpha+\sin\theta\sin q_{22}E_3(\sin\alpha s_z-h_y+\\
& d_{B_2})\sin q_{21}-\sin\alpha E_2(h_z-s_x\sin\theta)
\end{aligned}
$$

and

$$
\begin{aligned}
K_9 := {} & (d_{A_1}-d_{A_2})(\cos^2 q_{22}-1)(((h_y-d_{B_2})\sin\alpha-s_z)\cos\theta+\cos\alpha(-\sin\theta s_x+h_z))\cos^3 q_{21}\\
& +((-(d_{A_1}-d_{A_2})((h_y-d_{B_2})\cos(\alpha)+d_{A_2}-s_y)\sin q_{21}\cos^2 q_{22}-((h_y-d_{B_2})\cos\alpha+d_{A_2}\\
& -s_y)E_3\cos q_{22}+(d_{A_1}-d_{A_2})((h_y-d_{B_2})\cos\alpha+d_{A_2}-s_y)\sin q_{21}-E_2(d_{B_2}-h_y)\sin\alpha+\\
& E_1(d_{B_2}-h_y)\cos\alpha-E_1 d_{A_2}+s_y E_1-s_z E_2)\cos\theta+\sin\alpha\sin q_{21}(d_{A_1}-d_{A_2})(-\sin\theta s_x+\\
& h_z)\cos^2 q_{22}+\sin\alpha((d_{A_2}(d_{A_1}-d_{A_2})\sin q_{22}-E_3 s_x)\sin\theta+h_z E_3)\cos q_{22}-(\sin\alpha\sin q_{21}(d_{A_1}\\
& -d_{A_2})-E_2\cos\alpha-\sin\alpha E_1)(-s_x\sin\theta+h_z))\cos^2 q_{21}+(((\sin\alpha(d_{B_2}-h_y)+s_z)(d_{A_1}\\
& -2d_{A_2})\cos^2 q_{22}+(\sin\alpha(d_{B_2}-h_y)+s_z)\sin q_{21}E_3\cos q_{22}+(E_1(d_{B_2}-h_y)\sin\alpha+E_2(d_{B_2}\\
& -h_y)\cos\alpha-E_2 d_{A_2}+s_z E_1+E_2 s_y)\sin q_{21}+d_{A_2}(\sin\alpha(d_{B_2}-h_y)+s_z))\cos\theta-\cos\alpha(d_{A_1}\\
& -2d_{A_2})(-\sin\theta s_x+h_z)\cos^2 q_{22}+((-\sin\theta\sin q_{22}s_z(d_{A_1}-d_{A_2})\sin\alpha+((-s_y(d_{A_1}\\
& -d_{A_2})\sin q_{22}+E_3 s_x)\sin\theta-h_z E_3)\cos\alpha-\sin\theta\sin q_{22}(d_{B_2}-h_y)(d_{A_1}-d_{A_2}))\sin q_{21}\\
& -\sin\theta\sin q_{22}E_1(d_{B_2}-h_y+\sin\alpha s_z+\cos\alpha s_y))\cos q_{22}-(E_1\cos\alpha-E_2\sin\alpha)(-\sin\theta s_x+\\
& h_z)\sin q_{21}-E_3\sin\alpha\sin\theta\sin q_{22}s_z+((-E_3\sin q_{22}s_y+d_{A_2}s_x)\sin\theta-h_z d_{A_2})\cos\alpha\\
& -\sin\theta\sin q_{22}E_3(d_{B_2}-h_y))\cos q_{21}-(d_{A_2}\sin q_{21}+E_1)(\cos q_{22}+1)((h_y-d_{B_2})\cos\alpha+d_{A_2}\\
& -s_y)(\cos q_{22}-1)\cos\theta+\sin\alpha((d_{A_2}\sin q_{21}+E_1)(-s_x\sin\theta+h_z)\cos^2 q_{22}\\
& -\sin\theta\sin q_{22}(d_{A_1}E_1\sin q_{21}+d_{A_2}d_{A_1}-d_{A_2}{}^2+E_1{}^2)\cos q_{22}-(d_{A_2}\sin q_{21}+E_1)((\sin q_{22}E_3\\
& -s_x)\sin\theta+h_z))
\end{aligned}
$$

Appendix C

Multiple solutions for the IKP and the FKP of the Exechon robot

C.1 Solutions of the IKP of the parallel module

Given the eight uni-variable equations obtained from the two solutions for each α, q_{22} and θ, all possible real solutions for the IKP are numerically obtained for the tool position ${}^{O}\mathbf{r}_{S} = (300, 500, 900)$ mm. The dimensions of the mechanism are shown in Table 9.1. In order to better appreciate the difference between solutions, an exaggerated offset of 60 mm was used. Figures C.1 and C.2 show the 16 solutions obtained, including a picture of the parallel module and the corresponding values of the actuated joint variables q_{13}, q_{24} and q_{33}. These 16 solutions refer to the configuration of legs 1 and 3 shown in figure 9.8a. Other three solutions can be obtained for each of the 16 presented here by changing the configuration of legs 1 and 3 as shown in cases b, c and d in figure 9.8, only affecting the values of q_{13} and q_{33} but keeping all other values unaffected. In total, 64 solutions are obtained.

C.2 Solutions of the FKP of the parallel module

Given the sixteen systems of equations obtained from the eight sets of solutions for e_x and k and the two solutions for q_{22}, all possible real solutions for the FKP are numerically obtained for the values of actuated joint variables $q_{13} = 670$mm, $q_{24} = 570$mm and $q_{33} = 800$mm. The dimensions of the mechanism are shown in Table 9.1. In order to better appreciate the difference between solutions, an exaggerated offset of 60 mm was used. A total of 57 solutions were obtained. Figures C.3 and C.4 show the 16 solutions obtained for the configuration of legs 1 and 3 shown in figure 9.8, including a picture of the parallel module and the corresponding position of the end-effector ${}^{O}\mathbf{r}_{S}$.

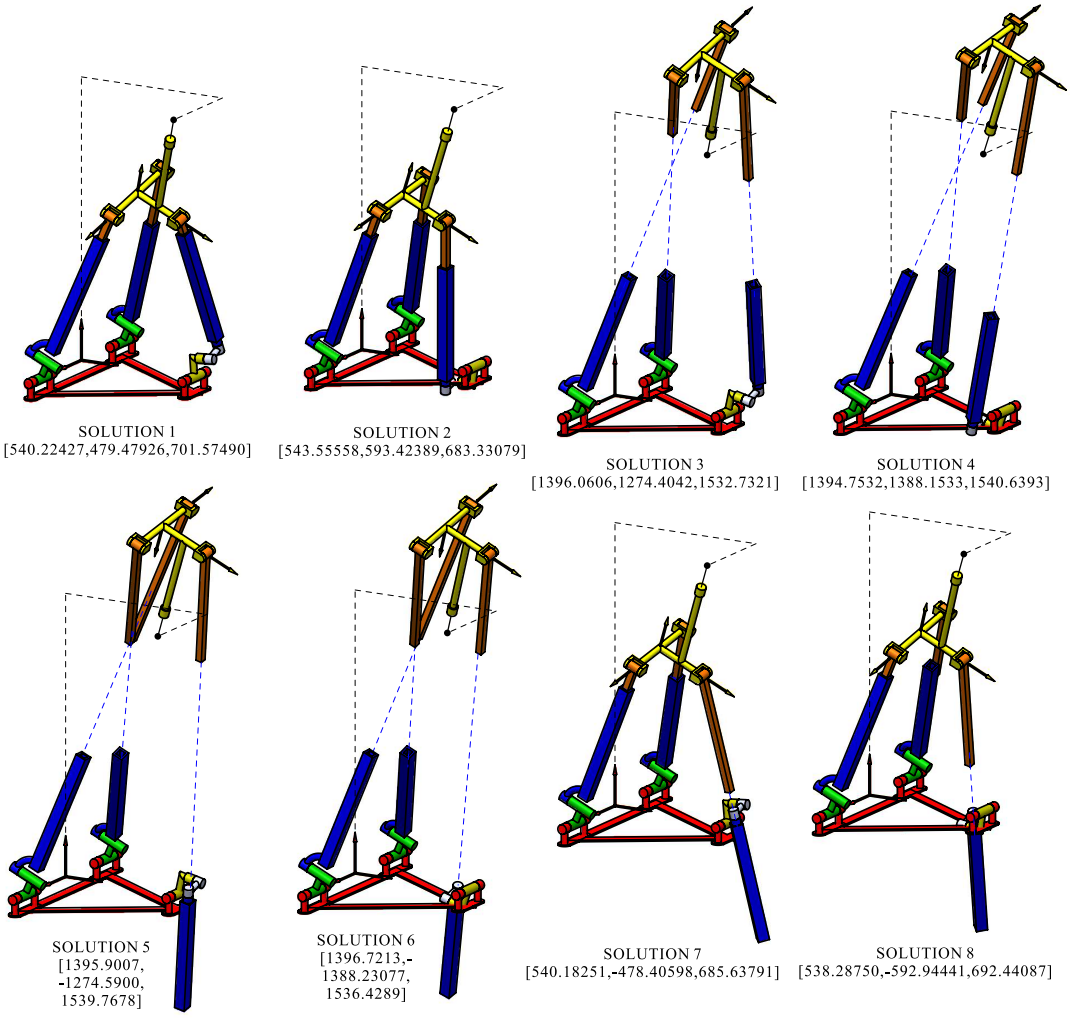

FIGURE C.1: 16 solutions for the inverse kinematics problem of the parallel module with ${}^{O}\mathbf{r}_{S} = (300, 500, 900)$ mm. With every solution, the obtained vector $[q_{13}, q_{24}, q_{33}]$ is presented. (continues in figure C.2)

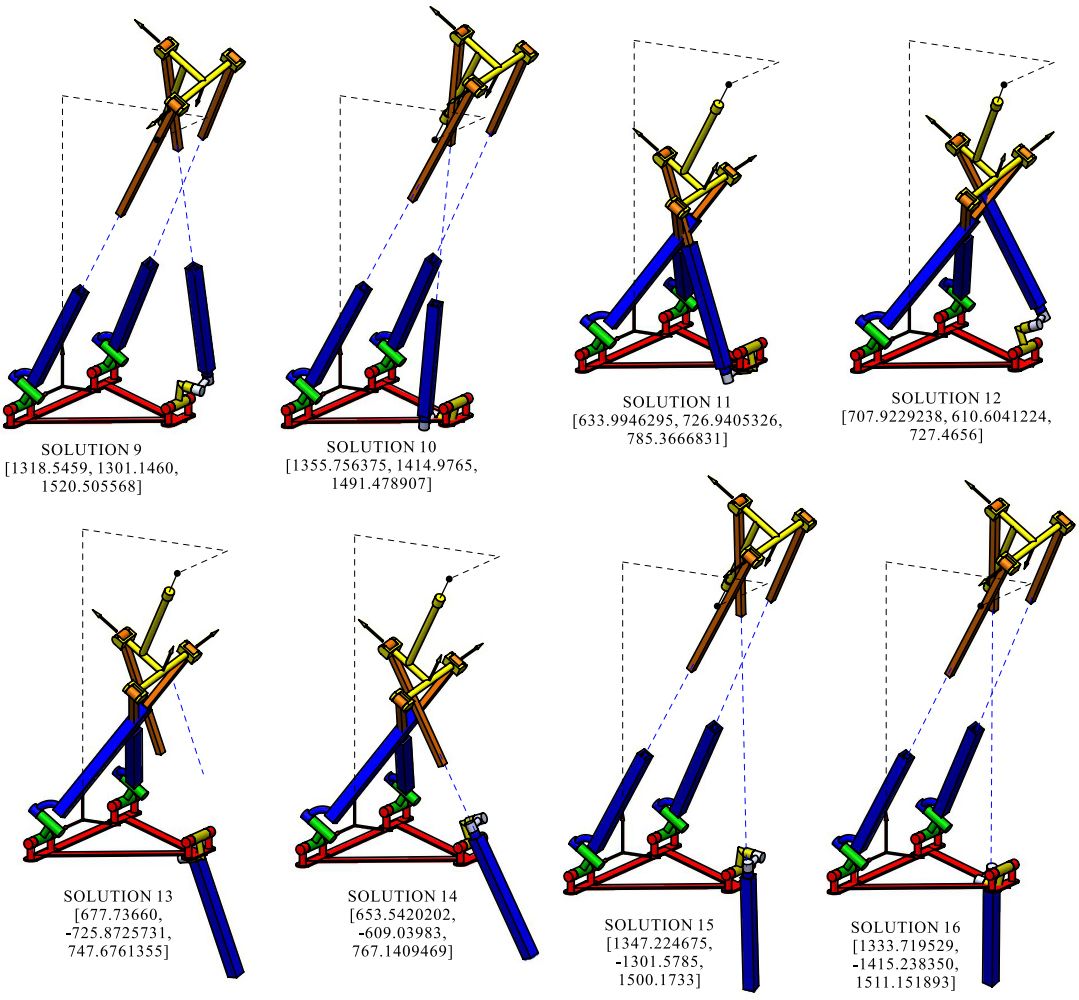

FIGURE C.2: (continuation of figure C.1) 16 solutions for the inverse kinematics problem of the parallel module with ${}^{O}\mathbf{r}_{S} = (300, 500, 900)$ mm. With every solution, the obtained vector $[q_{13}, q_{24}, q_{33}]$ is presented.

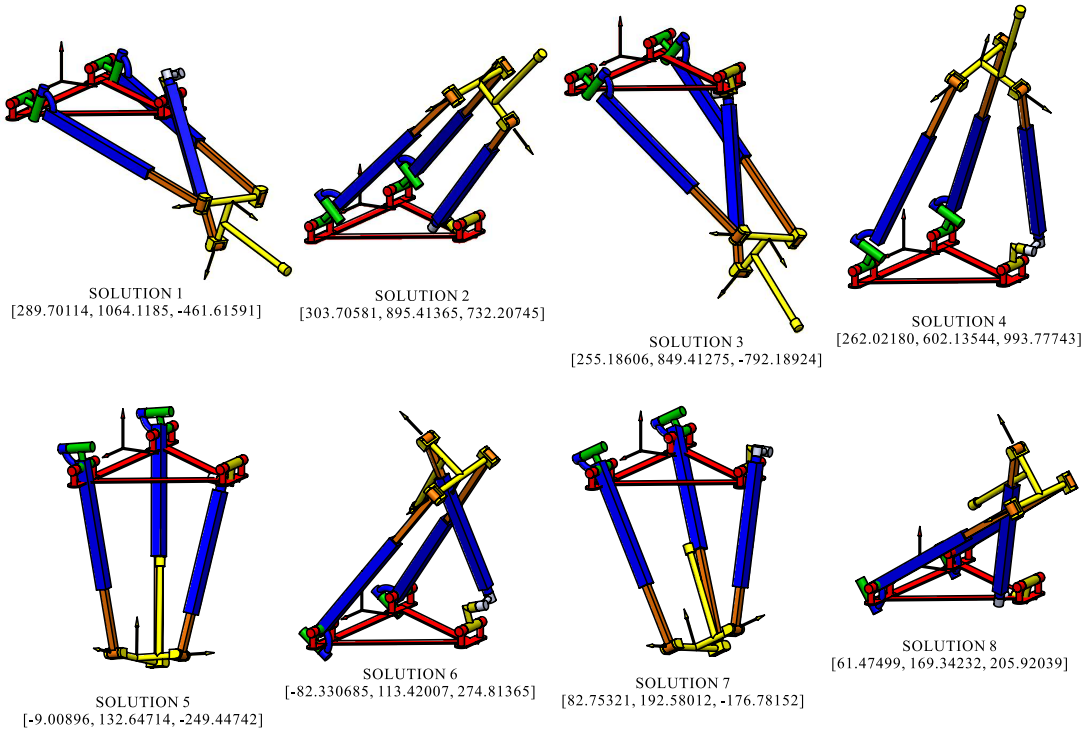

FIGURE C.3: 16 solutions for the FKP of the parallel module with $q_{13} = 670$mm, $q_{24} = 570$mm and $q_{33} = 800$mm. With every solution, the obtained vector ${}^{O}\mathbf{r}_S$ is presented. (continues in Fig. C.4)

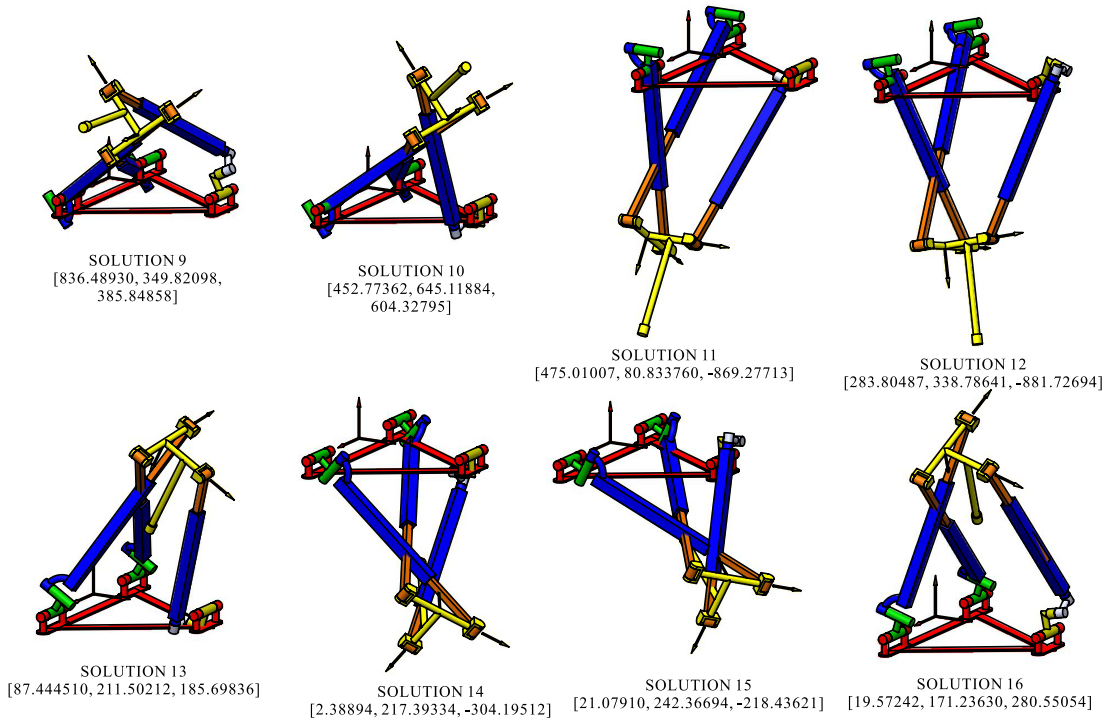

FIGURE C.4: (Continuation of Fig. C.3) 16 solutions for the FKP of the parallel module with $q_{13} = 670$mm, $q_{24} = 570$mm and $q_{33} = 800$mm. With every solution, the obtained vector ${}^{O}\mathbf{r}_S$ is presented.

References

[1] E. M. Jenkins, F. R. E. Crossley, and K. H. Hunt, "Gross motion attributes of certain spatial mechanisms," *Journal of Engineering for Industry*, vol. 91, no. 1, pp. 83–90, 1969.

[2] L. E. Torfason and F. R. E. Crossley, "Use of the intersection of surfaces as a method for design of spatial mechanisms," in *Proceedings of the 3rd World Congress for the Theory of Machines and Mechanisms*, Paper B-20, Kupari, Yugoslavia, vol. **B**, 1971, pp. 247–258.

[3] L. E. Torfason and A. K. Sharma, "Analysis of spatial RRGRR mechanisms by the method of generated surfaces," *Transactions of the ASME: Journal of Engineering for Industry*, vol. 95, no. 3, pp. 704–708, 1973.

[4] A. K. Shrivastava and K. H. Hunt, "Dwell motion from spatial linkages," *Transactions of the ASME: Journal of Engineering for Industry*, vol. 95, no. 2, pp. 511–518, 1973.

[5] K. H. Hunt, "Constant-velocity shaft couplings: A general theory," *Journal of Engineering for Industry*, vol. 95, no. 2, pp. 455–464, 1973.

[6] E. F. Fichter and K. H. Hunt, "The fecund torus, its bitangent-circles and derived linkages," *Mechanism and Machine Theory*, vol. 10, no. 2-3, pp. 167–176, 1975.

[7] Y. Liu and P. Zsombor-Murray, "Intersection curves between quadric surfaces of revolution," *Transactions of the Canadian Society for Mechanical Engineering*, vol. 19, no. 4, pp. 435–453, 1995.

[8] C. C. Lee and J. M. Hervé, "A discontinuously movable constant velocity shaft coupling of Koenigs joint type," in *Advances in Reconfigurable Mechanisms and Robots I*, M. Z. J.S. Dai and X. Kong, Eds., 2012, pp. 35–43.

[9] C.-C. Lee and J. M. Hervé, "Oblique circular torus, Villarceau circles, and four types of Bennett linkages," *Proceedings of the Institution of Mechanical Engineers, Part C: Journal of Mechanical Engineering Science*, vol. 228, no. 4, pp. 742–752, 2014.

[10] H. J. Su and J. M. McCarthy, "Dimensioning a constrained parallel robot to reach a set of task positions," in *Proceeding of the 2005 IEEE International Conference on Robotics and Automation*, Barcelona, Spain, 2005, pp. 4026–4030.

[11] P. C. López-Custodio, J. M. Rico, J. J. Cervantes-Sánchez, and G. I. Pérez-Soto, "Reconfigurable mechanisms from the intersection of surfaces," *ASME Journal of Mechanisms and Robotics*, vol. 8, no. 2, 021 029–1
bibrangedash 021029–19, 2016.

[12] K. Wohlhart, "Kinematotropic linkages," in *Recent Advances in Robot Kinematics*, J. Lenarčič and V. Parent-Castelli, Eds., Portoroz, Slovenia. Dordrecht: The Netherlands, 1996, pp. 359–368.

[13] C. Galletti and P. Fanghella, "Single-loop kinematotropic mechanisms," *Mechanism and Machine Theory*, vol. 36, no. 3, pp. 743–761, 2001.

[14] X. Kong, "Type synthesis of variable degrees-of-freedom parallel manipulators with both planar and 3T1R operation modes," in *Proceedings of the ASME 2012 International Design Engineering Technical Conferences*, Paper number DETC2012-70621, Chicago, IL, U.S.A., 2012, pp. 497–504.

[15] Y. Qin, J. Dai, and G. Gogu, "Multi-furcation in a derivative queer-square mechanism," *Mechanism and machine theory*, vol. 81, pp. 36–53, 2014, ISSN: 0094-114X.

[16] G. Gogu, "Branching singularities in kinematotropic parallel mechanisms," in *Computational Kinematics*, A. Kecskeméthy and A. Müller, Eds., Berlin, Heidelberg: Springer Berlin Heidelberg, 2009, pp. 341–348, ISBN: 978-3-642-01947-0.

[17] K. Wohlhart, "New overconstrained spheroidal linkages," in *Proc. 9th World Congress IFToMM,*, Milano, Italy, 1995, pp. 149–154.

[18] X. Qi, H. Huang, Z. Miao, B. Li, and Z. Deng, "Design and mobility analysis of large deployable mechanisms based on plane-symmetric Bricard linkage," *ASME Journal of Mechanisms and Robotics*, vol. 139, no. 2, pp. 022 302–022302–11, 2016.

[19] Y. Chen, Z. You, and T. Tarnai, "Threefold-symmetric Bricard linkages for deployable structures," *International Journal of Solids and Structures*, vol. 42, no. 8, pp. 2287 –2301, 2005, ISSN: 0020-7683.

[20] S. Lu, D. Zlatanov, X. Ding, M. Zoppi, and S. D. Guest, "Reconfigurable chains of bifurcating type III Bricard linkages," in *Advances in Reconfigurable Mechanisms and Robots II*, X. Ding, X. Kong, and J. S. Dai, Eds., Cham: Springer International Publishing, 2016, pp. 3–14, ISBN: 978-3-319-23327-7.

[21] J.-S. Zhao, F. Chu, and Z.-J. Feng, "The mechanism theory and application of deployable structures based on sle," *Mechanism and Machine Theory*, vol. 44, no. 2, pp. 324 –335, 2009, ISSN: 0094-114X.

[22] J. S. Dai and J. Rees Jones, "Mobility in metamorphic mechanisms of foldable/erectable kinds," *Transactions of the ASME: Journal of Mechanical Design*, vol. 121, no. 3, pp. 375–382, 1999.

[23] D. Gan, J. Dai, and Q. Liao, "Mobility change in two types of metamorphic parallel mechanisms," English, *Transactions of the ASME Journal of Mechanisms and Robotics*, vol. 1, no. 4, 9 pages, 2008, ISSN: 1942-4302.

[24] F. Aimedee, G. Gogu, J. S. Dai, C. Bouzgarrou, and N. Bouton, "Systematization of morphing in reconfigurable mechanisms," *Mechanism and Machine Theory*, vol. 96, Part 2, pp. 215 –224, 2016, Reconfigurable mechanisms, ISSN: 0094-114X.

[25] J. S. Dai and G. Gogu, "Special issue on reconfigurable mechanisms: Morphing, metamorphosis and reconfiguration through constraint variations and reconfigurable joints," *Mechanism and Machine Theory*, vol. 96, Part 2, pp. 213 –214, 2016, Reconfigurable mechanisms, ISSN: 0094-114X.

[26] K. Zhang and J. S. Dai, "Reconfiguration of the plane-symmetric double-spherical 6R linkage with bifurcation and trifurcation," *Proceedings of the Institution of Mechanical Engineers, Part C: Journal of Mechanical Engineering Science*, vol. 230, no. 3, pp. 473–482, 2016.

[27] K. Zhang and J. S. Dai, "Geometric constraints and motion branch variations for reconfiguration of single-loop linkages with mobility one," *Mechanism and Machine Theory*, vol. 106, pp. 16 –29, 2016, ISSN: 0094-114X.

[28] X. Ma, K. Zhang, and J. S. Dai, "Novel spherical-planar and Bennett-spherical 6R metamorphic linkages with reconfigurable motion branches," *Mechanism and Machine Theory*, vol. 128, pp. 628 –647, 2018, ISSN: 0094-114X.

[29] P. C. López-Custodio, "Nuevas herramientas en la síntesis de mecanismos metamórficos y cinematotrópicos," M.Sc. Thesis, Universidad de Guanajuato, Salamanca, Gto. Mexico, 2015.

[30] P. C. López-Custodio, J. M. Rico, and J. J. Cervantes-Sánchez, "Local analysis of helicoid-helicoid intersections in reconfigurable linkages," *ASME Journal of Mechanisms and Robotics*, vol. 9, no. 3, pp. 031008 –031008–17, 2017.

[31] W. Chai and Y. Chen, "The line-symmetric octahedral bricard linkage and its structural closure," *Mechanism and Machine Theory*, vol. 45, no. 5, pp. 772 –779, 2010, ISSN: 0094-114X.

[32] J Eddie Baker, "Limiting positions of a bricard linkage and their possible relevance to the cyclohexane molecule," *Mechanism and Machine Theory*, vol. 21, no. 3, pp. 253 –260, 1986, ISSN: 0094-114X.

[33] A. Müller, "Local investigation of mobility and singularities of linkages," in *Singular Configurations of Mechanisms and Manipulators*, A. Müller and D. Zlatanov, Eds., Cham: Springer International Publishing, 2019, pp. 181–229, ISBN: 978-3-030-05219-5.

[34] E. Peisach, "Analytical kinematics of overconstrained 20-link 24R mechanism: Branches with one, two and three degrees of freedom," in *Advances in Robot Kinematics: Analysis and Control*, J. Lenarčič and M. L. Husty, Eds. Dordrecht: Springer Netherlands, 1998, pp. 297–306, ISBN: 978-94-015-9064-8.

[35] P. C. López-Custodio, J. S. Dai, and J. M. Rico, "Branch reconfiguration of Bricard linkages based on toroids intersections: Line-symmetric case," *ASME Journal of Mechanisms and Robotics*, vol. 10, no. 3, pp. 031 003–1–031003–11, 2018.

[36] ——, "Branch reconfiguration of Bricard linkages based on toroids intersections: Plane-symmetric case," *ASME Journal of Mechanisms and Robotics*, vol. 10, no. 3, pp. 031 002–031002–12, 2018.

[37] P. C. López-Custodio and J. S. Dai, "Design of a variable-mobility linkage using the bohemian dome," *ASME Journal of Mechanical Design*, vol. 141, no. 9, pp. 092 303–1–092303–12, 2019.

[38] P. C. López-Custodio, A. Müller, and J. S. Dai, "A kinematotropic parallel mechanism reconfiguring between three motion branches of different mobility," in *Advances in Mechanism and Machine Science - IFToMM WC 2019*, T. Uhl, Ed., Cham: Springer International Publishing, 2019, pp. 2611–2620.

[39] P. C. López-Custodio, A. Müller, J. M. Rico, and J. S. Dai, "A synthesis method for 1-DOF mechanisms with a cusp in the configuration space," *Mechanism and Machine Theory*, vol. 132, pp. 154 –175, 2019, ISSN: 0094-114X.

[40] P. C. López-Custodio, A. Müller, X. Kang, and J. S. Dai, "Tangential intersection of branches of motion," *Mechanism and Machine Theory*, vol. 147, p. 103 730, 2020.

[41] P. C. López-Custodio, J. S. Dai, R. Fu, and Y. Jin, "Kinematics and Constraints of the Exechon Robot Accounting Offsets Due to Errors in the Base Joint Axes," *Journal of Mechanisms and Robotics*, vol. 12, no. 2, 2020, 021109.

[42] P. C. López-Custodio, "Análisis cinemáticos de orden superior y movilidad de cadenas cinemáticas," B. Sc. Thesis, Universidad de Guanajuato, Salamanca, Gto. Mexico, 2012.

[43] C. Crane and J. Duffy, *Kinematic analysis of robot manipulators*. Cambridge: Cambridge University Press, 1998.

[44] J. M. Hervé, "Analyse structurelle des mécanismes par groupe des déplacements," *Mechanism and Machine Theory*, vol. 13, no. 4, pp. 437–450, 1978.

[45] J. M. Rico, J. J. Cervantes-Sánchez, and E. Olivares-Conraud, "On the history of the discovery of the subgroups of the euclidean group," in *Advances in Mechanism and Machine Science*, T. Uhl, Ed., Cham: Springer International Publishing, 2019, pp. 1233–1239.

[46] J. M. Rico, L. D. Aguilera, J. Gallardo, R. Rodriguez, H. Orozco, and J. M. Barrera, "A More General Mobility Criterion for Parallel Platforms," *Journal of Mechanical Design*, vol. 128, no. 1, pp. 207–219, 2005.

[47] M. Hausner and J. T. Schwartz, *Lie Groups, Lie Algebras*. New York, NY, USA: Gordon and Breach, 1968.

[48] J. M. Rico, J. Gallardo, and J. Duffy, "Screw theory and the higher order kinematic analysis of serial and closed chains," *Mechanism and Machine Theory*, vol. 34, no. 4, pp. 559–586, 1999.

[49] J. Gallardo, "Análisis cinemático de orden superior de cadenas espaciales mediante el álgebra de tornillos y sus aplicaciones," PhD Thesis, Institute of Technology of La Laguna, Torreon, Coahuila. Mexico, 1999.

[50] P. C. López-Custodio, J. M. Rico, J. J. Cervantes-Sánchez, G. I. Pérez-Soto, and C. R. Díez-Martínez, "Verification of the higher order kinematic analyses equations," *European Journal of Mechanics - A/Solids*, vol. 61, pp. 198 –215, 2017, ISSN: 0997-7538.

[51] J. J. Cervantes-Sánchez, M. A. Moreno-Báez, J. M. Rico-Martıínez, and E. J. González-Galván, "A novel geometrical derivation of the Lie product," *Mechanism and Machine Theory*, vol. 39, no. 10, pp. 1067 –1079, 2004, ISSN: 0094-114X.

[52] A. Müller, "Generic mobility of rigid body mechanisms," *Mechanism and Machine Theory*, vol. 44, no. 6, pp. 1240 –1255, 1998.

[53] J. Lerbet, "Analytic geometry and singularities of mechanisms," *Zeitschrift für Angewandte Mathematik und Mechanik.*, vol. 78, no. 10, pp. 687–694, 1998.

[54] A. Müller, "Recursive higher-order constraints for linkages with lower kinematic pairs," *Mechanism and Machine Theory*, vol. 100, pp. 33 –43, 2016.

[55] D. A. Cox, J. B. Little, and D. O'Shea, *Ideals, Varieties and Algorithms*. Springer, 2007.

[56] M. L. Husty, M. Pfurner, H.-P. Schröcker, and K. Brunnthaler, "Algebraic methods in mechanism analysis and synthesis," *Robotica*, vol. 25, no. 6, 661–675, 2007.

[57] T. Arponen, A. Müller, S. Piipponen, and J. Tuomela, "Kinematical analysis of overconstrained and underconstrained mechanisms by means of computational algebraic geometry," *Meccanica*, vol. 49, no. 4, pp. 843–862, 2014, ISSN: 1572-9648.

[58] K. H. Hunt, *Kinematic Geometry of Mechanisms*. New York, USA: Oxford University Press, 1978.

[59] H. Whitney, "Tangents to an analytic variety," *Annals of Mathematics*, vol. 81, pp. 496 –549, 1965.

[60] A. Müller, "Local analysis of singular configuration of open and closed loop manipulators," *Multibody System Dynamics*, vol. 8, no. 3, pp. 297–326, 2002.

[61] A. Müller, "Higher derivatives of the kinematic mapping and some applications," *Mechanism and Machine Theory*, vol. 76, pp. 70 –85, 2014, ISSN: 0094-114X.

[62] A. Müller, "Local kinematic analysis of closed-loop linkages mobility, singularities, and shakiness," *ASME Journal of Mechanisms and Robotics*, vol. 8, no. 4, 041 013–1 bibrangedash 041013–11, 2016.

[63] X. Kong, "Reconfiguration analysis of a 3-DOF parallel mechanism using Euler parameter quaternions and algebraic geometry method," *Mechanism and Machine Theory*, vol. 74, pp. 188–201, 2014.

[64] D. Zlatanov, I. A. Bonev, and C. Gosselin, "Constraint singularities as configuration space singularities," in *Advances in Robot Kinematics*, J. Lenarčič and F. Thomas, Eds., Springer Netherlands, 2002, pp. 183–192.

[65] F. C. Park and J. W. Kim, "Singularity analysis of closed kinematic chains," *Journal of Mechanical Design*, vol. 121, no. 1, 32–38, 1999.

[66] C. Gosselin and J. Ángeles, "Singularity analysis of closed-loop kinematic chains," *IEEE Transactions on Robotics and Automation*, vol. 6, no. 3, pp. 281–290, 1990, ISSN: 1042-296X.

[67] L. Zhang, J. Dai, and Q. Liao, "Reconfiguration of spatial metamorphic mechanisms," English, *Transactions of the ASME Journal of Mechanisms and Robotics*, vol. 1, no. 1, 8 pages, 2008, ISSN: 1942-4302.

[68] C. H. Kuo, J. S. Dai, and H. S. Yan, "Reconfiguration principles and strategies for reconfigurable mechanisms," in *Reconfigurable Mechanisms and Robots, 2009. ReMAR 2009. ASME/IFToMM International Conference on*, 2009, pp. 1–7.

[69] L. Zhang, D. Wang, and J. S. Dai, "Biological modeling and evolution based synthesis of metamorphic mechanisms," *ASME Journal of Mechanical Design*, vol. 130, no. 7, 072303 (11 pages), 2008.

[70] D. Gan, J. S. Dai, and Q. Liao, "Constraint analysis on mobility change of a novel metamorphic parallel mechanism," *Mechanism and Machine Theory*, vol. 45, no. 12, pp. 1864 –1876, 2010, ISSN: 0094-114X.

[71] X. Kong and Y. Jin, "Type synthesis of 3-DOF multi-mode translational/spherical parallel mechanisms with lockable joints," *Mechanism and Machine Theory*, vol. 96, Part 2, pp. 323 –333, 2016, Reconfigurable mechanisms, ISSN: 0094-114X.

[72] W. Ye, Y. Fang, K. Zhang, and S. Guo, "A new family of reconfigurable parallel mechanisms with diamond kinematotropic chain," *Mechanism and Machine Theory*, vol. 74, pp. 1 –9, 2014, ISSN: 0094-114X.

[73] C. Y. Song, Y. Chen, and I.-M. Chen, "A 6R linkage reconfigurable between the line-symmetric Bricard linkage and the Bennett linkage," *Mechanism and Machine Theory*, vol. 70, pp. 278 –292, 2013, ISSN: 0094-114X.

[74] X. Kong, "Reconfiguration analysis of multimode single-loop spatial mechanisms using dual quaternions," *ASME Journal of Mechanisms and Robotics*, vol. 9, no. 5, 031 004–1
bibrangedash 031004–8, 2017.

[75] K. Zhang, A. Müller, and J. S. Dai, "A novel reconfigurable 7R linkage with multifurcation," in *Advances in Reconfigurable Mechanisms and Robots II*, X. Ding, X. Kong, and J. S. Dai, Eds., Cham: Springer International Publishing, 2016, pp. 3–14, ISBN: 978-3-319-23327-7.

[76] K. Zhang, J. S. Dai, and Y. Fang, "Geometric constraint and mobility variation of two 3SvPSv metamorphic parallel mechanisms," *ASME Journal of Mechanical Design*, vol. 135, no. 1, pp. 011 001–011001–8, 2013.

[77] C.-C. Lee and J. M. Hervé, "Discontinuously movable seven-link mechanisms via group-algebraic approach," *Proceedings of the Institution of Mechanical Engineers, Part C: Journal of Mechanical Engineering Science*, vol. 219, no. 6, pp. 577–587, 2005.

[78] P. Fanghella, C. Galletti, and E. Giannotti, "Parallel robots that change their group of motion," in *Advances in Robot Kinematics*, J. Lennarčič and B. Roth, Eds., Dordrecht: Springer Netherlands, 2006, pp. 49–56.

[79] Q. Li and J. M. Hervé, "Parallel mechanisms with bifurcation of Schoenflies motion," *IEEE Transactions on Robotics*, vol. 25, no. 1, pp. 158–164, 2009, ISSN: 1552-3098.

[80] D. R. Walter, M. L. Husty, and M. Pfurne, "A complete kinematic analysis of the SNU 3-UPU parallel robot," in *Interactions of Classical and Numerical Algebraic Geometry, Contemporary Mathematics*, D. J. Bates, G. M. Besana, S. D. Rocco, and C. W. Wampler, Eds., 2009, pp. 331–346.

[81] T. Arponen, S. Piipponen, and J. Tuomela, "Kinematical analysis of Wunderlich mechanism," *Mechanism and Machine Theory*, vol. 70, pp. 16 –31, 2013, ISSN: 0094-114X.

[82] Q. Zeng, K. F. Ehmann, and J. Cao, "Design of general kinematotropic mechanisms," *Robotics and Computer-Integrated Manufacturing*, vol. 38, pp. 67 –81, 2016, ISSN: 0736-5845.

[83] X. Kong and M. Pfurner, "Type synthesis and reconfiguration analysis of a class of variable-dof single-loop mechanisms," *Mechanism and Machine Theory*, vol. 85, pp. 116–128, 2015.

[84] J. Wang and X. Kong, "A novel method for constructing multimode deployable polyhedron mechanisms using symmetric spatial compositional units," *ASME Journal of Mechanisms and Robotics*, vol. 11, no. 2, (8 pages), 2019.

[85] R. Bricard, "Mémoire sur la thèorie de l'octaèdre articulè," *Journal of Pure and Applied Mathematics*, vol. 3, pp. 113–150, 1897.

[86] ——, *Leçons de cinématique*. Paris, France: Gauthier-Villars, 1927.

[87] K. J. Waldron, "Symmetric overconstrained linkages," *Journal of Engineering for Industry*, vol. 91, no. 1, pp. 158 –162, 1969, ISSN: 0022-2569.

[88] K. H. Hunt, "Screw axes and mobility in spatial mechanisms via the linear complex," *Journal of Mechanisms*, vol. 2, no. 3, pp. 307–327, 1967.

[89] J. Phillips, *Freedom in Machinery: Volume 2, Screw Theory Exemplified*. Cambridge ,UK: Cambridge University Press, 1990.

[90] J. E. Baker, "An analysis of the Bricard linkages," *Mechanisms and Machine Theory*, vol. 15, pp. 267–286, 1980.

[91] C. Mavroidis and B. Roth, "Analysis of overconstrained mechanisms," *Journal of Mechanical Design*, vol. 117, no. 1, pp. 69 –74, 1995, ISSN: 1050-0472.

[92] ——, "New and revised overconstrained mechanisms," *Journal of Mechanical Design*, vol. 117, no. 1, pp. 75 –82, 1995, ISSN: 1050-0472.

[93] J. S. Dai, Z. Huang, and H. Lipkin, "Mobility of overconstrained parallel mechanisms," *Journal of Mechanical Design*, vol. 128, no. 1, pp. 220 –229, 2006, ISSN: 1050-0472.

[94] J. Phillips, *Freedom in Machinery: Volume 1, Introducing Screw Theory*. Cambridge ,UK: Cambridge University Press, 1984.

[95] K. H. Hunt, "Note on complexes and mobility," *Journal of Mechanisms*, vol. 3, no. 3, pp. 199 –202, 1968, ISSN: 0022-2569.

[96] J. E. Baker and K. Wohlhart, "On the single screw reciprocal to the general line-symmetric six-screw linkage," *Mechanism and Machine Theory*, vol. 29, no. 1, pp. 169 –175, 1994, ISSN: 0094-114X.

[97] Y. Chen and W. H. Chai, "Bifurcation of a special line and plane symmetric Bricard linkage," *Mechanism and Machine Theory*, vol. 46, no. 4, pp. 515 –533, 2011, ISSN: 0094-114X.

[98] K. Zhang and J. Dai, "A kirigami-inspired 8R linkage and its evolved overconstrained 6R linkages with the rotational symmetry of order two," *ASME Journal of Mechanisms and Robotics*, vol. 6, no. 2, pp. 021 007–021007–12, 2014.

[99] F. E. Myard, "Contribution á la géométrie des systémes articulés," *Societe Mathématiques de France*, vol. 59, pp. 183–210, 1931.

[100] R. Bricard, "Démonstrations élémentaires de propriétés," *Nouvelles Annales de Mathèmatiques*, vol. 3, pp. 308–313, 1925.

[101] T. Bil, "Analysis of the Bennett linkage in the geometry of tori," *Mechanisms and Machine Theory*, vol. 53, pp. 122–127, 2012.

[102] J. E. Baker, "On 5-revolute linkages with parallel adjacent joint axes," *Mechanism and Machine Theory*, vol. 19, no. 6, pp. 467 –475, 1984, ISSN: 0094-114X.

[103] T. Bil and Z. Budniak, "Model of 5R spatial linkages in geometry of tori," *International Journal of Applied Mechanics and Engineering*, vol. 19, no. 4, pp. 823–830, 2014.

[104] T. Bil, "Kinematic analysis of a universal spatial mechanism containing a higher pair based on tori," *Mechanism and Machine Theory*, vol. 46, no. 4, pp. 412 –424, 2011, ISSN: 0094-114X.

[105] W.-Y. Chung, "Mobility analysis of RSSR mechanisms by working volume," *ASME Journal of Mechanical Design*, vol. 127, no. 1, pp. 156–159, 2005.

[106] X.-M. Liu, C.-Y. Liu, J.-H. Yong, and J.-C. Paul, "Torus/torus intersection," *Computer-Aided Design and Applications*, vol. 8, no. 3, pp. 465–477, 2011.

[107] C.-Y. Song, Y. Chen, and I.-M. Chen, "Kinematic study of the original and revised general line-symmetric bricard 6R linkages," *Journal of Mechanisms and Robotics*, vol. 6, no. 3, pp. 031 002–1–031002–10, 2014.

[108] Y. Villarceau, "Théorème sur le tore," *Novelles Annales de Mathématiques*, vol. 7, pp. 345–347, 1848.

[109] G. T. Bennett, "A new mechanism," *Engineering*, vol. 76, pp. 777–778, 1903.

[110] C. C. Lee and J. M. Hervé, "The metamorphic Bennett linkages," in *The 14th World Congress in Mechanisms and Machine Science*, Taipei, Taiwan, 2015.

[111] J. G. Altmann, "Communications to Grodzinski P. and Mewen E.: Link mechanisms in modern kinematics," *Proceedings of the Institution of Mechanical Engineers*, vol. 168, pp. 877–896, 1954.

[112] J. E. Baker, "A geometrico-algebraic exploration of Altmann's linkage," *Mechanism and Machine Theory*, vol. 28, no. 2, pp. 249–260, 1993.

[113] ——, "On the closure modes of a generalised Altmann linkage," *Mechanism and Machine Theory*, vol. 52, pp. 243 –247, 2012, ISSN: 0094-114X.

[114] L. Cui and J. Dai, "Axis constraint analysis and its resultant 6R double-centered overconstrained mechanisms," *ASME Journal of Mechanisms and Robotics*, vol. 3, no. 3, 031 004–1
bibrangedash 031004–9, 2011.

[115] Y. Chen and Z. You, "Two-fold symmetrical 6R foldable frame and its bifurcations," *International Journal of Solids and Structures*, vol. 46, no. 25, pp. 4504 –4514, 2009, ISSN: 0020-7683.

[116] S. N. Krivoshapko and V. N. Ivanov, *Encyclopedia of Analytical Surfaces*. Switzerland: Springer, 2015.

[117] J. A. Thorpe, *Elementary Topics in Differential Geometry*. New York, USA: Springer-Verlag, 1979.

[118] C. R. Diez-Martínez, J. M. Rico, and J. J. Cervantes-Sánchez, "Mobility and connectivity in multiloop linkages," in *Advances in Robot Kinematics*, J. Lenarčič and B. Roth, Eds., Springer Netherlands, 2006, pp. 455–464.

[119] R. Connelly and H. Servatius, "Higher-order rigidity—what is the proper definition?" *Discrete & Computational Geometry*, vol. 11, no. 2, pp. 193–200, 1994.

[120] K. C. Gupta and R. Ma, "A direct rotatability criterion for spherical four-bar linkages," *Journal of Mechanical Design*, vol. 117, no. 4, 597–600, 1995.

[121] K. J. Waldron, "Elimination of the branch problem in graphical Burmester mechanism synthesis for four finitely separated positions," *Journal of Engineering for Industry*, vol. 98, no. 1, pp. 176–182, 1976.

[122] C. F. Reinholtz, G. N. Sandor, and J. Duffy, "Branching analysis of spherical RRRR and spatial RCCC mechanisms," *Journal of Mechanisms, Transmissions, and Automation in Design*, vol. 108, no. 4, 481–486, 1986.

[123] J. Wang and X. Kong, "A novel method for constructing multi-mode deployable polyhedron mechanisms using symmetric spatial RRR compositional units," in *International Design Engineering Technical Conferences and Computers and Information in Engineering Conference*, Quebec, Canada, 2018.

[124] M. Tale Masouleh, C. Gosselin, M. H. Saadatzi, X. Kong, and H. D. Taghirad, "Kinematic analysis of 5-RPUR (3T2R) parallel mechanisms," *Meccanica*, vol. 46, no. 1, pp. 131–146, 2011, ISSN: 1572-9648.

[125] J. M. Rico and B. Ravani, "On mobility analysis of linkages using group theory," *Transactions of the ASME: Journal of Mechanical Design*, vol. 125, no. 1, pp. 70–80, 2003.

[126] K. Zhang and J. S. Dai, "Screw-system-variation enabled reconfiguration of the Bennett plano-spherical hybrid linkage and its evolved parallel mechanism," *ASME Journal of Mechanical Design*, vol. 137, no. 6, 10 pages, 2015.

[127] X. Kong and C. M. Gosselin, "Type synthesis of parallel mechanisms with multiple operation modes," *ASME Journal of Mechanical Design*, vol. 129, pp. 595 –601, 2006.

[128] J. M. Selig, *Geometric Fundamentals of Robotics*. New York, NY, USA: Springer-Verlag New York, 2005.

[129] J. Dai, "Finite displacement screw operators with embedded Chasles' motion," English, *Transactions of the ASME Journal of Mechanisms and Robotics*, vol. 4, no. 4, pp. –, 2012, ISSN: 1942-4302.

[130] K. Shirazi, "A study of the Jacobian matrix of serial manipulators," *ASME Journal of Mechanisms, Transmissions and Automation in Design*, vol. 107, no. 2, pp. 230 –237, 2009.

[131] F. L. Litvin, Z. Yi, V. P. Castelli, and C. Innocenti, "Singularities, configurations, and displacement functions for manipulators," *The International Journal of Robotics Research*, vol. 5, no. 2, pp. 52–65, 1986.

[132] K Sugimoto, J Duffy, and K. Hunt, "Special configurations of spatial mechanisms and robot arms," *Mechanism and Machine Theory*, vol. 17, no. 2, pp. 119 –132, 1982, ISSN: 0094-114X.

[133] C. G. Gibson and K. H Hunt, "Geometry of screw systems - 1," *Mechanism and Machine Theory*, vol. 25, no. 1, pp. 1 –10, 1990.

[134] C. G. Gibson and K. H. Hunt, "Geometry of screw systems - 2: Classification of screw systems," *Mechanism and Machine Theory*, vol. 25, no. 1, pp. 11 –27, 1990, ISSN: 0094-114X.

[135] T. Tarnai and J. Szabó, "On the exact equation of inextensional, kinematically indeterminate assemblies," *Computers & Structures*, vol. 75, no. 2, pp. 145 –155, 2000, ISSN: 0045-7949.

[136] ——, "Finite mechanisms have no higher-order rigidity," *Acta Technica Acad. Sci-Hung.*, vol. 106, no. 3, pp. 119 –125, 2000, ISSN: 0045-7949.

[137] E. N. Kuznetsov, "Singular configurations of structural systems," *International Journal of Solids and Structures*, vol. 36, no. 6, pp. 885 –897, 1999, ISSN: 0020-7683.

[138] Z. Hortobágyi, "Numerical analysis of inextensional, kinematically indeterminate assemblies," *Periodica Polytechnica Civil Engineering*, vol. 44, no. 1, pp. 43 –55, 2000.

[139] I. K. Sabitov, "On the relations between infinitesimal bendings of different orders," *Journal of Mathematical Sciences*, vol. 72, no. 4, pp. 3237–3241, 1994, ISSN: 1573-8795.

[140] A. Müller, "Higher-order analysis of kinematic singularities of lower pair linkages and serial manipulators," *ASME Journal of Mechanisms and Robotics*, vol. 10, no. 1, (13 pages), 2018.

[141] P. C. López-Custodio, A. Müller, and J. S. Dai, "The double-Koenigs mechanism – a spatial linkage with cusp singularities and multiple branches in the configuration space –," in *Proceedings of the 4th IEEE/IFToM International Conference on Reconfigurable Mechanisms and Robots*, Delft, The Netherlands, 2018.

[142] A. B. Kempe, *How to Draw a Straight Line: A Lecture on Linkages*. London, UK: Macmillan and Company, 1877, ISBN: 3744678482.

[143] E. S. Ferguson, *Kinematics of Mechanisms from the Time of Watt*. Washington D.C., USA: Smithsonian Institution, 1962, ISBN: 9781318908660.

[144] A. Müller, "A screw approach to the approximation of the local geometry of the configuration space and of the set of configurations of certain rank of lower pair linkages," in *International Design Engineering Technical Conferences and Computers and Information in Engineering Conference*, Quebec, Canada, 2018.

[145] W. Kühnel, *Differential Geometry: Curves - Surfaces - Manifolds*, ser. Europe and Central Asia Environmentally and Socially Sustain. Providence, RI, USA: American Mathematical Society, 2002, ISBN: 9780821826560.

[146] X. Ye and T. Maekawa, "Differential geometry of intersection curves of two surfaces," *Computer Aided Geometric Design*, vol. 16, no. 8, pp. 767 –788, 1999.

[147] E. Kreyszig, *Differential Geometry*. Toronto, Canada: University of Toronto Press, 1959.

[148] D.-M. Lu and W.-M. Hwang, "Spherical four-bar linkages with symmetrical coupler-curves," *Mechanism and Machine Theory*, vol. 31, no. 1, pp. 1 –10, 1996.

[149] K. H. Shirazi, "Symmetrical coupler curve and singular point classification in planar and spherical swinging-block linkages," *ASME Journal of Mechanisms and Robotics*, vol. 128, no. 2, pp. 436 –443, 2005.

[150] C. Chiang, *Kinematics of Spherical Mechanisms*. Krieger Publishing Company, 2000.

[151] J. Angeles, *Spatial Kinematic Chains: Analysis — Synthesis — Optimization*. Heidelberg, Germany: Springer-Verlag Berlin Heidelberg, 2012, ISBN: 9783642488191.

[152] J. M. Rico and B. Ravani, "Group theory can explain the mobility of paradoxical linkages," in *Advances in Robot Kinematics*, J. Lenarčič and F. Thomas, Eds., Dordrecht: Springer Netherlands, 2002, pp. 245–254.

[153] J. Denavit and R. S. Hartenberg, "A kinematic notation for lower-pair mechanisms based on matrices," *ASME Journal of Applied Mechanics*, vol. 23, pp. 215–221, 1955.

[154] X. Kong, "Kinematic analysis of conventional and multi-mode spatial mechanisms using dual quaternions," in *Proceedings of the ASME 2016 International Design Engineering Technical Conferences*, Paper number DETC2016-59194, Charlotte, North Carolina, USA, vol. 5B, 2016.

[155] D. Gan and J. S. Dai, "Geometry constraint and branch motion evolution of 3-pup parallel mechanisms with bifurcated motion," *Mechanism and Machine Theory*, vol. 61, pp. 168 –183, 2013, ISSN: 0094-114X.

[156] S. Piipponen, E. Hyry, and T. Arponen, "Kinematic analysis of multi-4-bar mechanisms using algebraic geometry," in *International Design Engineering Technical Conferences and Computers and Information in Engineering Conference*, Cleveland, Ohio, USA, 2017.

[157] A. Müller and S. Piipponen, "On regular kinematotropies," in *14th World Congress in Mechanisms and Machine Science*, Taipei, Taiwan, 2015.

[158] W. Wunderlich, "Ein merkwürdiges zwölfstabgetriebe," *Österreichisches Ingenieurarchiv*, vol. 8, no. 2/3, pp. 224–228, 1954.

[159] A. Müller, "An overview of formulae for the higher-order kinematics of lower-pair chains with applications in robotics and mechanism theory," *Mechanism and Machine Theory*, vol. 142, p. 103 594, 2019, ISSN: 0094-114X.

[160] P. Schatz, *Rhytthmusforschung und Technik*. Stuttgart, Germany: Freies Geistesleben, 1975.

[161] C. C. Lee and J. S. Dai, "Configuration analysis of the Schatz linkage," *Proceedings of the Institution of Mechanical Engineers, Part C: Journal of Mechanical Engineering Science*, vol. 217, no. 7, pp. 779–786, 2003.

[162] D. Stewart, "A platform with six degrees of freedom," *Proceedings of the Institution of Mechanical Engineers*, vol. 180, no. 1, pp. 371–386, 1965.

[163] B. Dasgupta and T. Mruthyunjaya, "The Stewart platform manipulator: A review," *Mechanism and Machine Theory*, vol. 35, no. 1, pp. 15 –40, 2000, ISSN: 0094-114X.

[164] J. P. Merlet, *Parallel Robots*. Heidelberg, Germany: Springer Netherlands, 2006.

[165] X. Kong and C. M. Gosselin, *Type Synthesis of Parallel Mechanisms*. Springer-Verlag Berlin Heidelberg, 2007.

[166] K.-E. Neumann, *Robot*, US Patent US4732525A, 1985.

[167] B. Siciliano, "The Tricept robot: Inverse kinematics, manipulability analysis and closed-loop direct kinematics algorithm," *Robotica*, vol. 17, no. 4, 437–445, 1999.

[168] K.-E. Neumann, "The key to aerospace automation," in *SAE Technical Paper*, SAE International, Sep. 2006.

[169] ——, *Parallel-kinematical machine*, US Patent US20090205457A1, 2014.

[170] M. Shang and J. Butterfield, "The experimental test and fea of a PKM (Exechon) in a flexible fixture application for aircraft wing assembly," in *2011 IEEE International Conference on Mechatronics and Automation*, 2011, pp. 1225–1230.

[171] Z. M. Bi and Y. Jin, "Kinematic modeling of Exechon parallel kinematic machine," *Robotics and Computer-Integrated Manufacturing*, vol. 27, no. 1, pp. 186 –193, 2011.

[172] Y. Jin, Z. Bi, H. Liu, C. Higgings, M. Price, W. Chen, and T. Huang, "Kinematic analysis and dimensional synthesis of Exechon parallel kinematic machine for large volume machining," *Journal of Mechanisms and Robotics*, vol. 7, no. 4, 8 pages, 2015.

[173] M. Zoppi, D. Zlatanov, and R. Molfino, "Kinematics analysis of the Exechon tripod," in *International Design Engineering Technical Conferences and Computers and Information in Engineering Conference*, Montreal, Quebec, Canada, 2010, pp. 1381–1388.

[174] J. Zhang, Y. Zhao, and Y. Jin, "Kinetostatic-model-based stiffness analysis of Exechon PKM," *Robotics and Computer-Integrated Manufacturing*, vol. 37, pp. 208 – 220, 2016, ISSN: 0736-5845.

[175] ——, "Elastodynamic modeling and analysis for an Exechon parallel kinematic machine," *Journal of Manufacturing Science and Engineering*, vol. 138, pp. 138 –141, 2015.

[176] X. Li, D. Zlatanov, M. Zoppi, and R. Molfino, "Stiffness estimation and experiments for the Exechon parallel self-reconfiguring fixture mechanism," in *International Design Engineering Technical Conferences and Computers and Information in Engineering Conference*, Chicago, IL, Canada, 2012, pp. 637 –645.

[177] M. Wang, H. Liu, T. Huang, and D. G. Chetwynd, "Compliance analysis of a 3-SPR parallel mechanism with consideration of gravity," *Mechanism and Machine Theory*, vol. 84, pp. 99 –112, 2015, ISSN: 0094-114X.

[178] D. Zlatanov, M. Zoppi, and R. Molfino, "Constraint and singularity analysis of the Exechon tripod," in *International Design Engineering Technical Conferences and Computers and Information in Engineering Conference*, Chicago, IL, Canada, 2012, pp. 679 –688.

[179] S. Amine, S. Caro, and P. Wenger, "Constraint and singularity analysis of the Exechon," in *Mechanisms, Mechanical Transmissions and Robotics*, ser. Applied Mechanics and Materials, vol. 162, Trans Tech Publications, Apr. 2012, pp. 141–150.

[180] B. Hu, "Kinematically identical manipulators for the Exechon parallel manipulator and their comparison study," *Mechanism and Machine Theory*, vol. 103, pp. 117 – 137, 2016, ISSN: 0094-114X.

[181] Y. Jin and I.-M. Chen, "Effects of constraint errors on parallel manipulators with decoupled motion," *Mechanism and Machine Theory*, vol. 41, no. 8, pp. 912 –928, 2006, Special issue on CK 2005, International Workshop on Computational Kinematics.

[182] J. S. Dai and J. R. Jones, "Null space construction using cofactors from a screw algebra context," *Proceedings of the Royal Society of London. Series A: Mathematical, Physical and Engineering Sciences*, vol. 458, no. 2024, pp. 1845–1866, 2002.